

**Cross section of W and Z inclusive production
and the W/Z cross section ratio in association
with one jet for the boson decaying into
electron(s) with ATLAS 7 TeV data**

THÈSE

présentée à la Faculté des sciences de l'Université de Genève
pour obtenir le grade de Docteur ès sciences, mention physique

par

Elina Berglund

de la Suède

Thèse N° 4345



**UNIVERSITÉ
DE GENÈVE**

FACULTÉ DES SCIENCES

**Doctorat ès sciences
Mention physique**

Thèse de *Madame Frida Elina BERGLUND*

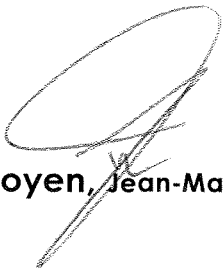
intitulée :

**"Cross Section of W and Z Inclusive Production and the
W/Z Cross Section Ratio in Association with One Jet for the
Boson Decaying into Electron(s) with ATLAS 7 TeV Data"**

La Faculté des sciences, sur le préavis de Messieurs A. G. CLARK, professeur ordinaire et directeur de thèse (Département de physique nucléaire et corpusculaire), D. FROIDEVAUX, docteur (Département de physique, CERN – Organisation Européenne pour la Recherche Nucléaire, Genève, Suisse), A. G. CLARK, professeur ordinaire (Département de physique nucléaire et corpusculaire), A. BRAVAR, docteur (Département de physique nucléaire et corpusculaire) et K. EINSWEILER, docteur (Lawrence Berkeley National Lab, Physics Division - CERN – Organisation Européenne pour la Recherche Nucléaire, Genève, Suisse), autorise l'impression de la présente thèse, sans exprimer d'opinion sur les propositions qui y sont énoncées.

Genève, le 14 septembre 2011

Thèse - 4345 -


Le Doyen, Jean-Marc TRISCONE

N.B.- La thèse doit porter la déclaration précédente et remplir les conditions énumérées dans les "Informations relatives aux thèses de doctorat à l'Université de Genève".

Till min Ralle

Acknowledgements

The last three years at CERN have provided me with a great opportunity to collaborate with numerous people in ATLAS from different universities and institutes. This has not only been an exciting experience but it has, I believe, also been a great support for achieving the results presented in this thesis. I would therefore like to take the opportunity to thank the many individuals who have supported me throughout my PhD.

Firstly, I am truly grateful to my professor and thesis advisor, Prof. Allan G. Clark, for giving me the opportunity to pursue a PhD in the UNIGE ATLAS group and for the constant encouragement during my time here. A very special thanks also goes to my post-doc and office mate, Jose E. Garcia Navarro, for following me closely and supporting me every step of the way. I would also like to thank my other UNIGE colleagues for improving my time at CERN both professionally and personally: Snežana, Alison, Andrew, Till, Andree, Valerio, Moritz, Francesca, Gauthier, Gaetano, Katalin, Will, Sergio, Xin, Szymon, Eleonora, Didier, Kilian, Paul, Anna, Marc, Clemencia and Gabi.

I would also like to thank the SCT people whom I shared many hours in the ATLAS control room with: Pippa Wells, Sandra Ciocio, Heinz Pernegger, Dave Robinson, Martin White, Nick Barlow, Per Johansson, Helen Hayward, Saverio D'Auria, Alex Kastanas, Heidi Sandaker, Lucie de Nooij and Chris Boddy.

A thanks to Daniel Froidevaux and Thomas Koffas for struggling together with me for more than a year to understand the cosmic electrons. I would also like to express my gratitude to the entire e/γ group for supporting me throughout my cosmic electrons and electron efficiency studies, especially Laurent Serin, Maria Fiascaris, Mauro Donega, Fabrice Hubaut, Sarah Heim, Olivier Arnaez and Andrea Bocci.

An additional thanks goes to my collaborators in the W/Z physics group, for working with me on cut flows and definitions to finally agree, resulting in beautiful first ATLAS electroweak results: Elzbieta Richter-Was, Manuella Vinciter, Matthias Schott, Maarten Boonekamp, Corinne Goy, Kevin Einsweiler, Lucia di Ciaccio, Jan Kretschmar, Jochen Hartert, Alessandro Tricoli, Thorsten Kuhl, Gerhard Brandt, Marisa Sandhoff, Hugo Beauchemin and many more.

Last but not least I would like to thank my family; my dad (the eternal professor)

for keeping me on my toes by always asking about the relevance of my research for the greater good of humankind, and my mom for never giving up on trying to grasp what it really is that I am doing. I would also like to take the opportunity to thank Louise for spending part of her PhD at CERN and hence keeping me company in Geneva. Finally, I would like to thank Raoul for standing by me during every day of my PhD, making the quality of life in Geneva the best in the world.

Abstract

This thesis investigates the inclusive production cross section of W and Z bosons as well as their ratio in association with one jet. The cross sections are estimated with 7 TeV LHC proton-proton collision data, collected by ATLAS during 2010, resulting in an integrated luminosity of approximately 40 pb^{-1} . This thesis focuses on the analysis performed in the electron channel, while comparisons with the results obtained in the muon channel also are included. This is the first time the W and Z production cross sections are measured at this center-of-mass energy and the results are important for various reasons, such as testing perturbative theoretical calculations and understanding these signatures as backgrounds to other physics processes. The final inclusive cross section values obtained in the electron channel are the following:

$$\begin{aligned}\sigma(W \rightarrow e\nu) &= 10.255 \pm 0.031(\text{stat}) \pm 0.190(\text{syst}) \pm 0.349(\text{lumi}) \pm 0.156(\text{acc}) \text{ nb} \\ \sigma(Z \rightarrow ee) &= 0.952 \pm 0.010(\text{stat}) \pm 0.026(\text{syst}) \pm 0.032(\text{lumi}) \pm 0.019(\text{acc}) \text{ nb}\end{aligned}$$

The results agree well with NNLO Standard Model predictions within the uncertainties of the measurement.

In addition, the measurement of $\sigma(W + 1jet)/\sigma(Z + 1jet)$ as a function of cumulative jet p_T is presented for the first time. This measurement has the advantage of partial and full cancellations of various uncertainties, which are parametrized in the equivalent p_T distribution. The results are found to be compatible within uncertainties with perturbative LO and NLO QCD predictions.

Résumé

Le détecteur ATLAS a accumulé avec succès des données depuis sa mise en service en 2008. Jusqu'aux premières collisions du LHC vers la fin de l'année 2009, des données issues de muons cosmiques ont été accumulées. Cette thèse présente des études de performance d'une part du détecteur intérieur d'ATLAS, et en particulier du détecteur à micro-pistes de silicium, le Semiconductor Tracker, sur les données prises pendant les périodes de maintenance et d'acquisition de données. De plus, les données de rayons cosmiques ont été analysées pour identifier les premiers électrons dans ATLAS. Environ 800 électrons ont pu être détectés parmi les millions de traces de muons enregistrées par le détecteur intérieur.

Pendant l'année 2010, une luminosité intégrée de 40 pb^{-1} de collisions proton-proton a été délivrée par le LHC à une énergie de $\sqrt{s} = 7 \text{ TeV}$. Cette thèse décrit les premières mesures de la section efficace inclusive des bosons W and Z ainsi que de leur rapport en association avec un jet de hadrons. Ces résultats se concentrent sur le désintégration des bosons en électrons, mais une comparaison avec les résultats des muons est également décrite. La mesure de l'efficacité de reconstruction et d'identification des électrons est parmi les composantes les plus importantes dans le calcul de la section efficace. Une méthode, basée sur les données, est utilisée pour déterminer un événement $Z \rightarrow ee$ en identifiant un des électrons et en appliquant le calcul d'efficacité pour le deuxième électron non-biaisé. Les mesures sont présentées en fonction de la pseudorapidité et de l'impulsion transverse des électrons.

Pour la première fois, les sections efficaces de W et Z sont mesurées à cette énergie dans le centre de masse. Ces résultats sont de grande importance pour beaucoup de raisons, notamment la comparaison avec les calculs perturbatifs théoriques et la compréhension de ces processus comme bruits de fond pour d'autres processus physiques. Les valeurs de la section efficace inclusive finale, obtenues dans le canal des électrons, sont les suivantes:

$$\begin{aligned}\sigma(W \rightarrow e\nu) &= 10.255 \pm 0.031(\text{stat}) \pm 0.190(\text{syst}) \pm 0.349(\text{lumi}) \pm 0.156(\text{acc}) \text{ nb} \\ \sigma(Z \rightarrow ee) &= 0.952 \pm 0.010(\text{stat}) \pm 0.026(\text{syst}) \pm 0.032(\text{lumi}) \pm 0.019(\text{acc}) \text{ nb}\end{aligned}$$

Ces résultats sont en accord avec les prédictions du modèle standard de la physique des particules et les erreurs sont déjà dominées par les incertitudes systématiques. De plus, la section efficace différentielle est calculée en fonction de la pseudorapidité des électrons pour le W , $d\sigma/d\eta^e$, et de la rapidité du boson pour le Z , $d\sigma/dy^Z$. La mesure différentielle est plus sensible aux fonctions de distributions de partons dans le proton que la section efficace inclusive.

Finalement, la mesure de $\sigma(W+1jet)/\sigma(Z+1jet)$ en fonction du seuil d'impulsion transverse (p_T) du jet est présentée pour la première fois. Cette mesure a l'avantage d'éliminer partiellement ou entièrement certaines incertitudes et permettrait éventuellement d'accéder à de la nouvelle physique avec plus de statistique à grand p_T des jets. Les résultats avec les prédictions perturbatives de chromodynamique quantique du premier et second ordre sont en accord.

List of Publications and Notes

Since all ATLAS published papers and notes have the whole collaboration as author, I hereby specify the public results (papers and conference notes), together with their supporting internal notes that I have personally and directly contributed to during the course of completing the PhD.

Papers about to be published:

- The ATLAS Collaboration, G. Aad, et al., *Study of the W -boson production with jets in pp collisions at $\sqrt{s} = 7$ TeV with the ATLAS detector*, To be submitted to: Phys. Rev. D (2011) no. ATLAS-STDM-2011-08. With supporting document:
 - G. Arabidze, E. Berglund et al., *Measurement of the cross section for jets produced in association with a W -boson in pp collisions at $\sqrt{s} = 7$ TeV*, ATL-COM-PHYS-2011-769, CERN, Geneva, May, 2011.
- The ATLAS Collaboration, G. Aad, et al., *A measurement of the ratio of the W and Z cross sections with one associated jet in pp collisions at $\sqrt{s} = 7$ TeV with the ATLAS detector*, To be submitted to: Phys. Lett. B (2011) no. CERN-PH-EP-2011-126; arXiv:1108.4908v1. With supporting document:
 - R. Apolle, S. Ask, M. Barisonzi, H. Beauchemin, E. Berglund et al., *A measurement of the ratio of the $W + 1$ jet to $Z + 1$ jet cross sections with ATLAS*, ATL-COM-PHYS-2011-457, CERN, Geneva, May, 2011.
- The ATLAS Collaboration, G. Aad, et al., *A measurement of the inclusive W^\pm and Z/γ^* cross sections in the e and μ decay channels in pp collisions at $\sqrt{s} = 7$ TeV with the ATLAS detector*, To be submitted to: PRD (2011) no. CERN-PH-EP-2011-143. With supporting document:
 - M. Aharrouche, G. Artoni, M. Bellomo, A. Belloni, E. Berglund et al., *Total and differential $W \rightarrow \ell\nu$ and $Z \rightarrow \ell\ell$ cross-sections measurements*

in proton-proton collisions at $\sqrt{s} = 7$ TeV with the ATLAS Detector, ATL-COM-PHYS-2011-751, CERN, Geneva, June, 2011.

- The ATLAS Collaboration, G. Aad, et al., *Electron performance measurements with the ATLAS detector using the proton-proton collision data*, To be submitted to: Eur. Phys. J. C (2011) no. CERN-PH-EP-2011-117. With relevant supporting document:
 - G. Aad, E. Berglund et al., *Electron efficiency measurements using ATLAS 2010 data at $\sqrt{s} = 7$ TeV: Supporting note for the 2010 egamma paper*, ATL-COM-PHYS-2011-322, CERN, Geneva, March, 2011.
- The ATLAS Collaboration, G. Aad, et al., *Measurement of the production cross section for Z/γ^* in association with jets in pp collisions at $\sqrt{s} = 7$ TeV with the ATLAS Detector*, To be submitted to: Phys. Rev. D (2011) no. ATLAS-STDM-2011-27. With supporting document:
 - E. Berglund et al., *Measurement of the cross section for jets produced in association with Z bosons*, ATL-COM-PHYS-2011-647, CERN, Geneva, June, 2011.
- The ATLAS Collaboration, G. Aad, et al., *Measurement of the b-jet cross section in events with a W boson in pp collisions at $\sqrt{s} = 7$ TeV*, To be submitted to: Phys. Lett. B. (2011) no. ATLAS-STDM-2011-21. With supporting document:
 - G. Aad, E. Berglund et al., *Measurement of the b-jet cross section in events with a W boson*, ATL-COM-PHYS-2011-411, CERN, Geneva, June, 2011.
 - The ATLAS Collaboration, G. Aad et al., *Performance of the ATLAS Trigger System in 2010*, To be submitted to: Eur. Phys. J. C (2011) no. CERN-PH-EP-2011-078. With relevant supporting document:
 - * H. S. Bansil, E. Berglund, et al., *Performance of the Electron and Photon Trigger in p-p Collisions at $\sqrt{s} = 7$ TeV*, ATL-COM-DAQ-2011-008, CERN, Geneva, Jan, 2011.

Published papers:

- The ATLAS Collaboration, G. Aad et al., *Measurement of the production cross section for W-bosons in association with jets in pp collisions at $\sqrt{s} = 7$ TeV with the ATLAS detector*, 698 (2011) no. arXiv:1012.5382. CERN-PH-EP-2010-081, 12. With supporting document:

- A. Ahmad, P. Beauchemin, E. Berglund, et al., *Measurement of the cross-section for jets produced in association with a W -boson in pp collisions at $\sqrt{s} = 7$ TeV*, ATL-PHYS-INT-2011-020, CERN, Geneva, Mar, 2011.
- The ATLAS Collaboration, G. Aad et al., *Measurement of the $W \rightarrow \ell\nu$ and $Z/\gamma^* \rightarrow \ell\ell$ production cross section in proton-proton collisions at $\sqrt{s} = 7$ TeV with the ATLAS detector*, J. High Energy Physics **12** (2010) no. arXiv:1010.2130. CERN-PH-EP-2010-037, 1-65. With supporting documents:
 - M. Aharrouche, A. Ahmad, J. Alison, O. Arnaez, I. Besana, T. Berry, H. S. Bawa, K. Benslama, E. Berglund, et al., *W $\rightarrow e\nu$ and Z $\rightarrow ee$ cross section measurements in proton-proton collisions at $\sqrt{s} = 7$ TeV with the ATLAS Detector*, ATL-PHYS-INT-2010-130, CERN, Geneva, Dec, 2010.
 - M. Aharrouche, A. Ahmad, J. Alison, O. Arnaez, J. Barreiro Guimaraes da Costa, H. S. Bawa, M. Bellomo, A. Belloni, K. Benslama, E. F. Berglund, et al., *Supporting Document: Total inclusive W and Z boson cross-section measurements, cross-section ratios and combinations in the electron and muon decay channels at 7 TeV based on 300 nb⁻¹*, ATL-PHYS-INT-2010-125, CERN, Geneva, Nov, 2010.
 - A. Belloni, M. Aharrouche, A. Ahmad, J. Alison, O. Arnaez, J. Barreiro Guimaraes da Costa, H. S. Bawa, M. Bellomo, A. Belloni, K. Benslama, E. F. Berglund, et al., *Measurement of W $\rightarrow \ell\nu$ charge asymmetry in proton-proton collisions at $\sqrt{s} = 7$ TeV with the ATLAS detector*, ATL-COM-PHYS-2010-696, CERN, Geneva, Aug, 2010.
- The ATLAS Collaboration, G. Aad et al., *Studies of the performance of the ATLAS detector using cosmic-ray muons*, Eur. Phys. J. C **71** (2011) 1-36. arXiv:1011.6665. CERN-PH-EP-2010-070. With relevant supporting document:
 - E. Berglund, D. Froidevaux, J. E. Garcia Navarro and T. Koffas *Low momentum electrons in ATLAS cosmic ray data*, ATL-PHYS-INT-2010-033, CERN, Apr, 2010.

Conference notes:

- The ATLAS Collaboration, G. Aad et al., *Measurement of the production cross section for W-bosons in association with jets in pp collisions using 33 pb⁻¹ at $\sqrt{s} = 7$ TeV with the ATLAS detector*, ATLAS-CONF-2011-060, CERN, Geneva, Apr, 2011. With supporting document:

- G. Arabidze, E. Berglund, et al., *Measurement of the cross-section for jets produced in association with a W-boson in pp collisions at $\sqrt{s} = 7$ TeV*, ATL-COM-PHYS-2011-280, CERN, Geneva, Mar, 2011.
- The ATLAS Collaboration, G. Aad et al., *Measurement of the production cross section for Z/γ^* in association with jets in pp collisions at $\sqrt{s} = 7$ TeV with the ATLAS Detector*, ATLAS-CONF-2011-042, CERN, Geneva, Mar, 2011.
 - H. Bauchemin, E. Berglund et al., *Measurement of the cross section for jets produced in association with Z bosons*, ATL-COM-PHYS-2011-141, CERN, Geneva, Feb, 2011.
- The ATLAS Collaboration, G. Aad et al., *A measurement of the total W^\pm and Z/γ^* cross sections in the e and μ decay channels and of their ratios in pp collisions at $\sqrt{s} = 7$ TeV with the ATLAS detector*, ATLAS-CONF-2011-041, CERN, Geneva, Mar, 2011. With supporting document:
 - M. Aharrouche, G. Artoni, J. Barreiro Guimaraes da Costa, M. Bellomo, A. Belloni, E. Berglund, et al., *W and Z cross-sections measurements in proton-proton collisions at $\sqrt{s} = 7$ TeV with the ATLAS Detector*, ATL-COM-PHYS-2011-178, CERN, Geneva, Feb, 2011.
- The ATLAS Collaboration, G. Aad et al., *Measurement of the production cross section for Z/γ^* in association with jets in pp collisions at $\sqrt{s} = 7$ TeV with the ATLAS Detector*, ATLAS-CONF-2011-001, CERN, Geneva, Feb, 2011. With supporting document:
 - H. Bauchemin, E. Berglund, et al., *Measurement of the cross-section for jets produced in association with a Z-boson in pp collisions at $\sqrt{s} = 7$ TeV*, ATL-PHYS-INT-2011-006, CERN, Geneva, Feb, 2011.
- The ATLAS Collaboration, G. Aad et al., *Measurement of the $Z \rightarrow \ell\ell$ production cross section in proton-proton collisions at $\sqrt{s} = 7$ TeV with the ATLAS detector*, ATLAS-CONF-2010-076, CERN, Geneva, Jul, 2010.
- The ATLAS Collaboration, G. Aad et al., *Measurement of the $W \rightarrow \ell\nu$ production cross-section and observation of $Z \rightarrow \ell\ell$ production in proton-proton collisions at $\sqrt{s} = 7$ TeV with the ATLAS detector*, ATLAS-CONF-2010-051, CERN, Geneva, Jul, 2010. With supporting documents:
 - A. Ahmed, J. Alison, M. Bellomo, A. Belloni, E. Berglund, et al., *Supporting Document: Measurement of the W cross section and asymmetry in the electron and muon decay channels at $\sqrt{s} = 7$ TeV*, ATL-PHYS-INT-2010-116, CERN, Geneva, Sep, 2010.

- M. Aharrouche, A. Ahmad, J. Alison, A. Arnaez, I. Besana, T. Berry, H. Bawa, K. Benslama, E. Berglund, et al., *W → eν and Z → ee observation supporting note*, ATL-PHYS-INT-2010-109, CERN, Geneva, Sep, 2010.
- The ATLAS Collaboration, G. Aad et al., *Observation of W → lν and Z → ll production in proton-proton collisions at √s = 7 TeV with the ATLAS detector*, ATLAS-CONF-2010-044, CERN, Geneva, Jul, 2010. With electron supporting document:
 - A. Ahmad, J. Alison, A. Arnaez, I. Besana, T. Berry, H. Bawa, K. Benslama, E. Berglund, et al., *W → eν and Z → ee observations supporting note*, ATL-PHYS-INT-2010-108, CERN, Geneva, Sep, 2010.

Contents

Acknowledgements	iv
Abstract	vi
Résumé	vii
List of Publications and Notes	ix
1 Introduction	1
2 Theoretical Background and Motivation	3
2.1 The Standard Model of Particle Physics	4
2.2 W/Z physics at the LHC	6
2.2.1 Production processes at hadron colliders	7
2.2.2 Decay of massive vector bosons	10
2.2.3 Inclusive and differential W and Z cross sections	12
2.2.4 W and Z bosons in association with jets	14
2.2.5 $\mathcal{R}_{\text{jets}} = \sigma(W + \text{jets})/\sigma(Z + \text{jets})$	15
2.2.6 Prospects for early measurements in the electroweak sector . .	16
2.3 Monte Carlo generators	16
3 The ATLAS Experiment at the LHC	19
3.1 The Large Hadron Collider	20
3.1.1 The CERN accelerator complex	21
3.1.2 The functionality of the LHC	21
3.1.3 The path towards LHC physics	24
3.1.4 Different experiments at the LHC	25
3.2 Overview of the ATLAS detector	26
3.2.1 Orientation	29
3.2.2 The Inner Detector	29
3.2.3 Calorimetry	33

3.2.4	The muon spectrometer	37
3.2.5	Forward detectors	38
3.2.6	ATLAS data acquisition and trigger system	39
3.3	The Semi-Conductor Tracker	42
3.3.1	Description and design of the SCT	42
3.3.2	SCT modules and front-end electronics	43
3.4	Summary	45
4	Commissioning of ATLAS	46
4.1	Cosmic ray data collected by ATLAS prior to first collisions	46
4.2	Installation and commissioning of the Semiconductor Tracker	49
4.2.1	SCT installation and integration in ATLAS	49
4.2.2	SCT performance results with cosmic ray data	51
4.2.3	SCT with collision data	53
4.3	Online Data Quality Monitoring of the SCT	54
4.3.1	The Athena monitoring framework	55
4.3.2	The Data Quality Monitoring Display	59
4.3.3	The Online Histogramming Presenter	61
4.3.4	Recent progress and future outlook for the SCT monitoring	64
4.4	Identifying electrons in cosmic ray data	65
4.4.1	The nature of electrons in cosmic ray events	66
4.4.2	Data samples considered in the analysis	67
4.4.3	Reconstruction of electrons in cosmic ray data	68
4.4.4	Tracking with cosmic rays	68
4.4.5	Electromagnetic topological clusters in the calorimeter	69
4.4.6	Matching between track and cluster	71
4.4.7	Electron identification	72
4.4.8	Truth matching with the Monte Carlo sample	72
4.4.9	Track selection	73
4.4.10	Cluster requirements	73
4.4.11	Final requirements after track-cluster matching	74
4.4.12	Background estimation	78
4.4.13	Positrons among the electron signal	80
4.4.14	Results	81
4.5	Conclusion	84
5	Electron Efficiency Measurement Using the $Z \rightarrow ee$ Tag-and-Probe Method	86
5.1	Electron reconstruction and identification in ATLAS	87
5.1.1	Reconstruction algorithms	87

5.1.2	Electron identification	88
5.1.3	Reconstruction and identification efficiency	89
5.2	$Z \rightarrow ee$ tag-and-probe methodology	89
5.2.1	Tag and probe selection	92
5.2.2	Track quality	94
5.2.3	Background subtraction	96
5.2.4	Efficiency estimates from Monte Carlo events	101
5.3	η dependent efficiencies	104
5.3.1	Estimated background with the OS-SS sideband method	104
5.3.2	Reconstruction and track quality efficiency vs η	106
5.3.3	Identification efficiency vs η	107
5.3.4	Official e/γ ID efficiency scale factors	111
5.4	E_T dependent efficiencies	115
5.4.1	Efficiency vs E_T measured by fitting M_{ee}	116
5.4.2	Efficiency vs E_T measured by fitting the E_T distribution	119
5.4.3	Official e/γ ID efficiency scale factors	124
5.5	Electron trigger efficiency	125
5.6	Conclusion	128
6	$W \rightarrow e\nu$ and $Z \rightarrow ee$ Inclusive Cross Section Measurements with ATLAS 2010 Data	130
6.1	W/Z cross section analysis methodology	132
6.1.1	Data and Monte Carlo samples	132
6.1.2	W/Z event selection	133
6.1.3	Cross section calculation	135
6.2	First inclusive W and Z results with $< 1 \text{ pb}^{-1}$	138
6.2.1	W/Z observation and cross section with the very first data	138
6.2.2	W and Z cross section measurement with 315 nb^{-1}	139
6.3	W and Z cross section measurement with ATLAS 2010 data (36 pb^{-1})	144
6.3.1	Reconstruction efficiency	145
6.3.2	Identification efficiency	145
6.3.3	Charge mis-identification probability	151
6.3.4	Trigger efficiency	152
6.3.5	Electron energy scale and resolution	152
6.3.6	Background estimation	154
6.3.7	Signal acceptances	155
6.3.8	Preliminary results with the 2010 dataset	157
6.3.9	Improved analysis for differential measurements	161
6.4	Conclusion	173

7	The \mathcal{R}_{jets} Measurement	176
7.1	\mathcal{R}_{jets} analysis methodology	177
7.1.1	Data and MC samples	177
7.1.2	Theoretical predictions	178
7.1.3	Jet reconstruction	180
7.1.4	Event selection	182
7.1.5	Control distributions	183
7.1.6	Cross section ratio calculation	184
7.2	Electron efficiencies in the \mathcal{R}_{jets} measurement	184
7.2.1	Tag-and-probe results with release 15	185
7.2.2	Boson reconstruction correction	186
7.2.3	Electron identification efficiencies in MC	186
7.2.4	Electron efficiencies as a function of jet kinematics	187
7.2.5	Correcting the \mathcal{R}_{jets} results for the efficiency ratio	189
7.2.6	Systematic uncertainty on the efficiency ratio	190
7.2.7	Trigger efficiency	191
7.3	Additional corrections and uncertainties	192
7.3.1	Background estimation	192
7.3.2	Pile-up and JVF	194
7.3.3	Correction of the jet spectrum	195
7.3.4	Jet energy scale and resolution	197
7.4	The resulting ratio	197
7.4.1	\mathcal{R}_{jets} results in the fiducial phase space	197
7.4.2	Generator level acceptances	200
7.4.3	\mathcal{R}_{jets} results extrapolated to full phase space	202
7.5	Conclusion	204
8	Conclusions	207
A	2010 Data Periods	210
B	Tag-and-probe efficiency and background tables	211
C	W/Z differential cross section tables	221
	Bibliography	225

Chapter 1

Introduction

The quest for understanding nature and our universe in the most fundamental way has a long-standing history, dating back thousands of years. Around 450 BC, the Greek philosopher Democritus stated that our world is composed of *atoms*, meaning “indivisible”. Although, the word lost its meaning through the discoveries of the particles that the modern atom is composed of, the desire to understand the fundamental constituents of matter remains. The currently accepted hypothesis describing the fundamental particles and underlying forces of the universe, is known as the *Standard Model of Particle Physics* (SM). The theory has been essentially unchanged since the 1970’s. Since it has been proven remarkably accurate, through the successful discoveries of all predicted particles except for the Higgs boson, it has been rewarded with several Nobel prizes during the late 20th century.

To search for the yet undiscovered Higgs boson, which explains the origin of mass, as well as to answer some of the questions that the SM does not address, such as incorporating the gravitational force and understanding dark matter, the world’s currently most powerful particle accelerator, the Large Hadron Collider, was built. The LHC currently collides protons at a centre-of-mass energy of 7 TeV, producing numerous elementary particles in each collision that are then detected by the particle detectors situated at the four collision points. The data analyzed in this thesis have been collected by the ATLAS detector during 2010 operation, which corresponds to about 40 pb^{-1} of integrated luminosity. ATLAS is a general purpose detector, designed to be able to answer as many of the unresolved questions in particle physics as possible. It is however crucial to first measure the already existing spectrum of SM particles in order to explore the new energy regime of the LHC as well as to understand the performance of the detector with a good accuracy.

The study of W and Z leptonic decays is one of the first milestones in the ATLAS physics program for early LHC data. The production cross sections are predicted theoretically at the few percent level, so a precise measurement of W and Z production

will provide a stringent test of the perturbative QCD calculations. The high rates provided by the LHC allow for early measurements of these properties, resulting in a better understanding of the strong interaction and parton distribution function (PDF) uncertainties.

A data-driven measurement of electron efficiencies, both in terms of absolute normalization and of relative shapes, is discussed in this thesis. This is a key aspect towards precision measurements of W and Z inclusive cross sections in the electron channel. The electron efficiency results are incorporated in the inclusive W/Z cross section analysis, as well as the differential cross section measured as a function of electron pseudorapidity in the case of the $W \rightarrow e\nu$ channel and boson rapidity in the case of the $Z \rightarrow ee$ channel that are presented in this thesis. Such differential cross section results will provide excellent sensitivity for constraining the proton PDFs.

In addition, the measurement of the W and Z production cross section ratio in association with one jet (\mathcal{R}_{jets}), completed with the 2010 data, is included in this thesis. The uncertainty cancellations in the ratio improve the sensitivity of the measurement and can be exploited when searching for new physics with electrons, missing transverse energy and hard jets as possible final state signatures. The \mathcal{R}_{jets} results are presented as a function of minimum jet p_T threshold within the range of 30 to 190 GeV.

The ATLAS detector is described, focusing on the detector elements that are important for measuring and identifying electrons. Prior to first LHC collisions at the end of 2009, the ATLAS detector was commissioned by recording cosmic ray muon events. As the tracking performance is a crucial component of the electron reconstruction, the commissioning of one of the main tracking devices in ATLAS, the Semiconductor Tracker (SCT), is discussed in detail. The author has contributed to the development of the data quality monitoring of the SCT. In addition, a study of the identification of delta-ray electrons produced by cosmic ray muons in the detector, is presented.

The tasks and analyses performed during the course of the doctoral studies are multiple and diverse and to limit the length of this thesis, not all the work completed is documented here. This thesis attempts to discuss the major analyses and contributions, while other results are briefly summarized and referenced. All results and figures included in the thesis which were not directly produced by the author alone are referenced.

Chapter 2

Theoretical Background and Motivation

The purpose of this thesis is to assess a first measurement of the inclusive W and Z production cross sections in the electron decay channel and their ratio \mathcal{R} , in particular in the presence of hadronic jets. The study of the production of W and Z bosons is fundamental in several aspects. Firstly, the calculation of the higher-order corrections to these color-singlet final states is well advanced and measurements in this field provide a stringent test of quantum chromodynamics (QCD). Secondly, the clean and fully reconstructed leptonic final state of the Z boson allow for a precise measurement of the transverse momentum distribution providing further constraints on non-perturbative aspects related to the summation of initial parton emissions. Also, a measurement of the rapidity distribution of the Z is of significant importance since it is a direct probe of the parton density functions (PDFs) of the proton. In the case of the W , the differential cross section as a function of lepton pseudorapidity as well as the charge asymmetry will provide early constraints on the PDFs. The high counting rates for these processes at the Large Hadron Collider will bring significant improvement on these aspects with early data.

From the experimental point of view, the precisely measured properties of the W and Z leptonic decays at LEP and at the Tevatron aid in providing an initial understanding of the detector performance, which is crucial for the first data-taking periods of the experiment. The mass, width and leptonic decays of the bosons can be exploited to measure the detector resolution, the energy and momentum scale as well as the lepton identification efficiency to a high precision.

Finally, a number of fundamental electroweak parameters can be accessed through W and Z final states; the mass of the W (M_W) through the W boson decay distributions, $\sin^2\theta_W$ via the forward-backward asymmetry of the Z boson and the lepton universality by comparing the measured electron and muon cross sections. These

measurements are longer-term projects that are beyond the scope of this thesis, but an initial understanding of the hadronic environment at the LHC is a first crucial step.

This chapter briefly describes the Standard Model of Particle Physics in section 2.1, followed by a more detailed description of W/Z theoretical predictions and prospects for such measurements at the LHC in section 2.2. The theoretical background and advantages of the W/Z ratio in association with jets (\mathcal{R}_{jets}) are also discussed in this section. Finally, section 2.3 summarizes the different Monte Carlo event generators that are utilized in this thesis.

2.1 The Standard Model of Particle Physics

The Standard Model of Particle Physics (SM), which has been developed over the last fifty years, describes the elementary particles and their interactions that comprise our world. The model is divided into particles of matter (quarks and leptons) and force mediating particles (gauge bosons). All particles have corresponding anti-particles, except for the neutral gauge bosons that constitute their own anti-particles. There are three generations of quarks and leptons, where each generation is a more massive duplicate of the former. It is not known why nature is duplicating itself in this manner. A summary of the fundamental particles of the Standard Model can be found in Table 2.1.

Particle	Species	Spin
Quarks	u, d, c, s, t, b $\bar{u}, \bar{d}, \bar{c}, \bar{s}, \bar{t}, \bar{b}$	1/2
Leptons	e^\pm, μ^\pm, τ^\pm $\nu_e, \nu_\mu, \nu_\tau, \bar{\nu}_e, \bar{\nu}_\mu, \bar{\nu}_\tau$	1/2
Bosons	W^\pm, Z, γ, g	1
	Postulated: H	0

Table 2.1: Overview of the fundamental particles of the Standard Model. The Higgs particle (H) has yet to be discovered.

The theory of the Standard Model is constructed through imposing local gauge invariance on the quantized fields describing the fundamental particles, which leads to the emergence of gauge fields. The gauge field operators induce the force-mediating bosons such as the photon, W^\pm , Z^0 bosons and the gluons. The gauge symmetry group of the Standard Model is the following

$$\mathcal{G}_{SM} = SU(3)_C \otimes SU(2)_L \otimes U(1)_Y, \quad (2.1)$$

where Y represents hypercharge, L left-handed helicity and C color charge as the conserved quantities of the symmetry group. The symmetry group $SU(2)_L \otimes U(1)_Y$ represents the electroweak sector (quantum electrodynamics, QED, together with the weak interactions), while the addition of the group $SU(3)_C$ includes quantum chromodynamics (QCD). The corresponding charge of the $SU(2)$ group is the weak isospin, T . The electron charge, Q , is defined as $Q = T^3 + Y/2$. The imposition of gauge symmetry \mathcal{G}_{SM} on the group assumes the massless gauge fields; A_μ^i ($i = 1, 2, 3$), B_μ and eight gluons.

For the gauge bosons to acquire their proper mass, the electroweak gauge symmetry is broken spontaneously by the Higgs mechanism within the theory of the Standard Model. This infers that a scalar field ϕ in the spinor representation of $SU(2)$ must be added to the gauge theory to spontaneously break the symmetry (for more details, consult [1]). The SM gauge symmetry is broken in the following way.

$$\mathcal{G}_{SM} \rightarrow SU(3)_C \otimes U(1)_Q, \quad (2.2)$$

If the field ϕ acquires a vacuum expectation value of the form

$$\langle \phi \rangle = \frac{1}{\sqrt{2}} \begin{pmatrix} 0 \\ v \end{pmatrix} \quad (2.3)$$

a gauge transformation in $SU(2) \otimes U(1)$ then leaves $\langle \phi \rangle$ invariant. After the spontaneous symmetry breaking, the W^\pm , Z^0 and the photon are described by linear combinations of A_μ^i and B_μ such that W^\pm and Z^0 acquire mass terms proportional to the arbitrary coupling parameters, g and g' (which depend on the weak mixing angle, θ_W ; $g'/g = \tan \theta_W$), while the photon remains massless:

$$\begin{aligned} W_\mu^\pm &= \frac{1}{\sqrt{2}}(A_\mu^1 \mp iA_\mu^2), & \text{with mass } m_W &= g\frac{v}{2} \\ Z_\mu^0 &= \frac{1}{\sqrt{2}}(gA_\mu^3 - g'B_\mu), & \text{with mass } m_Z &= \sqrt{g^2 + g'^2}\frac{v}{2} \\ A_\mu^\pm &= \frac{1}{\sqrt{g^2 + g'^2}}(gA_\mu^3 + g'B_\mu), & \text{with mass } m_A &= 0 \end{aligned} \quad (2.4)$$

$$(2.5)$$

A_μ is the electromagnetic potential orthogonal to Z_μ^0 . The Higgs mechanism provides mass for the charged fermions (quarks and leptons) in a similar manner. The exact value of the masses are however not predicted directly by the theory, due to the

presence of arbitrary coupling constants.

An important consequence of the spontaneous symmetry breaking is the scalar field, ϕ , that must be added to the Lagrangian, which generates a massive scalar boson known as the Higgs boson. Since this section only crudely summarizes the principles of the Standard Model, consult [1] and [2] for more details.

The Standard Model has experimentally been proven to be remarkably successful in predicting the elementary constituents of matter and their interactions, but there are certain limitations with the theory as well as an inelegance since it includes numerous arbitrary and unrelated parameters. Examples of a limitation with the SM is that it does not incorporate mixing in the neutrino sector, assuming massless neutrinos, which has been proven to be wrong [3]. The theory also does not attempt to explain gravitation which becomes important at the Planck scale (10^{19} GeV). The vast difference between the Planck scale and the scale of the particle masses, which have been precisely measured by different experiments, is known as the *hierarchy problem*. Furthermore, the SM does not explain the matter-antimatter asymmetry observed in the universe and does not provide a satisfactory dark matter candidate. In order to extend the SM to account for these shortcomings, various Beyond the Standard Model (BSM) theories have developed over the past years and decades. One of the more popular extensions is known as *Supersymmetry*, which searches at the LHC experiments will hopefully confirm or exclude.

2.2 W/Z physics at the LHC

The vector bosons, W^\pm and Z^0 , were predicted by Glashow, Weinberg and Salam in the 1960's in order to formulate a theory of the weak nuclear force and simultaneously incorporate quantum electrodynamics [1, 2]. Weak neutral currents were first observed in the Gargamelle bubble chamber in 1973 and the W and Z particles themselves were discovered by the UA1 and UA2 experiments at the CERN $p\bar{p}$ collider in 1983 [4, 5, 6, 7].

Since their discovery, the W and Z bosons have been extensively studied at the CERN LEP e^+e^- collider [8] and at the Fermilab Tevatron $p\bar{p}$ collider [9, 10]. The currently most precise value of their respective masses and widths are [11]:

$$M_W = 80.399 \pm 0.023 \text{ GeV} \tag{2.6}$$

$$\Gamma_W = 2.085 \pm 0.042 \text{ GeV} \tag{2.7}$$

$$M_Z = 91.1876 \pm 0.0021 \text{ GeV} \tag{2.8}$$

$$\Gamma_Z = 2.4952 \pm 0.0023 \text{ GeV} \tag{2.9}$$

2.2.1 Production processes at hadron colliders

In a hadron collider such as the LHC, the electroweak gauge bosons (V ; W and Z) are produced at leading order (LO) via a parton-parton interaction (hard scattering) from constituents of the colliding hadrons [12]. The additional partons in the event will undergo *fragmentation* (hadronization), implying that they will form colorless hadrons from the existing free gluons and quarks that did not take part in the hard scattering. This additional hadronic activity from the beam remnants results in hadronic deposits in the detector and is referred to as the *underlying event*. Figure 2.1 illustrates the LO production process of the vector bosons together with the underlying event.

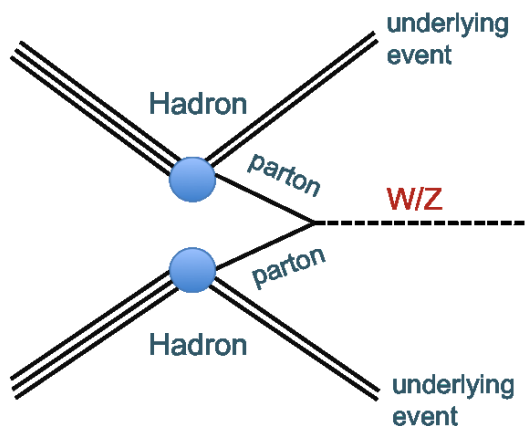


Figure 2.1: A schematic illustration of the W/Z boson production process in a hadron collider through hard scattering of the incoming partons in the collision. The additional partons undergo fragmentation and result in hadronic deposits in the detector.

The leading order W/Z production process at LHC (as well as at the Tevatron) occurs through Drell-Yan annihilation of an incoming quark-antiquark pair, $q\bar{q} \rightarrow V$, which occurs about 65% of the time [13]. Both valence-sea and sea-sea quark interactions contribute to the process. The dominant higher order correction is the scattering of a quark with a gluon, which contributes roughly with 20% to the overall cross section. To higher order the bosons can be produced in association with one or several hard gluons or quarks, which are reconstructed as hadronic jets in the detector. Figure 2.2 shows the leading order Feynman diagrams of the production process of W and Z , with leptonic decay mode, in the zero and one jet case. A summary of the LO, next-to leading order (NLO) and next-to-next-to leading order (NNLO) contributions to the W and Z production is listed in Table 2.2.

The probability of producing a specific particle in a single collision is represented by their cross section, σ , which is a function of several non-trivial variables. The

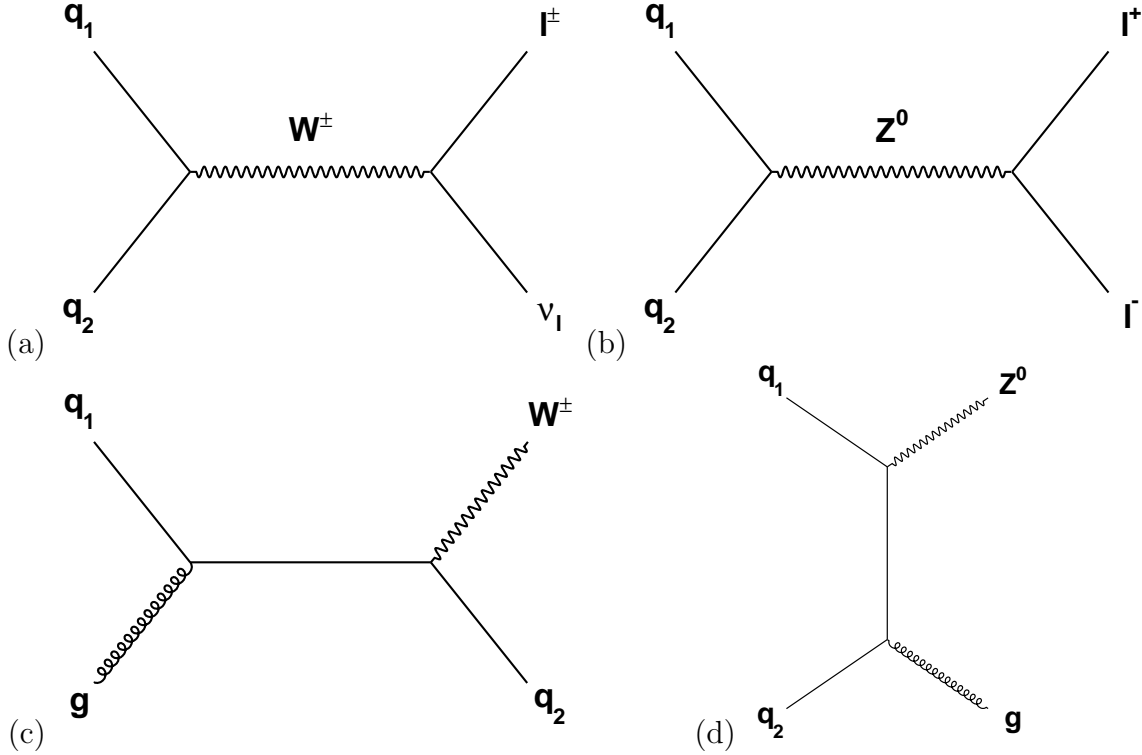


Figure 2.2: LO Feynman diagrams for production of W and Z bosons in a hadron collider with leptonic decay mode for (a) W and (b) Z and NLO production in association with one jet for (c) W and (d) Z .

cross section is calculated from the sum of the individual amplitudes for each initial state shown in Table 2.2. The likelihood of these processes is mainly affected by the momentum distribution of the incoming partons and the energy scale of the momentum transfer of the interacting particles. The cross section of an interaction can be estimated by employing parton density functions (PDFs), $f(x_i, Q^2)$ [14]. Each PDF gives the probability density of a particular parton i (i.e. valence quark, sea quark or gluon) in a hadron for a given energy scale of the process, Q^2 , as a function of the momentum fraction of the parton:

$$x_i = \frac{p_i}{P} = \frac{p_i}{\sqrt{s}/2}, \quad (2.10)$$

where \sqrt{s} is the centre-of-mass energy of the collider. The energy scale, Q^2 , is given by the sum of the four vectors of the partons entering the interaction. In case of the LO resonant scattering $q\bar{q} \rightarrow V$, the energy scale is given by:

Order	W/Z production sub-processes
α_s^0	$q + \bar{q} \rightarrow V$
α_s^1	$q + \bar{q} \rightarrow V$ (one-loop correction)
	$q + \bar{q} \rightarrow V + g$ $q(\bar{q}) + g \rightarrow V + q(\bar{q})$
α_s^2	$q + \bar{q} \rightarrow V$ (two-loop correction)
	$q + \bar{q} \rightarrow V + g$ (one-loop correction)
	$q + \bar{q} \rightarrow V + g + g$
	$q(\bar{q}) + g \rightarrow V + q(\bar{q})$ (one-loop correction)
	$q(\bar{q}) + g \rightarrow V + q(\bar{q}) + g$
	$q + \bar{q} \rightarrow V + q + \bar{q}$ $q(\bar{q}) + q(\bar{q}) \rightarrow V + q(\bar{q}) + q(\bar{q})$ $g + g \rightarrow V + q + \bar{q}$

Table 2.2: The different contributing processes to the production of W/Z bosons (denoted V) for LO, NLO and NNLO at the LHC.

$$Q^2 = (p_1^\mu + p_2^\mu)^2 = sx_1x_2 = M_V^2. \quad (2.11)$$

Also, the momentum fraction of the respective parton flavors depend strongly on the energy scale of the process in question. Examples of quark and gluon PDFs for two different energy scales can be seen in Figure 2.4.

Perturbative QCD is not sufficient to properly calculate the PDFs needed for determining the hadronic cross section, so the PDFs must therefore be estimated from data. Fortunately, PDFs are universal and can be evaluated using existing data from other colliders and applied to simulations made for the LHC experiments. In data, it is only possible to measure the four vectors of the final states of the interacting particles in the event. For theoretical calculations of proton-proton scattering, the initial states are input parameters that need to be known to make predictions of cross sections, etc. The initial states are described by the PDFs and the only way to gain information about them is to conduct measurements with a certain sensitivity to the PDFs.

The number of W/Z bosons produced in a collider is simply the product of the cross section and the integrated luminosity produced by the accelerator; $N_V = \sigma_V \times \int \mathcal{L}$. The predicted cross sections of different processes, including W and Z bosons, are shown in Figure 2.3 as a function of \sqrt{s} .

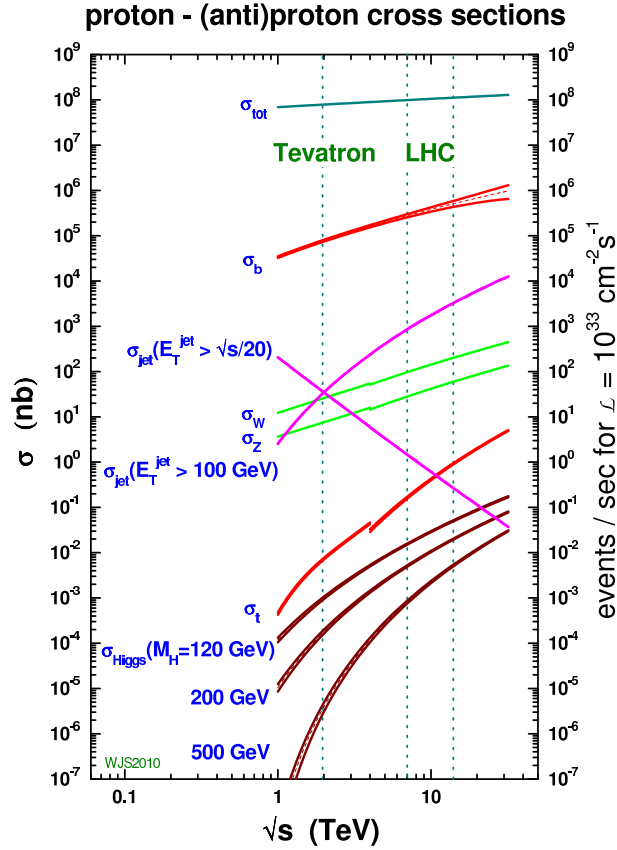


Figure 2.3: Cross sections for different processes in hadron colliders as a function of centre-of-mass energy. The centre-of-mass energy of the Tevatron and the current as well as the foreseen energy of the LHC are presented with dotted lines. The break points in the curves correspond to the difference in the estimated cross sections between proton-proton (LHC) and proton-antiproton (Tevatron) production [15].

2.2.2 Decay of massive vector bosons

Due to their very limited lifetime of the W or Z boson, the production is instantaneously followed by the decay and the particle must therefore be detected through its decay products. The amplitude of the decay rate is calculated in a manner, similar to the production probability, but summing over all possible final states rather than the initial states. The probability of a certain decay mode is described by the *branching ratio*, $\text{Br}(X \rightarrow a + b)$, which is the fraction of the partial decay rate of the decay mode of interest and the total decay rate of the boson.

The W boson can decay into a fermion-antifermion pair for all fermions except

for the top quark, since the mass of the top exceeds that of the W . If the W decays leptonically, one of the leptons must be a neutrino/anti-neutrino belonging to the same flavor as the other lepton due to lepton number conservation. The Z boson decays into a fermion and its corresponding anti-fermion. The different decay modes of the W and Z , with their respective predicted branching ratios, are summarized in Table 2.3. The dominant decay mode of the bosons is through hadronic decay due to the threefold of colors - a decay into a certain quark is possible for each color state of the quark due to the color blindness. It is, however, experimentally very difficult to detect the hadronic channels among the abundant QCD background and the W/Z cross sections at the LHC is measured through the leptonic decay. The fraction of Z bosons decaying into charged leptons is smaller than for the W boson, due to the possibility of the Z decaying into a neutrino and an anti-neutrino (indicated by *invisible* in Table 2.3).

	Decay mode	Measured branching ratio	Expected branching ratio
W^+	$e^+\nu_e$	$(10.75 \pm 0.13) \%$	
	$\mu^+\nu_\mu$	$(10.57 \pm 0.15) \%$	11.1%
	$\tau^+\nu_\tau$	$(11.25 \pm 0.20) \%$	
	hadrons	$(67.60 \pm 0.27) \%$	66.7%
Z^0	e^+e^-	$(3.363 \pm 0.004) \%$	
	$\mu^+\mu^-$	$(3.366 \pm 0.007) \%$	3.4%
	$\tau^+\tau^-$	$(3.370 \pm 0.008) \%$	
	invisible	$(20.00 \pm 0.06) \%$	20.5%
	hadrons	$(69.91 \pm 0.06) \%$	69.2%

Table 2.3: Branching ratios of the different W^+ and Z^0 decay modes [11]. W^- is the charge conjugate of W^+ . Invisible denotes the Z decays with a neutrino-antineutrino pair as a final state. The predicted values are estimated with $\sin^2 \theta_W = 0.23$.

The couplings between leptons and gauge bosons are flavor independent (lepton universality) and their measured branching ratios are therefore homogeneous. At $\sqrt{s} = 7$ TeV, the expected NNLO production cross sections times their respective $W \rightarrow \ell\nu$ and $Z/\gamma^* \rightarrow \ell\ell$ decay branching ratios, estimated with the FEWZ program [16], are

$$\sigma_{W \rightarrow \ell\nu}^{NNLO} = 10.46_{-0.28}^{+0.15}(\text{scale})_{-0.20}^{+0.18}(\text{PDF}) \text{ nb} \quad (2.12)$$

and

$$\sigma_{Z/\gamma^* \rightarrow \ell\ell}^{NNLO} = 0.989_{-0.024}^{+0.015}(\text{scale})_{-0.016}^{+0.017}(\text{PDF}) \text{ nb}, \quad (2.13)$$

where the scale uncertainty originates from the choice of the momentum transfer squared, fixed at a value of $Q^2 = M_V^2$. (The measured mass values of the gauge boson with uncertainties was shown in equation 2.9.) The remaining uncertainty on the cross section predictions arises from the modeling of the PDFs.

The production rates of W^+ and W^- are asymmetric in a $p-p$ collider due to the higher probability of producing a u quark than a d quark in the PDF, which originates from their respective different valence distributions. Figure 2.4 shows the PDFs for gluons and quarks (except t and \bar{t}) at the LHC, predicted by MSTW2008 NLO [17]. W^+ production mainly depends on the $u(x)$ and $\bar{d}(x)$ distributions (LO production through $u\bar{d} \rightarrow W^+$), while the W^- production is dependent on the $\bar{u}(x)$ and $d(x)$. The cross sections of each process at $\sqrt{s} = 7$ TeV are

$$\sigma_{W^+ \rightarrow \ell\nu}^{NNLO} = 6.16 \pm 0.31 \text{ nb} \quad \text{and} \quad \sigma_{W^- \rightarrow \ell\nu}^{NNLO} = 4.30 \pm 0.21 \text{ nb}. \quad (2.14)$$

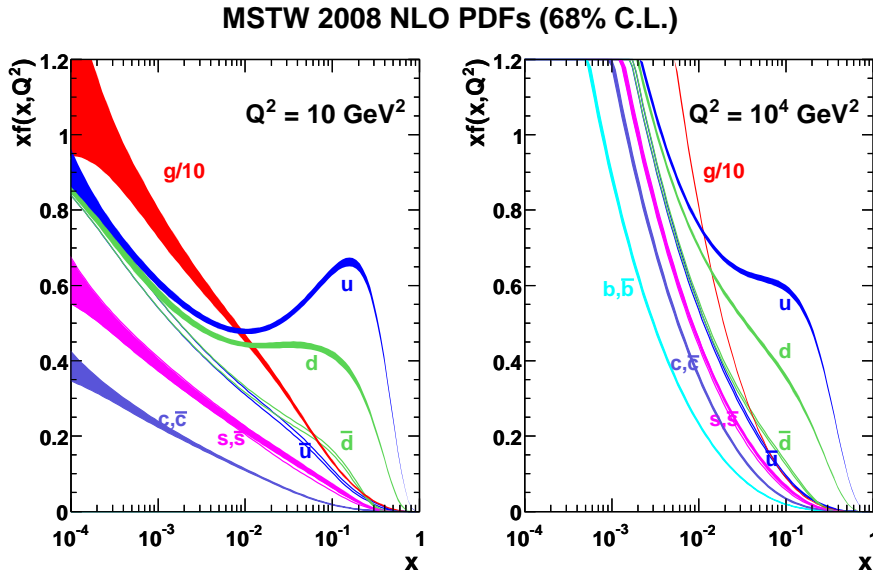


Figure 2.4: PDFs for gluons and quarks (except t, \bar{t}) at the LHC as a function of x shown for two different scales, $Q^2 = 10$ and 10^4 GeV^2 , as predicted by the MSTW PDF fitting group with 68% confidence level [17].

2.2.3 Inclusive and differential W and Z cross sections

Measurements of the inclusive production cross sections of the W and Z bosons at hadron colliders constitute an important test of the Standard Model. The theoretical

calculations involve PDFs and different couplings of the partons to the weak bosons, which are significantly affected by higher order QCD corrections.

Since W^\pm and Z bosons are produced at a high rate at the LHC, their projected large datasets allows for detailed measurements with early data. The 7 TeV LHC centre-of-mass energy allows for a measurement of the production properties of the W and Z in a previously unexplored kinematic domain. These conditions, together with the proton-proton nature of the collisions, will provide new constraints on the PDFs and precise tests of perturbative QCD, such as the choice of QCD renormalization and factorization scales in the theoretical predictions.

The cross section ratios $\mathcal{R}_{W^\pm/Z} = \sigma_{W^\pm \rightarrow \ell^\pm \nu} / \sigma_{Z \rightarrow \ell \ell}$ and $\mathcal{R}_{W^+/W^-} = \sigma_{W^+ \rightarrow \ell^+ \nu} / \sigma_{W^- \rightarrow \ell^- \nu}$ can be measured with a higher precision due to partial or full cancellations of both experimental and theoretical uncertainties. The QCD scale dependence of the theoretical cross section predictions generally cancels in the ratio and is consequently found to be negligible. In addition the PDF uncertainties as well as the value chosen for the strong coupling term, α_s , partially cancel. With larger data samples the measured cross section ratios can be used to provide constraints on the W boson width Γ_W .

The differential W and Z cross sections are interesting and important measurements where the cross section calculation is performed as a function of for example the boson transverse momentum (p_T) or the boson rapidity:

$$y = \frac{1}{2} \ln\left(\frac{E + p_z}{E - p_z}\right) = \frac{1}{2} \ln\left(\frac{x_1}{x_2}\right) \quad (2.15)$$

or the pseudorapidity ($\eta = -\ln(\tan\frac{\theta}{2})$) of the lepton. The differential cross section measurements are crucial for fine tuning specific parameters of the theoretical predictions. For instance, it was demonstrated in [18] that the rapidity distribution of W and Z bosons are highly sensitive to the momentum fraction (x_i) distributions of quarks and anti-quarks, which can be used to constrain the PDFs.

Another interesting differential measurement is the W charge asymmetry, defined as

$$A_W = \frac{\sigma(W^+) - \sigma(W^-)}{\sigma(W^+) + \sigma(W^-)}. \quad (2.16)$$

The overall asymmetry is significantly different from zero at proton-proton colliders such as the LHC, since the probability of having a u quark in a proton is larger than a d quark (as was mentioned above). A_W is thus very sensitive to the u and d valence quark distributions, which are only loosely constrained in the kinematic range of the p - p collisions at the LHC. The asymmetry also has a strong dependence on the pseudorapidity of the lepton, η^l , since η^l is strongly correlated to the kinematic phase space of the incoming partons and hence the momentum fraction x .

A differential cross section measurement can thus be used to improve the PDFs in the kinematic regime of the LHC, which is sensitive to a novel region of low x_i values at high Q^2 . Additionally, measurement at high pseudorapidity can be performed with ATLAS at the LHC, which is not possible at the experiments at the Tevatron.

2.2.4 W and Z bosons in association with jets

The production of a W or Z boson in association with one or more jets is an interesting process on its own, but also as a background to several other physics processes both within the Standard Model and beyond. It therefore serves as an early test of the SM at the LHC. Early $W/Z + \text{jets}$ results also allow an important comparison with QCD expectations, which incorporates large theoretical uncertainties. The wide kinematic range and different jet multiplicities for production of $W/Z + \text{jets}$ serves as a testing ground for perturbative QCD predictions.

The production of $W/Z + \text{jets}$, in contrast to W/Z inclusive production, involves not only an electroweak vertex but also a strong interaction vertex. Figure 2.2 above shows Feynman diagrams for the production of $W/Z + 0$ and 1 jets. The LO diagram in the case of 0 jets only has an electroweak vertex and requires two quarks in the initial state (for example $u\bar{d} \rightarrow W^+$). The production process of $W/Z + 1$ jet has an additional α_S vertex and can thus be produced either by $qq \rightarrow Wg$ or $qg \rightarrow Wq$. Any additional final state parton implies another α_S vertex. The full treatment of the partonic cross section calculation for W/Z bosons in association with jets events can be found in [19].

The PDFs are a dominant source of theoretical systematic uncertainty for $W/Z + \text{jets}$ predictions and the experimental measurements performed with the LHC experiments will thus be the main contribution for improving the knowledge of multi-parton final state modeling. Minimizing the experimental systematic uncertainties to increase the sensitivity of the measurement is therefore of great significance.

Theoretical predictions for $W/Z + \text{jets}$ have been calculated for next-to-leading-order in QCD for a jet multiplicity up to four [20]. The main reason for extending theoretical calculations to NLO is the reduction of the unphysical dependence on the renormalization and factorization scales, reflecting a more reliable normalization of cross sections and distributions. NLO calculations up to two jets are implemented in the MC program MCFM [21]. While being the most accurate, such predictions are parton-level cross sections and cannot account for hadronization and underlying event. To be able to make direct comparisons with data other Monte Carlo event generators, which include parton shower approaches simulating final states at the hadron level, must be utilized. For information concerning MC event generators relevant to this thesis see section 2.3.

2.2.5 $\mathcal{R}_{\text{jets}} = \sigma(W + \text{jets})/\sigma(Z + \text{jets})$

The cross section ratio of the massive vector bosons, measured in the leptonic decay channels in the presence of hadronic jets, is defined by

$$\mathcal{R}_{\text{jets}} = \frac{\sigma_{W+n\text{jets}} \cdot Br(W \rightarrow \ell\nu)}{\sigma_{Z+n\text{jets}} \cdot Br(Z \rightarrow \ell\ell)} = \frac{\sigma(W \rightarrow \ell\nu + n\text{jets})}{\sigma(Z \rightarrow \ell\ell + n\text{jets})}. \quad (2.17)$$

The cross section ratio of W and Z in association with jets is not a trivial measurement since it requires numerous components both experimentally and for the theoretical calculations. The theoretical prediction depends on the production PDFs, the masses of the bosons and their couplings. Parton level predictions at NLO in perturbative QCD can be calculated for the $W + \text{jets}$ and $Z + \text{jets}$ cross sections and subsequently their ratio using MCFM.

The advantage of the $\mathcal{R}_{\text{jets}}$ measurement is that many uncertainties either fully cancel or are significantly reduced, while the measurement is still sensitive to the interesting quantities of the W and Z cross sections. The most important gain from the cancellations is the independence of the uncertainty from the luminosity estimation, which is the dominating uncertainty for measurements with early data. In addition, certain PDF approximations cancel in the ratio. A natural consequence of the cancellations is that all the components of both numerator and denominator must be well understood and studied to high precision.

An additional possible advantage of the $\mathcal{R}_{\text{jets}}$ measurement is that it could be used in data-driven background predictions of $W/Z + \text{jets}$ backgrounds with final states that are not easily accessible (such as $Z \rightarrow \nu\nu$) or have a low cross-section \times branching ratio.

Assuming a sufficiently small uncertainty, the ratio can be measured in various interesting kinematic and topological regimes, such as versus jet multiplicity or jet p_T . The ratio $\mathcal{R}_{\text{jets}}$ is thus sensitive to the dynamics of $W/Z + \text{jets}$ production. Varying how the measurement is conducted could however also be a way of searching for new physics. Several new physics signatures are predicted to be similar to $W/Z + \text{jets}$ (one or two leptons with possible missing transverse energy and higher jet multiplicities/ p_T). Such decay channels would affect the $\mathcal{R}_{\text{jets}}$ measurement, which would be an early indication of physics beyond the Standard Model. For example, new physics is produced at high Q^2 with an electron, missing transverse energy and jets in the final state, the $\mathcal{R}_{\text{jets}}$ measurement as a function of the leading jet p_T would be distorted at higher jet energies deviating from the predicted SM values towards higher values of the ratio.

This is the first time the $\mathcal{R}_{\text{jets}}$ measurement is performed directly, at any experiment. Only the inclusive W/Z ratio has been previously measured, for example at CDF resulting in $\mathcal{R} = 10.92 \pm 0.15(\text{stat}) \pm 0.14(\text{syst})$ [22]. These results are compared

to the measurements performed at ATLAS in chapter 6.

In this thesis the one-jet case is considered, which is what the full 2010 integrated luminosity permits with a reasonable statistical uncertainty. The ratio is measured as a function of the p_T threshold of the recoiling jet. The advantage of such a definition is that it reduces the statistical and systematic uncertainty originating from jet p_T bin migrations affecting the ratio of differential cross sections, while conserving the important property of probing various kinematic regimes of the ratio of observables. This measurement can thus be seen as several total cross section ratio measurements in successively smaller phase space corresponding to a more energetic region.

2.2.6 Prospects for early measurements in the electroweak sector

A large effort has been dedicated to studies using simulated data during the years before first LHC collisions, to establish the feasibility of different measurements at ATLAS. The many results obtained with $\sqrt{s} = 14$ TeV Monte Carlo, covering all areas of expected physics studies at ATLAS [23], include detailed W and Z analyses. Prospects for early $W/Z + \text{jets}$ analyses, performed using $\sqrt{s} = 10$ TeV Monte Carlo (MC) [24], present a complete “analysis walk through” for such measurements corresponding to a data sample of 100 pb^{-1} .

A summary of the prospects for what measurements can be achieved with early data, using simulated data, are outlined in Table 2.4. For each analysis the crucial components required for carrying out the measurement and/or what information can be extracted, are stated in the table. The W/Z measurements that are actually realized with the first 40 pb^{-1} of 7 TeV data, collected in 2010, are presented in detail in chapters 5, 6 and 7.

2.3 Monte Carlo generators

The purpose of Monte Carlo event generators is to describe theoretical predictions for physics processes, for instance the production of a W boson in a proton-proton collision and its decay into an electron and a neutrino. Such theoretical predictions are crucial for the interpretation and understanding of the measured data and for tuning the MC generators for future physics analyses. In addition, the MC is used to extrapolate data measurements to a larger phase space, beyond the acceptance of the detector.

In order to model the events at an LHC experiment, the Monte Carlo generators must describe the structure of hadrons, parton showers, the hard scattering process

and the hadronization. Various MC event generator programs use different approximations for the different steps in the calculations and the theoretical predictions thus rely, to a certain extent, on the choice of MC generator. A few of the existing event generators, which are relevant to this thesis, are outlined below:

- **Pythia** [25] is a general purpose event generator, which is commonly used in high energy physics due to its easy handling and relatively large predictive power. It can simulate lepton-lepton, lepton-hadron and hadron-hadron interactions with a broad field of theoretical models. The hard scattering process is however calculated in leading order approximation and the higher order corrections are approximated with a parton shower approach, which has limited accuracy for predicting events with higher jet multiplicity. PYTHIA is interfaced with PHOTOS [26] for QED bremsstrahlung simulation.
- **HERWIG** (Hadron Emission Reactions With Interfering Gluons) [27] is an additional general purpose event generator, similar to PYTHIA. The main differences are the modeling of the parton shower and the hadronization process.
- **ALPGEN** [28] is a LO MC generator which implements the exact matrix element LO calculation for multi-partonic final states. ALPGEN is thus useful for analyses including jets. The hard matrix element calculation for a $2 \rightarrow n$ process is interfaced with HERWIG for hadronization simulation and JIMMY [29] for modeling of the underlying event.
- **MC@NLO** [30] includes full NLO calculations of rates for QCD processes during the hard scattering. MC@NLO is thus useful for precision measurement where LO calculations are not sufficient. The output of the simulation is further handled by HERWIG event generator, which adds higher order approximations of the parton shower and simulates the hadronization step.
- **POWHEG** [31] The POWHEG method is a prescription for interfacing NLO QCD calculations with parton shower generators. Unlike MC@NLO, POWHEG produces events with positive (constant) weight and furthermore, does not depend on the subsequent shower Monte Carlo program. POWHEG can be interfaced with any modern shower generator such as HERWIG and PYTHIA.

Measurement	Available data	Crucial component(s)
W/Z observation	$\int \mathcal{L} \approx 100 \text{ nb}^{-1}$	<ul style="list-style-type: none"> - First real data studies; development of methodology - Initial performance studies - Early data/MC discrepancy studies
W/Z + jets observation	$\int \mathcal{L} \approx 1 \text{ pb}^{-1}$	<ul style="list-style-type: none"> - Jet reconstruction algorithms
W/Z cross section, σ_V $\mathcal{R} = \sigma_W/\sigma_Z$	$\int \mathcal{L} \approx 10 \text{ pb}^{-1}$	<ul style="list-style-type: none"> - Test of NNLO QCD predictions - PDF constraints - Efficiency studies
W/Z + jets cross section Differential σ_W, σ_Z $\mathcal{R}_{\text{jets}} = \sigma_{W+1\text{jet}}/\sigma_{Z+1\text{jet}}$	$\int \mathcal{L} \approx 100 \text{ pb}^{-1}$	<ul style="list-style-type: none"> - Further PDF constraints - Test of NLO predictions - SM background to top and new physics searches - Strong coupling constant α_S - Γ_W extraction - New physics?
W mass Z asymmetry $\mathcal{R}_{\text{jets}} = \sigma_{W+n\text{jets}}/\sigma_{Z+n\text{jets}}$	$\int \mathcal{L} \approx 1 - 10 \text{ fb}^{-1}$	<ul style="list-style-type: none"> - Indirect Higgs mass measurement - Weak mixing angle, $\sin^2 \theta_W$ - New physics?

Table 2.4: Prospects for early measurements in the electroweak sector with ATLAS, with increasing amount of available data (integrated luminosity). The feasibility of W/Z measurements with early LHC data has been studied in great detail on simulated data prior to first collisions and has been thoroughly documented in [23, 24].

Chapter 3

The ATLAS Experiment at the LHC

The Large Hadron Collider (LHC) is a large accelerator located at CERN outside Geneva, Switzerland (see Figure 3.1). The accelerator is designed to collide two proton beams at a centre-of-mass energy of 14 TeV (currently 7 TeV), as well as lead ions (Pb^{82+}) for a certain part of the time. The official starting point for the planning of the LHC took place as early as 1984 in a symposium organized in Lausanne, Switzerland and was approved as a project by the CERN council a decade later. The first expressions of interest for the LHC experiments took place in 1992. The LHC has four interaction points. ATLAS and CMS, which are the two general purpose experiments, are located at two of them. LHCb, which mainly focuses on physics involving B -hadrons, and ALICE, which makes use of the heavy ion runs in the LHC to perform nuclear physics research, constitute the remaining two major experiments on the LHC ring. The LHC and its experiments are sensational results of a project that took decades to engineer. The first proton collisions were seen in the LHC in late 2009, marking the beginning of an exciting new era of high energy physics.

The ATLAS detector is designed to measure the proton collisions delivered by the LHC at the TeV energy scale. Nearly 3000 physicists helped build and/or analyze the data collected by the ATLAS experiment. This implies a collaboration of 174 institutes from 38 countries around the world.

This chapter commences by introducing the Large Hadron Collider in section 3.1 followed by an overview of the ATLAS detector in section 3.2. Section 3.3 provides a more detailed description of one of the ATLAS sub-detectors; the Semiconductor Tracker.



Figure 3.1: Geneva area with the French Alps in the background. The (red) ring represents the location of the underground LHC tunnel.

3.1 The Large Hadron Collider

The Large Hadron Collider at CERN [32] is currently the largest and most powerful synchrotron in the world; it is the biggest machine ever built in the field of fundamental science. The LHC is located in the already existing tunnel of the LEP accelerator [33] at the border between Switzerland and France and is 26.7 km long in circumference. LEP ran from 1989 until 2000. Due to the geological conditions of the region, the accelerator tunnel is situated between 45 and 170 m underground and has a 1.4% incline from the planar, with the slope towards the Geneva lake. At the time of writing, the LHC recently exceeded the Tevatron at Fermilab [34] by setting a new world record for providing the highest instantaneous luminosity.

The LHC circulates two proton beams traveling in the opposite direction in the accelerator tunnel. In the first extended data-taking period of 2010-2012, the LHC accelerates each proton to an energy of 3.5 TeV providing a centre-of-mass energy of 7 TeV in each collision. This energy can be compared with the particle accelerator with the previously highest energy in the world; the Tevatron, which collides protons with anti-protons at the centre-of-mass energy of 1.96 TeV. The 14 TeV design collision

energy of the LHC is expected to be reached in 2014.

3.1.1 The CERN accelerator complex

Before the protons are accelerated by the LHC, the beams first travel through other accelerators at CERN, increasing their energy in several stages [35]. The protons also need to be grouped into bunches with the LHC frequency, before the final injection into the LHC ring. Figure 3.2 illustrates the path traveled by the protons through the accelerator complex at CERN. The protons are first extracted from hydrogen gas using an electric field and then accelerated to 50 MeV with a linear accelerator; LINAC2. The current output from LINAC2 is 170 mA and with a pulse length of 30 μ s needed for LHC operation. The beam is then injected into the Proton Synchrotron Booster (PSB), which then accelerates the beam to 1.4 GeV before it is transferred to the Proton Synchrotron (PS) where the extraction energy is 26 GeV. The PS pulses the beam with the equivalent frequency and bunch spacing as the LHC. The bunches are then sent through the transfer lines TT2 and TT10 to reach the Super Proton Synchrotron (SPS), where the proton energy reaches 450 GeV by being accelerated in the 7 km circumference SPS ring.

When finally injected into the LHC ring, through transfer lines TI2 and TI8, the protons are accelerated to the speed of $0.99999999c$, which enables them to circulate the 27 km LHC ring about 11 000 times per second. The storage ring contains ultra-high vacuum in order to minimize the interaction between the protons and random molecules and thereby sustain the high energy of the beam. Figure 3.2 shows an overview of the complex of accelerators, through which the proton beams travel, together with the locations of the different experiments.

3.1.2 The functionality of the LHC

The proton bunch

In order to accelerate the proton beams, the protons need to be grouped into bunches. Each bunch contains up to 10^{11} protons and have a length of a few centimeters along the beam axis [32]. The bunches are squeezed into a transverse size of 16 μ m at the collision points in order to increase the probability of collision between the protons. Despite the large number of protons in each bunch, there will only be about 20 proton-proton collisions in one bunch crossing event during a high luminosity run, which is due to the small cross section of the proton. Although this number seems small, the fact that a bunch crossing occurs as often as 30 million times per second in the LHC, makes the total number of collisions over 600 million per second. More protons in each bunch implies higher instantaneous luminosities. The number of collisions in one bunch crossing determines the amount of “pile-up” in the data.

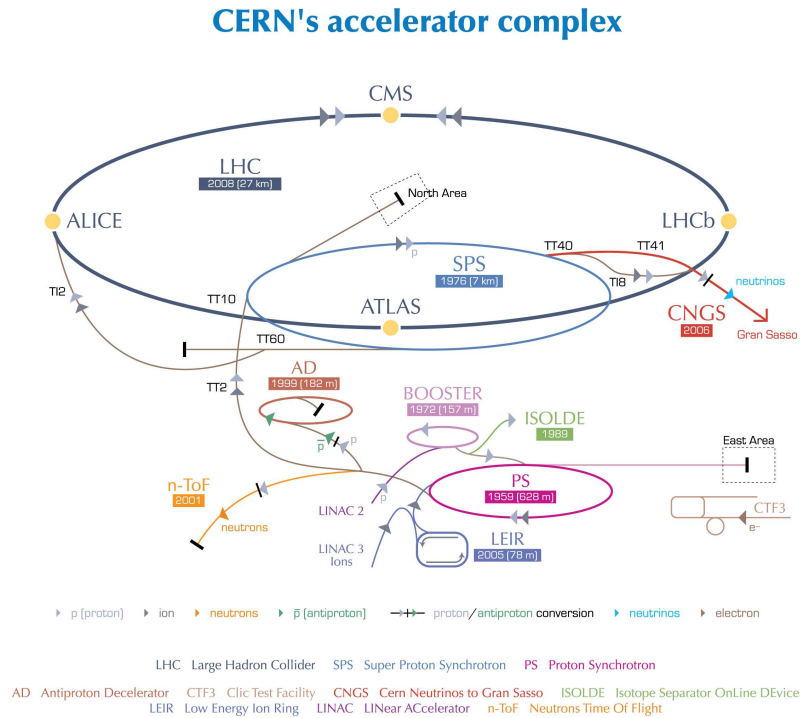


Figure 3.2: The accelerator complex at CERN, which gradually accelerates the proton beams. The locations of the different experiments are indicated [36].

Magnetic and electric fields

The bunches in the proton beams are accelerated in the LHC using 2 groups of 4 superconducting radio frequency (RF) oscillators per beam [37]. The RF oscillators are also necessary to compensate for the relativistic effects at these high energies. It is important to match the phase of the bunch frequency with the RF oscillators such that the acceleration of the protons becomes optimal. In the case of the LHC, the oscillation frequency of the RF cavities is around 40 MHz. The magnetic field must simultaneously increase to avoid dispersion and therefore keep the radius constant.

The RF oscillator also assists in keeping the particles within the bunches. Consider for instance a proton at the end of a bunch, arriving somewhat later in the oscillation than average. The proton feels a stronger electric field than the protons in the middle of the bunch and will be accelerated to a greater extent. Protons that arrive early in the RF oscillator will be slightly delayed and will therefore also become closer to the center of the bunch. The oscillations of particles around the optimal phase in the center of the bunch are called synchrotron oscillations, hence the name of the

accelerator type.

A magnetic field of 8.3 T deflects the proton beams along the LHC ring, using 1232 superconducting dipole magnets, each of the length of 14.3 m. The beam is focused by 858 smaller quadrupole magnets and another 6200 correction magnets are required to suppress unwanted resonances in the accelerator. To keep the LHC magnets superconducting, a cryogenic system is utilized, which uses superfluid helium that has a high efficiency of heat transportation. The superconducting magnets bathe in the superfluid helium at the temperature of 1.9 K.

Luminosity

The instantaneous luminosity delivered by the accelerator depends mainly on the number of bunches in the beam as well as the number of protons in each bunch. The design criteria of the LHC is to reach 2808 colliding bunches with a minimum distance of approximately 7 m in between. The design luminosity of the LHC is $10^{34} \text{ cm}^{-2}\text{s}^{-1}$. For the 7 TeV running in 2010, the initial luminosity delivered by the LHC was at the level of $10^{26} \text{ cm}^{-2}\text{s}^{-1}$ but this rapidly increased to $2 \times 10^{32} \text{ cm}^{-2}\text{s}^{-1}$ by the end of the run period.

The instantaneous luminosity is defined as

$$L = \frac{n_b N_b^2 f_{rev} \gamma_r}{4\pi \epsilon_n \beta^*} F, \quad (3.1)$$

where n_b is the number of bunches per beam, N_b is the number of particles per bunch, f_{rev} is the revolution frequency, γ_r is the relativistic gamma factor, ϵ_n is the normalized transverse beam emittance and β^* is the beta function at the collision point. The geometric luminosity reduction factor, F , due to the crossing angle at the interaction point (IP), is approximated by

$$F \approx \left(1 + \left(\frac{\theta_c \sigma_z}{2\sigma_t} \right)^2 \right)^{-1/2}, \quad (3.2)$$

where θ_c is the full crossing angle at the IP, σ_z is the RMS bunch length and σ_t is the transverse RMS beam size at the IP. Equation 3.2 assumes circular and identical beams with $\sigma_z \ll \beta$.

A summary of some of the LHC design beam parameters together with the parameters reached during the 2010 run can be found in Table 3.1. Comparing the values shows great progress for first run period of the LHC, but there is still room for improvement before the design criteria is reached.

Beam parameter	Nominal	2010
Energy per beam [TeV]	7	3.5
β^* [m]	0.55, 10, 0.55, 10	3.5, 3.5, 3.5, 3.5
Emittance ϵ_n [$\mu\text{m rad}$]	3.75	2.0-3.5
Transverse beam size σ_t [μm]	16.7	~ 60
Bunch current N_b	1.15×10^{11}	1.2×10^{11}
Colliding bunches n_b	2808	348
Stored energy [MJ]	360	28
Peak luminosity [$\text{cm}^{-2}\text{s}^{-1}$]	10^{34}	2×10^{32}

Table 3.1: Nominal design values of the LHC beam parameters together with the numbers reached during 2010 data-taking [37, 38].

3.1.3 The path towards LHC physics

The LHC was originally designed to collide protons at a centre-of-mass energy of $\sqrt{s} = 14$ TeV. When beam was first circulated in the machine, the 10th of September 2008, all went surprisingly smoothly. However, a week later when the LHC was commissioning some of its magnets, an accident occurred, where a large number of magnets were damaged or misplaced in sectors 3 and 4 of the LHC [39].

The end of 2008 and majority of 2009 was spent on warming up the damaged sectors, repairing and analyzing the damaged magnets and finally cooling them down again. A total of 53 magnets were damaged and repaired during the shut-down. The LHC delivered first collisions in November 2009 at a centre-of-mass energy of 900 GeV. The beginning of 2010 saw the LHC ramping up the beam to higher energies and the first 7 TeV collisions occurred in late March, setting a new record for high energy physics. The first 7 TeV p - p run period lasted up to November 2010. At the end of 2010, up to the winter shut-down, the first heavy ion run took place in the LHC, with an acceleration and collision of Pb^{82+} ions at the energy of $\sqrt{s_{NN}} = 2.76$ TeV.

During the 7 months of p - p running in 2010, the instantaneous luminosity was augmented by increasing the bunch intensities and adding more bunches to the beam. The LHC started with only one proton bunch circulating per beam but managed to include 348 colliding bunches in the final runs of 2010 [38]. This is an impressive achievement for the first months of operation, but there is still room for improvement before reaching the nominal 2808 bunches. Figure 3.3 shows the exponential increase of the cumulative data delivered (green) by the LHC and collected (yellow) by ATLAS. The total recorded luminosity by ATLAS in 2010 was 45.0 pb^{-1} out of the 48.1 pb^{-1} that was delivered by the LHC¹. The ATLAS data-taking efficiency is thus about 94%,

¹The integrated luminosity shown in Fig. 3.3 was determined online from counting rates measured

with the inefficiencies accounting for turning on high-voltage or individual problems concerning different sub-detectors.

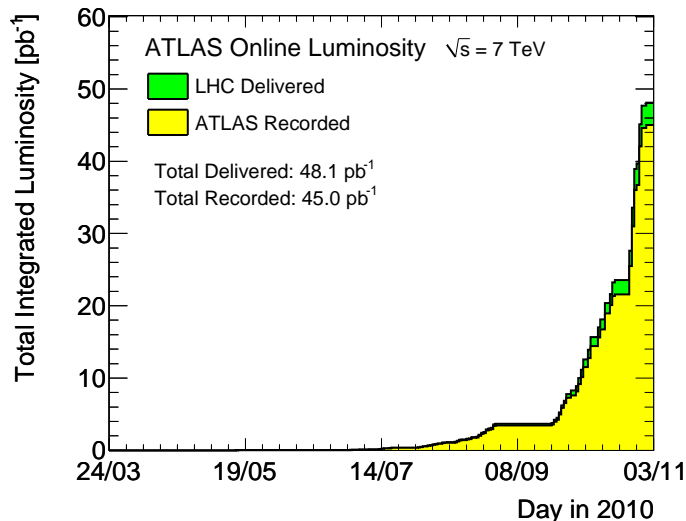


Figure 3.3: Cumulative integrated luminosity delivered to (green), and recorded by ATLAS (yellow) versus day in 2010. The measured data is during stable beams with 7 TeV centre-of-mass energy [42].

The current plan for the LHC is to run at the centre-of-mass energy of 7 TeV until the end of 2012. At the time of writing (August 2011), the peak luminosity for the 2011 run so far was $2 \times 10^{33} \text{ cm}^{-2}\text{s}^{-1}$ with 1331 colliding bunches. With such intensities, the LHC is expected to deliver up to 3 fb^{-1} of integrated luminosity during 2011. After the 2011-2012 run at 7 TeV, with sufficient amount of data for the experiments to be pleased, a longer shut-down will be required in order to take the accelerator to the design energy of 14 TeV.

3.1.4 Different experiments at the LHC

The four different collision points at the LHC can be seen in Figure 3.2 together with the experiments that have been constructed around each of the collision regions. The four major LHC experiments are ATLAS (A Toroidal LHC ApparatuS), CMS (Compact Muon Solenoid) [43], ALICE (An LHC Ion Collision Experiment) [44]

by the luminosity detectors and includes a systematic uncertainty of 11% [40]. The offline luminosity, determined in [41], has been found to be 3.6% lower than the online luminosity measurement, with a decreased systematic uncertainty of 3.4%.

and LHCb (LHC beauty) [45]. CMS and ATLAS are general-purpose experiments designed to capture as broad variety of physics as possible. The ALICE detector is optimized to study heavy ion collisions. LHCb is a smaller experiment dedicated to B-physics, where the detector is a single-arm spectrometer.

In addition, there are several smaller experiments at the LHC; TOTEM measures the total cross section, elastic scattering and diffractive dissociation [46] and LHCf aims to measure neutral particles emitted in the very forward region [47]. The MoEDAL experiment [48] searches for massive stable particles, such as magnetic monopoles, and shares cavern with LHCb.

3.2 Overview of the ATLAS detector

The ATLAS experiment is a general-purpose detector, implying that it collects data taking as many different physical parameters into consideration as possible to be able to detect a wide spectrum of physics processes. The ATLAS detector is a massive device of 42 meters length and with a diameter of 25 meters, and therefore being the largest experiment at the LHC. The detector weights approximately 7000 tons. The technical specification of ATLAS is published in detail in the Technical Design Report (TDR) [49, 50] and, after installation at collision point 1, in the ATLAS technical paper [51]. An overview of the different parts of the detector is laid out in this section, focusing on aspects more relevant to this thesis such as the Inner Detector, the electromagnetic calorimeter and the trigger system. The Semiconductor Tracker (SCT) is dealt with in more detail in section 3.3.

The original basic design criteria of ATLAS [49], enabling full event reconstruction, includes the following:

- Accurate tracking and calorimetry required to identify and make measurements on electrons, photons and jets as well as to record missing transverse energy (E_T^{miss}).
- Precise measurements of muon momentum at the highest luminosity.
- Capability of full event reconstruction at low luminosity.
- Triggering on particles with low- p_T thresholds in order to increase the efficiency of the physics processes of interest.
- Capability of detecting particles with the largest possible acceptance in pseudo-rapidity and full coverage in the azimuthal plane in order to measure the total transverse energy from each event.

The ATLAS detector is divided into sub-systems with different aims and capabilities in order to meet these requirements (see Figure 3.4). From the interaction point a final state particle traverses the Inner Detector (ID) in a solenoid magnetic core, the Liquid Argon calorimeter, the Tile calorimeter and the muon spectrometer. Different types of particles yield different signatures in the sub-detectors. Figure 3.5 illustrates the path and location of detection in ATLAS for electrons (ID track and energy deposit in the EM calorimeter), photons (energy deposit in the EM calorimeter), protons (ID track and energy deposit in the hadronic calorimeter), neutrons (energy deposit in the hadronic calorimeter), muons (ID track and muon spectrometer) and neutrinos (invisible to the detector, but measured as missing transverse energy, E_T^{miss}).

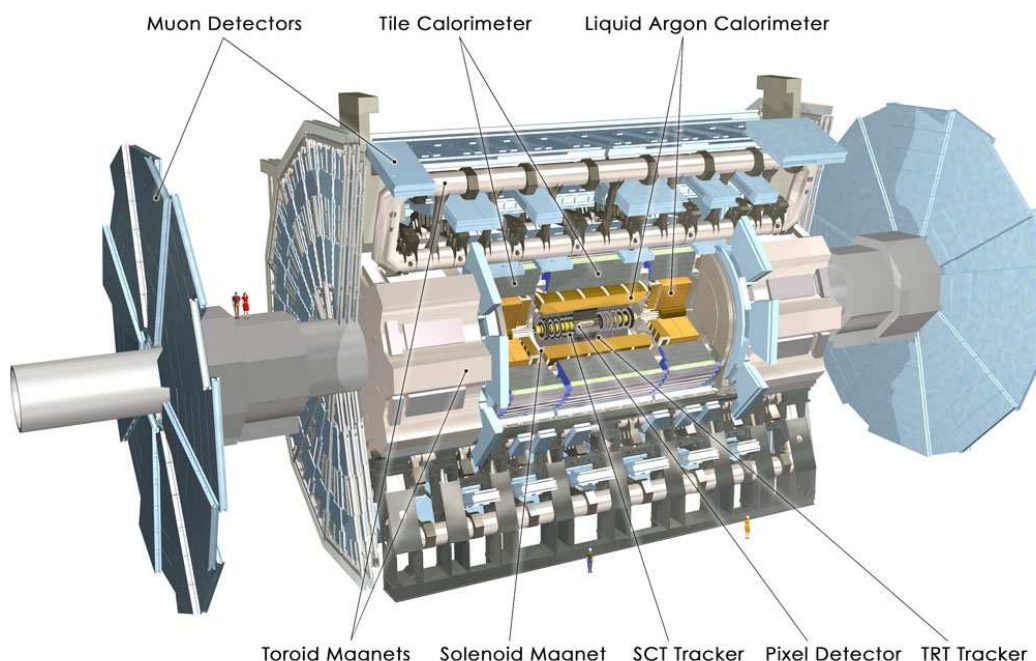


Figure 3.4: The ATLAS detector with its different components [52].

The Inner Detector, which consists of a pixel detector, a silicon micro-strip detector and a transition radiation tracking detector, is located close to the point of collision. It is equipped with a central solenoid magnet that provides a magnetic field with the strength of 2 T. The Inner Detector is surrounded by an electromagnetic and a hadronic calorimeter, which measure energy and position with high resolution. The largest and the most outer detector is the muon spectrometer that prevents the muons from escaping the interaction region undetected. There are three large air-cooled toroid magnets as part of the muon spectrometer providing a 4 T magnetic field.

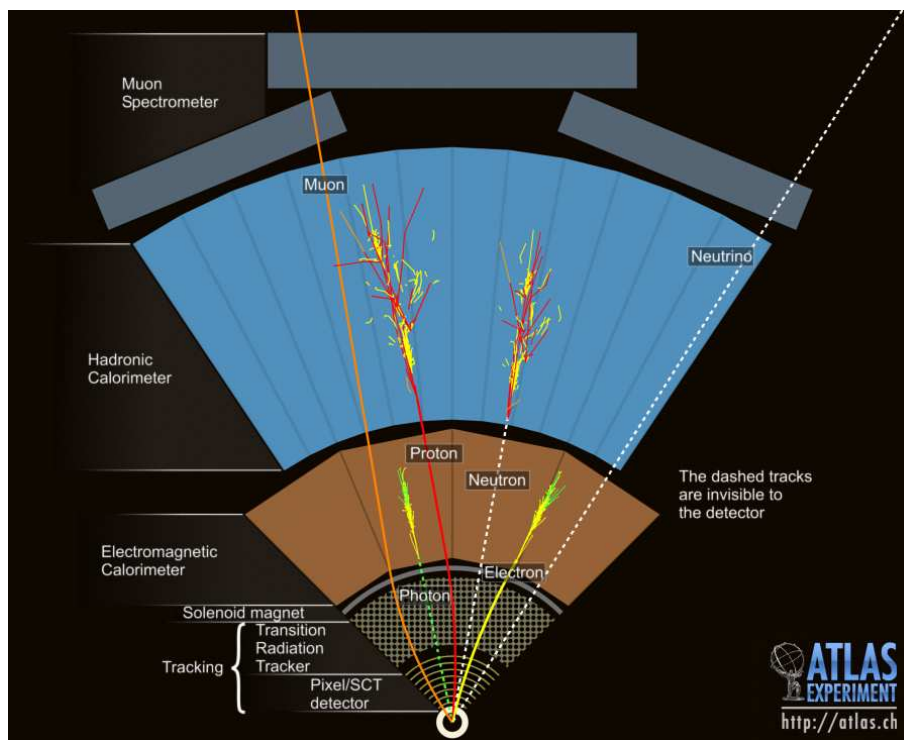


Figure 3.5: An illustration of signatures of different types of particles traversing a slice of the ATLAS detector [53].

The main performance goals and resolutions, as well as η coverage, for the different sub-systems of ATLAS, are listed in Table 3.2. The design resolution of for example the Inner Detector is parametrized according to

$$\frac{\Delta p_T}{p_T} \approx 0.00036 p_T [\text{GeV}] \oplus \frac{0.013}{\sqrt{\sin \phi}}, \quad (3.3)$$

where the first term corresponds to the intrinsic resolution and the second term parameterizes the multiple scattering effects due to more material in the forward region [50]. The available resolution of the different sub-detectors measured with data are specified in the sections below.

ATLAS has a three-level selective trigger system that operates at a very high rate and efficiency. An effective trigger system is crucial in order to be able to select and record interesting physics events while avoiding being submerged by the immense amount of collisions provided by the LHC. More details concerning the ATLAS trigger and data acquisition system will follow in section 3.2.6.

Detector component	Required resolution	η coverage	
		Measurement	Trigger
Inner Detector	$\sigma_{p_T}/p_T = 0.05\%p_T \oplus 1\%$	± 2.5	
EM calorimetry	$\sigma_E/E = 10\%/\sqrt{E} \oplus 0.7\%$	± 3.2	± 2.5
Hadronic calorimetry barrel and end-cap forward	$\sigma_E/E = 50\%/\sqrt{E} \oplus 3\%$	± 3.2	± 3.2
	$\sigma_E/E = 100\%/\sqrt{E} \oplus 10\%$	$3.1 < \eta < 4.9$	$3.1 < \eta < 4.9$
Muon spectrometer	$\sigma_{p_T}/p_T = 10\%$ at $p_T = 1$ TeV	± 2.7	± 2.4

Table 3.2: General performance goals and acceptance of the ATLAS sub-detectors [51].

3.2.1 Orientation

Since ATLAS has a cylindrical shape with the beam pipe in its core, it is a natural choice to define the beam direction as the z-axis. The x-y plane is therefore orthogonal to the beam axis (see Figure 3.4). The transverse variables, such as transverse momentum p_T , are in the x-y plane unless stated otherwise. The positive x-axis is defined as pointing from the detector to the origin of the LHC ring and the y-axis points upwards towards the surface of the earth.

In cylindrical coordinates this translates into an azimuthal angle, ϕ which is measured around the beam axis with the x-axis defining $\phi = 0$. The polar angle θ is measured from the positive beam direction towards the y-axis.

An important quantity in high energy physics is the rapidity, y , defined as

$$y = \frac{1}{2} \ln\left(\frac{E + p_z}{E - p_z}\right), \quad (3.4)$$

where E is the overall energy of the particle and p_z is the momentum of the particle in the z-direction. Rapidity is a Lorentz invariant quantity in the z direction (or Δy). The rapidity of the complete event cannot be measured directly in ATLAS due to the limited resolution in the z-direction. In the limit of vanishing masses, the rapidity simplifies to the pseudorapidity $\eta = -\ln(\tan(\frac{\theta}{2}))$, which is a measurable quantity. The pseudorapidity is zero at $\theta = \pi/2$ and $+\infty$ and $-\infty$ at $\theta = 0$ and π respectively. The distance ΔR in the η - ϕ space is given by $\Delta R = \sqrt{(\Delta\eta)^2 + (\Delta\phi)^2}$.

3.2.2 The Inner Detector

The intense conditions provided by the LHC collisions at the high bunch-crossing rate of 40 MHz imposes rigorous requirements on the ATLAS detector. The Inner Detector, which is closest to the collision point and responsible for the tracking of

charged particles in ATLAS, is designed to withstand such conditions and provide pattern recognition, primary and secondary vertex measurements as well as exceptional momentum resolution for charged particles within $|\eta| < 2.5$.

The ID consists of three sub-detectors; the Pixel detector, the Semiconductor Tracker (SCT) and the Transition Radiation Tracker (TRT). The structure and components of the Inner Detector can be seen in Figure 3.6 and 3.7. The tracking detector combines high spatial resolution with the two innermost parts (silicon pixels and micro-strip detectors) with a larger number of hits with reduced resolution (transition radiation detection) in the external part. The Pixel, SCT and TRT are immersed inside a 2 T solenoidal field in order to resolve charged particle momentum. A more detailed overview of the design resolution and technical performance of the Inner Detector can be found in [23, 51]. The momentum resolution of the ID measured with muons in data is discussed in section 3.2.4.

The Pixel Detector

The operating principles of a silicon detector, such as the Pixel and the SCT, are based on the simplest condensed matter physics device; the diode [54]. The Pixel system is the innermost part of the ATLAS detector and therefore needs to be both robust against high radiation and able to perform accurate tracking. It is constructed to accomplish high-precision measurements as close to the primary interaction point as possible and has a full coverage up to $|\eta| < 2.5$. The Pixel sensors uses n-in-n technology in order to improve radiation hardness; oxygenated n-type wafers are used with readout pixels on the n⁺ implanted side of the detector. To provide limited particle identification the Time-over-Threshold (ToT) technique is used to encode the pulse height as an indication of the specific energy loss, dE/dx , of the particles.

The detector consists of three barrels of radii 5, 9 and 12 cm as shown in Figure 3.6. The pixel detector also consists of two end-caps containing pixel elements on three disks on each side of the barrel in order to complete the angular coverage (see Figure 3.7). The innermost barrel layer is called the b-layer, since it is constructed to find secondary vertices with high precision in order to measure lifetimes of short-lived particles such as *B*-hadrons. The b-layer is also used for measuring the primary vertex (the original proton-proton collision vertex) position. It is foreseen that a new detector, an Insertable B-Layer (IBL), will be inserted between the existing b-layer and a new (smaller radius) beam pipe, in 2013 during an LHC shut-down. The purpose of the IBL is to cope with the increase in radiation and pixel occupancy as well as to improve the physics performance of the existing pixel detector.

The Pixel detector contains more than 80 million silicon pixel elements with dimensions of $50 \times 400 \mu\text{m}^2$ [51]. A precision of $10 \mu\text{m}$ in the in-plane transverse direction (R - ϕ) and $115 \mu\text{m}$ in the in-plane longitudinal direction (z for the barrel and R for the

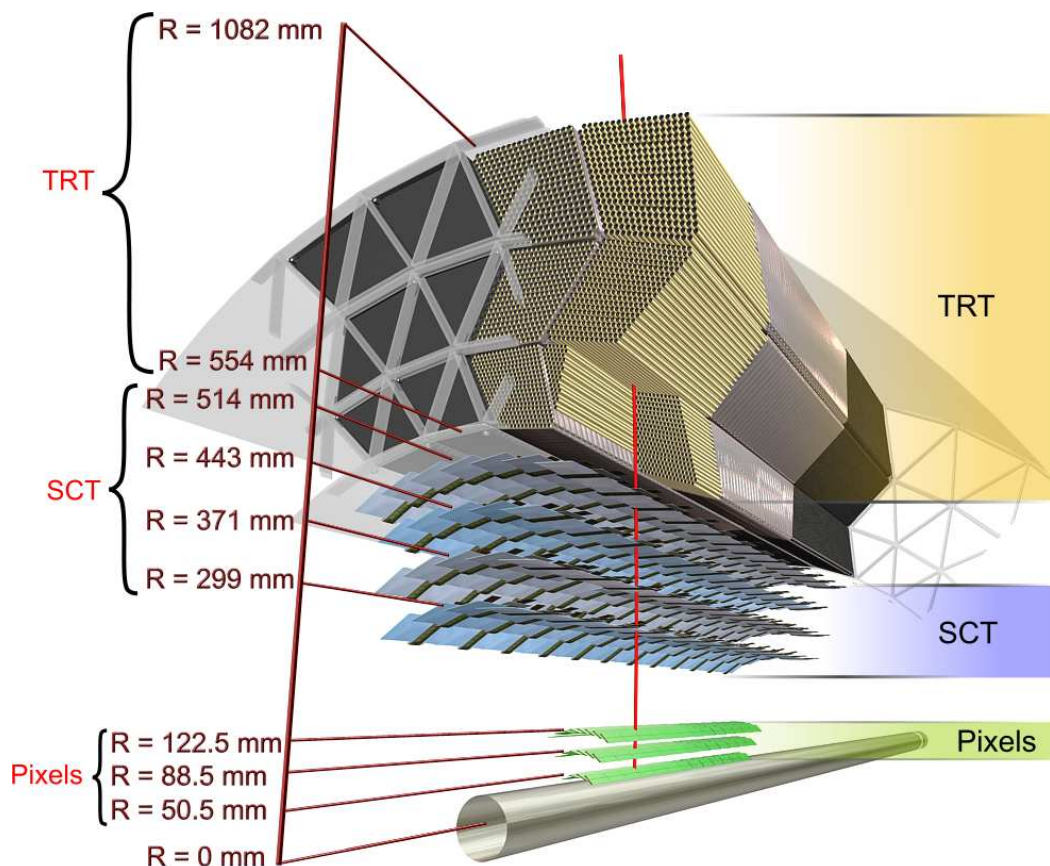


Figure 3.6: Illustration showing the structural elements of the Inner Detector of ATLAS, which is composed of the Pixel detector, the Semiconductor Tracker (SCT) and the Transition Radiation Tracker (TRT). The barrel region of the sub-detectors are traversed by a charged track of $p_T = 10$ GeV at $\eta = 0.3$ [51].

end-caps) is achieved. The pixels are contained in 1744 identical rectangular modules whereas each module includes 16 chips that are read out with binary electronics. A total of 13 barrel modules are assembled into a longitudinal ladder structure, called a stave. Two staves are assembled together to form a bi-stave. Each stave is cooled by a single cooling loop (the cooling system of the Pixel detector is shared with the SCT and described in more detail in section 3.3.1). A total of 48 end-cap modules are combined to form a wheel.

The pixel detector is currently fully operational and performing close to design specifications [55]. At the time of writing (August 2011) only about 3% of the modules are disabled and the track association efficiency for clusters is approximately 99%. The noise occupancy is at a low level; of the order of 10^{-9} hits/pixel/bunch-crossing

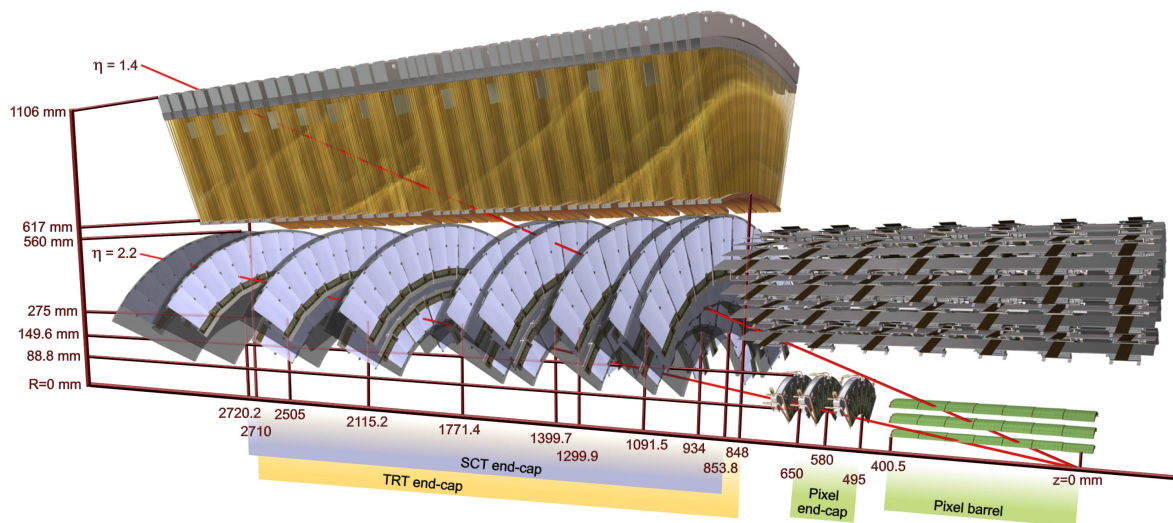


Figure 3.7: Illustration of the sensors and structural elements of the Inner Detector traversed by two charged tracks of transverse momentum of about 10 GeV in the end-cap ($\eta = 1.4$ and 2.2) [51].

for offline track reconstruction.

The Semiconductor Tracker

The SCT is the second innermost detector in ATLAS, located between the Pixel and the TRT (see Figure 3.6), and is based on a silicon micro-strip technology. Due to cost and reliability the SCT sensors use a classic single-sided p-in-n technology. The purpose of the SCT is to provide precise tracking information, together with the other sub-systems of the Inner Detector, for achieving high quality measurements of particle momentum and location in the detector. The details concerning the design and capabilities of the Semiconductor Tracker are outlined in section 3.3.

The Transition Radiation Tracker

The Transition Radiation Tracker (TRT) is a gaseous drift (straw) tube detector. The main goals of the TRT are to enhance the tracking capability of the silicon detectors and to provide particle identification, in particular by identifying electrons from pions and other charged particles.

The detector technique applied to the TRT uses 351 000 straw detectors, which are about 150 cm long, located axially in the barrel and radially in the end-caps [51]. In the barrel the detector is divided into 32 modules composed of three rings and in each end-cap 20 wheels are assembled together. With this geometry, the TRT

provides $R\text{-}\phi$ information, but has no or little spatial resolution in the z -direction. The advantage of the straw detectors is that they are able to operate at the high rate at which the particles are being produced at the LHC. A large number of position measurements are acquired for each track; on average 36 in the barrel and over 40 in the end-caps. This is due to the small diameter of the straw as well as the fact that the sense wires are isolated within separate gas volumes.

An important functionality of the TRT is based on detection of transition radiation photons which are created in the gas by traversing charged particles. This is made possible by using a gas containing 70% xenon to detect the transition-radiation photons which are created in between the straws. Electrons can thus be distinguished from pions through their transition radiation characteristics. Above a momentum of a few GeV, electrons have a much higher probability of depositing an energy above a certain threshold in comparisons with pions with the equivalent momentum. The TRT, in addition to the Pixel detector, uses ToT to measure dE/dx to carry out particle identification for heavily ionizing particles.

Studies of the TRT performance have been completed with cosmic ray as well as collision data [56]. The sub-detector has remained fully operational during the 2009 and 2010 physics runs and has a hit efficiency of above 94% for the operational threshold chosen for tracking. Approximately 2% of the channels were disabled during the 2010 data-taking.

Material in the Inner Detector

Silicon detectors are beneficial for high tracking accuracy but disadvantageous for the material budget. The services located in front of the calorimeter are especially dense between the barrel and the end-caps as shown in Figure 3.8. Charged particles traversing the tracking detectors are affected by the material since they undergo bremsstrahlung and hence lose part of their energy before reaching the calorimeter. Electrons tend to shower due to their low mass while muons are not significantly affected. Photons are also affected by the material through conversion into electron-positron pairs. Details concerning the material impact on the reconstruction of electrons, originating from W and Z decays, are further discussed in chapter 6.

3.2.3 Calorimetry

Once the neutral and charged particles have traversed the ID tracking system, traveling from the interaction point, they reach the highly granular ATLAS calorimetry system. Here, the electrons, photons and hadrons shower and therefore deposit their energy, which can then be measured together with their position. Since electromagnetic and hadronic objects behave differently in this aspect, they need to be treated

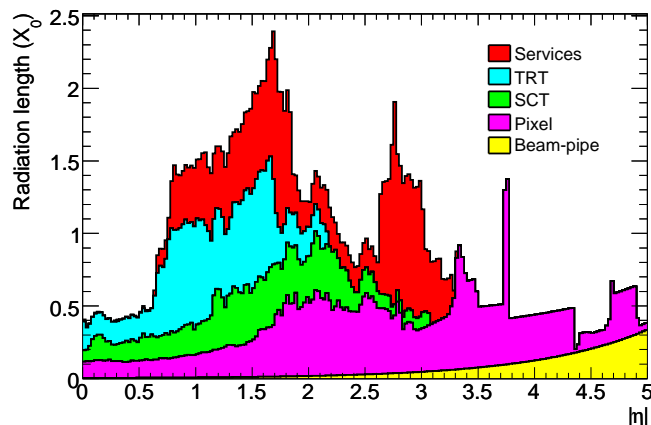


Figure 3.8: Material distribution (X_0) at the exit of the ID envelope, including the services and thermal enclosures. The distribution is shown as a function of $|\eta|$ and averaged over ϕ . The break down indicates the contributions of external services and individual sub-detectors, including services in their active volume [23].

by two different calorimetry systems; the electromagnetic and the hadronic calorimeter. As the naming suggests, the electromagnetic calorimeter is used to identify and measure the energy of electrons and photons, while the hadronic calorimeter is used for the identification and energy measurement of hadrons (mainly charged pions). The EM calorimeter is therefore optimized to have short radiation length while the hadronic calorimeter is optimized for short interaction length. The EM calorimeter and the end-cap and forward components of the hadronic calorimeters use a highly granular liquid argon technique (LAr). The barrel of the hadronic calorimeter consists of a Tile Calorimeter. The overall pseudorapidity coverage is $|\eta| < 4.9$. For an illustrative overview of the different components of the ATLAS calorimetry system see Figure 3.9.

Apart from providing precise measurements of e/γ objects, jets and E_T^{miss} , another important feature of the calorimetry system is to limit punch-through into the muon system. The calorimeter must thus contain all final state particles except for muons and non-interacting particles, and calorimeter depth is therefore an important quality. Approximately 9.7 interaction lengths (λ) of active calorimeter in the barrel (10 λ in the end-caps) ensures good E_T^{miss} resolution, which is particularly important for BSM searches, for instance for SUSY particles. The total thickness, including 1.3 λ from the outer support, is 11 λ at $\eta = 0$; a thickness that is adequate to provide good resolution and sufficient punch-through reduction for high energy jets.

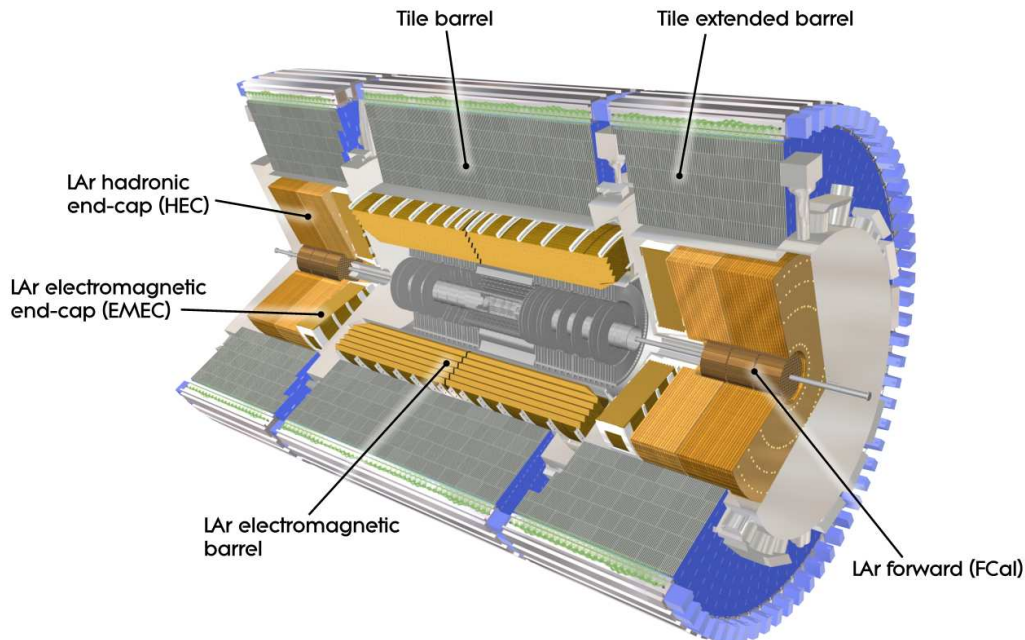


Figure 3.9: The different components of the ATLAS hadronic and electromagnetic calorimetry system. The LAr and Tile detectors are indicated with yellow and grey colors respectively. The FCal extends the coverage up to $|\eta| = 4.9$ [51].

LAr electromagnetic calorimeter

The EM calorimeter consists of a barrel ($|\eta| < 1.475$) and two end-cap components ($1.375 < |\eta| < 3.2$), with a transition (“crack”) region at $1.37 < |\eta| < 1.52$. The barrel is divided into two identical parts of length 3.2 m with a 4 mm gap separating them at $z = 0$ [51]. Each of the four sectors is enclosed within a separate cryostat.

The calorimeter uses liquid argon (LAr) as the detector medium with lead plates as the absorbing medium. An accordion geometry has been chosen for the absorbers since such a geometry naturally provides full azimuthal coverage without any gaps together with a fast signal extraction at the rear or at the front of the electrodes. In the barrel, the accordion waves are axial (see Figure 3.10) and in the end-caps, the waves are parallel to the radial direction.

The calorimeter modules are divided into three radial layers (strip, middle and back layer) and has decreasing granularity in the R direction since the LAr gap increases with radius. The typical granularity of a barrel module is shown in Figure 3.10. The strip layer is more finely segmented in order to measure the direction with higher precision. The middle layer contains most of the energy in the shower and the

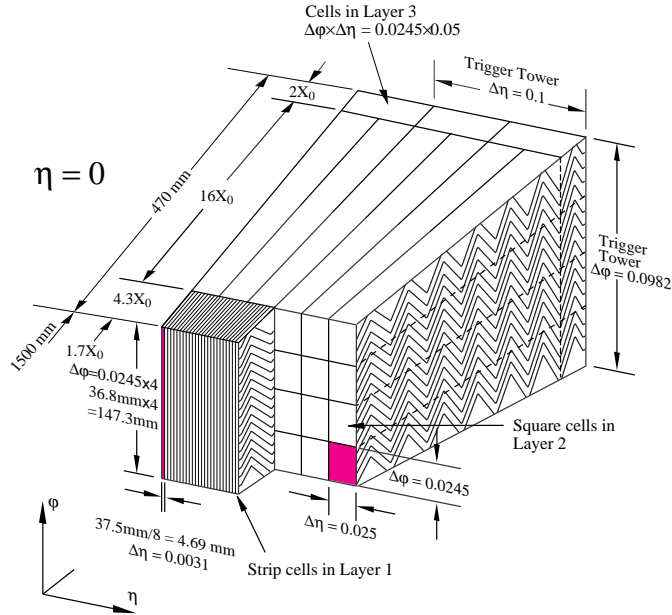


Figure 3.10: A sketch of the accordion geometry of an EM calorimeter barrel module [51].

back layer is designed to contain the electromagnetic shower. Due to the large amount of material between the Inner Detector and the calorimetry, a presampler is installed to determine the energy loss for $|\eta| < 1.8$. The different setup in the different regions of the detector leads to a uniform performance in terms of linearity and resolution as a function of ϕ . The granularity of the entire calorimeter system for different $|\eta|$ is summarized in Table 3.3.

The design resolution for the LAr EM calorimeter, obtained from test beam studies, is stated in Table 3.2. The uncertainty on the absolute EM scale, measured with 2010 data, is 0.5%-1.5% for $|\eta| < 2.5$ and about 3% in the forward region [57]. Only the constant term of the energy resolution has been measured with the 2010 data due to the limited statistics. More details on electron energy scale and resolution, measured with Z boson decays in data, can be found in section 6.3.5.

Hadronic and forward calorimeters

The main goal of the hadronic calorimeter is to provide accurate energy measurements of jets and of the missing transverse energy. It must therefore be sufficiently thick and have a large coverage in $|\eta|$ in order to contain the hadronic shower.

The hadronic calorimeter system consists of the barrel-shaped Tile Calorimeter (TileCal) and LAr end-cap and forward calorimeters for higher pseudorapidity

		Barrel		End-cap	
Pre-sampler		0.025×0.1	$ \eta < 1.52$	0.025×0.1	$1.5 < \eta < 1.8$
Calorimeter	1st layer	$0.025/8 \times 0.1$	$ \eta < 1.40$	0.050×0.1	$1.375 < \eta < 1.425$
		0.025×0.025	$1.4 < \eta < 1.475$	0.025×0.1	$1.425 < \eta < 1.5$
				$0.025/8 \times 0.1$	$1.5 < \eta < 1.8$
				$0.025/6 \times 0.1$	$1.8 < \eta < 2.0$
				$0.025/4 \times 0.1$	$2.0 < \eta < 2.4$
			0.025×0.1	$2.4 < \eta < 2.5$	
			0.1×0.1	$2.5 < \eta < 3.2$	
	2nd layer	0.025×0.025	$ \eta < 1.40$	0.050×0.025	$1.375 < \eta < 1.425$
		0.075×0.025	$1.4 < \eta < 1.475$	0.025×0.025	$1.425 < \eta < 2.5$
	3rd layer	0.050×0.025	$ \eta < 1.35$	0.050×0.025	$1.5 < \eta < 2.5$
TileCal	First two layers	0.1×0.1	$ \eta < 1.0$	0.1×0.1	$0.8 < \eta < 1.7$
	Last layer	0.2×0.1	$ \eta < 1.0$	0.2×0.1	$0.8 < \eta < 1.7$
Hadronic end-cap	First two layers			0.1×0.1	$1.5 < \eta < 2.5$
	Last layer			0.2×0.2	$2.5 < \eta < 3.2$

Table 3.3: Granularity of the EM and hadronic calorimeter for $\Delta\eta \times \Delta\phi$ versus $|\Delta\eta|$ [51].

where the radiation is more intense. The hadronic end-caps (HECs) and the forward calorimeter system (FCal) use the same LAr technology as the EM calorimeter and share their cryostats [51]. The FCal extends the pseudorapidity coverage up to $|\eta| = 4.9$. It consists of three layers: one for EM particle detection using copper plates as the absorber and an additional two layers for hadronic particle detection using tungsten plates as the absorber.

The Tile calorimeter, which is placed directly outside the EM and HEC calorimeters, consists of one central barrel ($|\eta| < 1.0$) and two extended barrels ($0.8 < |\eta| < 1.7$). The TileCal is a sampling calorimeter with steel as the absorber and plastic scintillating tiles as the active material. The tiles are placed in a periodic pattern, where every tile is connected via fiber optics to a photomultiplier on each side. The granularity of the hadronic calorimeters are stated in Table 3.3.

The Tile calorimeter delivered 100% usable data for the 2010 physics runs [58]. The validation of the EM scale at the cell level has been pursued with cosmic ray data in 2009 and the uncertainty agrees with the required resolution shown in Table 3.2. The jet energy scale (JES) uncertainty has been measured with the 2010 collision data, from single hadron response measurements, to be approximately 2 – 3% in the central detector [59].

3.2.4 The muon spectrometer

Except for neutrinos, which escape ATLAS undetected, muons are the only known final state particles that traverse the calorimetry and reach the muon spectrometer. Muons originate as decay products of various interesting physics processes, such as

W and Z decays and are therefore important to detect and to select as a trigger signature. To measure the properties of the muons, the spectrometer is constructed to surround all the other ATLAS sub-detectors, which can be seen in Figure 3.4. It is the muon spectrometer that defines the large dimensions of the ATLAS detector.

The muon spectrometer deflects the path of the muons with the superconducting toroidal magnet system, consisting of a long barrel and two inserted end-cap magnets [51]. The barrel toroid provides a bending power of 2-6 Tm in the pseudorapidity range $0 < |\eta| < 1.3$ while the end-cap toroids deliver 4-8 Tm in the range $1.6 < |\eta| < 2.6$. Due to the presence of the magnetic field, high resolution measurements of the muon momentum can be obtained. The precision measurements of the muon tracks are made in the R - z projection, which is parallel to the bending direction of the magnetic field.

The trigger chambers of the muon spectrometer have three main purposes. Firstly, they must identify individual bunch crossings, requiring a small time resolution. The trigger must also have well-defined p_T cut-offs in moderate magnetic fields, implying a granularity of the order of 1 cm. The final purpose is to measure the coordinate orthogonal to the coordinate measured in the precision chambers with a resolution of 5-10 mm. More information about the ATLAS trigger system is given in section 3.2.6 below.

The muon spectrometer ran stably during 2010, with nearly 100% data-taking efficiency during the physics runs [60]. The momentum resolution was measured with both cosmic data in 2009 as well as collision data in 2010. In 2010 data, combined muons from $Z \rightarrow \mu\mu$ and $W \rightarrow \mu\nu$ decays were used to measure the resolution and alignment of both the Inner Detector and the muon spectrometer [61]. The results show that the expected detector design resolution, shown in Table 3.2, is not fully achieved with the use of the preliminary alignment and calibration constants in the first-pass reconstruction. However, the resolution improved with the more detailed alignment and calibrations in the re-processed 2010 data.

3.2.5 Forward detectors

The LHC delivers beam at a given luminosity, which can in principle be evaluated using the measured beam parameters. However, each experiment needs to make an independent measurement of the luminosity recorded by the detector. In ATLAS, this measurement is performed by two detectors located in the forward region, along the beam pipe.

At ± 17 m from the interaction point lies the LUCID detector (LUminosity measurement using Cerenkov Integrating Detector) [62]. It is the main real-time relative-luminosity monitor for ATLAS, using the detection of inelastic p - p scattering in the forward direction. The second detector, ALFA (Absolute Luminosity For ATLAS)

[63], is located much further down the beam at ± 240 m from ATLAS. ALFA consists of scintillating fiber trackers and measures the absolute luminosity using the detection of elastic p - p scattering.

The integrated luminosity estimated for the delivered 2010 data was first determined online from counting rates measured independently by the luminosity detectors and included a systematic uncertainty of $\pm 11\%$ [40]. The luminosity scale was later calibrated by using dedicated *van der Meer* scans, which measure the event rates while scanning the two proton beams first in the horizontal, then in the vertical direction [41]. The offline luminosity was found to be lower than the online luminosity with a reduced systematic uncertainty of $\pm 3.4\%$.

Later on, when the W boson production cross section has been measured with high precision in ATLAS, such events can be used to measure the luminosity itself. One simply counts number of observed W bosons and calculates back to the luminosity using the measured cross section.

3.2.6 ATLAS data acquisition and trigger system

An efficient trigger system is of fundamental importance for the LHC detectors in order to select rare particle signatures from the overwhelming background of other collisions ($\sim 10^8$ per second at design luminosity). Note that most particles produced by the LHC are of lower energy, while the physics most relevant to ATLAS is usually of higher energy and smaller cross section (see Figure 2.3).

Another reason for not being able to store all the collision events is that the hardware that is recording the data has intrinsic limitations in bandwidth. The data acquisition system receives and buffers the event data from the detector-specific readout electronics, over 1600 point-to-point readout links, at the first trigger level accept rate [51]. The rate of selected events must be reduced from the 40 MHz bunch crossing frequency to a few hundred Hz to be able to store the data permanently. In the ATLAS experiment, the trigger system provides a solution to this problem by filtering the data recorded by selecting events of interest by the different sub-detectors. During the first runs of the LHC, the bandwidth of data was of course less of an issue due to the much lower instantaneous luminosity.

The ATLAS trigger system contains three different levels of triggering, where each level significantly reduces the number of accepted events. The Data Acquisition (DAQ) system then records the interesting data selected by the trigger. For a schematic overview of the data flow of the Trigger-DAQ (TDAQ) system in ATLAS see Figure 3.11.

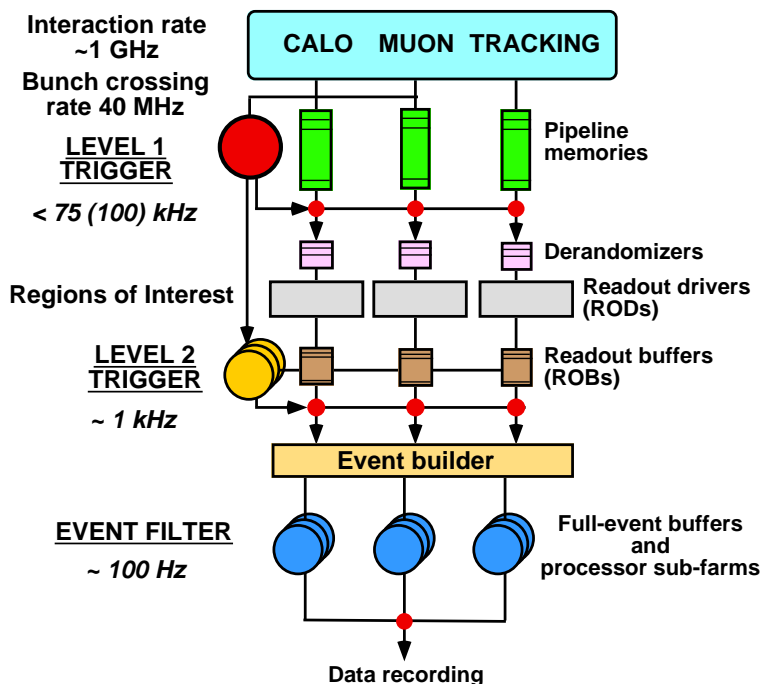


Figure 3.11: An overview of the ATLAS Trigger-DAQ system [49].

First level trigger

The Level 1 (L1) trigger makes the initial decision whether or not to pass on the data to the next trigger level, for each of the individual collision events. The data that passes the L1 trigger is initially stored in so-called pipeline memories. Because of the limited size of the memories together with the relatively long time-of-flight until the muon spectrometers are reached, the decision has to be made in a very limited time-scale; $2.5 \mu\text{s}$ [51]. The L1 selection of events is therefore only based on reduced-resolution information from the trigger systems in the muon spectrometer and the calorimeters. Objects that the L1 trigger is searching for are for example jets in the Tile calorimeter, higher p_T e/γ objects in the EM calorimeter, large amount of missing transverse energy in the entire calorimeter system and high p_T muons in the muon spectrometer. The location where one of these objects is registered is then defined as a region of interest (RoI) for a potentially interesting event. The RoIs extend as a cone from the interaction point to the outer parts of the ATLAS detector.

The L1 trigger decision is hardware based and has programmable thresholds that can be adjusted according to luminosity and physics requirements in a particular run. Most of the physics requirements of ATLAS can be met by using relatively simple criteria already at the first trigger level. In the case of electron analyses with

the very first data, a L1 electromagnetic trigger with a E_T threshold of 5 GeV was sufficient, while for later runs with higher luminosity, the rate of recording low energy triggers was significantly reduced (the trigger is “pre-scaled”). Pre-scaling of trigger menu items allows for optimal use of the bandwidth as luminosity and background conditions change.

Second level trigger

Events selected by L1 are read out from electronic systems at the front-end of the detector into readout drivers (RODs), where some processing may occur, and further on into readout buffers (ROBs). Multiple ROBs are part of one Read Out System (ROS). The ROS fragments are then joined and the full event is built upon receipt of a Level 2 (L2) trigger signal. The Level 2 trigger scans the events from the ROBs, now reading the data with full-resolution using all subsystems within the RoI. The aim of the L2 trigger is then to reduce the event rate from L1 by two orders of magnitude [51], which can be obtained by applying restrictions on the information available within the RoIs. The decision making time for this step of the trigger system is on average about 40 ms, which is a significantly longer time scale than for the L1 trigger. The L2 trigger menus are designed to reduce the data rate to 3.5 kHz, which is made possible due to the buffering of events in a multiprocess system.

Event filter

The data accepted by the L2 trigger system is further passed on to the Event Builder (EB), which performs a full reconstruction of the event and sends it to the final stage of the ATLAS trigger system; the Event Filter (EF). The EF reduces the event rate to approximately 200 Hz. The data passed by the EF is then to be used in the offline analysis. This level of the trigger is commonly denoted as the high level trigger (HLT).

The total rejection factor of the whole ATLAS trigger system reaches a factor of about $5 \cdot 10^6$. For more details about the TDAQ system see [49, 51].

The event data model

The events recorded by the Event Filter need to be processed in order to reduce in memory size before being used in an offline physics analysis. The data from the HLT is first stored as object based RAW format, which undergoes event reconstruction by the offline software used in ATLAS known as *Athena* [64]. A similar chain applies to the simulated data, where the events first pass through a GEANT4 simulation of the ATLAS detector before physics objects can be reconstructed. After reconstruction, the Event Summary Data (ESD) as well as the smaller Analysis Object Data (AOD) can be produced. Both the ESDs and AODs contain collections of objects required

to perform physics analysis. The ESDs contain more information through including additional collections than the AODs. For most analyses, however, the AODs contain sufficient information.

When first data became available in ATLAS, a simplified and significantly smaller data format was produced from the ESDs/AODs. The data format is called D3PD (Derived Physics Data) and consists of a flat ROOT ntuple containing different variables from various physics objects. The D3PDs are centrally produced by ATLAS performance and physics groups, such as the e/γ group or the Standard Model group. The information available in the D3PD depends on the group that produces the data samples. The SM D3PDs, for instance, contain the same level of electron information as the e/γ D3PDs, but include additional variables for muon and jet objects.

3.3 The Semi-Conductor Tracker

In this section, a more detailed review of the technical specification of the Semiconductor Tracker (SCT) is outlined. As was briefly mentioned in the previous section, the SCT is the second closest sub-detector to the beam pipe in ATLAS, after the Pixel detector, and is based on a silicon micro-strip technology. A large fraction of the silicon modules, which constitute the building blocks of the SCT, were developed, produced and tested at University of Geneva before the sub-detector was assembled at CERN.

3.3.1 Description and design of the SCT

The requirements for the Inner Detector as a whole (described in chapter 3.2.2) translates in the case of the SCT into the following layout conditions [49]:

- Leptons of $p_T > 5$ GeV must be reconstructed with a 95% efficiency within the limit of $|\eta| < 2.5$ and with a fake track rate of $< 1\%$. Helices are therefore required to be reconstructed in 3D, which imposes at least six tracking layers in the combined SCT and pixel system to provide space point information.
- To be able to separate multiple pile-up events and to be able to reconstruct very high p_T tracks impose a resolution of $z < 1$ mm in the SCT. Achieving a granularity of $(\delta p_T/p_T) < 0.3$ at $p_T = 500$ GeV with a beam constraint requires an R - ϕ measurement accuracy of approximately $20 \mu\text{m}$ at the SCT radius.
- In order to keep track losses in b-jets to a maximum of 5%, a high tracking resolution is required.

The Semiconductor Tracker is designed to provide accurate position measurements for the intermediate radii of the ID (30 to 52 cm from the beam pipe), from four precision space points per track [51]. The SCT has an active silicon area of 61 m² with 6.3 million read-out channels. The SCT barrel consists of four cylindrical layers with a total of 2112 modules and a pseudorapidity range of $|\eta| < 1.1$ to $|\eta| < 1.4$ depending on the barrel layer. Each of the two SCT end-caps comprise nine disks with 988 modules arranged in up to three rings within the disks. The end-caps extend the range of the SCT up to $|\eta| < 2.5$.

The silicon detectors of the ID must be particularly radiation hard due to the proximity to the beam pipe. The operational lifetime of the SCT modules is specified to be at least 10 years of running, assuming 3 years of LHC operation at a luminosity of $10^{33} \text{cm}^{-2} \text{s}^{-1}$ followed by 7 years at $10^{34} \text{cm}^{-2} \text{s}^{-1}$. Including a 50% uncertainty, this implies that the innermost barrel must be able to withstand a 1 MeV neutron equivalent flux of $2 \times 10^{14} \text{n/cm}^2$.

To improve the radiation hardness and reduce reverse annealing and leakage current the module sensors are cooled to around -7°C using an evaporative cooling system. The system is shared with the pixels and uses C_3F_8 as an evaporative coolant. The temperature of the coolant in the cooling pipes is kept around -25°C in order to achieve the desired temperature in the modules. A major cooling problem occurred in May 2008 with the failure of three out of six compressors in the plant. By August 2008, the plant was repaired and upgraded and has since been running relatively stably. Only one cooling loop is turned off for the foreseeable future due to a leak, affecting 13 SCT modules.

3.3.2 SCT modules and front-end electronics

An SCT module consists of two pairs of identical single-sided micro-strip p-on-n sensors glued back-to-back at a stereo angle of 40 mrad to enable position identification [51]. The effective space point resolution provides $17 \mu\text{m}$ in the R - ϕ direction and $580 \mu\text{m}$ in the z (R) direction for a barrel (end-cap) module. The barrel modules are all identical while there are three different designs of end-cap modules depending on the ring within the disk (see Figure 3.12). The barrel module has a strip-pitch of $80 \mu\text{m}$, while the pitch of the end-cap modules vary from 55 to $94 \mu\text{m}$.

Each module sensor consists of 768 channels read out by 6 ABCD3T ASIC chips in the radiation hard technology DMILL [65]. Each chip provides binary readout of 128 detector channels. The signal from the silicon detector is amplified, shaped and compared to a programmable discriminator threshold of 1fC . The hit information from each channel is stored in a 132-deep binary pipeline buffer. The chips also contain a charge injection circuitry used for calibration.

The SCT data acquisition system and read-out consists of several components (see

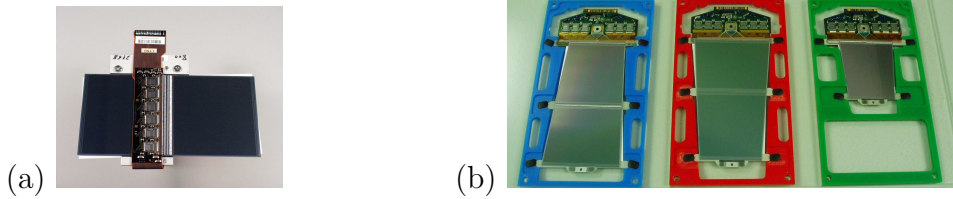


Figure 3.12: Photograph of (a) an SCT barrel module and (b) the three models of end-cap modules (outer, middle and inner ring from left to right) [51].

Figure 3.13). The Read Out Driver (ROD) module performs the main control and data handling and is responsible for module configuration, trigger propagation and event data formatting, as well as module calibration and monitoring. A complementary Back Of Crate (BOC) card interfaces the opto-signals with the electrical signals in the ROD. The BOCs contain two kinds of electro/optical converter plug-ins: an RX plug-in with an array of PIN diodes and a data receiver, and a TX plug-in with an array of VCSELs to return data from each side of one module. Each ROD/BOC pair deals with the control and data for 48 front-end modules.

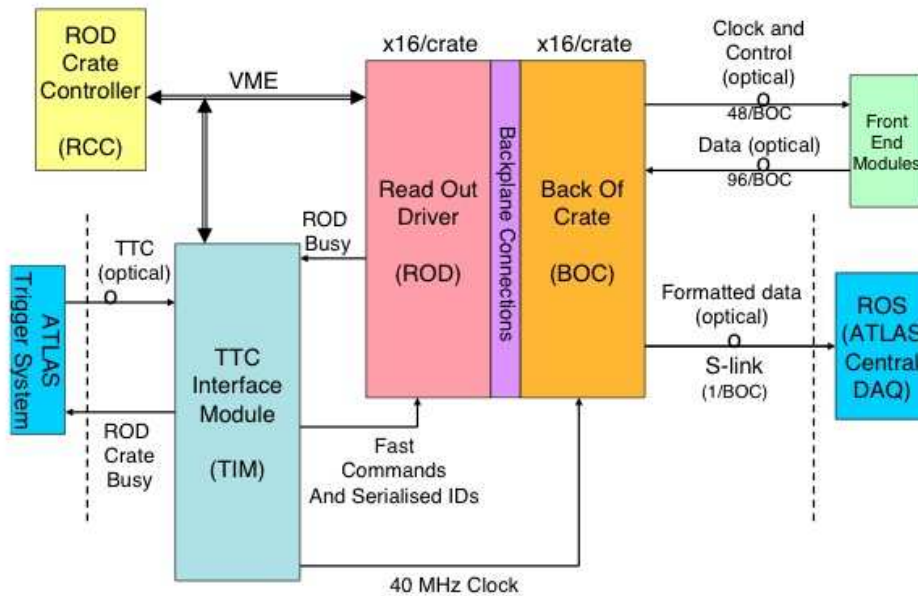


Figure 3.13: A detailed schematic illustration of the SCT data acquisition and read-out architecture [66].

One of the issues encountered with the SCT is an elevated infant mortality of the TX plug-ins. Initial investigations suggested to that the VCSELs had been exposed to electro-static discharge (ESD) during manufacturing. Improved plug-ins

were produced and installed during summer 2009, but these TXs are also failing (a continuing issue during the 2010 data-taking period). Fortunately, failed TX units could be replaced during data-taking and redundancy is used, such that no data were lost due to this problem. A similar issue has been observed with the OTxs in the LAr calorimeter. Here, the failed components cannot be replaced during data-taking and a considerable fraction (a few %) of the calorimeter has become unusable. The dead OTxs in the calorimeter were replaced during the 2010-2011 winter shut-down.

The SCT is currently fully operational and meeting the design requirements. A detailed description of the SCT performance measured with cosmic ray data is presented in section 4.2.2, while the current status of the sub-detector during collision data-taking is briefly discussed in section 4.2.3.

3.4 Summary

The LHC and the ATLAS detector are impressive engineering accomplishments that were installed during the last decade at CERN. The LHC is currently carrying out an aggressive commissioning program, delivering an impressive amount of new data for each run.

The ATLAS detector comprises of different layers of sub-detectors that can measure the properties of different elementary particles. ATLAS is currently fully operational and recording the data that is being delivered by the LHC. At the time of writing (August 2011), ATLAS has recorded over 2 fb^{-1} of proton-proton collision data at $\sqrt{s} = 7 \text{ TeV}$. All sub-detectors as well as the Trigger-DAQ system are functional and meeting the design specifications. The maybe largest issue encountered so far is the dying OTx plug-ins for the LAr calorimeter, which cannot be replaced during the run period and is affecting the acceptance of the calorimeter. The SCT and Pixel detectors are subject to a similar problem with their TXs. However, this does not affect the current data-taking since they can be accessed and replaced without opening up the detector.

Chapter 4

Commissioning of ATLAS

The ATLAS detector was fully installed, prior to the first LHC beam operation, in September 2008. Subsequent to the LHC mal-function that prevented first collisions until November 2009 (see section 3.1.3), the ATLAS detector continued its commissioning phase with three more extensive ATLAS combined cosmic ray data-taking periods in 2008 and 2009. During this period, more than five hundred million events were recorded in the whole ATLAS volume and several million tracks with SCT hits reconstructed in the much smaller volume of the Inner Detector. The majority of these tracks originate from cosmic ray muons but a small fraction of the tracks originate from δ -ray electrons. Identification of electrons in cosmic ray data was studied in great detail by the author and is discussed in section 4.4.

The performance results from the commissioning phase of cosmic data-taking with the SCT are described in section 4.2 and have been presented by the author in [67]. During this commissioning period and more importantly during collision data-taking, the online data quality monitoring (DQM) is extremely important in order to recognize any issue with the detector and the data at the time data collection. Section 4.3 describes the technicalities and the development of the SCT DQM as part of the author's service task during the commissioning and first data period.

4.1 Cosmic ray data collected by ATLAS prior to first collisions

The first extended cosmic ray data-taking periods in ATLAS took place in September and October 2008. The number of total recorded events during this time, as well as the number of events from the individual trigger streams, are shown in Figure 4.1 as a function of run number. A total of 216 million events were recorded during this time, while the Inner Detector trigger stream collected around 7 M events. The

relative cosmic data rate for the ID trigger is low due to the small volume of the ID in comparison with the muon spectrometer. The majority of the events are hence triggered by the muon triggers. The background colors in Fig. 4.1 show the status of the solenoid and toroid magnetic fields, which were turned off during a considerable fraction of the runs. The full ATLAS detector was included in the data-taking for the majority of the time. In some higher rate runs the LAr calorimeter was taken out, allowing trigger accept rates of approximately 500 Hz (corresponding to the step rises in the curves).

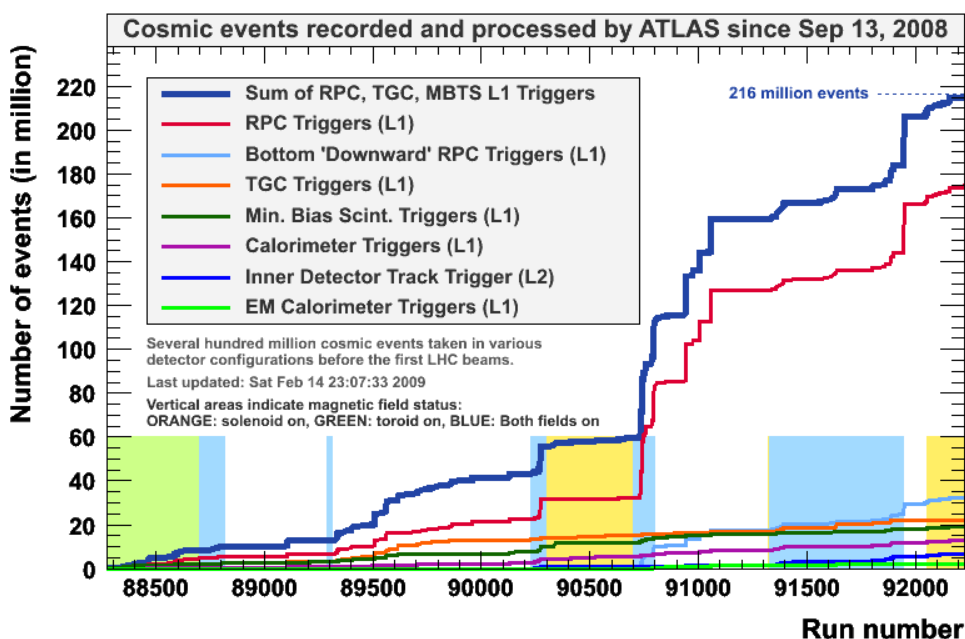


Figure 4.1: Integrated cosmic data rate for ATLAS as a function of run number for the 2008 September/October combined cosmic data-taking period. The total number is approximate, taking bilinear overlaps between the inclusive streams into account for nearly all runs (the overlap information is not available for some runs, where the run ended in a incorrect manner). The background colors in the plot show the status of the solenoid and toroid magnetic field (orange: solenoid on, green: toroid on and blue: both fields on) [42].

The succeeding cosmic data period occurred in the beginning of summer 2009 and the corresponding number of recorded cosmic ray events is shown in Figure 4.2. During this two week period of data-taking a total of 93 M cosmic ray events were recorded whereas nearly 20 M events were triggered in the Inner Detector. The increase of the tracking rate was due to the enabling of the TRT “Fast-OR” trigger,

which directly sends a signal to the Central Trigger Processor (CTP) from the front-end electronics of the TRT. Also the fraction of runs with the solenoid magnet on is larger than for the 2008 cosmic data-taking, encouraging the pursuit of tracking studies.

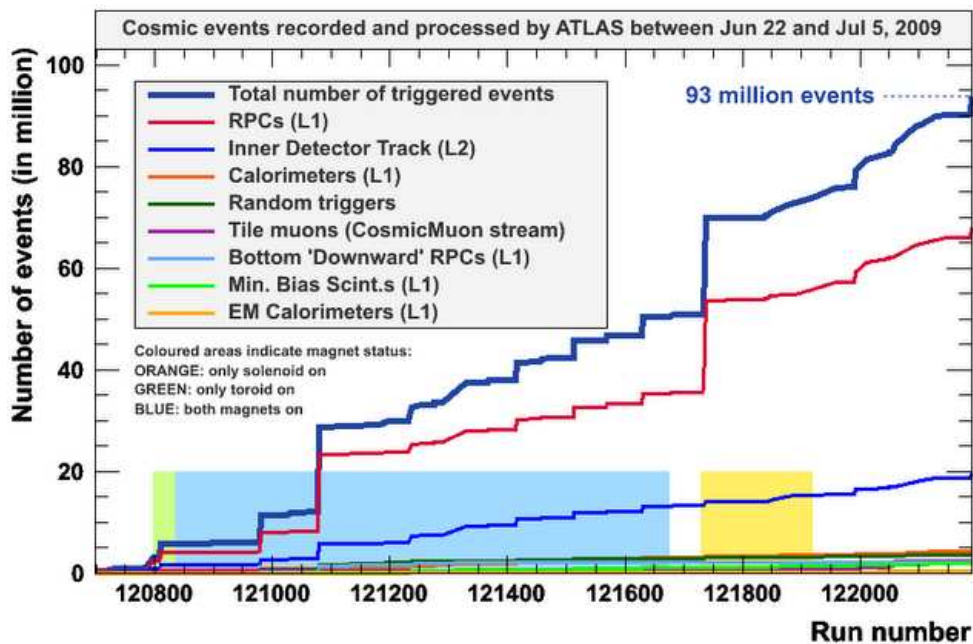


Figure 4.2: Equivalent to Figure 4.1, showing number of recorded events during the cosmic ray data-taking period in early summer 2009. The relative increase of events triggered in the Inner Detector is due to the TRT Fast-OR trigger [42].

The third and final combined continuous ATLAS cosmic ray data-taking period began in October 2009 and continued until the first proton-proton collisions were seen in ATLAS in November 2009 (see Figure 4.3). A total of 266 million events were recorded, while about 25 million events were triggered by either the TRT Fast-OR or the ID high-level trigger. The solenoid magnetic field was enabled during most of this period.

Table 4.1 summarizes the number of total cosmic ray events collected during the three extended data-taking periods in ATLAS. The number of events collected with the Inner Detector trigger (or TRT Fast-OR) as well as after requiring the solenoid and toroid magnets to be on are also included in the table. These are the cosmic ray events considered for electron identification, which is discussed in section 4.4. However, due to the gas mixture applied in the TRT, the data collected during summer 2009 cannot be used for this study (for more details see section 4.4).

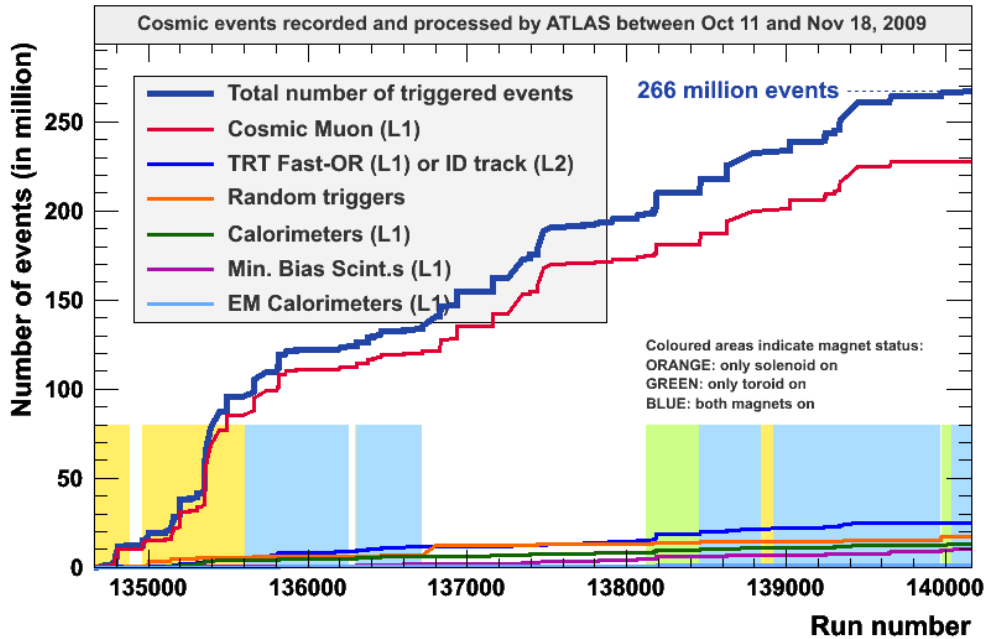


Figure 4.3: Equivalent to Figure 4.1 and 4.2, showing number of recorded events during the cosmic ray data-taking period in fall 2009 lasting up to first collisions [42].

[million events]	Fall 2008	Summer 2009	Fall 2009	All periods
Total nbr of events	216	93	266	575
with ID track	7	20	25	52
and magnets on	4	10	10	24

Table 4.1: Approximate rates of cosmic ray events (in millions) in total, collected with the ID trigger (or TRT Fast-OR) and collected with the ID trigger while the solenoid and toroid magnets were both on. The numbers of events are shown for the different data-taking periods as well as all together.

4.2 Installation and commissioning of the Semiconductor Tracker

4.2.1 SCT installation and integration in ATLAS

The construction of the Semiconductor Tracker has been a worldwide undertaking with the participation of 31 institutes from 13 different countries [67]. After the construction of the modules in several locations, the macro-assembly took place in

2005 at Oxford, UK for the barrel, Nikhef, Holland for end-cap A and Liverpool, UK for end-cap C. The SCT was later integrated and tested, together with the TRT, in the SR1 building at Point 1, CERN. The SCT and TRT barrels were simultaneously installed in the ATLAS cavern in August 2006 and the SCT barrel was fully commissioned by May 2007. End-cap A and C were inserted into the cavern during May and June 2007 and were commissioned during January and February 2008. After the complete system was fully installed, the SCT joined the ATLAS combined Milestone cosmic ray run (M6) in March 2008, which included most of the ATLAS sub-detectors as well as all trigger levels.

The SCT barrel was off due to safety reasons when the first proton beam was circulated in the LHC on September 10th 2008. The main concern was that particles from the unfocused beam might traverse the barrel modules at a small angle and damage the modules. The end-caps, however, were operating at reduced bias voltage (20 V) and high threshold and could detect particle events from beam splashes created in the collimators 140 m upstream from ATLAS. As the first beam splashes were detected by ATLAS, the SCT crew shouted with excitement as the SCT end-caps lit up like light bulbs on the Atlantis event display in the ATLAS control room. The event display, together with some cheerful SCT collaborators, can be seen in Figure 4.4.



Figure 4.4: Picture of part of the SCT crew in the ATLAS control room, September 10th, 2008, aka. “First Beam Day”. The Atlantis event display in the background shows one of the first beam splash events in ATLAS. The SCT displays a large amount of recorded hits in the end-caps.

4.2.2 SCT performance results with cosmic ray data

Since the SCT was fully installed about 18 months before the first collisions, it was properly tested and analyzed through the combined cosmic data-taking as well as stand-alone and calibration runs. During the time of commissioning, the SCT had about 99.3% of its 4088 modules fully calibrated and operational. This included the 13 modules excluded due to the non-operational cooling loop, as was discussed in section 3.3.1. The SCT performance results using cosmic ray and single beam data can be found in [68], while more updated collision performance results are available in [69].

Hit efficiency

A hit is defined as a cluster with signal on at least one strip. The hit efficiency for a given threshold is measured through expected hits; tracks passing through an active region of silicon should result in a hit being read out. The SCT barrel hit efficiency was accurately measured with the cosmic data and the requirements for the tracks analyzed include having 10 SCT hits, 30 TRT hits and $\chi^2/DoF < 2$. The silicon efficiency of the barrel modules for a threshold of 1 fC was found to be 99.75% with the solenoid field on. The hit efficiency for the end-caps was measured to be between 99.0% and 99.5% with cosmic ray data, with the larger uncertainties due to lack of statistics as well as not being accurately timed in with respect to the trigger. More precise barrel and end-cap hit efficiency results have now been completed with collision data (see [69]). The hit efficiency has been measured to be 99.89% in the barrel, 99.75% in end-cap A and 99.76% in end-cap C for combined tracks.

Noise occupancy

A hit is defined as noise if it is not part of a space point, where a space point is a hit on each side of the module. Noise occupancy can be measured with cosmic data runs using random triggers or during stand-alone calibrations. For the SCT barrel and end-caps, the noise occupancy measured per channel at the operating voltage of 150 V is significantly less than the design specification of $5 \cdot 10^{-4}$ (see Figure 4.5). A mean of $1.5 \cdot 10^{-5}$ for inner barrel, $2.2 \cdot 10^{-5}$ for outer barrel, $3.6 \cdot 10^{-5}$ for outer end-cap and $2.5 \cdot 10^{-5}$ for middle end-cap modules was measured for a threshold of 1 fC .

Alignment and timing

The alignment of the Inner Detector is accomplished by track-based offline alignment algorithms minimizing a χ^2 function defined from the track residuals. A residual is defined as the measured hit position minus the expected hit position from the

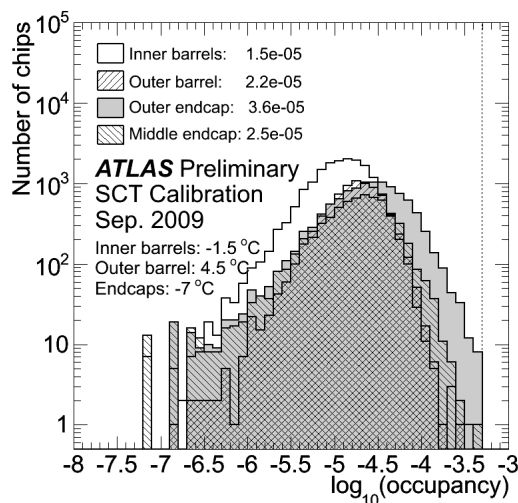


Figure 4.5: Noise occupancy measured in the barrel and end-cap modules in the calibration period during September 2009. A mean of $1.5 \cdot 10^{-5}$ for the inner barrel, $2.2 \cdot 10^{-5}$ for the outer barrel, $3.6 \cdot 10^{-5}$ for the outer end-cap and $2.5 \cdot 10^{-5}$ for the middle end-cap modules was measured, which is significantly less than the design specification of $5 \cdot 10^{-4}$ [68].

track extrapolation. Three different levels of alignment are used for the SCT, from barrel and end-cap structures to the individual module level. Figure 4.6 shows the unbiased residual distribution at module level integrated over all hits-on-tracks in the SCT barrel for the nominal geometry and the preliminary aligned geometry for 2008 cosmic ray data. A single Gaussian fit was performed and the resolution of the fit was compared with the nominal geometry as well as the Monte Carlo simulation of a perfectly aligned detector. The results indicated satisfactory alignment for the barrel. The final accuracy will later be achieved with careful studies of LHC collision data. Due to the geometry of the cosmic tracks, the alignment of the end-caps was not possible with cosmic data and was first achieved with collision data.

Lorentz angle studies

Analyzing the Lorentz angle provides a deeper understanding of the detector alignment and spatial resolution and is required by the data simulation to allow an accurate comparison with data. Details of the SCT Lorentz angle analysis from the 2008 cosmic ray data can be found in [70].

The Lorentz angle originates from the Hall effect. In the presence of electric and magnetic fields, the charge carriers created in the silicon sensor drift along a direction slightly shifted in comparison to that expected without magnetic field. Depending

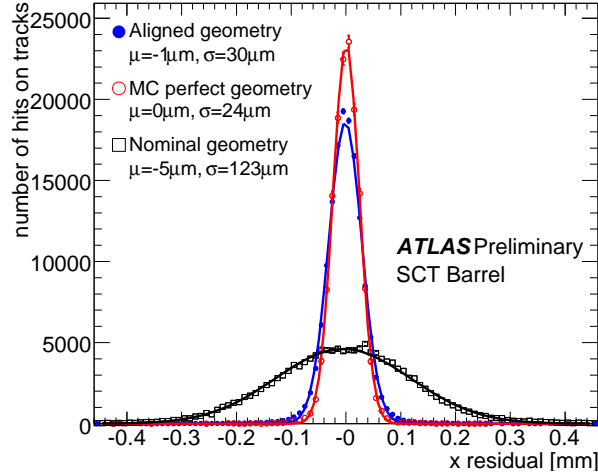


Figure 4.6: Unbiased residual distribution integrated over all hits-on-tracks in the SCT barrel for the nominal geometry and the preliminary aligned geometry for 2008 cosmic ray data [68].

on the incidence angle of the particles, the charge is spread over several strips. Since this spread is minimal for an incidence angle equal to the Lorentz angle (θ_L), it can be extracted from the minimum of the average strip cluster-size as a function of the incidence angle of the track to the module surface accounting for the binary electronics for a given threshold. The angle has been measured with cosmic ray data in the SCT barrel to be $\theta_L = 3.93 \pm 0.03(\text{stat}) \pm 0.10(\text{syst})$, which is in good agreement with the predicted value of $\theta_L = 3.69 \pm 0.26(\text{syst})$ (see Figure 4.7).

4.2.3 SCT with collision data

The SCT is currently fully operational and performing very well. A persistent issue is, as mentioned in section 3.3, the dying optical links (TXs) but this fortunately does not have any impact on the offline data. The cooling loop affecting 13 modules is still not operational at the time of writing, but there are otherwise no significant issues affecting the SCT performance. The intrinsic efficiency of the modules is very high; approximately 99.8% overall and 99.0% of the SCT configuration was fully functional as of May 2010 (including the disabled cooling loop) [69]. Table 4.2 shows the configuration of the disabled modules, chips and masked strips in the SCT as of that date. At the time of writing (August 2011) only 29 SCT modules are disabled in the entire SCT (13 modules due to the leaking cooling loop and 16 modules due to HV and LV errors), while there are 81 dead TX channels using the redundancy readout path.

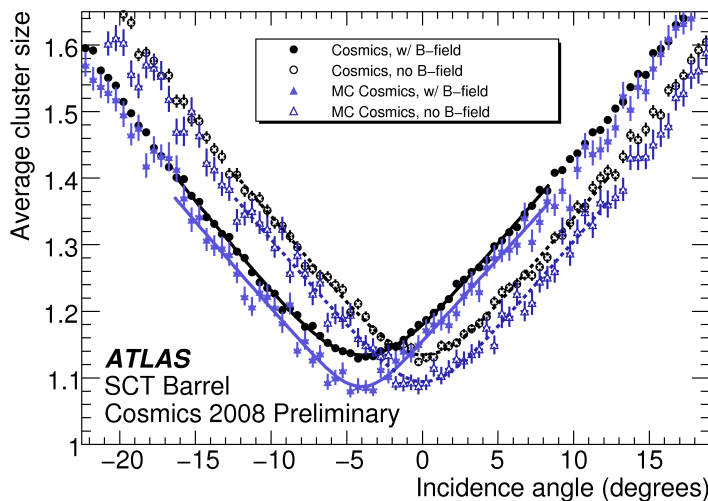


Figure 4.7: Measurement of mean cluster size as a function of incidence angle with 2008 cosmic ray data. The measurements are shown with and without magnetic field together with the Monte Carlo predictions. The value of the Lorentz angle is extracted from the position of the minimum of the field ON data [70].

4.3 Online Data Quality Monitoring of the SCT

The data quality monitoring (DQM) runs on data taken in real time while being acquired by ATLAS and the SCT. The DQM produces online histograms with the purpose of describing the status of the detector. A selected subset of these histograms are included in a user-friendly display to provide an overview of the SCT status as well as a simple way of finding the source of possible problems with the detector during data-taking.

A schematic overview of the data flow structure of the online monitoring is shown in Figure 4.8. A subset of the ATLAS TDAQ system, constituting 32 computing machines, is dedicated to monitor the performance of the different trigger chains and the quality of the data being recorded by the different sub-detectors. The ATLAS TDAQ system was discussed in section 3.2.6.

ATLAS and the SCT have two online monitoring frameworks; the lower level ROS monitoring, devoted to check the hardware conditions, and the high-level monitoring running on the full events from the HLT. Events from both the ROS and the EF are passed through the Event Monitoring (EMon) Service that provides online sampling of the events in parallel with the main data-taking. The work presented here mainly focuses on the high-level online monitoring.

Disabled readout components	End-cap A	Barrel	End-cap C	SCT	Fraction [%]
Disabled modules	5	10	15	30	0.73
Disabled chips	5	24	4	33	0.07
Masked Strips	3 364	3 681	3 628	10 673	0.17
Total disabled detector region					0.97

Table 4.2: The configuration of the SCT as of May 2010 [69]. Overall, 99.0% of the SCT configuration was fully functional. The status of the detector at the time of writing (August 2011) is mainly unchanged with 29 disabled modules; 13 modules due to the leaking cooling loop and 16 modules due to HV and LV errors.

As service work in ATLAS, the author was part of the development and maintenance of the online data quality monitoring for the SCT during commissioning and first data. Below is a brief summary of the online DQM and what was achieved with this task during the period between summer 2008 and the end of 2009 when first collisions arrived.

4.3.1 The Athena monitoring framework

The Athena framework provides a setup for producing histograms for online and offline Data Quality Monitoring. For the offline DQM, the Athena monitoring is the primary interface for producing histograms from the reconstruction that runs on Tier-0¹. The online DQM, on the other hand, runs in real time on a fraction of the events processed by the Event Filter level of the ATLAS trigger (see Figure 4.8). The advantage of the Athena monitoring is that it can run online, through the processing of Raw Data (RDOs), but is based on standard offline software and is thus able to reconstruct objects such as tracks. This also implies that the resulting online histograms can be reproduced offline at a later stage by accessing the RDOs.

The Athena monitoring runs on sampled events provided by the EMon service, which are selected specifying trigger type and other configurable parameters, such as event rate.

The SCT Athena monitoring is composed of several tools producing different types of histograms; *SCTHitsNoiseMonTool*, *SCTTracksMonTool*, *SCTHitEffMonTool* and *SCTErrMonTool*. As the naming suggests, these tools produces different kinds of histograms:

¹Tier-0 is a large computer farm located at CERN, where the data recorded by the experiments is first stored, before being distributed to the smaller Tier-1s and Tier-2s

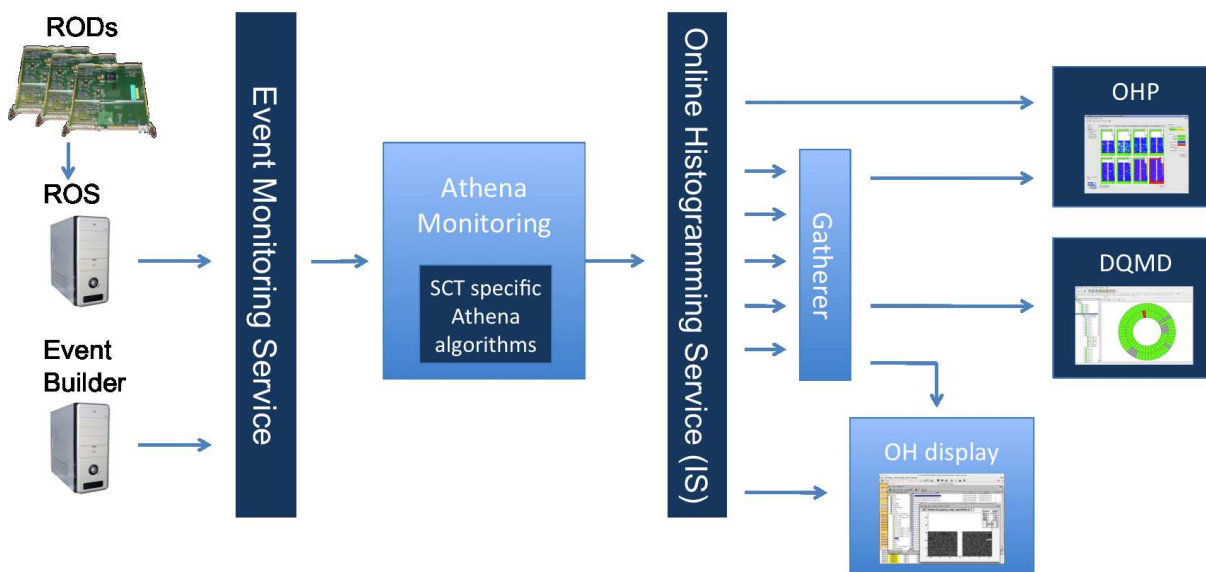


Figure 4.8: A schematic overview of the data flow in the online monitoring, starting with events recorded by the ATLAS trigger and the SCT RODs and finishing with the OHP and DQMD displays viewed by the SCT shifter.

- **Hits** histograms. The SCTHitsNoiseMonTool produces two-dimensional maps of the number of hits in the modules for each barrel layer and end-cap disk. The 2D maps are also produced for each link (side) of the module. Figure 4.9 shows the hit map for the second innermost SCT barrel layer, link 1. The monitoring is even capable of publishing hit maps for every module and side in the SCT (about 8000 histograms).
- **Noise** occupancy. The SCTHitsNoiseMonTool provides a 2-dimensional noise occupancy histogram for each link of every barrel layer and end-cap disk. The tool also provides summary histograms of the noise occupancy for the entire SCT as well as the barrel and end-caps separately. A hit is defined as noise if it is not part of a space point belonging to a reconstructed track (see section 4.2.2).
- **Tracking** histograms. The SCTTracksMonTool produces histograms such as hits-on-tracks, residuals, pulls and RMS of the tracks. It also publishes overall histograms such as the accumulative number of tracks for the current run. This is a useful histogram for immediate detection of a possible issue with the SCT, seen as a sudden decrease in the track rate. The track tool also produces histograms for the timing of the hits-on-tracks. The SCT is read out for three time bins for each bunch-crossing for each trigger. If the SCT signal arrives in

the time-slot before or after the trigger, it would be visible in these histograms as a shift compared to the reference.

- **Efficiency** histograms. The SCTEffMonTool calculates the hit efficiency of the modules and publishes 2D histograms for each barrel layer and end-cap disk (for each side) showing the efficiencies of the individual modules. It also produces summary histograms, such as the average efficiencies for each layer in the barrel and end-cap disk.
- Different type of **errors**. The SCTErrorMonTool produces the same setup of 2D histograms as the efficiency and noise tool for different type of errors. There are errors originating from the hardware, such as timeout errors and errors related to synchronization conflicts with the rest of ATLAS and the LHC, such as Level 1 ID errors and bunch-crossing ID errors. There are also summary 2D histograms combining the total of the individual errors. This particular tool also combines information from all tools in order to produce the so called *configuration* histogram. This histogram (shown in Figure 4.11) gives an overview of the SCT by presenting the number of disabled modules in the SCT, the number of noisy modules, modules giving errors, inefficient modules and finally the number of links that are masked off.

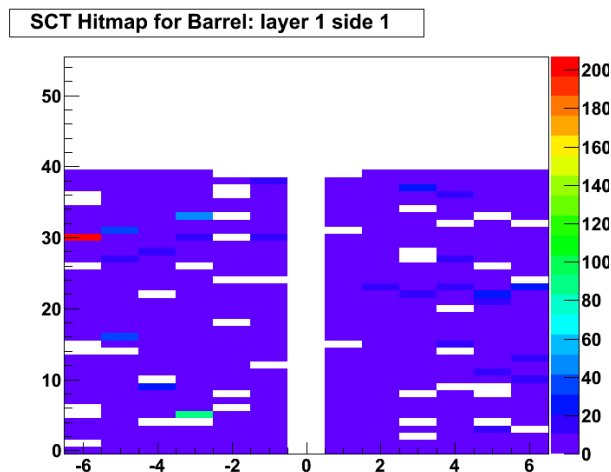


Figure 4.9: The 2D map of SCT hits for link 1 of the second innermost barrel, during data-taking.

The output produced by the monitoring is handled by the *Online Histogramming Service* (OHS), which supports raw and ROOT files. It allows for the routing of commands; any application can issue a command related to a particular histogram and

the OHS takes care of sending the command to the appropriate histogram provider. The OHS uses the *Informations Service* (IS) to manage histograms and provide a transient storage between histogram producers and displays. The IS is also used for archiving and sharing information among the various DAQ applications. It routes information such as run conditions, beam parameters, message logs, etc.

The Athena monitoring package produces an output ROOT file containing histograms grouped into directories and sub-directories according to the different types of histograms and which part of the detector they concern. The code processes the events in parallel through five instances running on different machines in order to increase the sampling rate. The maximum event processing rate is about 1 Hz. The five different instances are combined by a *Gatherer*, which publishes the summary through histograms containing the combined results. In this manner, if one of the Athena monitoring instances fails, the monitoring output will still be provided, merely at a lower rate.

The histograms provided by the Gatherer, as well as those provided by separate instances, are published to the IS server. These can be viewed, together with the histograms from the other sub-detectors, in the Online Histogramming (OH) display. The OH display is not as user-friendly as the more developed displays such as the OHP or DQMD (see below). The OH display simply shows the content of the OHS in a modified ROOT browser, which can be very useful for debugging and for back-up in case the OHP and/or DQMD presenters are temporarily not functioning.

The final step of the online DQM data flow is for the histograms to be passed to the more refined shifter-friendly displays; the *Online Histogramming Presenter* (OHP) and the *Data Quality Monitoring Display* (DQMD) (see Fig. 4.8), where the latter provides automatic data quality checks for the histograms. The histograms shown can be both from the combination of the different Athena monitoring instances provided by the Gatherer and histograms from one of the separate instances.

Trigger aware monitoring

During the last years of commissioning and data-taking, another tool has been added to the DQM in order to provide trigger awareness to the Athena monitoring. The trigger aware monitoring enables the option of producing different sets of histograms for the separate trigger streams. This function is useful if, for example, one would like to acquire information on SCT tracks from one particular trigger stream. One of the advantages with the trigger aware monitoring is the ability to measure the noise occupancy for only empty bunch triggers. The trigger aware monitoring then uses the collision-less trigger as input to produce noise occupancy histograms for the scenario where no tracks are expected. This is one of the prominent ways of properly measuring the noise while LHC is providing ATLAS with p - p collisions.

4.3.2 The Data Quality Monitoring Display

The Data Quality Monitoring Display (DQMD) is a powerful tool available in the DQM framework. It supports a configurable layout, which should render the physical layers and shapes of the detector to facilitate locating a problematic area. The display has a hierarchical structure with the entire sub-detector (e.g. the SCT) as the top layer and the individual modules as the bottom layer. The framework runs customizable and programmable automatic checks on the histograms and compares the results to set thresholds in order to determine if the result of the data quality check is “green”, “yellow” or “red” depending on the threshold settings. The color will propagate up the tree such that if any problem occurs it will be easily spotted.

The data quality checks on the individual histograms are defined by “DQParameters”, which specifies which test (“DQAlgorithm”) to apply and which thresholds (“DQThreshold”) to compare the outcome with in order to classify the result as good or bad. The DQParameters are grouped into DQRegions, which display a summary of the results from the lower level checks as e.g. a worst case summary of its parameters or a simple summary, implying that a certain amount of DQParameters must be flagged as bad for the DQRegion to be red. There are also flags other than the standard green, yellow and red; undefined, which either implies that the histogram is not found or that the statistics is not yet sufficient. There is also a flag for disabled, which implies that the DQRegion/DQParameter (e.g. a module) is not in the configuration. The latter is feasible through the ability of accessing the configuration information from a DAQ database with the framework.

The top DQRegion in the SCT DQMD reflects the entire SCT detector and includes a DQRegion for the barrel, the two end-caps and a separate region for the SCT configuration histogram (see Figure 4.10) that provides a summary of the status of the whole system. On the left side of the layout, the tree structure is displayed simplifying the navigation. The SCT configuration DQRegion contains two DQParameters, both displaying the SCT configuration histogram (see Figure 4.11). The first DQParameter uses a DQAlgorithm that simply prints the contents of every bin, providing with an overview of the amount of modules taken out of the configuration, being noisy, etc. The second DQParameter checks if any of the bins in the histogram are above a certain value and, if this is the case, flags the DQParameter as red. A more detailed description of the different checks applied to the histograms is given below.

The sub-levels of the barrel and end-caps in the DQMD are the barrel layers, as shown in Figure 4.12, and the end-cap disks, as can be seen in Figure 4.13. Propagating further down the hierarchy yields the module level. An example can be seen in Figure 4.14 for one of the end-cap disks.

In parallel with the module level, the end-cap disks or barrel layers also have DQParameters applying tests concerning the entire layer/disk. Some examples of

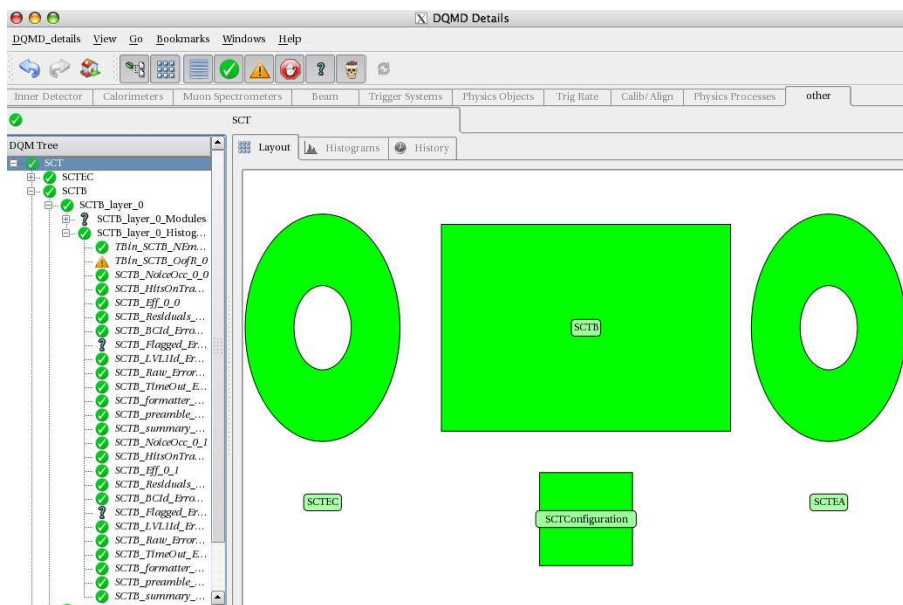


Figure 4.10: A screen-shot of the layout of the top tree level of the DQMD showing the SCT barrel and end-caps as well as the SCT configuration histogram.

DQAlgorithms applied to the different histograms are:

- *BinThreshold* and *BinThreshold2D*, which check if a certain bin (specified by the *DQParameter*) is above a certain threshold. This algorithm is for example applied at the module level in the DQMD, to check if the module is above the set noise, error and efficiency thresholds.
- *Bins_LessThan_Threshold* and *Bin_GreaterThan_Threshold* checks how many bins that are below or above a pre-defined threshold and determines the outcome depending on the set number of allowed bins above/below that threshold. These algorithms are applied to for instance the noise occupancy and hits 2D maps as well as the configuration histogram.
- *BinsFilledOutOfRange* checks how many bins are filled outside the allowed histogram range. The DQAlgorithm is applied to the time bin histograms for hits-on-tracks.
- *CheckHisto_RMS* checks the RMS of the track residual histograms.
- *BinPrint* prints the contents of each bin in the histogram, which is used for the configuration histogram.

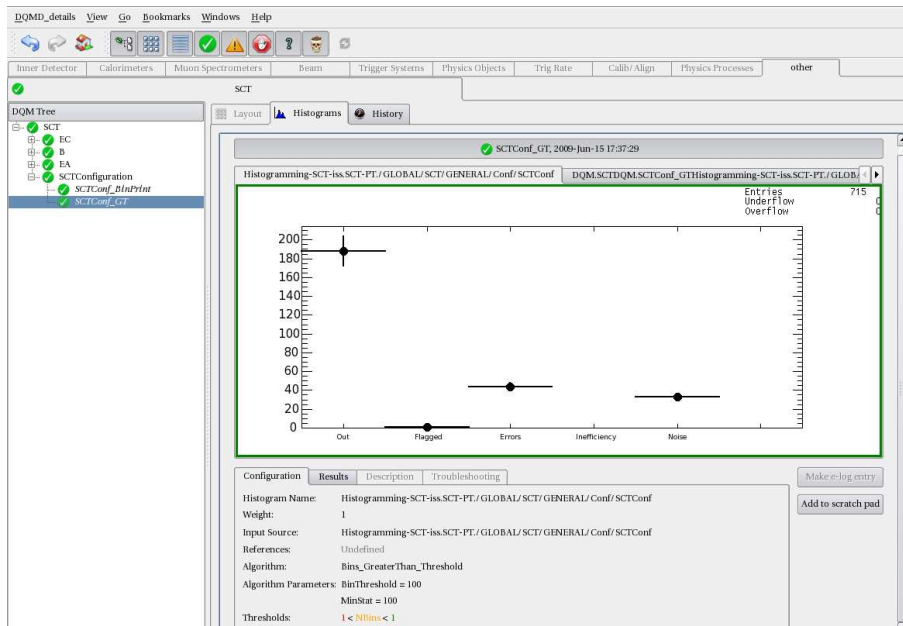


Figure 4.11: The SCT configuration histogram in the DQM Display for a random cosmic run. The bin showing the amount of inefficient modules is empty due to the insufficient statistics for measuring efficiency in online cosmic data.

The histograms in the DQMD have a history tab, which shows the history of the returned value of the DQAlgorithm. For example, the history plots of the 2D error histograms show the number of modules giving errors since the beginning of the run.

In summary, the DQMD is able to find and acquire all the available input histograms each time they are updated, executing SCT pre-defined tests as specified in the configuration, producing and making results available through visualization tools and writing to the data base. Through the automatic propagation of the checks, the tool facilitates rapid identification of detector issues and location of the problem. The DQMD also presents a summary display, showing the run status of ATLAS together with the status of the top level of the DQMD of each of the ATLAS sub-detectors.

4.3.3 The Online Histogramming Presenter

The Online Histogramming Presenter (OHP) is a supplementary display in the monitoring framework. It does not perform any automatic checks on the histogram, but rather displays the histograms in a manner that can provide a better overview and is easier to navigate through than the DQMD. The SCT OHP also includes more histograms than the DQMD since not all of the histograms are suitable for automatic tests. It receives histograms from the Online Histogramming Service and thus

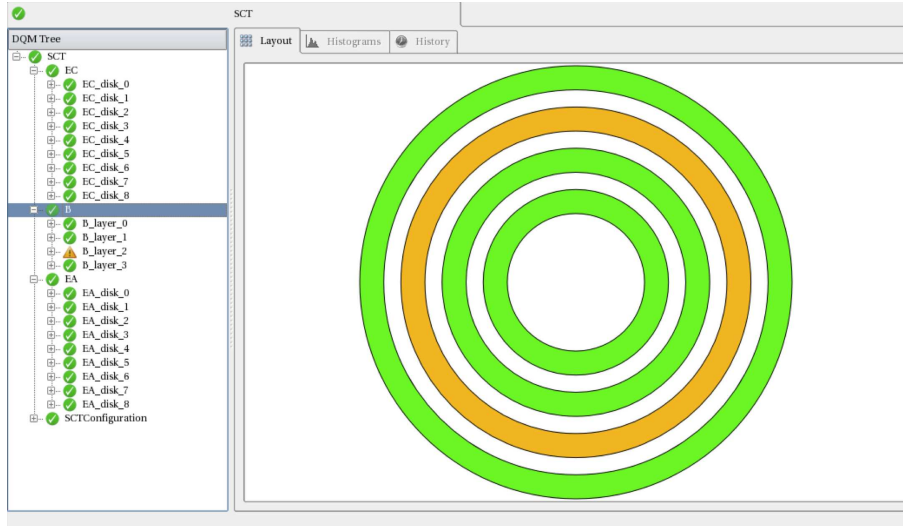


Figure 4.12: The DQMD layout for the barrel, showing the four layer as different DQRegions. Layer 2 is flagged as yellow.

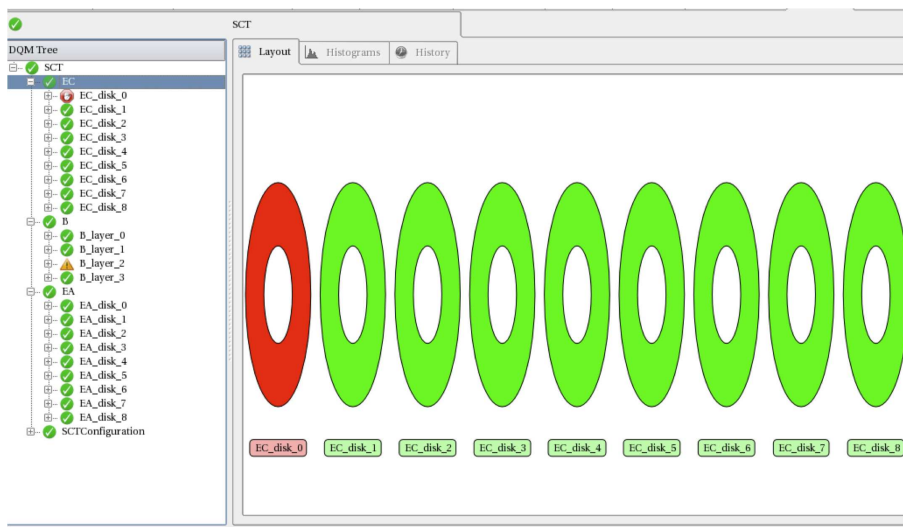


Figure 4.13: The DQMD layout for end-cap C, showing the nine disks as different DQRegions. Disk 0 is flagged as bad.

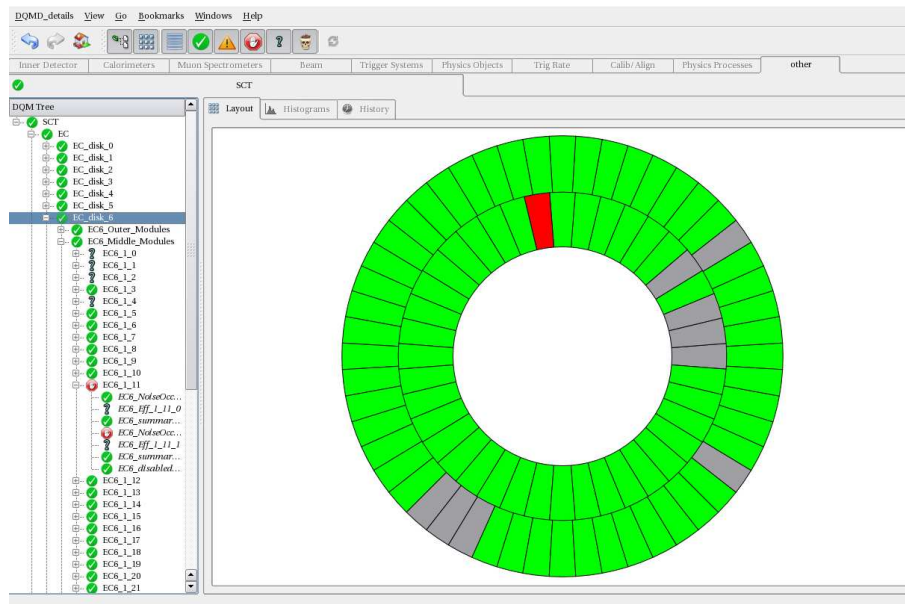


Figure 4.14: The layout for the SCT end-cap C, disk 6 during a cosmic run, with one red module and several disabled modules.

automatically updates when a histogram is published or updated in the IS server. The OHP displays a configurable set in different windows and tabs, organized for the convenience of the user. It also provides with the possibility of browsing all the histograms published in the OHS.

The SCT OHP includes several windows containing tabs with histograms of similar kind. Figure 4.15 shows a screen shot of the OHP with several windows open simultaneously during a cosmic ray run. The different windows show Noise Occupancy 2D histograms, hit maps, track residuals and a SCT global histogram displaying the maximum number of hits versus event number.

Even though the OHP does not apply checks on the histograms, it can display the outcome of the DQMD algorithm for a histogram that is included in both presenters. The OHP exhibits the flag by coloring the background of the histograms in green, yellow or red. An example is shown in Figure 4.16, where the noise occupancy maps for the barrel is displayed, with layer 3, side 1 having a red background due to having more noisy modules than the DQMD set threshold.

Overall, the OHP is a convenient tool for browsing the SCT histograms in a user-friendly way and provides an overview of the system. Due to the structure of windows and tabs, the OHP can give an overview of one kind of histogram for the different regions of the detector at once, which is more difficult in the DQMD. Together, the two presenters compliment each other and provide a robust way of accessing different

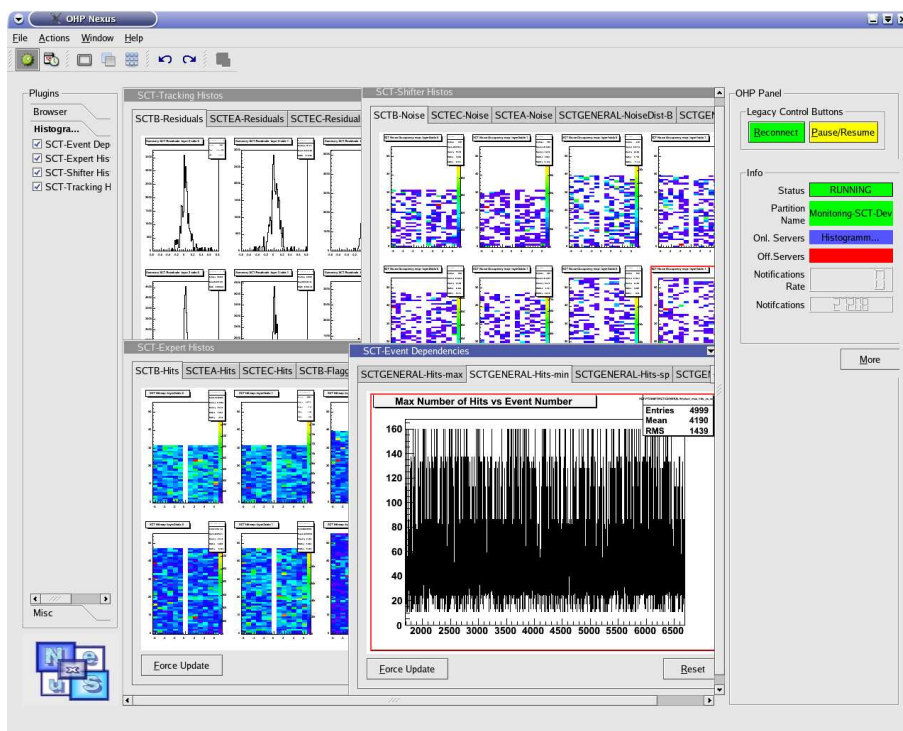


Figure 4.15: A screen-shot of the OHP, taken during a cosmic ray run, displaying several windows at once showing different types of histograms.

types of data quality information for the online SCT monitoring.

4.3.4 Recent progress and future outlook for the SCT monitoring

Since the first collisions were seen in SCT and ATLAS several major improvements have been made to the online DQM. One example is that the ROS monitoring has been subject to significant development and is currently integrated in the OHP and DQMD. In this manner, it can be easily monitored and specific problems are automatically flagged by the DQMD. The DQMD has become the main tool for the SCT shifter, while the OHP is dedicated for expert use.

The OHP also displays specific histograms for the beginning of a run (for the so called “warm start”), which have been added to the Athena online monitoring. For the initial part of the run, the SCT HV is reduced such that standard HLT algorithms are not applied and the data is processed by a specific trigger stream. In addition, the Athena monitoring is currently more efficient with a larger number of processes running simultaneously providing a higher event processing rate.

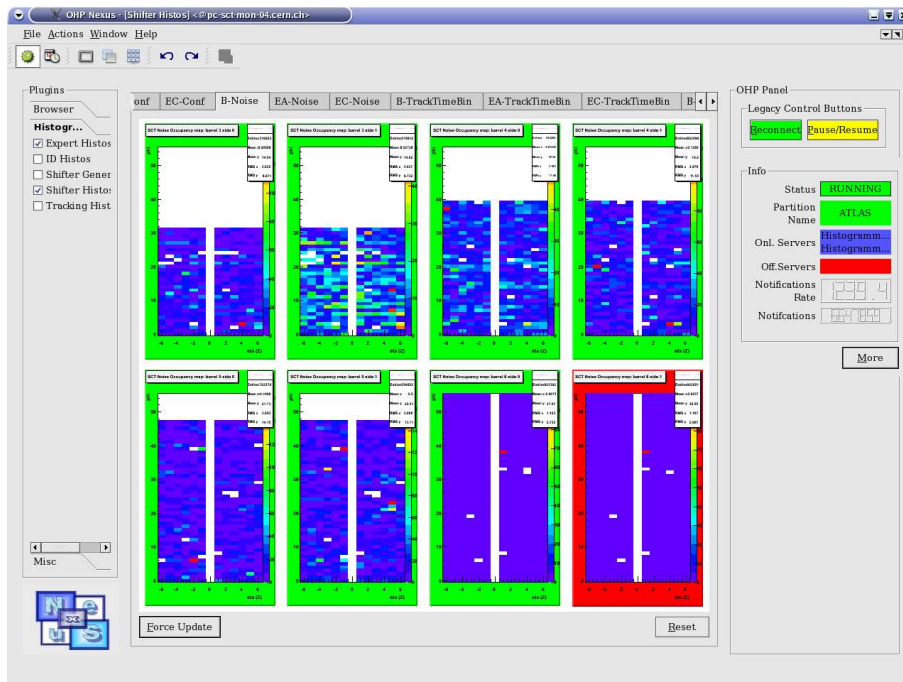


Figure 4.16: A screen-shot of the OHP, taken during a cosmic run, showing the noise occupancy maps for the barrel layers. The background color of the histograms show the outcome of the DQMD check for that particular histogram.

The Inner Detector sub-systems are currently working towards reducing the shift crew and the monitoring software and tools are therefore being merged across the sub-systems. The SCT DQMD has therefore recently been simplified to display a smaller number of histograms and checks (the module level histograms, for example, have been removed).

4.4 Identifying electrons in cosmic ray data

After the delay of the LHC start-up in September 2008, ATLAS continued with several periods of cosmic ray data-taking in order to calibrate and improve the performance of the detector. However, not only hardware performance studies were completed with ATLAS cosmic data. The numerous recorded cosmic ray events offered a first opportunity to evaluate the performance of the ATLAS detector and software by identifying the rare cases where electrons are produced by muons originating from the atmosphere.

A summary of the results from the analysis of identifying electrons in cosmic ray data has been published in [71]. The details of the analysis has been documented in

a separate internal note [72].

4.4.1 The nature of electrons in cosmic ray events

The muons traversing the ATLAS detector typically deposit a minor (minimum ionizing) fraction of their energy in the detector. However, in rare events, the interactions between a muon and the detector material can produce an electron, either from direct muon ionization (high energy δ -ray) or from a photon conversion originating from muon bremsstrahlung. Studying Monte Carlo simulations of cosmic ray data has shown that approximately 77% of reconstructed electron tracks (at any energy) originate from muon ionization, 22% from photon conversion and about 1% from muon decay in flight (see Figure 4.17 for a sketch of the different possible scenarios).

An important background process to electrons in cosmic ray data occurs when a muon leaves a proper track in the Inner Detector and emits bremsstrahlung, which does not convert in the ID. The combination of the cluster produced in the electromagnetic calorimeter by the photon and the muon track in the ID can then fake a reconstructed electron.

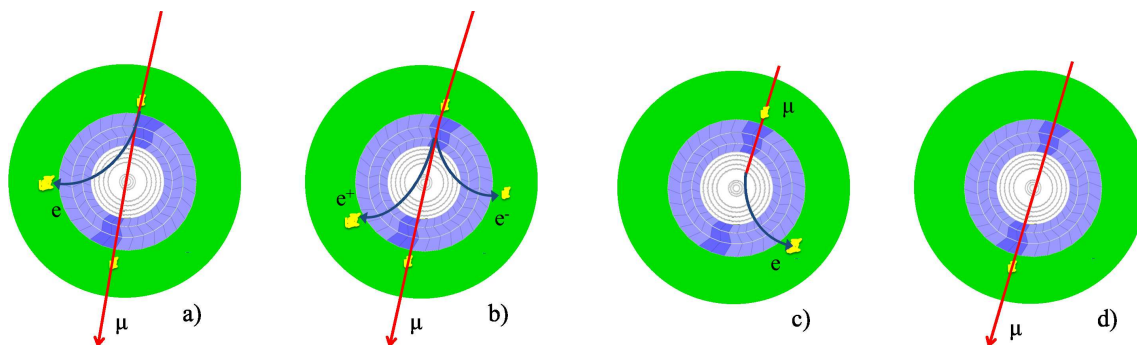


Figure 4.17: A schematic illustration of the three possible scenarios for an electron to be produced in cosmic ray data as well as the background process. From left to right: a) A δ -electron produced by direct muon ionization in the detector material. b) Muon bremsstrahlung, where the photon converts to an electron-positron pair in the Inner Detector. c) Muon decay in flight within the ID. d) Background process where the muon emits bremsstrahlung, which leaves a proper cluster in the calorimeter that is matched to the muon track.

The majority of the electrons found in cosmic ray data are of very low energy; of the order of a few hundred MeV. The probability of a muon inducing an electron with sufficiently high momentum to produce a standard e/γ cluster ($E_T > 2.5$ GeV) in the electromagnetic calorimeter is thus small. A method of matching a track in the

Inner Detector to an EM topological cluster is instead used, allowing for the analysis to include electrons with momentum as low as 500 MeV.

4.4.2 Data samples considered in the analysis

Collected cosmic ray data

The cosmic ray data considered in this analysis includes the runs which have been flagged as good by the offline data quality and with both the solenoid and toroid magnet on. The data from the IDCosmic trigger stream is used, which consists of events where a track in the Inner Detector can be found by the Level 2 trigger adapted for cosmic data-taking [73]. The number of events recorded during the three extended cosmic ray data-taking periods was discussed in section 4.1 and summarized in Table 4.1.

- Runs during the fall of 2008 containing more than 30000 events are considered, adding up to 3.5 million events recorded with the IDCosmic stream.
- The cosmic runs from summer of 2009 are not included in this analysis. Due to the low acceptance of cosmic tracks leaving hits in the silicon detectors, the tracking mainly reconstructs Transition Radiation Tracker (TRT) stand-alone tracks in the barrel (for more details see section 4.4.4). During the summer of 2009 the TRT did not make use of the xenon chamber gas mixture, which is optimal for electron identification. These cosmic runs are therefore excluded.
- The suitable runs during the fall of 2009 recorded with the IDCosmic trigger stream add up to a total of 9.7 million events. During the cosmic data-taking period of fall 2009, the correct gas mixture was used in the TRT. However, the TRT Fast-OR trigger was on during certain runs, which requires lowering of the High Threshold (HT) settings. HT is normally used to detect Transition Radiation (TR) photons that are used for particle identification and only runs where the Fast-OR trigger was turned off or only used in the end-cap regions were thus considered. More detailed information concerning the TRT Fast-OR trigger can be found in [74].

Simulated cosmic ray data

The simulated sample, studied in this analysis in order to better understand the cosmic ray data, is achieved with PYTHIA event generator and the detector simulation is realized with GEANT4. The cosmic ray events arise by generating single muons originating uniformly from a large square area centered above the ATLAS cavern.

Events pointing towards the detector volume are then propagated through the shaft and rock.

Simulated cosmic ray data differs from simulated collision data at several levels. The cosmic ray simulation includes various modifications to correct for particles originating from above rather than from the primary vertex. One example, which has proven to be especially important for cosmic electron studies, is that the truth information concerning particles with production vertex in the calorimeter (above the Inner Detector) must be kept.

The cosmic Monte Carlo production includes various samples that differ depending on the detector volume filter for the muons. The sample used in this analysis has a filter on the Inner Detector volume, implying that every event has a track in either the barrel or end-cap region of the ID. The 10.6 million events in this sample contain 3.1 million tracks in the barrel region of the Inner Detector.

4.4.3 Reconstruction of electrons in cosmic ray data

The geometry of cosmic ray events has obvious differences compared with ordinary collision data due to the fact that particles originate from above the detector rather than from the primary vertex. The standard electron reconstruction algorithms (described in more detail in section 5.1.1) must therefore be adjusted accordingly. Another difference due to the geometry of the cosmic ray data is that only a few tracks leave hits in the silicon detectors (SCT and Pixel) and the η resolution is much reduced with TRT stand-alone tracks.

The generally low energy of the cosmic data electrons must be accounted for. Therefore, a specific method has been developed using TRT tracks and electromagnetic topological clusters rather than of the standard e/γ algorithms that are optimized for collision data with more energetic electrons originating from the interaction point. In this manner a larger sample of electrons can be obtained with a momentum threshold as low as 500 MeV.

4.4.4 Tracking with cosmic rays

There are two software packages for track reconstruction in cosmic ray data; CTB-Tracking and New Tracking. The track-finding algorithms in either package have been adapted to correct for the differences between cosmic ray tracks and collision events. The tracks are extended over the entire detector, containing hits from both the upper and lower half. The algorithms have also been modified to reconstruct tracks that are traversing the cylindrical detector volumes tangentially and longitudinally and the assumption of a common or limited interaction point has been removed [75].

An additional problem arises for the TRT tracks due to the random arrival time

of the cosmic rays. The reconstruction algorithms in the two tracking packages are therefore modified to make the TRT track search initially without using the drift time and then use the fitted track parameters of the best TRT track to estimate the phase between the cosmic ray and the read-out clock. The drift circle formation is then initialized using the computed phase. Specific settings are also applied to other standard tracking tools to cope with the full-length tracks.

One important tool for identifying electrons among the large background of muons is the fraction of high threshold TRT hits, also known as the TR ratio. Transition radiation (TR) is produced by a charged particle crossing the boundaries of two materials with different dielectric constants [76]. The probability of producing TR photons depends on the Lorentz gamma factor (E/m) of the particle. The effect commences at gamma factors above 1000, which applies predominantly to electrons and is therefore useful for electron identification. TR photons are detected by absorption in the chamber gas consisting of a xenon mixture characterized by a short absorption length for photons. The absorption leads to a larger electronic pulse, measured as a high threshold hit. Pulses from particles, which do not produce TR, usually only pass a much lower threshold and a distinction can therefore be made between the two particle types.

In Figure 4.18, the turn-on of the production of TR photons as a function of the gamma factor is shown, measured for tracks from the cosmic data-taking in October 2008. The probability per hit of producing high-threshold TR is given on the y-axis. An electron with an energy of the order of 1 GeV produces a gamma factor of approximately 2000, indicating a high-threshold probability of 0.1 per straw, while a muon must have an energy of the order of 200 GeV to yield the same gamma factor [77].

4.4.5 Electromagnetic topological clusters in the calorimeter

The ATLAS software includes two main calorimeter clustering algorithms; the “sliding window” algorithm and the “topological” algorithm. The electromagnetic sliding-window algorithm is the standard algorithm used for electron and photon (“egamma” object) reconstruction. However, the threshold for such a cluster to be seeded is 3 GeV and is thus not suitable for most cosmic electrons which are of lower energy.

The topological cluster algorithm groups adjacent cells with energies above the noise threshold into clusters, resulting in clusters composed of varying number of cells [78]. Topological clusters are seeded by cells with a signal-to-noise ratio above the threshold t_{seed} . The clusters then grow by iteratively adding neighboring cells with signal-to-noise ratio above $t_{neighbor}$ and finalize by including all direct neighbor cells on the outer perimeter with signal-to-noise ratio above t_{cell} . There are several types of topological clusters reconstructed in ATLAS. The algorithm chosen for this

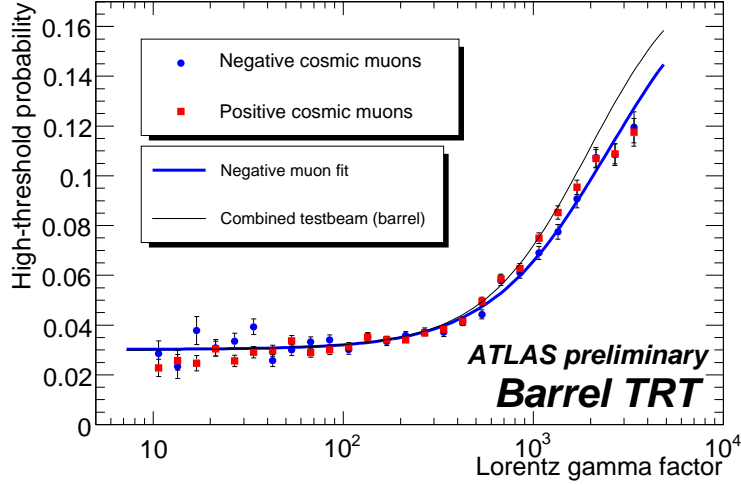


Figure 4.18: Distribution of the high-threshold prob per straw as a function of the Lorentz γ factor of the electrons from cosmic rays. The measurement is performed in the ATLAS TRT Barrel TRT in October 2008. A Lorentz gamma factor of approximately 2000, yielding a high-threshold probability of > 0.1 , is produced by a 1 GeV electron or a 200 GeV muon [76].

analysis is “EMTopoCluster430”, since it is optimized to efficiently find low energy clusters with a high suppression of noise. *EMTopoCluster430* reconstructs clusters in the electromagnetic calorimeter with the signal-to-noise ratio thresholds $t_{seed} = 4$, $t_{neighbor} = 3$ and $t_{cell} = 0$. With this method, an electron cluster can be reconstructed with a seed energy of a few hundred MeV.

In ATLAS, electrons in the forward region ($2.5 < |\eta| < 4.9$) are reconstructed with the topological clusters rather than with the sliding window algorithm. The variables used to distinguish between forward electron and hadrons are defined as the topological cluster moments or the combination of them. This method is also adopted in this analysis although the exact selection requirements imposed on the moments differ and have instead been optimized to fit the cosmic data scenario (see section 4.4.7).

The cluster moments are characteristic shower shape variables (see Figure 4.19 for an illustration). The moments used as distinguishing variables are the following [79]:

- $\langle r^2 \rangle$: The second moment in r , where r is the distance to the shower axis
- $\langle \lambda^2 \rangle$: The second moment in λ , where λ is the distance to the shower center along shower axis

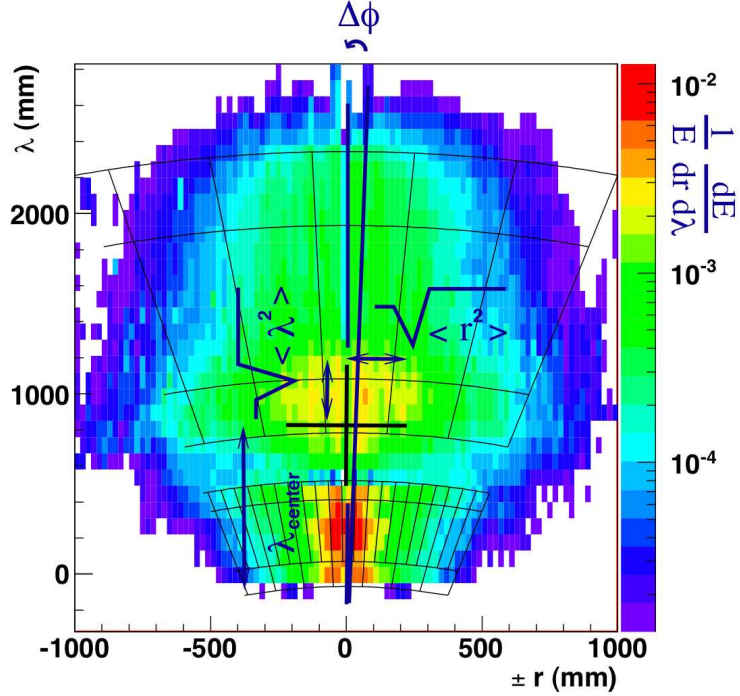


Figure 4.19: The energy density of a topological cluster per point in the λ - r space for single 25 GeV pion clusters in the barrel. λ is the distance to the shower center along the shower axis and r is the distance to the shower axis [79].

- *Lateral moment*: The normalized second lateral moment lat_2 , where $lat_2 = \langle r^2 \rangle$ with $r = 0$ for the two most energetic cells
- *Longitudinal moment*: The normalized second longitudinal moment $long_2$, where $long_2 = \langle \lambda^2 \rangle$ with $\lambda = 0$ for the two most energetic cells
- λ_{center} : the distance to the shower center from the calorimeter front face measured along the shower axis
- f_{max} : the energy fraction in the most energetic cell

4.4.6 Matching between track and cluster

Electrons are reconstructed by matching a track to an *EMTopoCluster*. Each track is extrapolated to the second sampling of the electromagnetic calorimeter and its impact point is determined by transforming its coordinates into those of the local frame of the electromagnetic calorimeter (η, ϕ) . The last measurement on the track

trajectory is taken as the starting point for the extrapolation, thus defining the initial track direction and momentum. Interactions with the material traversed during the extrapolation are treated appropriately. A detailed map of the solenoid magnetic field that the ATLAS tracker is placed in is used during the helix propagation. After determining the impact point, the collection of topological clusters is searched for and the distance of the cluster centroid from the track impact point $\Delta R = \sqrt{\Delta\phi^2 + \Delta\eta^2}$ is computed. The topological cluster with the smallest distance ΔR from the track impact point ($\Delta\phi$ in the case of tracks with only TRT hits) is selected as the one matching the track under consideration. The total energy of the cluster will then define the energy of the electron deposited in the electromagnetic calorimeter, whereas its momentum is estimated from the corresponding track parameters. No $\Delta\eta$ cut is used in this analysis due to the TRT stand-alone tracks lacking sufficient η resolution. To ensure a good match between track and cluster, a $\Delta\phi$ cut of 0.3 is applied.

An effective electron identification requirement is energy-to-momentum ratio, E/p , where E is the energy deposited in the topological cluster and p the momentum measured from the track (see section 4.4.7), which can be employed after a track-cluster match has been found.

The above method of matching a track to a topological cluster has also been applied for finding electrons from photon conversions in the minimum bias data delivered during first collisions.

4.4.7 Electron identification

With the method described in the previous section an event selection can be implemented to identify electrons. In this section, the Monte Carlo truth matching is discussed followed by the identification requirements, which have been optimized with the aid of the Monte Carlo. Note that the Monte Carlo cosmic ray sample has not been as carefully studied and optimized as for collision Monte Carlo and the shape therefore does not perfectly simulate the cosmic ray data. The agreement is however good considering the largely uncalibrated detector and limited accuracy in modeling the muon propagation through the ATLAS cavern and shaft.

4.4.8 Truth matching with the Monte Carlo sample

To estimate the number of background events within the signal region in the cosmic ray data analysis, a comparison with simulated cosmic data is conducted. The matching between the reconstructed electron candidates and the generator level truth is performed by a hit-by-hit basis for the electron track. The matching uses a map that links the reconstructed track to the associated true object. If a link is found from the track to the truth track and the truth information is properly stored, the

track can be matched to a true electron or muon.

4.4.9 Track selection

As a first selection, the events are divided into a signal and a background sample. The signal sample consists of all events containing more than one track, assuming that a muon track must exist apart from the electron candidate. The events containing only one track are thus used as a background control sample.

Another initial requirement for the electron track candidate is that it must traverse the Inner Detector barrel region, since the small incident angle between the cosmic rays and the end-cap disks imposes severe reconstruction problems. One major issue is the reconstruction of the charge of the track, which often fails when the track is located in the end-caps. The charge mismatch has been evaluated in the Monte Carlo sample by comparing the reconstructed charge to the charge of the true particle in the simulated sample. Only considering tracks located in the barrel region significantly improves the charge mismatch rate but does not completely eliminate it. This issue is especially prominent for tracks matched to true muons.

The selections applied on the track quality are based on TRT properties, since the majority of cosmic ray tracks are TRT tracks with few or no silicon hits. To be able to perform the analysis on TRT stand-alone tracks a minimum of 25 TRT hits is required. As discussed in section 4.4.4, an effective way of distinguishing between electron and muon TRT tracks is the probability of producing transition radiation reaching a high threshold. A selection requirement of a TR ratio above 0.10 for the track is thus applied (see Figure 4.20).

To summarize:

- Events with > 1 track are considered (events with only one track are used as background sample)
- The track is required to be in the barrel region of the TRT
- Number of TRT hits ≥ 25
- TR ratio > 0.10

4.4.10 Cluster requirements

Tracks passing the TRT requirements are matched to an *EMTopoCluster* employing the matching method described in section 4.4.6. A track is considered to be matched to a cluster if a match is found with $|\Delta\phi| < 0.3$. If a proper match is attained, selections can be made on the cluster moments in order to further separate the electrons

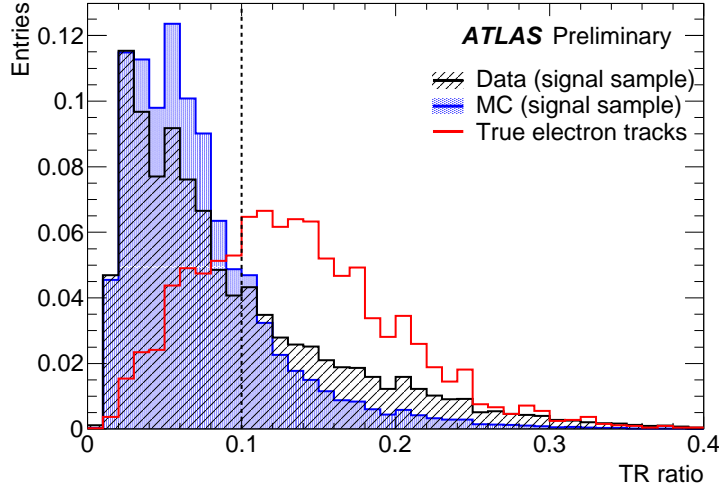


Figure 4.20: The fraction of high threshold TRT hits for tracks with ≥ 25 TRT hits for the data and MC signal samples. The tracks matching true electrons in the MC sample are overlaid. The areas of the histograms are normalized to unity due to the much less statistics for the true electron candidates. The dotted line illustrates where the selection cut is applied.

from the background muons, as was discussed in section 4.4.5. The cluster moments and the cuts applied are illustrated in Figure 4.21, 4.22, 4.23 and 4.24 for the MC and data signal samples after tracking cuts as well as a track-cluster match has been applied. The selection requirements applied on the cluster moments are summarized below:

- Second moment in λ (Fig. 4.21): $\langle \lambda^2 \rangle < 21000 \text{ mm}^2$
- Second lateral moment (Fig. 4.22): $lat_2 > 0.6$
- The distance to the shower center along the shower axis (Fig. 4.23): $\lambda_{center} < 220 \text{ mm}$
- The energy fraction in the most energetic cell (Fig. 4.24): $f_{max} < 0.36$

4.4.11 Final requirements after track-cluster matching

A variable effective in distinguishing the electron signal from background is E/p , where E is the energy reconstructed from the topological cluster and p the momentum

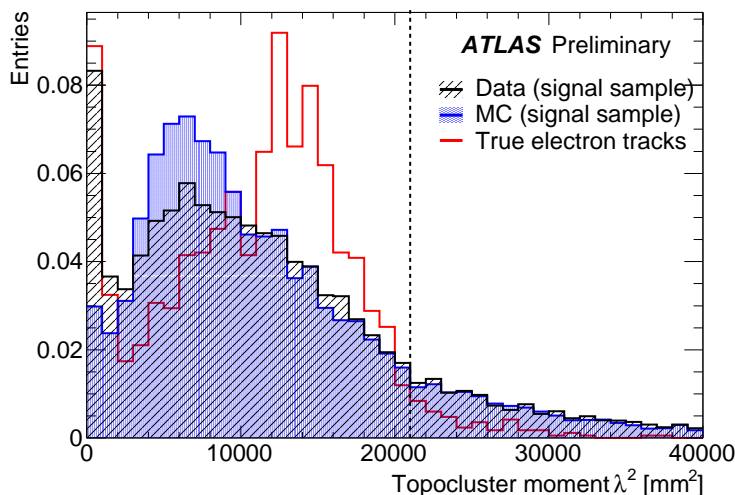


Figure 4.21: The second moment in λ of the EMTopocluster after TRT cuts and track-cluster matching have been applied for the data and MC signal samples. $\langle \lambda^2 \rangle$ for tracks matching true electrons in the MC sample are included. The areas of the histograms are normalized to unity due to the considerably smaller sample of true electron candidates. The dotted line illustrates where the selection cut is applied.

measured in the track. The background muons typically only deposit a small fraction of their energy in the calorimeter giving rise to a small E/p value. Electrons, on the other hand, deposit all their energy in the cluster resulting in an E/p distribution with a peak at around 1. In Figure 4.25 the E/p distribution after all other selection requirements applied is shown as well as an illustration of the final selection cut on $E/p > 0.5$.

Table 4.3 lists the number of electron candidates remaining after applying the different identification cuts consecutively on the signal and background sample for both data and MC. The number of candidates matched to true electrons in the Monte Carlo sample is shown within brackets. For the resulting MC sample, only 3% of the 1091 electron candidates are not matched to true electrons.

Note that also a considerable fraction of the MC background events, despite only incorporating one reconstructed track, consists of a track matched to a true electron after all selection requirements have been applied. One explanation is that there is a small probability of the muon entering the TRT end-cap with such a small incident angle that the muon track fails to be reconstructed. Another justification is that the muon and electron tracks occasionally are reconstructed as one single track. However, the fraction of true electrons in the background sample is considerably smaller than in the signal sample, especially before any identification requirements have been applied,

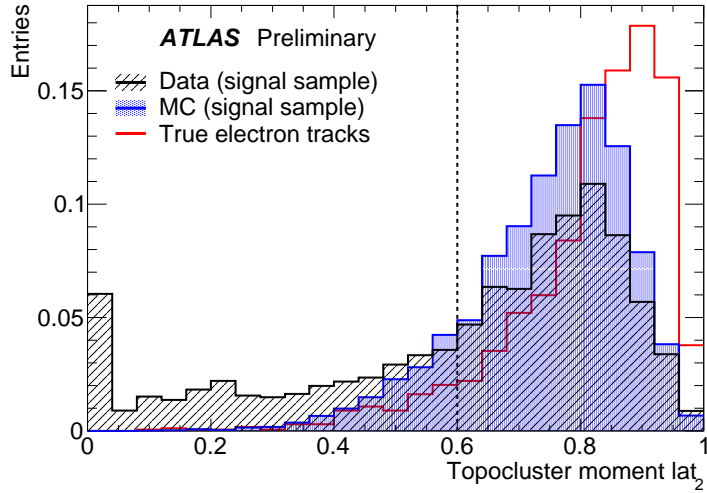


Figure 4.22: The lateral moment of the EMTopocluster after TRT cuts and track-cluster matching have been applied (the histograms are normalized). Tracks matching true electrons in the MC sample are included. The dotted line illustrates where the selection cut is applied.

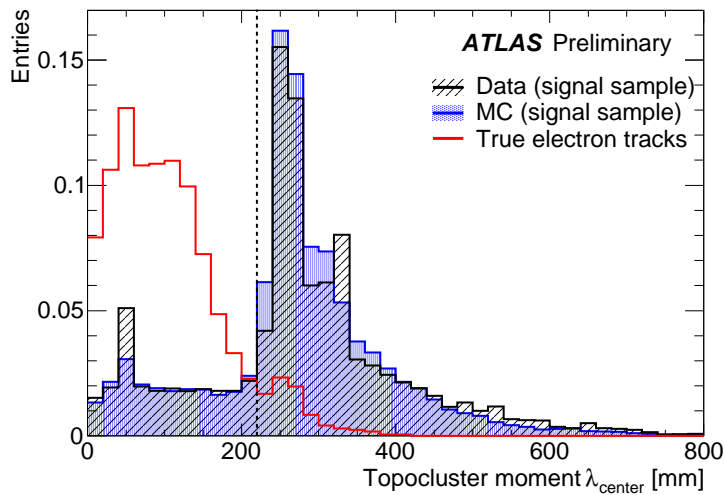


Figure 4.23: The distance to the shower center along the shower axis of the EM-Topocluster after TRT cuts and track-cluster matching have been applied (the histograms are normalized). Tracks matching true electrons in the MC sample are included. The dotted line illustrates where the selection cut is applied.

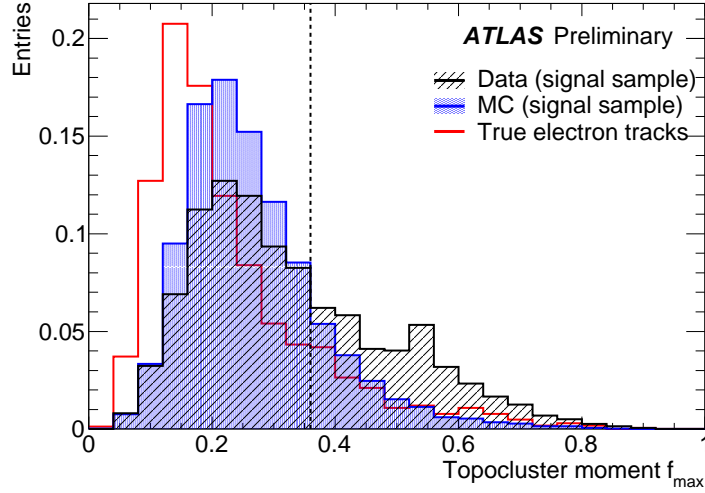


Figure 4.24: The energy fraction in the most energetic cell of the EMTopocluster after TRT cuts and track-cluster matching have been applied (the histograms are normalized). Tracks matching true electrons in the MC sample are included. The dotted line illustrates where the selection cut is applied.

Selection cuts ($p > 500$ MeV)	Signal sample		Background sample	
	Data 08/09	Monte Carlo	Data 08/09	Monte Carlo
Tracks in ID barrel	385222	358192 (6619)	4749835	2724748 (685)
TRT hits > 25	293016	297957 (4383)	4516429	2660092 (449)
TR ratio > 0.10	88915	53035 (2940)	808889	238688 (262)
Tracks-cluster match	15260	15796 (1667)	115080	87633 (151)
Cluster moment cuts	1930	2466 (1242)	6461	11276 (104)
$E/p > 0.5$	882	1091 (1058)	195	170 (84)
Electrons candidates	882	1091 (1058)		

Table 4.3: Number of tracks with $p_T > 500$ MeV after separating signal (> 1 track per event) and background events (one track per event) for data and MC. The different electron identification cuts are applied consecutively. The number of electron candidates matched to an electron in truth is listed in brackets for the simulated data. The MC is normalized to data.

justifying the signal-background sample separation. Also, the fact that the initially negligible fraction (0.03%) of true electrons in the background sample becomes 50% after all cuts are applied, is very promising in terms of the electron identification

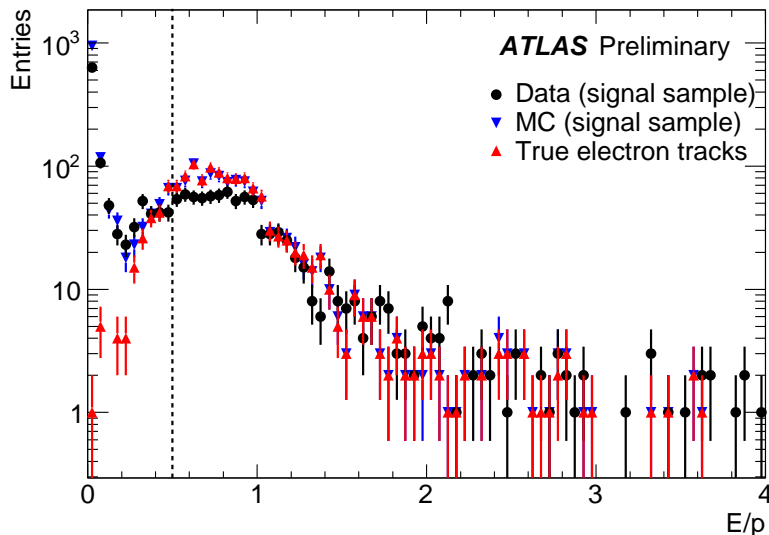


Figure 4.25: Energy over momentum for electron candidates in data and MC, with a comparison with the true electron tracks in the MC. The plot is in logarithmic scale and the dotted line illustrates where the final selection cut is applied.

capability of the ATLAS detector.

4.4.12 Background estimation

As indicated in the resulting numbers in Table 4.3, 1058 out of 1091 electrons candidates in the MC signal sample are matched to electrons in truth. The remaining 33 tracks (3.0%) are matched to true muons. Despite the low fraction of muon contamination in the signal region, it is desirable to find an accurate background estimation method that can be employed on the cosmic data where no truth information is available.

Several attempts have been made with different background estimation methods, but the low statistics induces difficulties. The best method compares a certain shape for the signal and background events by using the truth events from Monte Carlo together with the background sample in data in order to extract the fraction of signal and background in the electron candidate distribution. The fit is a standard likelihood fit using Poisson statistics, where every bin for each template is a fit parameter (see [80] for more details).

It is preferable to find a background sample, which contains as little signal as possible in order to optimize the method. The background sample with only one

track per event is thus utilized. After all other selection requirements are applied, the TR ratio vs. E/p space is divided into signal and background regions for both MC and data samples, as illustrated in Figure 4.26. The signal region within the signal sample is defined by using the same identification cuts that were applied before ($E/p > 0.5$ and TR ratio > 0.10). The true electron candidates in this region in the MC signal sample are used as truth template for the fit. As background template, the background region of the background sample is used. The background region consists of events with either $E/p < 0.25$ or TR ratio < 0.05 , excluding a buffer area towards the signal in order to minimize the number of electrons in the region. Due to the abundance of muons, the statistics in this small region is not an issue. Studying the MC background sample confirms that there is little signal contamination in the background region; only 8 true electrons out of 131k events.

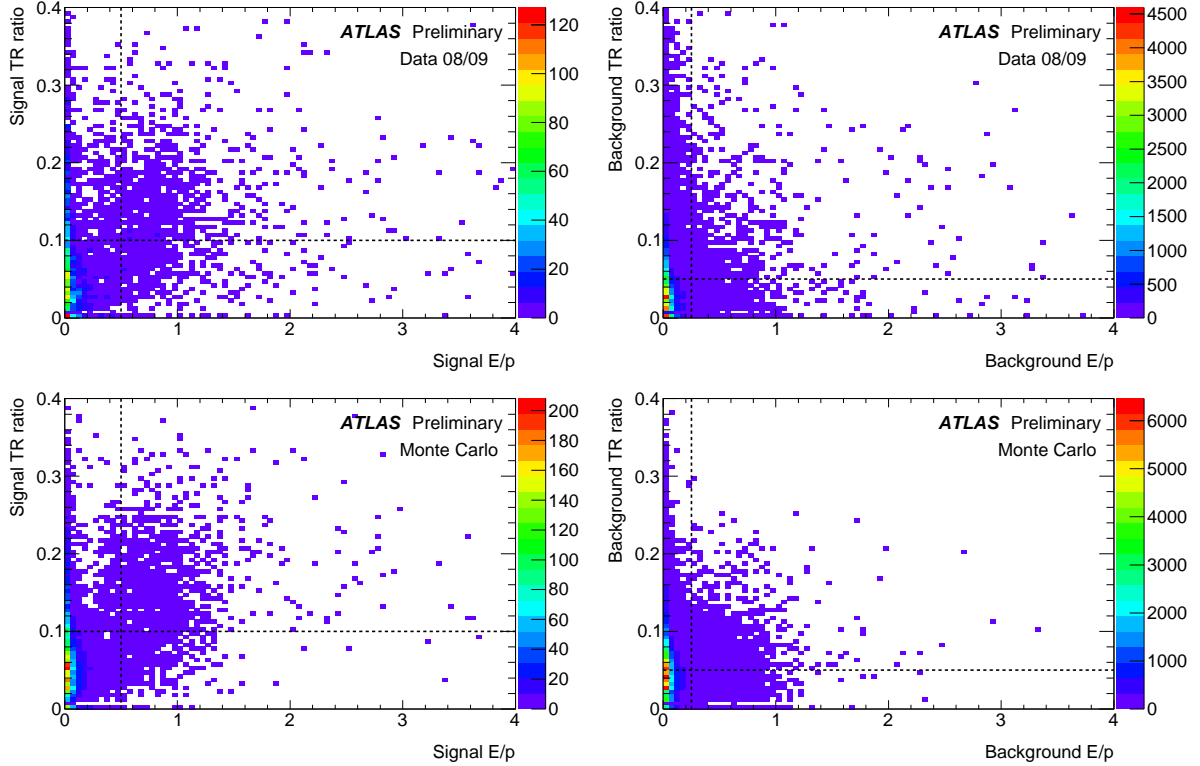


Figure 4.26: TR ratio vs. E/p for data and MC signal and background samples. The dotted lines isolate the signal region in the signal samples and the background region in the background samples in order to find suitable truth and background templates for the background estimation fit. The fit is applied to all electron candidates in the signal region for both data and MC.

As the discriminating variable, the topological cluster moment λ_{center} has been

chosen, since it differs considerably between signal and background and is therefore optimal for the background estimation (see Figure 4.23). The method also relies on the variables being independent, which makes TR ratio, E/p and λ_{center} suitable candidates. To conclude, the template method is performed the following way:

- The λ_{center} shape of the tracks in the background region, defined by $E/p < 0.25$ or TR ratio < 0.05 , in the data background sample (one track per event) is used as background template.
- The λ_{center} shape of the true electron tracks in the signal region, defined by $E/p > 0.5$ and TR ratio > 0.10 , in the MC signal sample ($>$ one track per event) is used as the truth template.
- The shape of the background and truth templates are fitted to the λ_{center} distribution of all electron candidates in the signal region within the signal sample for both the MC and data separately in order to acquire two separate background estimates.

Figure 4.27 shows λ_{center} for the templates and the electron candidates fitted in MC and data. The result of the fit on the MC sample yields a background estimate of $1.0 \pm 1.6\%$. Comparing the 3.0% estimate made on the basis of the MC truth, this method somewhat underestimates the amount of background. This is due to the low statistics in the signal region and the very few background events within. Applying the template method on data results in a background estimate of $5.5 \pm 1.9\%$, which is higher than that found for MC. It is also visible in Fig. 4.27 that the signal shape in data differs more than the MC from the true electron shape. Note, however, that the true electron shape in both cases is the simulated electron shape and that the MC does not describe the cosmic data perfectly. For the MC fit, the signal sample and the true electron template consist of the same 1058 events except for the addition of the 33 background events, which is not the case for data. Performing the fit using the MC as background template instead of data yields a compatible result.

4.4.13 Positrons among the electron signal

Studying the charge of the resulting electron candidates in the simulated sample concludes that 99 of the 1091 electrons have a positive reconstructed charge (9.1%). An investigation of the MC truth results in 84 positrons among the 1058 true electrons (8.0%). This is a clear indication of events where the electron is produced by a photon conversion, which is also to be expected from the conversion origin of 22% of all true electron tracks (as mentioned in section 4.4.1). However, the probability of two tracks passing the electron identification requirements in one event is low and there are only

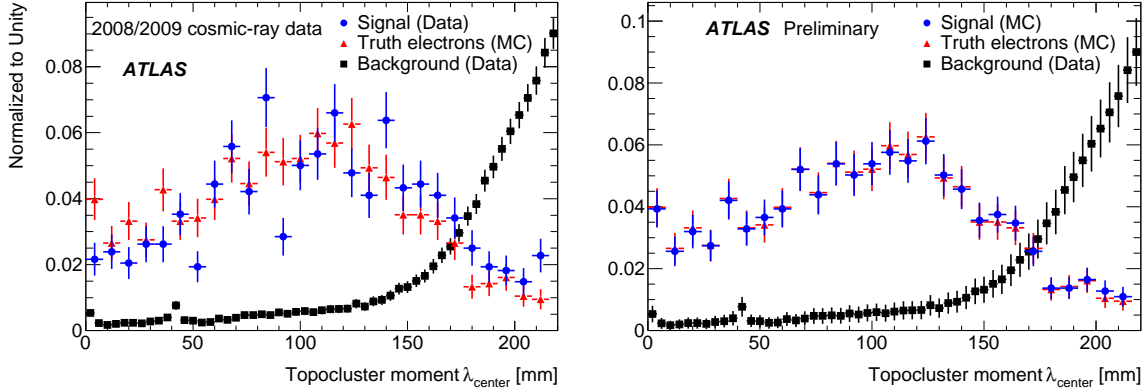


Figure 4.27: λ_{center} for the background template (data) and truth template (MC) as well as the electron candidates that are fitted for both data (left) and MC (right). The histograms are normalized to unity.

10 such events in the resulting electron sample. The selection cuts would therefore have to be loosened in order to find a convincing conversion signal. The ratio of positive electron candidates in data is slightly higher; 126 positrons out of the 882 electron candidates (14.3%), which might be an indication of a larger amount of background. The significant fraction of positrons in the signal makes it difficult to use the charge ratio as a background estimation method. The fact that numerous muon tracks have incorrect reconstructed charge, due to the majority of the tracks not leaving any silicon hits, adds a further complication to estimating the correct muon charge ratio.

4.4.14 Results

As stated in the sections above, the signal samples of electron candidates, after all identification requirements have been imposed, consist of 882 electrons in the 2008/2009 cosmic ray data and 1091 electrons in the simulated cosmic ray MC. For the latter, 97.0% are matched to electrons in the MC truth and the remaining 3.0% to background muons. Employing the template method with TFractionFitter in ROOT, a background estimation of $1.0 \pm 1.6\%$ in the simulated data and $5.5 \pm 1.9\%$ in data is found. The resulting numbers, including background estimates, are summarized in Table 4.4.

In Figure 4.28 the energy over momentum is shown for data and Monte Carlo separately after all other selection cuts have been applied. The resulting electron events in the signal and background samples are overlaid and the true electrons are included for the simulated data. A clear peak is visible at $E/p \approx 0.8$ in the signal

	2008/2009 cosmic data		Simulated cosmic data	
Total nbr of events	13.2 million		10.6 million	
Electron candidates	882		1091 (true: 1058)	
Background	[%]	muons	[%]	muons
MC truth	-	-	3.0%	33
Template method	$5.5 \pm 1.9\%$	48 ± 17	$1.0 \pm 1.6\%$	11 ± 17

Table 4.4: Resulting number of electron candidates and background estimates in data and MC.

sample indicating an electron signal. The reason for the peak being located at a lower value than 1 is that the topological cluster method does not include corrections for bremsstrahlung losses. Since the electrons have such low momentum, they bend more in the magnetic field, making it difficult for the cluster to incorporate all the bremsstrahlung. Studying the MC plot indeed shows an overlap between signal sample and true electrons except for low E/p values, below 0.3, which is still dominated by muons. The background sample on the other hand does not display a peak making it suitable as a background control sample. Note that also the background sample contains true electrons towards higher E/p .

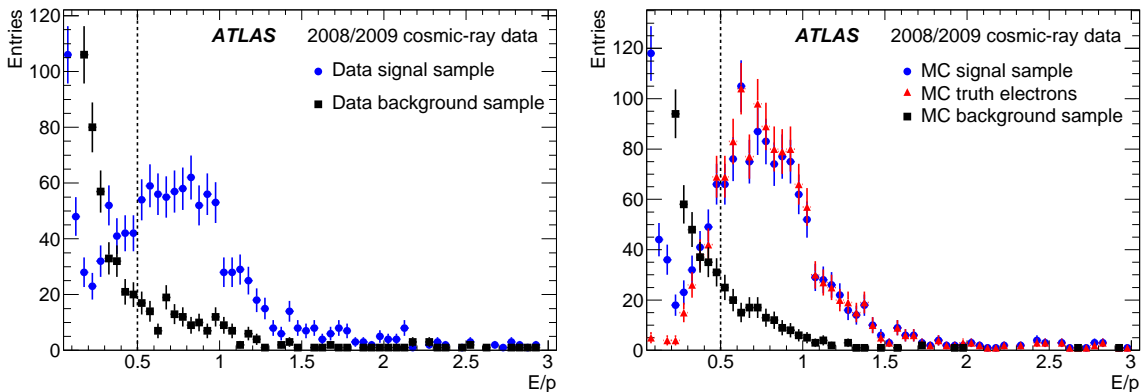


Figure 4.28: E/p of resulting electron candidates in the signal and background samples after all other selection cuts have been applied for data (left) and simulated data (right). The E/p of the electron candidates matched to true electrons in the MC signal sample is also included in the right plot. The dotted lines indicate the final cut at $E/p > 0.5$. The zero-bin, containing a large number of muon entries, is not included in order to be able to keep the plot in linear scale.

Similar histograms of the final TR ratio distribution are shown in Figure 4.29

after applying all other cuts. The highly efficient cut on E/p reduces the remaining background to a large extent. A comparison between the MC signal sample and the tracks matched to true electrons shows only a slight increase towards TR ratio values below the cut at 0.10, but otherwise shows complete agreement. The TR ratio of the data signal sample does contain more events at low values again indicating somewhat more background contamination than in MC. The TR ratio of the data background sample is nevertheless also shifted towards lower values compared to MC. This can be due to the imperfect Monte Carlo description or that the TRT response itself is not calibrated for data.

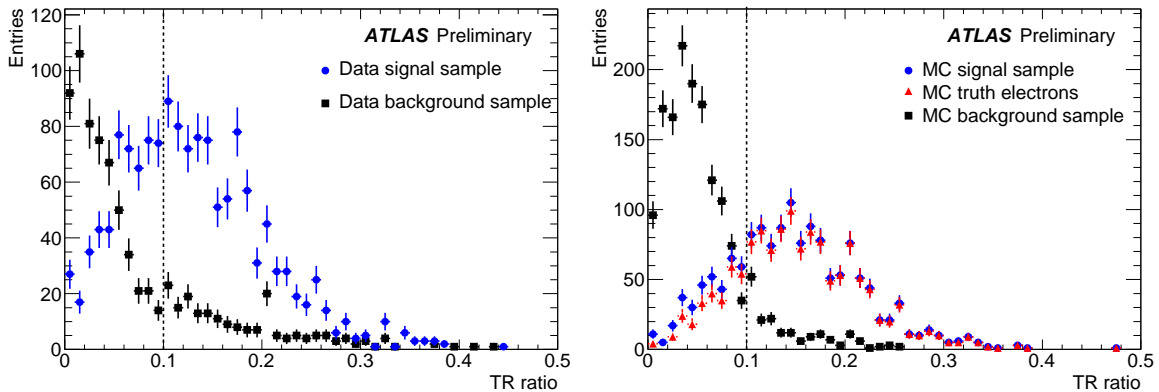


Figure 4.29: TR ratio of resulting electron candidates in the signal and background samples after all other selection cuts have been applied for data (left) and MC (right). The TR ratio of the electron candidates matched to true electrons in the MC signal sample is also included in the right plot. The dotted lines indicate the final cut at TR ratio > 0.10 .

After the selection requirements on E/p and TR ratio are applied, the final sample of electron candidates is isolated. Figure 4.30 displays the resulting momentum distribution of the electron candidates comparing the signal and background shapes. The momentum distribution of the electrons peak at low values; at around 1 GeV followed by a tail, while the background sample is flat since the incoming muons are generally more energetic.

In Figure 4.31 a typical event display of one of the low energy electrons passing all requirements is shown. The muon and electron tracks can be clearly distinguished by the TRT hits.

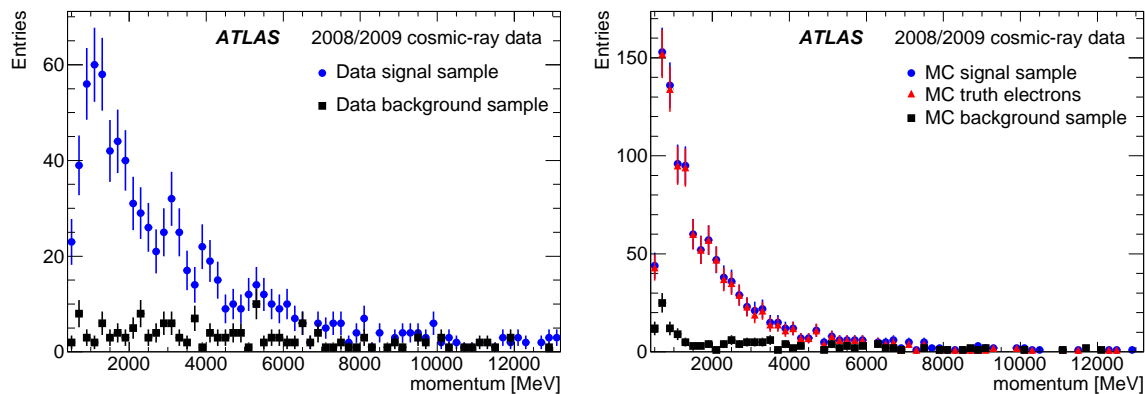


Figure 4.30: Momentum distribution of the final electron candidates separated into signal and background sample for the cosmic data (left) as well as MC (right), where the true electron candidates are also included.

4.5 Conclusion

This chapter summarizes the performance work and analyses completed during the commissioning phase of ATLAS using the 2008 and 2009 cosmic ray data. The Semiconductor Tracker was successfully integrated into ATLAS in the beginning of 2008, followed by a longer period of cosmic ray data-taking, allowing for the first performance studies to be carried out. The online data quality monitoring was developed as part of the SCT commissioning. The Athena DQM runs in real time producing multiple histograms describing the status of the SCT sub-detector as well as the data it is collecting. The histograms are used as input for the OHP and the DQMD displays, which perform automatic checks on the data quality and present the histograms in a user-friendly manner. The SCT is currently fully operational and smoothly collecting collision data.

In addition, the cosmic ray data were used for detection and identification of the first electrons in ATLAS through applying a customized method of matching tracks to electromagnetic topological clusters. A pure sample of 882 electrons was extracted from the extensive muon background after having passed several constraints applied on the track matched to an *EMTopoCluster*. The method of using tracks in conjunction with topological clusters was adopted for identifying electrons in first collision minimum bias data in ATLAS.

Performing the same analysis on simulated cosmic ray data a similar sample of 1091 electron candidates was obtained, whereas 1058 are matched to electrons in truth. This suggests a background of merely 3.0%. A background estimation method using the template method attains a background of $1.0 \pm 1.6\%$ in the simulated sample, where the upper limit is compatible with what the truth information implies.

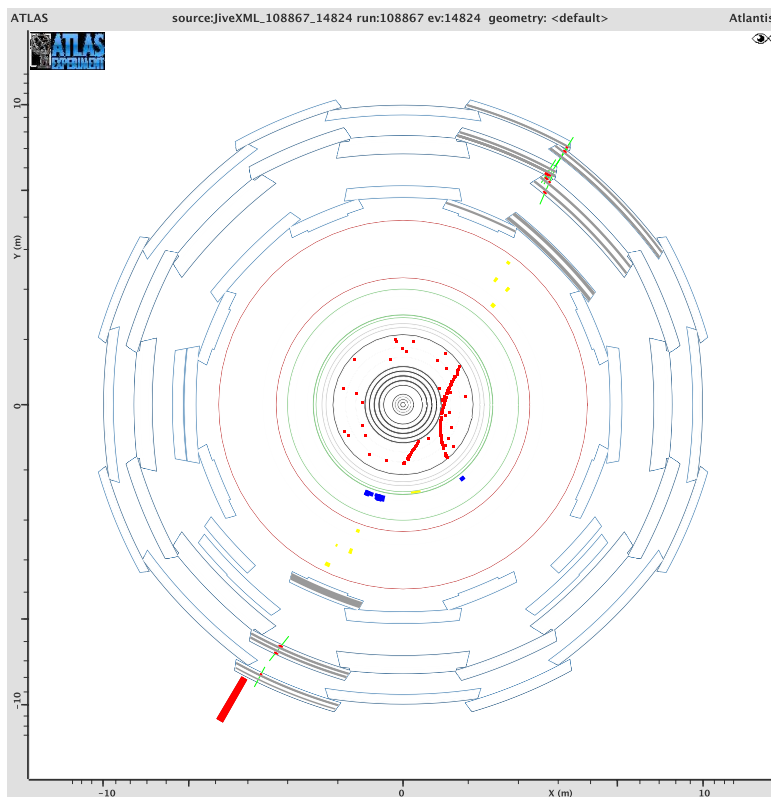


Figure 4.31: An Atlantis event display of an electron produced by muon ionization in the Inner Detector material. The TRT hits, visible in red, produced by the muon track (left) and the electron track (right) can clearly be distinguished from the noise. The blue dots are the topological clusters in the EM calorimeter. The electron in this particular event has a momentum of 650 MeV, 68 TRT hits and no hits in the silicon detectors. The muon has a momentum of 185 GeV.

Employing the background estimation fit on the cosmic data results in $5.5 \pm 1.9\%$ background contamination, which is considered to be an accurate estimate. Subtracting the estimated background of 48 ± 17 provides with an observation of 834 signal electrons, successfully isolated from several million of cosmic muon events. This analysis has led to the first observation of electrons in the installed ATLAS detector.

Chapter 5

Electron Efficiency Measurement Using the $Z \rightarrow ee$ Tag-and-Probe Method

In physics analyses with an electron as the final state particle, a set of identification requirements need to be applied to remove the large amount of QCD background that fakes electrons. These identification cuts are optimized by comparing the gain in background rejection and the loss in signal efficiency.

In a cross section analysis the observed events remaining after all cuts have been applied must be corrected for the reconstruction, identification and trigger efficiency of the electron. The standard e/γ reconstruction and identification algorithms and selections in ATLAS are briefly discussed in section 5.1.

The electron efficiencies can be estimated with data-driven methods and this chapter focuses on the studies completed with the tag-and-probe method on $Z \rightarrow ee$ events. The analysis has been performed using the full 2010 7 TeV data, reprocessed with Athena release 16, and has been published as part of [57], with a supporting note [81]. The electron efficiencies, derived from tag-and-probe studies, have also been evaluated with Athena release 15. This is however not discussed in this chapter (for release 15 results consult [82]).

Electron reconstruction and identification efficiencies extracted from Z events in the data are compared to efficiencies obtained from simulated data in order to produce data/MC scale factors (SFs). These SFs are then used by for example the W/Z cross section analyses presented in the following chapters of this thesis. The methodology of how to extract efficiencies and SFs with Z tag-and-probe is discussed in section 5.2. The emphasis of the work presented here lies with the electron identification efficiency rather than the reconstruction efficiency. Since the electron identification efficiency is highly dependent on the kinematics of the electron, the efficiencies and SFs are

measured as a function of η^e (described in section 5.3) and E_T^e (described in section 5.4). The efficiency binning benefits the differential measurements and also allows for the scale factors to be transferred to other analyses. It is, however, important to verify the efficiency independence of other variables, such as jet kinematics for W/Z + jet analyses. (The electron efficiency measured as a function of jet kinematics is addressed in chapter 7.) The efficiency of the electron trigger is also measured with Z tag-and-probe, which is discussed in section 5.5.

The studies presented in this chapter has been completed by the author. However, sections 5.3.4 and 5.4.3 shows the final official η and E_T dependent efficiency scale factors provided by the e/γ group, where the work of the author is one contribution out of several.

5.1 Electron reconstruction and identification in ATLAS

5.1.1 Reconstruction algorithms

There are two main electron-finding algorithms in the ATLAS reconstruction software. The standard “egamma” electron reconstruction, which is used in this analysis, ranges over the full acceptance of the Inner Detector system ($|\eta| < 2.5$) [83, 84]. This algorithm is more widely used throughout the physics analyses due to its wide range in η and E_T in comparison with the second track-seeded reconstruction algorithm (“softe”), which is more suitable for lower energy electrons.

The reconstruction of an *egamma* electron begins with the creation of a preliminary set of seed clusters in the EM calorimeter with an energy threshold of 2.5 GeV. The clusters are formed with a sliding window algorithm, where the seed clusters are of the size 3×5 in middle layer cell units of the calorimeter (0.025×0.025 in η/ϕ). After an energy comparison has been carried out, duplicate clusters are removed from nearby seed clusters.

The middle layer of the cluster is then matched to a track in the Inner Detector within a window of $\Delta\eta \times \Delta\phi = 0.05 \times 0.1$. The track is required to have a transverse momentum of at least 0.5 GeV. The extrapolation uses the η and ϕ coordinates from the last measurement on the track. If there are multiple tracks matched to the cluster, the closest match is kept as the electron track, with priority given to tracks with at least 4 silicon hits over TRT-only tracks. For the latter case, only track-cluster matching within $\Delta\phi = 0.1$ is applied since the TRT lacks resolution in η .

The final electron cluster has a size of $\Delta\eta \times \Delta\phi = 0.075 \times 0.175$ in the calorimeter barrel and 0.125×0.125 in the end-caps. The energy measured from the cells belonging to the electron cluster defines the electron energy in this analysis. The transition

(“crack”) regions between the barrel and end-caps of the EM calorimeter, $1.37 < |\eta| < 1.52$, are expected to have poorer performance due to the large amounts of material in front of the first active calorimeter layer.

5.1.2 Electron identification

The electron reconstruction provides a very loose definition of an electron in order to keep the reconstruction efficiency as high as possible. This indicates that further identification cuts are necessary to remove the majority of the large hadronic background. A sequence of calorimeter and track variable cuts have been optimized in order to provide efficient electron identification together with sufficient background rejection. The selection cuts depend on the kinematics of the electron and are therefore binned in $|\eta^e|$ and E_T^e . The optimization has been performed in 10 bins in cluster η within $|\eta| < 2.47$ (computed from the middle layer of the calorimeter), which have been defined by detector properties, and 11 bins in cluster E_T , starting from 5 GeV. There also exists pre-defined sets of identification cuts for the forward region ($2.5 < |\eta| < 4.9$), optimized purely on calorimeter variables such as topocluster moments (described in section 4.4.5).

Three sets of requirements have been defined for central electrons ($|\eta| < 2.47$) with increasing background rejection capacity: “loose”, “medium” and “tight”¹. Each selection set includes the requirements of the previous selection. The loose, medium and tight identification cuts are briefly described below and are outlined in more detail in Table 5.1. For more explicit details on electron identification, consult [83].

- **Loose ID** - This selection uses shower variables from the second layer in the EM calorimeter such as lateral shower containment and shower width. It also includes energy leakage in the hadronic calorimeter. The jet rejection obtained from the loose requirements for electron candidates with $E_T > 17$ GeV has been estimated on Monte Carlo to be of the order of $6 \cdot 10^2$ [23].
- **Medium ID** - The medium identification cuts include the loose electron requirements with the addition of applying requirements on the energy deposit variables in the first layer of the EM calorimeter cluster (the shower width and the ratio of the energy difference between the most energetic and second most energetic cell and the total sum of these energies). Furthermore, the set includes requirements on track quality variables, such as number of hits in the Pixel and the SCT as well as on the transverse impact parameter. Finally a cut is applied on the $\Delta\eta$ between the track and the first layer of the cluster. The jet rejection obtained by applying medium requirements is of the order of $2 \cdot 10^3$ [23].

¹Medium_WithTrackMatch and Tight_WithTrackMatch are applied as the standard medium and tight identification in release 16.

- **Tight ID** - This set of requirements provides additional hadronic background rejection using cuts on the ratio of the energy from the cluster and the momentum from the track, number of TRT hits and the ratio of high threshold TRT hits (as discussed in section 4.4.4). Secondary electrons from conversions are rejected by requiring at least one hit in the innermost layer of the Pixel detector (the b-layer) as well as removing electrons matching reconstructed conversion photons. The impact parameter cut from the medium level is further tightened as well as the track cluster matching through adding a cut on $\Delta\phi$. Jet rejection at tight level has been estimated to be of the order of $9 \cdot 10^4$ [23].

5.1.3 Reconstruction and identification efficiency

The efficiency of the electron reconstruction and identification algorithms and selections must be accurately estimated from the data to correctly measure the cross section times branching ratio of for instance $W \rightarrow e\nu$ and $Z \rightarrow ee$ decays. Two data-driven methods have been used for this purpose; Z and W tag-and-probe [57, 81]. Since the electron efficiency is intrinsically slightly different if it originates from a W or a Z (largely due to the differences of the η and E_T distributions of the electrons), it is important to compare the data/MC efficiency ratio (scale factor) for the two methods. In addition, the scale factors have the advantage of being easily incorporated in any physics analysis to correct the simulated data. The scale factors from W and Z tag-and-probe are thus combined to obtain smaller statistical uncertainties and hence more robust results.

While the methodology of Z tag-and-probe is discussed in great detail in the following sections, the W tag-and-probe is only briefly summarized here (for further details consult [57, 81]). The W tag-and-probe method consists of selecting events with a large value of E_T^{miss} and probing for an electron to perform the efficiency calculation on. To keep the electron from the W unbiased an E_T^{miss} trigger is used, instead of an electron trigger, for the event selection. To perform the necessary background subtraction at each level of the efficiency calculation, distributions from different calorimeter isolation variables are fitted.

5.2 $Z \rightarrow ee$ tag-and-probe methodology

One of the principal methods of assessing the electron efficiency with a data-driven technique is by applying “tag-and-probe” on $Z \rightarrow ee$ events. The Z tag-and-probe method consists of tagging a relatively clean sample of $Z \rightarrow ee$ events in data by applying strict electron requirements to one of the electrons, leaving the second electron unbiased to be used for the efficiency calculation.

Type	Description	Symbol
Loose cuts		
Hadronic leakage	<ul style="list-style-type: none"> • E_T ratio between the first layer of the hadronic calorimeter and the EM cluster (used over the range $\eta < 0.8$ and $\eta > 1.37$) 	R_{had1}
	<ul style="list-style-type: none"> • E_T ratio of the hadronic calorimeter and the EM cluster (used over the range $\eta > 0.8$ and $\eta < 1.37$) 	R_{had}
Second layer of the EM calorimeter	<ul style="list-style-type: none"> • Energy ratio in η of 3×7 versus 7×7 cells. 	R_η
	<ul style="list-style-type: none"> • Lateral width of the shower 	$w_{\eta2}$
Medium cuts (including Loose)		
First layer of the EM calorimeter.	<ul style="list-style-type: none"> • Total shower width 	w_{stot}
	<ul style="list-style-type: none"> • Ratio between the energy difference associated with the largest and second largest energy deposit and their total energy 	E_{ratio}
Track quality	<ul style="list-style-type: none"> • Number of hits in the pixel detector (≥ 1). 	nPix
	<ul style="list-style-type: none"> • Number of hits in the pixels and SCT (≥ 7). 	nSi
	<ul style="list-style-type: none"> • Transverse impact parameter (< 5 mm). 	d_0
Track matching	<ul style="list-style-type: none"> • $\Delta\eta$ between the cluster and the track (< 0.01). 	$\Delta\eta_1$
Tight cuts (including Medium)		
b-layer	<ul style="list-style-type: none"> • Number of hits in the b-layer (≥ 1) 	b-layer
Track matching	<ul style="list-style-type: none"> • $\Delta\phi$ between the cluster and the track (< 0.02) 	$\Delta\phi_2$
	<ul style="list-style-type: none"> • Ratio of the cluster energy and the track momentum 	E/p
	<ul style="list-style-type: none"> • Tight $\Delta\eta$ cut (< 0.005) 	$\Delta\eta_1$
Track quality	<ul style="list-style-type: none"> • Tight transverse impact parameter cut (< 1 mm) 	d_0
TRT	<ul style="list-style-type: none"> • Total number of hits in the TRT 	nTRT
	<ul style="list-style-type: none"> • Ratio of the number of high-threshold hits and the total number of hits in the TRT 	TRratio
Conversions	<ul style="list-style-type: none"> • Electron candidates matching to reconstructed photon conversions are rejected 	conversion

Table 5.1: Definition of variables used for loose, medium and tight electron identification requirements for the central region of the detector ($|\eta| < 2.47$)

Figure 5.1 shows an Atlantis event display of the first $Z \rightarrow ee$ candidate observed in ATLAS, in May 2010. The two electrons originating from the Z boson can clearly be distinguished in the event. The tag-and-probe method implies first tagging one of the electrons (tag electron) through applying tight identification. The tag is also matched to the equivalent trigger that the event is required to pass by searching within a cone of $\Delta R < 0.15$ between the trigger object and the offline electron reconstruction. Cluster variables are used for the L1 trigger matching, while track variables are used for the EF. In this manner, the probe is left unbiased from the trigger selection of the event. The probe electron is then asked to pass different sets of identification criteria and the efficiencies can be estimated. The event can be used more than once if both electrons pass the requirement of the tag, which thus increases the statistics of the probe sample. The method hence selects one of the electrons passing the tag requirements and probes for the other electron in the event. Subsequently the method investigates if there is another electron passing the tag requirements and then again probes for a different electron than the current tag and now finds the initial tag as the probe.

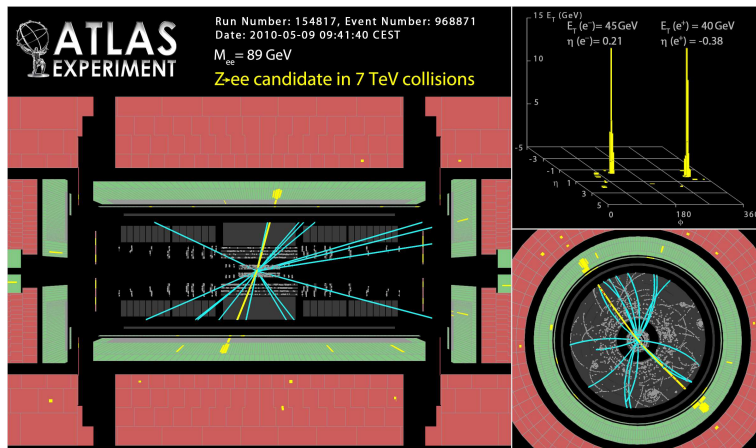


Figure 5.1: Atlantis event display of the first $Z \rightarrow ee$ event seen in ATLAS in May 2010. All ATLAS public event displays are available in [85].

Since there is a non-negligible amount of background present, which decreases when applying the different sets of identification requirements to the probe, it needs to be properly subtracted at each level in order to obtain the signal efficiencies. The background subtraction can be performed with several methods, which are discussed in section 5.2.3 below. Due to the small combinatorial background present in the signal Monte Carlo, the data-driven efficiencies are compared to identification efficiencies for truth-matched electrons in MC (see section 5.2.4).

After the efficiencies have been obtained in both the data and MC, data/MC scale

factors can be calculated. The scale factors are used by physics groups to correct the simulated data for the data-MC discrepancies. This is done for the W/Z cross section measurements outlined in the following chapters of this thesis.

The relatively low statistics of Z events available in the 2010 data does not allow for an efficiency measurement to be carried out in two-dimensional (η, E_T) space in sufficiently fine binning. The efficiencies are therefore estimated separately as a function of η and E_T using different background subtraction methods. The following one-dimensional binning has been chosen:

	(E_T, η) binning
$\eta^{probe} =$	-2.47, -2.01, -1.52, -1.37, -0.80, 0.0, 0.80, 1.37, 1.52, 2.01, 2.47
E_T^{probe} (GeV) =	20, 25, 30, 35, 40, 45, 50, 80

Table 5.2: Definition of binning in E_T, η space for electron efficiency measurements with 2010 data, chosen due to the limited statistics.

5.2.1 Tag and probe selection

The initial electron selection is common for the tag and the probe, while additional requirements are applied to the tag in order to remove background and to keep the probe unbiased from the trigger selection. The requirements on the event and the tag, up to the denominator level of the efficiency calculation, are listed below:

- The event is required to be included in the standard e/γ “good run list”² (**GRL**) listing the luminosity blocks (shorter periods of data-taking) where the sub-detectors crucial for electron analysis are in nominal conditions and flagged as good by the data quality flags. The GRL is also used to calculate the precise integrated luminosity used for a particular analysis. The e/γ GRL for the 2010 data yields 39.0 pb^{-1} .
- A loose **primary vertex** cut is applied to the event in order to reject non-collision background. The presence of a primary vertex with at least three tracks is required in the event.
- **Trigger selection:** The trigger stream used for the data is the L1Calo stream (for data period A-D) followed by the egamma stream (for data period E-I). The events in the data period A-E3 (about 2% of the total integrated luminosity,

²eg_standard_7TeV

see Appendix A) are required to pass L1_EM14. This is a Level 1 trigger, which triggers upon an EM cluster with a transverse energy of at least 14 GeV. This trigger became pre-scaled as the instantaneous luminosity of the LHC rapidly increased and the trigger used for period E4-I is EF_e15_medium. EF_e15_medium triggers upon an electron with transverse energy of above 15 GeV and passing requirements, similar to the offline medium ID but slightly looser, at Event Filter level. EF_e15_medium remained un-prescaled throughout the 2010 data-taking.

- The event must contain at least two electrons with **author** electron, implying that the electron must have been reconstructed with the standard *egamma* algorithm.
- The electrons must fall in the **kinematic region** of $|\eta| < 2.47$ and $E_T > 20$ GeV. The tag has the additional requirement of being located outside the calorimeter “crack” region of $1.37 < |\eta| < 1.52$. E_T is calculated with the energy from the cluster and the direction from the track if the track contains at least 4 silicon hits, otherwise from the cluster. The pseudorapidity, η , is estimated from the cluster.
- During 2010 several dead optical links (**OTx**) were present in the Liquid Argon calorimeter. To avoid mis-measuring the energy of the electron candidates located inside and close to these problematic regions, they are excluded. As a consequence of the profile of the integrated luminosity the majority of the data collected was obtained with the status of the dead OTxs as in run 167521. Due to the negligible gain of using the full run dependent OTx cuts, only the final map corresponding to run 167521 is applied. This also improves the consistency with simulated data, since the release 16 MC was re-processed with this map.

This level of selection requirements is what is nominally defined as “container” level. The preceding requirements only apply to the tag and not the probe:

- The offline electron must have **fired the trigger** to be qualified as tag. The tag is thus matched to the online trigger object. For period A-E3, the tag is matched to the L1_EM14 trigger, while for period A-E4 the tag is matched both to the EF_e15_medium object as well as the seeding L1 trigger: L1_EM10.
- In order to minimize background, strict electron identification requirements are applied on the tag. The exact requirements are varied to assess the systematic uncertainty, but the standard selection is **tight** identification.
- Another optional cut, which reduces the amount of background by approximately a factor two, is to require **opposite sign** (OS) between the tag and

the probe. However, this removes the Z events where the charge of one of the electrons have been incorrectly reconstructed.

The sequence of selection requirements described above is shown in Table 5.3 for the separate data periods in 2010 as well as overall. There are 23020 events with a tag and a probe having opposite sign, without constraining the invariant mass. The number of probes is however larger since than the number of events since there can be several probes in one event.

Pile-up simulation and re-weighting

The effect of multiple interactions per bunch crossing (“pile-up”) is modeled by overlaying simulated minimum bias events over the original hard-scattering event. The amount of pile-up in data increases rapidly with the instantaneous luminosity delivered by the LHC.

For the Z tag-and-probe studies performed on the full 2010 data, most of the data analyzed contains a significant number of bunches in the beam and hence *bunch-train pile-up* MC is used to for the efficiency data-MC comparisons. Here, individual bunches are separated by 150 ns and contained in trains of eight bunches. A second bunch train follows with a time separation equal to 225 ns, succeeded by a longer pause before the next bunch train. The average number of simulated additional minimum bias interactions per bunch crossing is Poisson distributed with the expectation value $\langle n \rangle = 2.2$.

The amount of bunch-train pile-up can be well measured from the distribution of the reconstructed primary vertex multiplicity and the MC is corrected by re-weighting the distribution to match the data. The definition of a primary vertex is the same as the definition above; it must contain at least three tracks. The distributions are acquired at the level of tight tag and container probe and the resulting weights are indicated in Table 5.4. The simulated data is thus re-weighted by applying these weights on an event-by-event basis.

To assess the dependence of the electron efficiencies of the pile-up re-weighting, in-time pile-up MC (corresponding to very early data) is used instead of bunch-train pile-up. The impact on the tight identification efficiency has been found to be negligible; less than 0.01%.

5.2.2 Track quality

The recommended electron identification efficiency scale factors, distributed to different physics groups by the e/γ group, are obtained from a combination of Z and W tag-and-probe results. The E_T^{miss} trigger used to select the W tag-and-probe events has been found to select events from non-collision beam background and a significant

data	e/ γ stream	GRL	trigger	pr. vertex	author	η	E_T	OTX	tight tag	trig. match	OS
ABC	29978584	26796570	121193	120465	78169	75478	4185	3581	11	11	11
D	94578936	82493872	2260144	2256067	1478494	1428273	76514	66050	256	254	179
E	41984880	38513200	3585857	3583076	2350613	2273074	124775	108269	843	839	560
F	23862972	22305614	379177	379165	217984	205492	9645	8441	1402	1402	987
G	20894156	17102376	1464941	1464914	849231	801821	37998	33354	5802	5792	4074
H	9122093	7818842	1552975	1552947	902943	852472	40187	35330	6085	6075	4344
I	19664056	18549792	4563566	4563510	2692252	2544581	118787	104515	18433	18389	12865
A-I	240085677	213580266	13927853	13920144	8569686	8181191	412091	359540	32832	32762	23020

Table 5.3: Cut flow for the different 2010 data periods for $Z \rightarrow ee$ tag-and-probe.

Nb. of reconstructed vertices	1	2	3	4	5	6	≥ 7
Pile-up weight	1.93206	1.24185	0.860027	0.633114	0.525451	0.464221	0.422034

Table 5.4: Pile-up weights applied to simulated data, obtained from the primary vertex multiplicity distribution in data and MC.

fraction of the probes at the W tag-and-probe container level are from such events. These fake probes originate from beam-halo background muons producing high-energy bremsstrahlung clusters in the EM calorimeter (for more details see [81]). It is therefore necessary to apply initial track quality cuts at denominator (container) level and measure the identification efficiencies with respect to track quality. Also the Z probes at container level have been investigated for non-collision beam background, but no indication of such events have been found.

The track quality cuts applied at container level are the silicon hit requirements included in the medium identification: at least 7 hits in the SCT and Pixel detector, whereas at least one hit must be in the pixels. These silicon hit requirements have been proven to be very efficient in removing the non-collision background in the W tag-and-probe events.

To be able to combine the two measurements, the Z tag-and-probe is forced to rearrange the measurement, such that the identification efficiencies are measured with respect to track quality and the efficiency of the track quality cut itself is measured as part of the electron reconstruction efficiency. For the remaining part of this chapter, the identification efficiency implies with respect to track quality if not otherwise indicated. Fortunately, the efficiency data/MC scale factor of the track quality cut itself has been found compatible with unity and without any large η dependence (see section 5.3 below). Re-shuffling the electron efficiency components in this manner therefore has little impact on the identification efficiency scale factor.

5.2.3 Background subtraction

The background subtraction is a crucial constituent of the tag-and-probe methodology and the largest source of uncertainty of the measurement. As was mentioned above, the background at each level of the efficiency estimation must be properly subtracted in order to estimate the electron efficiency in the data. There are different methods of subtracting the background, where most of the methods involve using the peak structure of the invariant mass (M_{ee}) distribution. Since it is desirable to measure the efficiencies as a function of electron η and E_T , the background subtraction must be carried out in each η or E_T bin. The poor statistics in certain bins, together with the fact that the signal and background invariant mass distribution changes significantly for different E_T bins, impose difficulties.

Figure 5.2 shows the invariant mass distribution for the tag and the probe at track quality level as well as E_T , η and ϕ for the probe after a requirement of $80 < M_{ee} < 100$ GeV for the tag and the probe has been imposed. Energy scaling and smearing, which is further discussed in section 6.3.5, is not applied. The plots contain signal MC only and the comparison with data provides some indication of the background distributions. The regions of lower E_T and lower M_{ee} have an evident excess of

background events in data. Figure 5.3 displays the equivalent distributions for the probe at medium level. Here the data and signal MC distributions agree well and no background is visible.

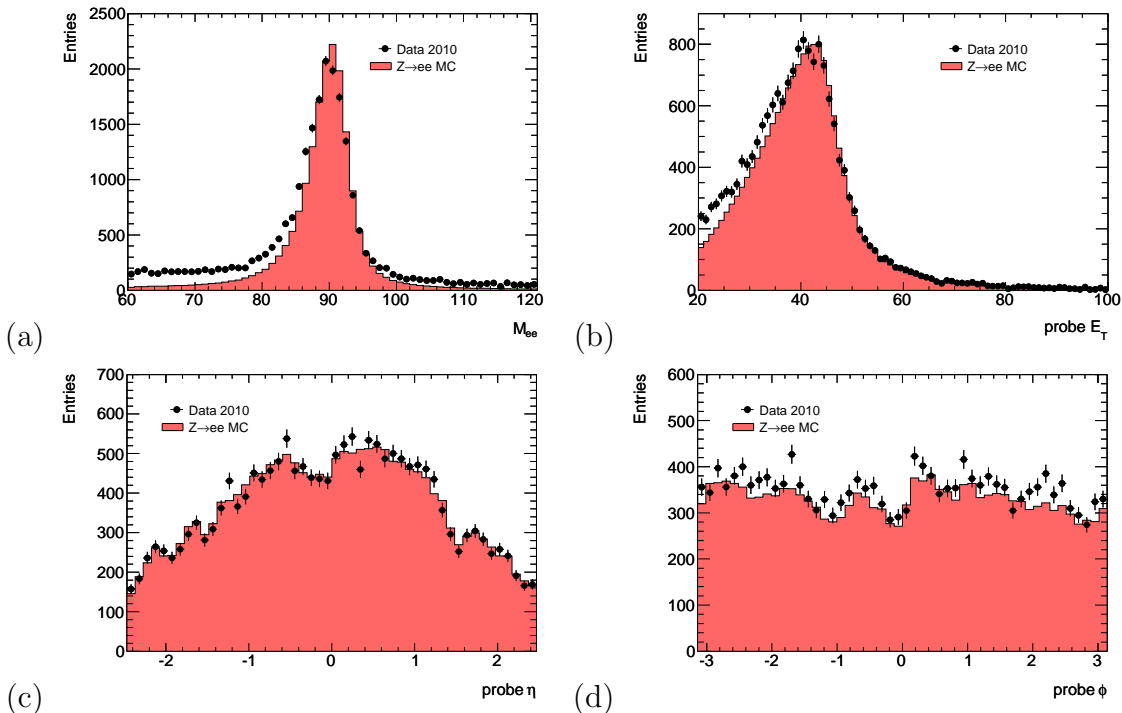


Figure 5.2: Distributions for the probe at track quality level in data and signal MC: (a) M_{ee} of the tag and the probe, (b) E_T of the probe, (c) η of the probe and (d) ϕ of the probe. An $80 < M_{ee} < 100$ GeV cut is imposed on the tag and the probe in all distributions except for (a) and the probe is required to be outside the crack region in all distributions except for (c). The MC is normalized to integrated luminosity (39 pb^{-1}). The distributions are not well described by the signal MC due to significant background present in certain kinematic regions.

Sideband methods

Sideband methods are robust against low statistics, since these methods count events rather than performing a fit on a distribution. Several different sideband methods have been tested in data and MC (for more explicit details see [81]). The method that has been proven the most accurate, called the “OS-SS sideband method”, divides the invariant mass distribution into three regions; a signal region B ($80 < M_{ee} < 100$ GeV) and two background sideband regions A ($60 < M_{ee} < 80$ GeV) and C ($100 <$

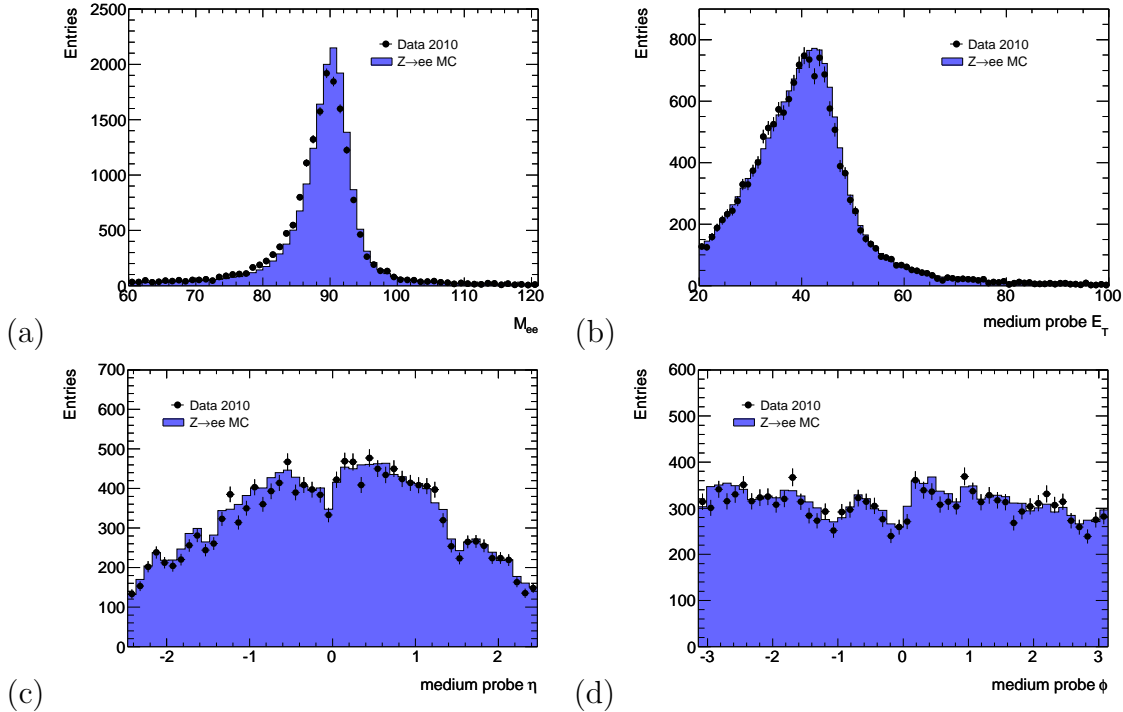


Figure 5.3: Distributions for the probe at medium level in data and signal MC: (a) M_{ee} of the tag and the probe, (b) E_T of the probe, (c) η of the probe and (d) ϕ of the probe. An $80 < M_{ee} < 100$ GeV cut is imposed on the tag and the probe in all distributions but (a) and the probe is required to be outside the crack region in all distributions except for (c). The MC is normalized to integrated luminosity (39 pb^{-1}). Background contamination is almost negligible and cannot be identified in the plots.

$M_{ee} < 120$ GeV). An opposite sign requirement is imposed for the tag and the probe in the signal region and due to a non-negligible amount of signal in the sideband regions, only same sign events are considered as background. A linear behavior of the background is assumed and the average number of same sign events in the background regions is subtracted from the opposite sign events in the signal region.

Figure 5.4 shows the invariant mass distribution for the tag and the probe at container, loose, medium and tight level with 2010 data. The opposite sign events are overlaid with the same sign events to illustrate the amount of background being subtracted in the OS-SS sideband method. There is also a larger number of OS events than SS events outside the signal region, arising from the tails of the M_{ee} distribution of the signal. It is therefore not correct to classify all OS events in the sideband regions as background. A Z mass peak is also visible in the signal region for the SS

events, especially from loose level on where the background is much reduced. These events arise from Z events where the charge of one of the two electrons has been mis-identified. SS events in the signal region can thus not be used for background estimation. What remains is to use OS events in the signal region and SS events in the background region, which corresponds to the OS-SS sideband method previously described.

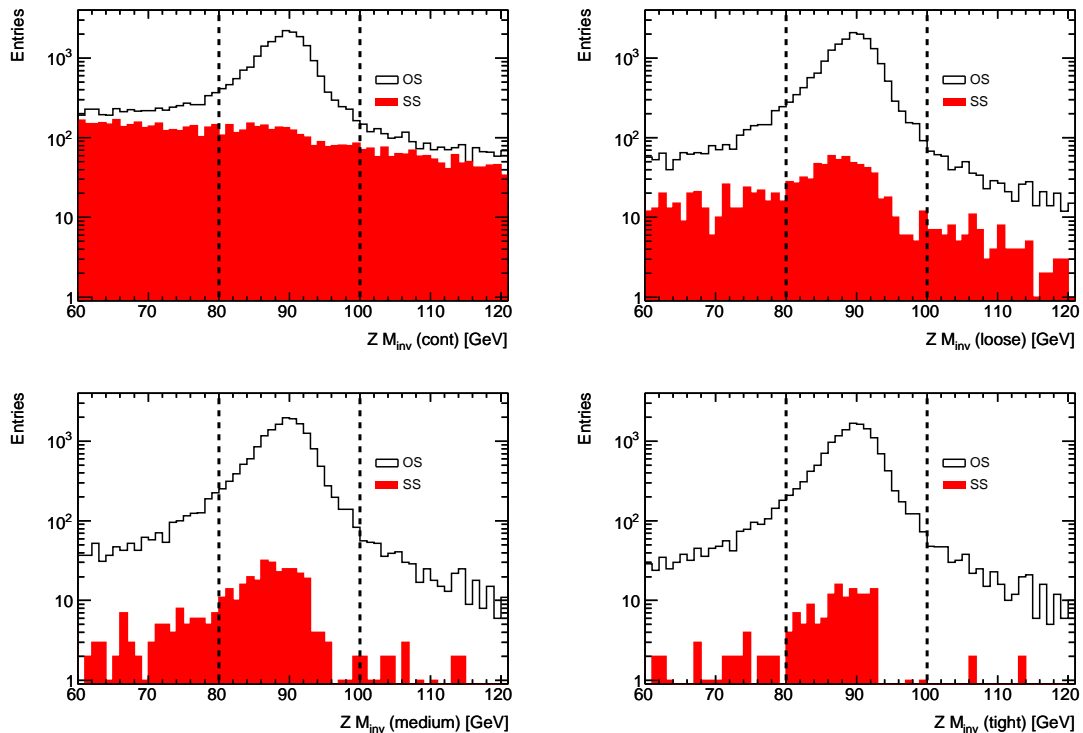


Figure 5.4: The invariant mass distribution of tight tag and the probe at container (not including track quality cuts), loose, medium and tight level in logarithmic scale, with 2010 data. The opposite sign events in white are overlaid with the same sign events in red. The dotted lines show the separation between signal and background regions for the OS-SS sideband background subtraction method.

Fitting methods

A crucial disadvantage of the OS-SS sideband method is that it relies on the linearity of the background shape as a function of the invariant mass. This is sufficient for the overall efficiency calculation as well as for the different η regions, but for higher E_T ranges, the background rather peaks in the signal region and the method is no longer

valid. This is illustrated in section 5.4, where the E_T dependent efficiency method and results are further discussed.

The primary background subtraction method for measuring the E_T dependent efficiencies is fitting the invariant mass distribution, which is presented in section 5.4.1. A secondary method of fitting the E_T spectrum directly has also been investigated and is discussed in section 5.4.2. The fitting methods have the disadvantage of difficulties with low statistics, leading to issues of finding the correct level of background, especially at the medium and tight selection levels.

Statistical uncertainty

Binomial or Bayesian methods are nominally used for calculating the statistical uncertainty of an efficiency where the numerator is a subset of the denominator. The tag-and-probe efficiency measured in data, however, includes a background subtraction, which must be taken into account in the uncertainty calculation. The methods used here to estimate the statistical uncertainty are described in [86], which addresses background subtraction methods using both sidebands and fits.

For sideband methods, the efficiency after background subtraction is defined as

$$\epsilon = \frac{N_{num} - \alpha N_{num,SB}}{N_{denom} - \alpha N_{denom,SB}}, \quad (5.1)$$

where α is the weight of the sidebands, which is 1/2 in the default OS-SS sideband method described above. The uncertainty for sideband methods is then calculated according to

$$(\Delta\epsilon)^2 = \frac{(1 - 2\epsilon)(N_{num} + \alpha N_{num,SB}) + \epsilon^2(N_{denom} + \alpha N_{denom,SB})}{(N_{denom} - \alpha N_{denom,SB})^2}. \quad (5.2)$$

If a fit is used to estimate the amount of background, the efficiency is defined as

$$\epsilon = \frac{N_{num,fit}}{N_{denom,fit}}, \quad (5.3)$$

where $N_{num,fit}$ is the number of signal events that the fit returns for the numerator and $N_{denom,fit}$ the equivalent for the denominator. The uncertainty of the efficiency is then calculated according to:

$$(\Delta\epsilon)^2 = \frac{(1 - 2\epsilon)(\Delta N_{num,fit})^2 + \epsilon^2(\Delta N_{denom,fit})^2}{N_{denom,fit}^2}. \quad (5.4)$$

5.2.4 Efficiency estimates from Monte Carlo events

The simulated data used for the Z tag-and-probe study in release 16 is a 5 million event $Z \rightarrow ee$ egamma D3PD PYTHIA sample. Whether to apply truth matching and with what method, has a significant impact on the electron efficiencies derived from MC. If no truth matching is applied, hadrons from combinatorial background in the signal MC can fake electron probes, in particular at the denominator level. These probes are much less likely to pass the identification cuts and will therefore contribute to a lower efficiency estimate.

Truth matching is applied through the MCTruthClassifier tool, which defines the match on a hit-by-hit basis from the track in the Inner Detector. A majority logic chooses the best matched generated track for any reconstructed track in the event. From this information, one can classify the reconstructed electron tracks in simulated data in two ways:

- **Direct truth matching** simply includes electrons directly matched to the true primary electrons from the Z boson.
- **Loose truth matching** is an extension of the direct truth matching through including electrons corresponding to electron tracks generated by bremsstrahlung photons or final-state-radiation (FSR) photons originating from the primary electron.

An example of a loosely truth matched event is when the electron undergoes an early hard bremsstrahlung and the photon converts in the first silicon layers in the ID, producing two additional tracks. This electron is of worse quality and has a lower probability of passing the identification cuts. The loose truth matching will therefore result in lower efficiencies than if one only includes directly truth matched electrons. The same statement is valid for relaxing the opposite sign requirement, which rejects the charge mis-identified events in the efficiency calculations. In the event described above, the electron with charge opposite to that of the primary electron may be chosen as the best match to the EM calorimeter cluster. The reconstructed electron charge will then be mis-measured and have the same sign as the second electron from the Z boson.

Table 5.5 shows the identification efficiencies in MC without any truth matching and with loose and direct truth matching applied, with respect to container level as well as track quality cuts. The difference between applying direct and loose truth matching is in fact larger than the difference between loose and no truth matching. The effect increases for tighter identification and is of course much reduced if the initial track quality cuts are applied at the denominator level.

Which truth matching should be applied in order to obtain the true electron identification efficiencies and subsequently the data/MC scale factors, is determined

Efficiency with respect to container [%]	no	loose	direct
	truth match	truth match	truth match
Loose	97.68 ± 0.01	98.18 ± 0.01	98.19 ± 0.01
Medium	92.57 ± 0.02	93.20 ± 0.02	94.83 ± 0.02
Tight	74.76 ± 0.03	75.28 ± 0.03	77.05 ± 0.03
Efficiency with respect to track quality [%]	no	loose	direct
	truth match	truth match	truth match
Loose	97.74 ± 0.01	98.19 ± 0.01	98.19 ± 0.01
Medium	95.68 ± 0.01	96.14 ± 0.01	98.18 ± 0.01
Tight	77.27 ± 0.03	77.65 ± 0.03	77.15 ± 0.03

Table 5.5: Identification efficiencies in MC for loose, medium and tight with respect to container (top) and track quality (bottom), comparing no, loose and direct truth matching.

by whether the events rejected by the truth match are subtracted in data analysis as background. Applying loose truth matching is thus motivated if the signal events with an electron that has showered is considered as signal in data. If this is the case, it would then be incorrect to compare the data-driven efficiencies with the directly truth matched MC efficiencies.

To determine whether loose truth matching should be applied to the MC, the fraction of non-truth matched electrons and their origin was investigated. At numerator level less than 0.1% of all electrons at medium level are excluded in the loose truth match. Whether or not to apply truth matching at the numerator level therefore has no impact and the study is more interesting at the container level where the effect is larger. The fraction of probes at the container level that are not included in the loose truth match is shown in Figure 5.5 as function of electron E_T , after requiring opposite sign and $80 < M_{ee} < 100$ GeV. The overall effect is only $0.7 \pm 0.01\%$, but the fraction increases rapidly towards lower E_T . If the opposite sign and $80 < M_{ee} < 100$ GeV requirements are relaxed, the effect increases from 0.7% to about 2%.

Investigating the origin of the probes at container level that are not included in the loose truth match shows that 59% are originating from hadrons, 24% are unknown, implying that the truth information was not kept in the truth tree, and 17% come from an electromagnetic process or conversion in the material of the detector that is not included in the loose truth matching.

A simple closure test is performed on MC in order to investigate whether the 0.7% of the probes that are not included in the loose truth matching would be subtracted as background on data. The OS-SS sideband background subtraction method described above is thus applied to the signal MC at container level. The method finds back $0.8 \pm 0.01\%$ as background, which is compatible with non truth matched fraction.

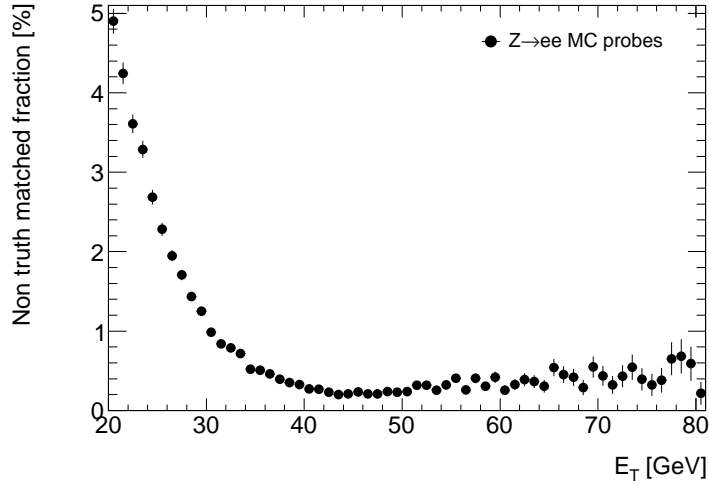


Figure 5.5: The fraction of non truth matched probes in signal MC for $Z \rightarrow ee$ tag-and-probe container level as a function of probe E_T .

Applying loose truth matching to the MC in order to extract electron efficiencies is therefore fully justified.

Table 5.6 and 5.7 display the loose, medium and tight identification efficiencies with respect to track quality cuts in bins of η and E_T respectively. Loose truth matching has been applied and the probes are within $20 < E_T < 50$ GeV. These values are then to be compared with the data-driven efficiencies in order to produce data/MC scale factors in the equivalent binning.

η	-2.47,-2.01	-2.01,-1.52	-1.52,-1.37	-1.37,-0.8	-0.8,0
Loose	98.39 ± 0.04	98.85 ± 0.03	94.94 ± 0.10	98.36 ± 0.03	98.11 ± 0.02
Medium	97.02 ± 0.05	96.99 ± 0.04	94.36 ± 0.10	96.85 ± 0.03	94.90 ± 0.04
Tight	73.89 ± 0.13	73.23 ± 0.11	62.27 ± 0.22	75.76 ± 0.09	82.72 ± 0.06
η	0,0.8	0.8,1.37	1.37,1.52	1.52,2.01	2.01,2.47
Loose	98.14 ± 0.02	98.47 ± 0.02	94.77 ± 0.10	98.88 ± 0.03	98.51 ± 0.04
Medium	95.69 ± 0.03	96.94 ± 0.03	94.28 ± 0.11	97.04 ± 0.04	97.14 ± 0.05
Tight	83.73 ± 0.06	76.03 ± 0.08	62.22 ± 0.22	73.33 ± 0.11	73.61 ± 0.14

Table 5.6: Identification efficiencies from MC with respect to track quality as a function of η measured for probes that are loosely truth matched and within $20 < E_T < 50$ GeV.

E_T	20-25 GeV	25-30 GeV	30-35 GeV	35-40 GeV	40-45 GeV
Loose	96.56 ± 0.05	97.48 ± 0.04	97.99 ± 0.03	98.40 ± 0.02	98.86 ± 0.01
Medium	94.38 ± 0.07	95.54 ± 0.05	95.85 ± 0.04	96.41 ± 0.03	96.56 ± 0.03
Tight	71.94 ± 0.13	74.54 ± 0.10	77.01 ± 0.08	78.63 ± 0.06	80.25 ± 0.06
E_T	45-50 GeV	50-80 GeV			
Loose	99.11 ± 0.02	99.11 ± 0.02			
Medium	96.98 ± 0.03	97.13 ± 0.03			
Tight	91.72 ± 0.07	82.93 ± 0.08			

Table 5.7: Identification efficiencies from MC with respect to track quality as a function of E_T measured for probes that are loosely truth matched. The crack region in $|\eta|$ is excluded.

5.3 η dependent efficiencies

The OS-SS sideband method, as was described in section 5.2.3, is applied to estimate the background to be subtracted in data to acquire η dependent electron efficiencies and data/MC scale factors. This is the most robust method against low statistics and assumes linear behavior of the background in the M_{ee} space. The method is performed in each desired η bin, to acquire binned efficiencies and scale factors.

The efficiencies and scale factors as a function of η are calculated for probes with $20 < E_T < 50$ GeV as a typical energy range for W/Z physics. This also facilitates the combination of W and Z scale factors. Efficiency scale factors have also been produced for 30-50 GeV probes in order to provide SFs to physics analyses using higher E_T electrons. The 30-50 GeV efficiencies are, however, not included here due to lack of space and the reader is asked to consult [57, 81] for more information.

5.3.1 Estimated background with the OS-SS sideband method

The amount of background in the different η regions, estimated with the OS-SS sideband method with tight tag and considering [80,100] GeV as signal region and [60,80] and [100,120] GeV as sideband regions, is displayed in Table 5.8. Overall, the method finds approximately 11% background at container level, which is reduced to about 9% by applying the track quality cuts. Applying loose identification on top of the track quality cuts decreases the background to less than percent level. At medium and tight ID level, the background is very small (0.3% and 0.1% respectively). The available statistics before and after background subtraction is also shown in the table. Studying the variation throughout the different η bins shows that, as expected, the crack region contains the largest amount of background, which in combination with the smallest statistics yields a much larger relative uncertainty for the estimated signal

CHAPTER 5. ELECTRON EFFICIENCY MEASUREMENT USING THE $Z \rightarrow ee$ TAG-AND-PROBE METHOD

than for the other η bins. The amount of background is overall larger in the end-cap regions ($1.52 < |\eta| < 2.47$) than in the barrel ($|\eta| < 1.37$).

η		Container	Track Quality	Loose + TQ	Medium	Tight
Total	Events	16933	16117	14444	14013	11850
	Bkg	10.9%	8.9%	0.6%	0.3%	0.1%
	Signal	15084 ± 144	14680 ± 138	14356 ± 121	13970 ± 119	11836 ± 109
-2.47,-2.01	Events	992	910	798	780	587
	Bkg	11.8%	10.5%	0.8%	0.6%	0.2%
	Signal	875 ± 35	814 ± 33	792 ± 28	776 ± 28	586 ± 24
-2.01,-1.52	Events	1354	1241	1081	1060	850
	Bkg	11.7%	8.4%	1.1%	0.6%	0.3%
	Signal	1195 ± 41	1137 ± 38	1069 ± 33	1054 ± 33	848 ± 29
-1.52,-1.37	Events	440	409	356	349	265
	Bkg	14.4%	11.5%	1.8%	1.0%	0.6%
	Signal	376 ± 24	362 ± 22	350 ± 19	346 ± 19	264 ± 16
-1.37,-0.8	Events	2107	2016	1790	1752	1467
	Bkg	11.4%	9.5%	0.7%	0.3%	0.2%
	Signal	1868 ± 51	1824 ± 49	1778 ± 43	1746 ± 42	1464 ± 38
-0.8,0	Events	3367	3276	2946	2808	2494
	Bkg	9.7%	8.2%	0.4%	0.1%	0.1%
	Signal	3039 ± 63	3006 ± 62	2934 ± 54	2804 ± 53	2492 ± 50
0,0.8	Events	3690	3571	3251	3128	2774
	Bkg	9.7%	8.1%	0.4%	0.2%	0.1%
	Signal	3332 ± 66	3281 ± 64	3236 ± 57	3122 ± 56	2772 ± 53
0.8,1.37	Events	2347	2255	2046	1990	1714
	Bkg	11.0%	9.1%	0.5%	0.2%	0.0%
	Signal	2088 ± 54	2050 ± 52	2036 ± 45	1987 ± 45	1714 ± 41
1.37,1.52	Events	398	367	315	315	228
	Bkg	14.8%	10.9%	1.1%	0.6%	0.2%
	Signal	339 ± 23	327 ± 21	312 ± 18	313 ± 18	228 ± 15
1.52,2.01	Events	1318	1224	1116	1097	896
	Bkg	12.1%	8.9%	0.7%	0.5%	0.2%
	Signal	1159 ± 40	1116 ± 38	1108 ± 34	1092 ± 33	894 ± 30
2.01,2.47	Events	920	848	745	734	575
	Bkg	11.5%	10.1%	0.5%	0.4%	0.0%
	Signal	814 ± 34	762 ± 32	742 ± 27	731 ± 27	575 ± 24

Table 5.8: Number of events before and after background subtraction as well as the fraction of background in each η bin and in total. The tag and probe are of opposite sign and with an invariant mass within $[80,100]$ GeV. The probes have a transverse energy within $[20,50]$ GeV.

5.3.2 Reconstruction and track quality efficiency vs η

Track quality efficiency

As was previously discussed in section 5.2.2, the electron Z tag-and-probe efficiencies are measured in two steps in order to be able to combine the scale factors with W tag-and-probe results. The measurement of the track quality cut efficiency and corresponding data/MC scale factor is measured with Z tag-and-probe with the OS-SS sideband method to calculate the overall, as well as η dependent, efficiency. The overall track quality efficiency in data and MC and their scale factor are shown in Table 5.9. The efficiency of the track quality cut is found to be somewhat higher in data than in MC, although close to unity.

[%]	track quality efficiency	data/MC scale factor
Data	97.37 ± 0.21	100.4 ± 0.2
MC truth	97.00 ± 0.01	

Table 5.9: Overall track quality efficiency measured with Z tag-and-probe and in MC truth as well as the data/MC scale factor. Track quality implies 7 silicon hits, whereas at least one hit must be in the Pixel detector. The data-driven efficiencies are obtained with the OS-SS sideband method for probes within $20 < E_T < 50$ GeV and outside the crack region.

The derived η dependent track quality efficiency is displayed in Figure 5.6. The upper plot in the figure shows the efficiency in data and MC separately and the bottom plot shows their corresponding ratio (scale factor). No significant η dependence is seen for the scale factor. Due to the compatibility of the track quality efficiency scale factor with unity, the identification scale factors can be calculated with respect to track quality rather than container without yielding significantly different results. Only one η bin [1.52,2.01] shows a scale factor that is not compatible with unity within the statistical uncertainties. The data-driven efficiencies and data/MC SFs for each η bin, with their statistical uncertainties, are explicitly stated in Table B.1, Appendix B.

Reconstruction efficiency

The reconstruction efficiency data/MC scale factors, provided by e/γ , have been calculated as overall values and in the different η bins with and without including the track quality cut [57, 81]. The efficiency of reconstructing an electron with the *egamma* algorithm (described in 5.1.1) is measured with respect to the collection of clusters stored by the algorithm. It has been verified using *EMTopoClusters* that the efficiency of reconstructing an sliding window cluster for an electron above 15 GeV is

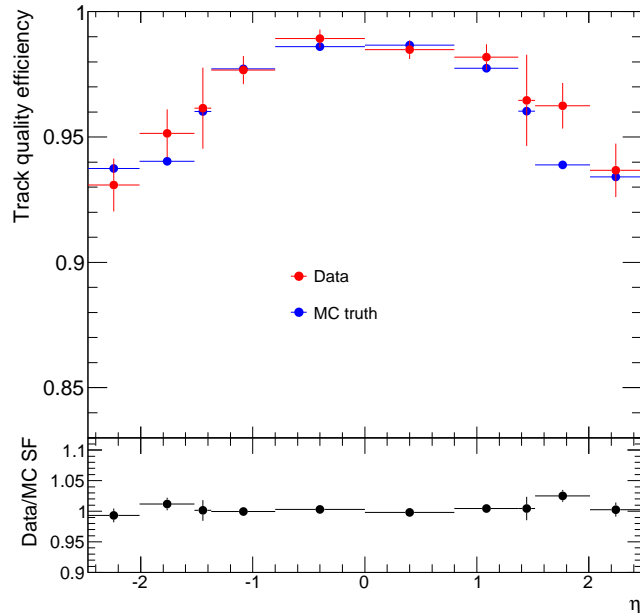


Figure 5.6: Track quality efficiency for data and MC in the upper plot and their ratio (scale factor) in the lower plot. The efficiency is calculated for 20-50 GeV probes.

100%. The resulting scale factors, integrated over η , for reconstruction efficiency alone as well as with the addition of track quality cuts, are [81]:

$$SF_{\text{reco}} = 1.005 \pm 0.000(\text{stat}) \pm 0.002(\text{syst}) = 1.005 \pm 0.002 \quad (5.5)$$

$$SF_{\text{reco} + \text{TQ}} = 1.013 \pm 0.002(\text{stat}) \pm 0.008(\text{syst}) = 1.013 \pm 0.008 \quad (5.6)$$

confirming the slightly higher efficiency of the track quality cut in data than in MC. For more details on the reconstruction efficiency method, including η dependent results, consult [81].

5.3.3 Identification efficiency vs η

The identification efficiencies are acquired through calculating the binomial mean of the estimated signal after the background has been subtracted at each level. (The background is estimated with the OS-SS sideband method as was presented in Table 5.8 above.) The η dependence of the resulting electron identification efficiency with respect to track quality cuts can be seen in Figure 5.7 for loose, medium and tight, together with the true efficiencies obtained from MC. The efficiencies are measured

for opposite sign tag and probe pairs with an invariant mass within $[80,100]$ GeV. Only probes with transverse energy within $[20,50]$ GeV are considered.

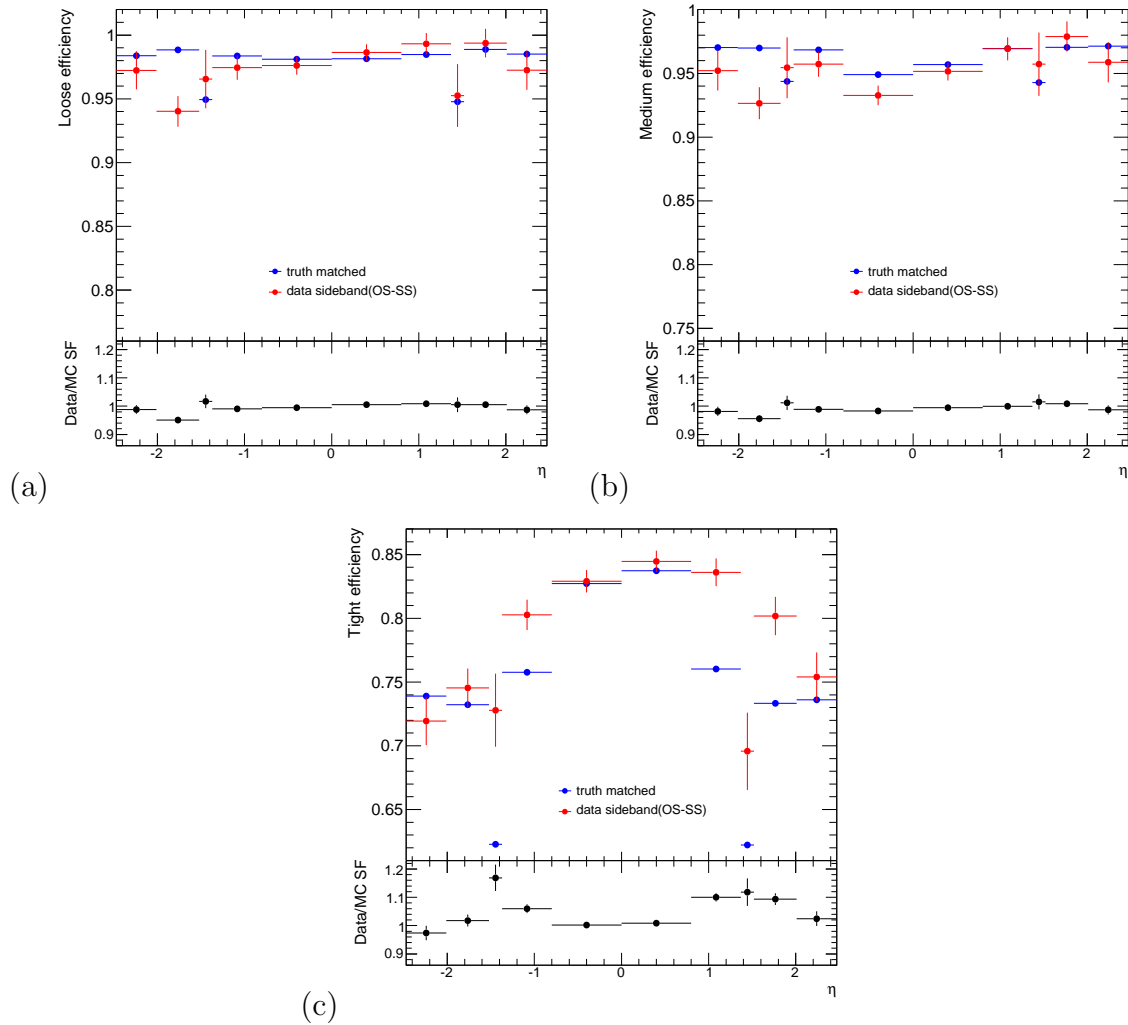


Figure 5.7: Electron efficiencies (upper plots) and data/MC scale factors (lower plots) for (a) loose, (b) medium and (c) tight identification. The data-driven efficiencies are obtained with the OS-SS sideband background subtraction method on Z tag-and-probe, with $20 < E_T < 50$ GeV probes.

The identification efficiencies and scale factors with their statistical uncertainty in each η bin are explicitly stated in Table B.2, B.3 and B.4 in Appendix B. The overall efficiencies and scale factors (integrated over all η except the crack regions) obtained with the OS-SS sideband method are shown in Table 5.10.

	[%]	Efficiency	Data/MC scale factor
Loose ID	Data	97.89 ± 0.33	99.51 ± 0.33
	MC truth	98.37 ± 0.01	
Medium ID	Data	95.14 ± 0.35	98.86 ± 0.37
	MC truth	96.24 ± 0.01	
Tight ID	Data	81.09 ± 0.42	103.34 ± 0.54
	MC truth	78.47 ± 0.03	

Table 5.10: Loose, medium and tight identification efficiencies, integrated over η , with respect to track quality for Z tag-and-probe, MC truth and their data/MC scale factor. The data-driven efficiencies are obtained with the OS-SS sideband method for probes within $20 < E_T < 50$ GeV and outside crack regions.

Tight versus medium scale factor

Studying the different plots in Fig. 5.7 shows that both loose and medium identification efficiencies are overall somewhat lower in data than in MC, yielding SFs below unity. This has been found to be due to broader shower shape distributions in data than in the Monte Carlo description [81]. The scale factors are however reasonably well-behaved as a function of η .

Taking a closer look at the tight identification efficiency in data and MC shows that the efficiency is significantly higher in data. In addition, the data/MC scale factor displays a strong η dependence. One or several of the tight identification cuts must be responsible for this large increase in the efficiency SF from medium to tight as well as the fluctuations of the scale factors in η^3 . An investigation is performed by adding one tight cut at the time to the medium identification and then computing the new SF normalized to the medium SF; $SF(\text{medium} + \text{tight cut})/SF(\text{medium})$. This double-double ratio is shown in Figure 5.8 as a function of η . In addition, the ratio of tight and medium scale factors is included in black. It is trivial to conclude from the figure that the cut on TR ratio is causing both the increase of the overall SF as well as the large fluctuations in η . Note that the TRT only extends up to $|\eta| = 2.0$ and the SF of the TR ratio as well as the cut on TRT hits is thus unity for $2.0 < |\eta| < 2.47$.

The mis-modeling of the signal efficiency of the TR ratio in simulated data is largely due to the fact that the optimization of the cut is based on background rejection rather than signal efficiency. Figure 5.9 shows the TR ratio for the probe at medium identification level for data and MC. The MC distribution is shifted towards lower values with respect to data, implying that placing a selection cut on the variable rejects more signal events in MC than in data.

³The cuts involved at the different identification levels are outlined in Table 5.1

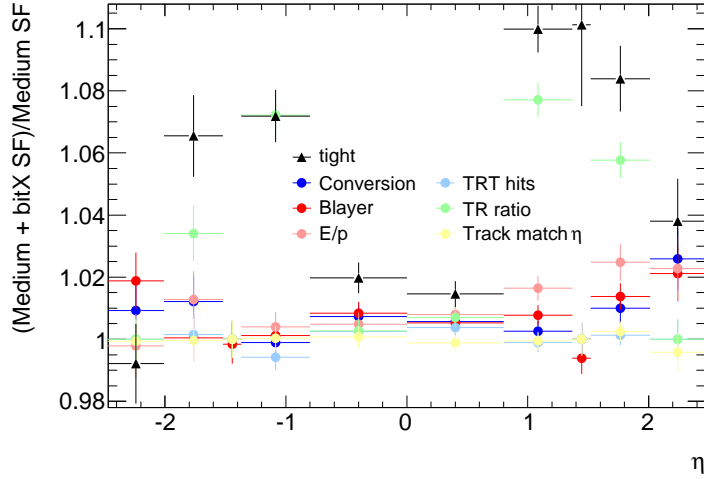


Figure 5.8: The ratio of efficiency scale factors for medium + tight cuts over medium. The ratio of the tight and medium scale factor is also included in black. The cut on the TR ratio is causing the increase of the efficiency scale factor between medium and tight level, as well as the strong η dependence.

The end-cap efficiency asymmetry

Another observation that can be made from Figure 5.7 is that the efficiency scale factors for the positive end-cap (end-cap A) is consistently a couple of percent higher than for the negative end-cap (end-cap C). There is no clear explanation for this behavior, but the effect has been found to be larger for period D-H (especially period G) than period I.

To investigate the origin of this effect, the efficiency of the different individual identification cuts for loose, medium and tight have been studied. No single cut is however responsible for the end-cap asymmetry in period D-H since the effect is already present at denominator level.

Table 5.11 shows the number of probes at track quality (denominator) level, before and after background subtraction, for period D-H and I as a function of η . After background subtraction, there are approximately 8% more probes in end-cap C than in end-cap A for period D-H. In period I the number of probes at track quality level is equivalent in both end-caps within the statistical uncertainties. Before background subtraction there is already approximately 7% more probes in end-cap C in period D-H. This, combined with about 1% less background in end-cap C yield the observed end-cap asymmetry.

The end-cap asymmetry is much reduced if the probes in the 20-30 GeV bins are excluded and the efficiency is only estimated for probes with $30 < E_T < 50$ GeV.

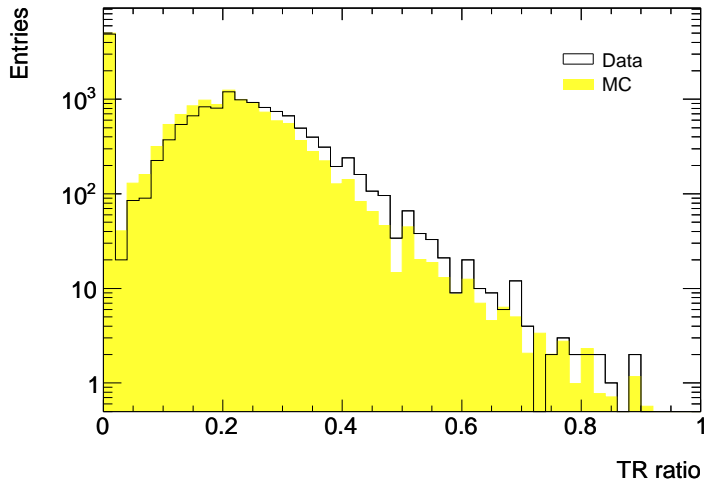


Figure 5.9: Electron TR ratio for data and MC obtained for probes at medium level. The MC distribution is shifted towards lower values with respect to data. The plot is in logarithmic scale and the MC is normalized to the data.

The cause of this effect must therefore be an excess of worse quality probes in end-cap C, that are only present in early data and mainly at lower E_T . Whether or not these probes are signal or background is not entirely clear, but they do fall in the narrow defined invariant mass range of 80-100 GeV and is thus treated as signal by the background subtraction method. There is also no excess of same sign events in the sideband region, since the fraction of background at the denominator level is consistent between the two end-caps, as was seen in Table 5.8.

To confirm that the end-cap asymmetry is not simply due to the OS-SS sideband method failing to classify the excess of probes as background, the background is also estimated by fitting the invariant mass at container level. The fitting method (which is further discussed in section 5.4.1) finds compatible background fractions in the two end-caps (9.9% in end-cap C and 10.2% in end-cap A) and the excess of probes in end-cap C is thus treated as signal.

5.3.4 Official e/γ ID efficiency scale factors

The final medium and tight identification efficiency scale factors provided by the e/γ group are a combination of Z and W tag-and-probe results⁴. A brief description of the Z tag-and-probe final η dependent results and the combination with W tag-and-probe is presented here. For more detailed information, consult [57, 81].

⁴Loose identification is excluded since it is not used by any of the physics analyses.

	end-cap C			barrel	
η	-2.47,-2.01	-2.01,-1.52	-1.52,-1.37	-1.37,-0.8	-0.8,0
D-H probes	400	581	200	900	1390
D-H signal	366 ± 22	540 ± 26	181 ± 15	818 ± 33	1277 ± 40
I probes	510	660	209	1116	1886
I signal	449 ± 25	598 ± 28	181 ± 16	1006 ± 37	1730 ± 47
	barrel		end-cap A		
η	0,0.8	0.8,1.37	1.37,1.52	1.52,2.01	2.01,2.47
D-H probes	1529	1011	161	553	368
D-H signal	1411 ± 42	925 ± 34	141 ± 14	507 ± 25	327 ± 21
I probes	2042	1244	206	671	480
I signal	1870 ± 49	1126 ± 38	186 ± 16	609 ± 28	436 ± 24

Table 5.11: The number of probes before and after background subtraction at track quality level (efficiency denominator) for period D-H and I separately, in the different η bins. In period D-H, the number of probes in the positive end-cap is significantly larger than in the negative end-cap leading to an end-cap asymmetry. This effect is greatly reduced for period I.

Z tag-and-probe variations

To assure stability of the method against for instance the choice of signal and background regions for the OS-SS sideband method, several variations of the method is performed to assess the systematic uncertainty as well as the central value. Not only the signal and background bands are altered, but also the requirement on the tag, which affects the overall level of background. All possible combinations of the following variations are used, resulting in 54 combinations.

- Three variations of the signal region: [80,100] GeV (default), [75,105] GeV and [85,95] GeV.
- Three variations of the background sidebands: [60,120] GeV (default), [58,122] GeV and [62,118] GeV.
- Six different tag requirements: tight (default), tight + isolation, medium, medium + isolation, medium + isolation + b-layer hit, medium + b-layer + E/p.

As the central value of the scale factors, the mean of the distribution from the different combinations is used. The spread of the distribution is taken as the systematic uncertainty of the measurement. This method is performed for every η bin and yields systematic uncertainties of the order of 1-2% for all bins outside the crack

regions, for both medium and tight ID. It is important to stress that applying these variations to acquire the central value is only valid for the efficiency scale factors, since the efficiencies themselves have a slight dependence on the invariant mass.

Additionally, other possible sources of systematic uncertainty are considered. The effect of pile-up has been found miniscule, as was mentioned in section 5.2.1. Another uncertainty is related to the energy scale, since the energy scaling and smearing is applied in the physics analyses (see section 6.3.5) where the SFs are to be included, while this is not the case in the Z tag-and-probe methodology. It has therefore been verified that the energy corrections does not have any significant impact on the efficiency scale factors and is well within the quoted systematic uncertainties.

An additional systematic uncertainty arises from the fact that all tags and probes in the event are chosen to enter the efficiency calculation, even though there are only two electrons originating from the Z boson. An alternative method is to choose the two electrons in the event with the invariant mass closest to the mass of the Z . This has been found not to have any large effect on the efficiencies, as is shown in Figure 5.10. The plot also includes the method of choosing the two electrons with the highest E_T as the tag and probe pair. This method has been found to frequently select the background electron and exclude the signal electron from the Z in the efficiency calculation. This leads to lower efficiencies and larger uncertainties as is seen in Figure 5.10 and should not be included as an input for the measurement.

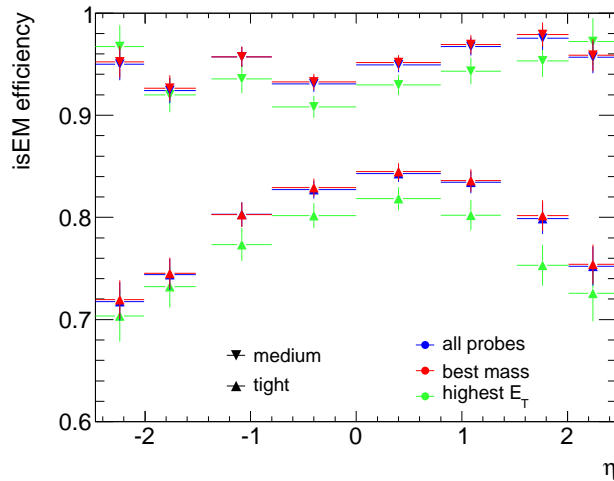


Figure 5.10: Medium and tight identification efficiencies in data from Z tag-and-probe, using all tags and probes in the event in blue (default), choosing the tag and probe pair with the invariant mass closest to the Z mass in red and choosing the two highest E_T electrons in green.

Finally, an additional systematic uncertainty deduced from a closure test performed on background and signal Monte Carlo is considered [81]. This uncertainty is added linearly to the systematic uncertainty derived from the variations of the method as described above. Since the worst case scenario from the closure test is used, this increases the total systematic uncertainty of the η dependent scale factors to about 3-4%.

Combination with W tag-and-probe

The medium and tight identification efficiency scale factors used to correct the simulated data in physics analyses is a combination of Z and W tag-and-probe results. Note that the efficiencies themselves are more difficult to combine due to slight intrinsic differences between $W \rightarrow e\nu$ and $Z \rightarrow ee$ events. The resulting scale factors as a function of η , for both methods, with their statistical and systematic uncertainties are shown in Figure 5.11. The Z tag-and-probe scale factors show a clear trend of higher values of around one percent compared to the W tag-and-probe scale factors. One reason for this could be that the W measurement includes the charge mis-identified electrons, while this is not the case for the Z due to the opposite charge requirement. As was discussed above, the charge mis-identified electrons are of lower quality and hence yield lower identification efficiency values. This is seen in both data and MC, but leads to additional uncertainties from the possibility of having a larger amount of charge mis-identified electrons in data than in MC, resulting in lower scale factors.

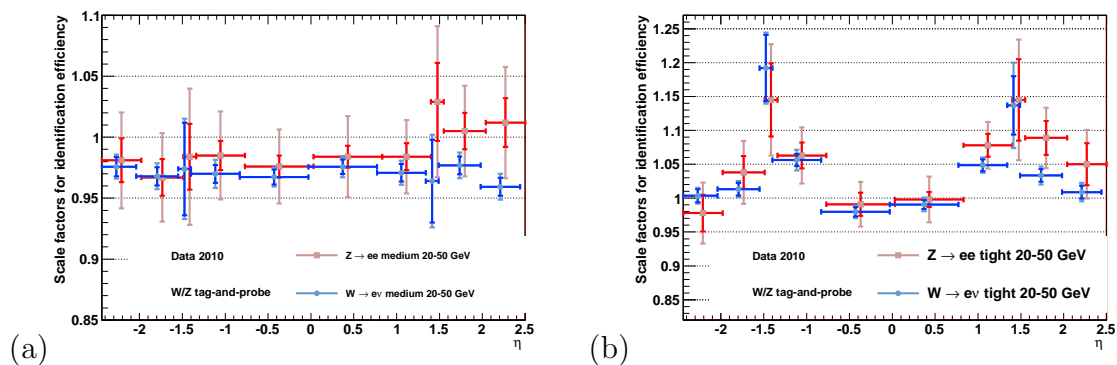


Figure 5.11: Resulting W and Z tag-and-probe efficiency data/MC scale factors for (a) medium and (b) tight identification. The scale factors are obtained with probes with 20-50 GeV transverse energy [81].

To combine the results, the W and Z scale factors are weighted by their individual uncertainties and the total uncertainty is propagated accordingly. For the η bin [1.52,2.01], the estimated combined uncertainty is not compatible with the separate

W and Z scale factors and an additional uncertainty of half the difference between the two measurements is applied. The final combined η dependent scale factors for medium and tight identification are shown in Figure 5.12, for both the typical W/Z energy range of $20 < E_T < 50$ GeV as well as the “plateau” energy range of $30 < E_T < 50$ GeV to be used by higher energy electron analyses.

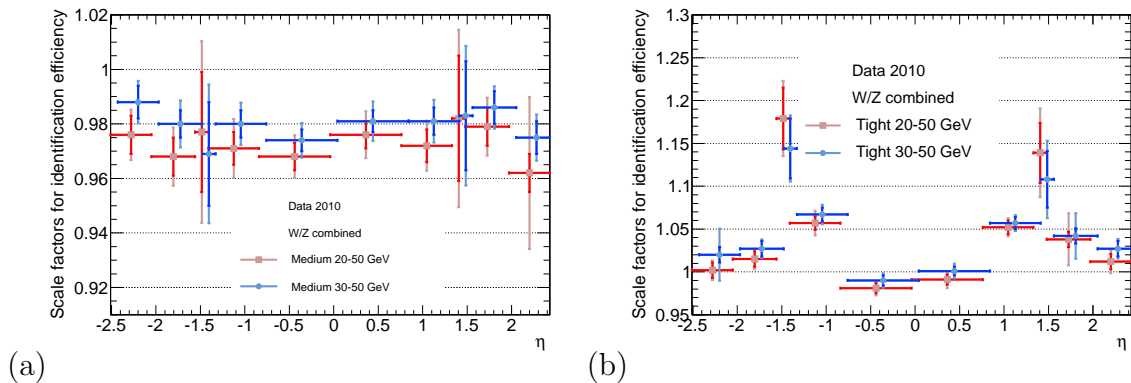


Figure 5.12: Final data/MC efficiency scale factors for (a) medium and (b) tight identification. The results are acquired from combining scale factors from W and Z tag-and-probe, with probes in the transverse energy range of 20-50 GeV (red) as well as 30-50 GeV (blue) [81].

5.4 E_T dependent efficiencies

As was mentioned above, the limited statistics in 2010 data requires E_T and η dependent efficiencies to be assessed separately. For analyses concerning W and Z bosons decaying into electrons, it is not necessary to apply the E_T dependent efficiency scale factors once the η dependent SFs have been applied. This is due to the equivalence of the energy range between the tag-and-probe and physics analysis electrons. Only analyses using on average higher or lower E_T electrons are required to correct the simulated data for both the η and the E_T efficiency differences with data. This is not the case for the SM analyses presented in the following chapters of this thesis. The E_T dependent scale factors are nonetheless included here for completeness. For a more detailed description and results for E_T dependent efficiencies and scale factors consult [57, 81].

The OS-SS sideband background subtraction method, developed for measuring efficiency as a function on η , assumes the shape of the background to be linear over the invariant mass range. This assumption breaks down for higher E_T bins where the background rather peaks in the signal region. Other background subtraction methods

must therefore be considered and two methods that make use of a fit are presented here. The default method, used to derive the official e/γ SFs, fits the invariant mass spectrum in the different E_T bins. The second method, which is used as a cross check, fits the E_T spectrum directly to extract the background as a function of E_T . Fitting methods are more statistically dependent than the OS-SS sideband method, which simply counts number of events, and it is thus more difficult to obtain reliable results.

The official e/γ E_T dependent scale factors, which are outlined in 5.4.3, are provided with respect to track quality cuts in order to combine W and Z results. No scale factors have, however, been derived for E_T dependent reconstruction or track quality efficiency with 2010 data. The E_T dependent results shown here, therefore instead present the author's own work on the efficiencies and scale factors for the standard identification cuts with respect to container, obtained with Z tag-and-probe.

5.4.1 Efficiency vs E_T measured by fitting M_{ee}

The 2010 statistics are fully sufficient to fit the Z invariant mass spectrum integrated over all E_T bins. The distribution is fitted using RooFit with a Breit-Wigner convoluted with a Crystal Ball⁵ as signal probability density function (PDF). Since the majority of the electrons are at lower E_T the background is well described by an exponential function. The invariant mass distribution is then simultaneously fitted with the signal and background function to obtain the global PDF:

$$\text{PDF}(M_{ee}) = N_{Sig} \cdot \text{PDF}(M_{ee})_{Sig} + N_{Bkg} \cdot \text{PDF}(M_{ee})_{Bkg}, \quad (5.7)$$

where, N_{Sig} and N_{Bkg} are the number of signal and background events found by the fit. Figure 5.13 shows the invariant mass together with the fit for the different identification levels (container, loose, medium and tight) for probes outside the crack region and with opposite sign as the tag. All four fits have a $\chi^2/Ndof$ of about 1.4.

The fraction of background estimated by the fitting method can then be assessed for different invariant mass ranges and the case of $80 < M_{ee} < 100$ GeV is presented in Table 5.12. The uncertainty of the background fraction is propagated from the uncertainty of the fit. Due to the very small background at medium and especially tight level, the uncertainty is large compared to the estimated background. Comparing the amount of background at medium and tight level in Table 5.12 shows that the background fraction at tight level is clearly overestimated, since the fit finds compatible background for medium and tight although the tight background rejection is notably higher than for medium. Due to the small values, however, this has little effect on the final efficiencies. The uncertainty of the background estimated at container level has a much higher impact on the efficiency measurements due to the significantly

⁵A Crystal Ball function is a Gaussian PDF with an exponential tail

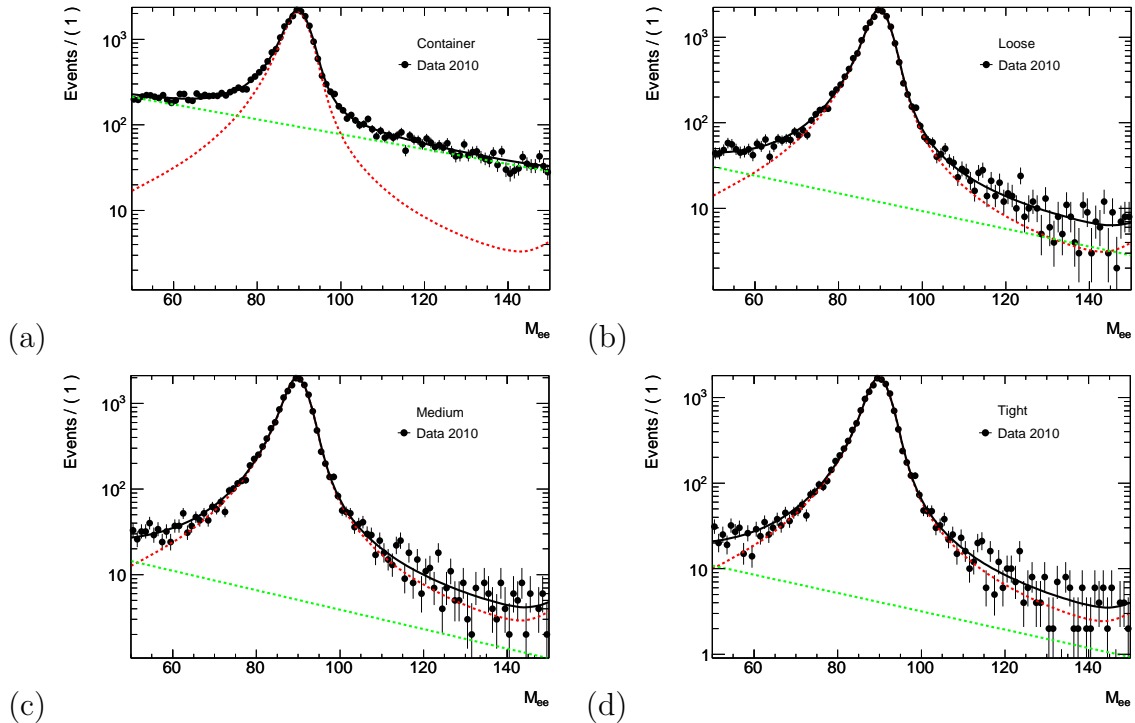


Figure 5.13: The fitted invariant mass distributions in data for opposite sign tag and probe pairs integrated over all E_T and η regions (except the crack) at (a) container, (b) loose, (c) medium and (d) tight level. The red line shows the signal fit, the green line shows the background fit and the black line shows the global fit. $\chi^2/Ndof = 1.4$ for all four fits.

larger background. The values obtained at container, medium and tight level can be compared with the overall background estimated with the OS-SS sideband method, shown in Table 5.8. The results agree within the uncertainties.

ID level	Background [%]
Container	9.92 ± 0.76
Loose	1.40 ± 0.78
Medium	0.64 ± 0.81
Tight	0.60 ± 0.89

Table 5.12: Resulting background fraction and statistical uncertainty obtained through fitting the invariant mass at the different identification levels for opposite signed tag and probe pairs within $80 < M_{ee} < 100$ GeV.

Subtracting the estimated background at each level allows for the overall identification efficiencies and data/MC scale factors to be calculated. The results are documented in Table 5.13. Comparing the values with the overall scale factors estimated through the OS-SS sideband background subtraction method (Table 5.10), shows an overall agreement within the statistical uncertainties between the two methods. Note, however, that the scale factors obtained with the fitting method are for efficiencies with respect to container while Table 5.10 shows results with respect to track quality cuts. This effect on the scale factors is however small since the track quality cut itself has been estimated to be well described in MC. Another observation that can be made from the tables is that the uncertainties from the fitting method are 3-4 times larger than for the OS-SS sideband method, originating from the large uncertainty of the fit.

[%]		Efficiency	Data/MC scale factor
Loose ID	Data	97.27 ± 1.16	98.80 ± 1.18
	MC truth	98.45 ± 0.01	
Medium ID	Data	92.00 ± 1.09	98.34 ± 1.16
	MC truth	93.56 ± 0.02	
Tight ID	Data	78.69 ± 0.91	102.52 ± 1.19
	MC truth	76.75 ± 0.03	

Table 5.13: Loose, medium and tight identification efficiencies, integrated over E_T , with respect to container for Z tag-and-probe applied to data, MC truth and their data/MC scale factor. The data-driven efficiencies are obtained with fitting the invariant mass spectrum for all tag and probe pairs with opposite sign, within $80 < M_{ee} < 100$ GeV and outside the crack region.

To estimate an efficiency binned in E_T , the invariant mass distribution must be fitted for each bin in order to assess the background for each bin. The shape of the background changes for higher E_T bins and the exponential distribution is no longer satisfactory. A second order Chebychev polynomial is thus used for $E_T > 40$ GeV. Figure 5.14 shows two example fits for container level probes for the [25,30] GeV and the [45,50] GeV range. It is clear from the figure that both the amount of background and the shape of the background strongly depends on the E_T range of the probes.

The fit is problematic in some E_T regions with little statistics, especially for medium and tight level with miniscule background. For lower E_T bins, the number of events in the tail at high invariant mass are very scarce, which imposes difficulties on the background fit. This affects the stability of the results and the fit does often not converge at tight level.

The largest uncertainty, however, originates from the denominator level, where background is significantly increased. Figure 5.15 shows the estimated background

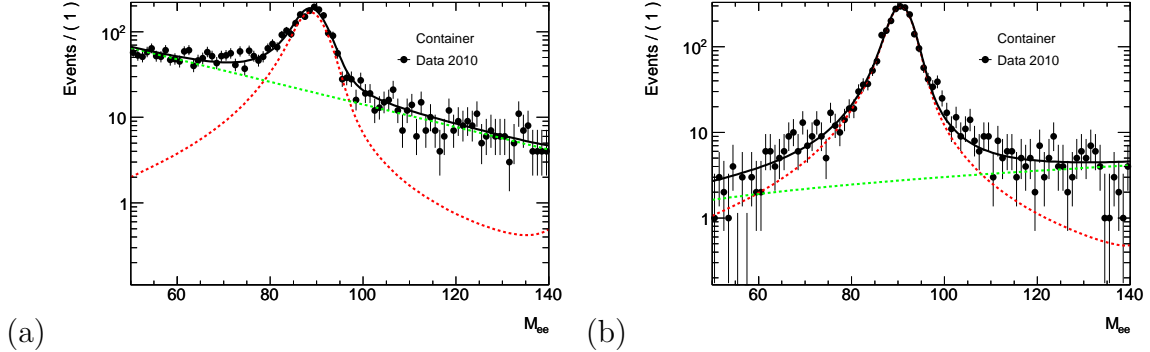


Figure 5.14: Fitted invariant mass distribution for tag and probe pairs with the probe at container level in data for opposite sign pairs, for (a) $25 < E_T < 30$ GeV and (b) $45 < E_T < 50$ GeV. The red line shows the signal fit, the green line shows the background fit and the black line the global fit. The background shape for the invariant mass distribution changes throughout the probe E_T spectrum.

fraction from the fit, for the different E_T bins, at container and loose level. The estimated background fractions for medium and tight identification level are negligible compared to container and loose level. The background fractions with errors estimated from the fit at all identification levels are documented in Table B.5 in Appendix B.

After the estimated background has been subtracted in each bin, the E_T dependent efficiencies are calculated. These are displayed in Figure 5.16 together with MC true efficiencies. The data-driven efficiencies show an increase of the efficiency for the lowest E_T bin. There is a large uncertainty in this region due to the large background and low signal statistics. The method overestimates the amount of background at denominator level and consequently also the efficiency of this bin.

The data-driven efficiencies as well as the data/MC scale factors, obtained with the method of fitting the invariant mass, are explicitly stated in Table B.6 in Appendix B for the different E_T ranges.

5.4.2 Efficiency vs E_T measured by fitting the E_T distribution

As an alternative to using the invariant mass distribution as the discriminating variable to subtract the background from the probe sample, one can fit the E_T distribution directly in order to obtain the background as a function of E_T . The results can then be used as a cross check for the E_T binned efficiencies derived through fitting the invariant mass of the Z boson. The background estimation using the E_T spectrum is performed with the template method using TFractionFitter. Tag and probe pairs with opposite sign electrons outside the crack region and with an invariant mass of

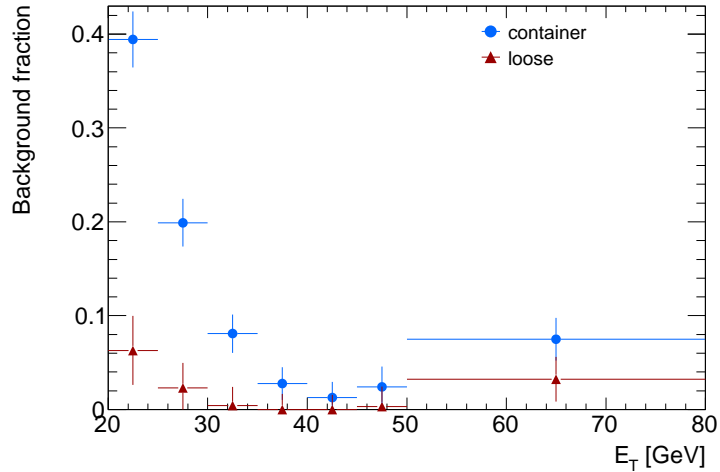


Figure 5.15: The background fraction as a function of E_T , at container and loose level, estimated by fitting the invariant mass of the tag and the probe for each E_T bin.

80-100 GeV are used for the efficiency extraction.

The background template is extracted from probes in the data. In order to minimize signal contamination in the background distribution, the tag requirement is relaxed to loose identification and only events where the probe has same sign as the tag are used. No invariant mass requirement is applied here. The trigger requirement for the background template must be altered from the standard EF_e15_medium to EF_e20_loose due to the relaxation of the tag requirement from tight to loose. EF_e20_loose has a small inefficiency for lower E_T values (20-25 GeV), which introduces a bias on the E_T shape for the background template. Another caveat is that the background shape at container level is also applied for the loose fit, since acquiring a background template at loose level is prevented by the significant signal contamination. The distribution used as background template is shown in Figure 5.17.

The different shapes used as signal templates are taken from signal MC at container, loose, medium and tight level after having applied loose truth matching to the probe in order to avoid any combinatorial background. The signal templates at the different levels are presented in Figure 5.18.

Due to the low statistics together with the minimal background fraction, the fit does not converge at the medium and tight level. Instead, rejection factors are applied to the estimated loose background. Background rejection factors are calculated by estimating the fraction of background events passing the electron identification criteria. The jet rejection factors applied to the estimated loose background are $R_{loose}^{medium} = 0.1286 \pm 0.0004(\text{stat})$ and $R_{loose}^{tight} = 0.0313 \pm 0.0001(\text{stat})$.

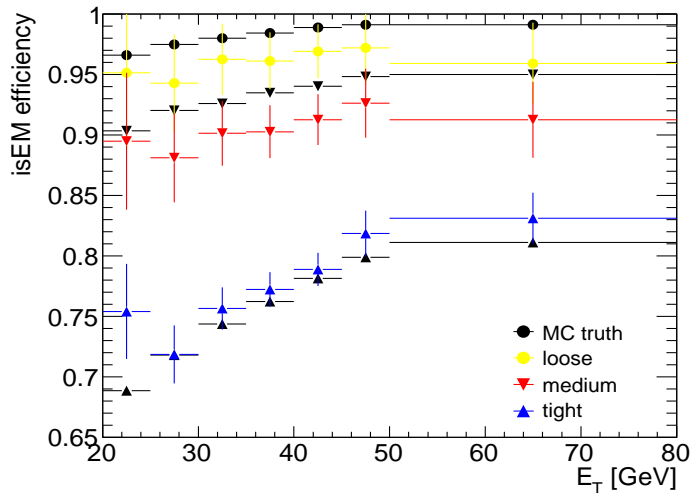


Figure 5.16: The efficiency as a function of E_T for loose, medium and tight identification, in MC truth (black) and estimated in data (color) by fitting the invariant mass for each E_T bin in order to subtract the background at each level.

The resulting fits at container and loose level are shown in Figure 5.19. A total of $9.2 \pm 0.6\%$ background at container level and $0.6 \pm 0.6\%$ at loose level are measured. The χ^2/DoF of the fits are low; 1.2 for the container fit and 1.1 for the loose fit. Comparing with the method of fitting the invariant mass as background estimation method (see section 5.4.1 above), these results show a 0.8% smaller background at container and loose level.

The background fraction is then computed separately for each E_T range in the efficiency binning presented in Table 5.2. The background fraction in the desired binning for container and loose level can be found in Figure 5.20. Comparing with the background estimation with the previously described method of fitting the invariant mass (Figure 5.15) shows that even though the E_T fit finds smaller amounts of background at loose and container level, there is a fair agreement of the behavior of the background as a function of E_T .

The background fraction at tight and medium level are estimated by applying the jet rejection factors on the result from the fit on the loose probes and results in $0.1 \pm 0.1\%$ and $0.0 \pm 0.0\%$ for the total medium and tight background respectively. For an overview of the amount of estimated background in each E_T bin at the different levels consult Table B.7 in Appendix B.

The efficiencies are then calculated through subtracting the estimated background at each level and for each E_T bin. The overall efficiencies obtained are $97.1 \pm 0.8\%$ for loose, $91.6 \pm 0.6\%$ for medium and $78.4 \pm 0.5\%$ for tight identification. The

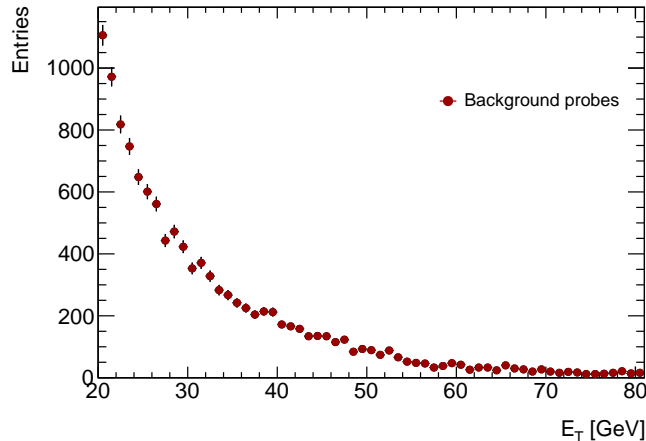


Figure 5.17: Background template extracted from data; container probes in events with a loose tag. A same sign requirement on the tag and probe is applied.

results are compatible with the efficiencies estimated using the method of fitting the invariant mass (see Table 5.13). The efficiencies as a function of E_T in data together with MC true efficiencies are shown in Figure 5.21. The behavior of the efficiency for low E_T follows the one observed with the main fitting method even though the two methods are largely uncorrelated. What is common between the methods is that the lower E_T bins suffer from a large uncertainty due to low signal statistics and increasing fraction of background, especially at container level. The inconsistency with MC is however larger for this method. One possible explanation is that the background template is acquired with the EF_e20_loose trigger which has a few percent inefficiency for the 20-25 GeV range. Except for the two bins at lower E_T , the method provides a reasonable efficiency estimate, which follows the shape in the MC. Table B.8, Appendix B, documents the data efficiencies together with the data/MC scale factors for each E_T range.

An evaluation of the systematic uncertainty is performed through altering the method and the fit conditions in different ways. One variation and cross check is to apply the electron energy scaling in data and energy smearing in MC. This has little effect on the data/MC SFs (see Table 5.14). Larger effects are seen if the histograms are re-binned before performing the fit. Another method is to widen the invariant mass spectrum from 80-100 GeV to 75-105 GeV, which also has a notable impact, especially on the loose scale factor.

To summarize, the efficiency scale factors as a function of electron E_T , from fitting the E_T spectrum directly, are in reasonable agreement with, and provide a cross check for, the main method of fitting the invariant mass spectrum of the Z . This method is, however, less stable than the M_{ee} fitting method. A few of the concerns are:

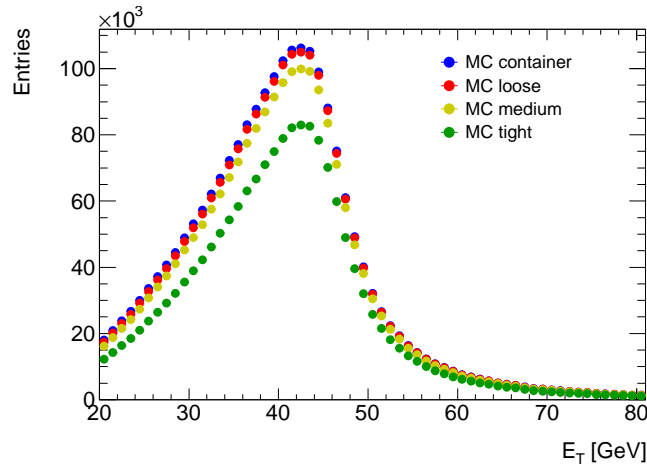


Figure 5.18: Signal templates obtained from MC; the E_T distribution of loosely truth matched probes at the different identification levels.

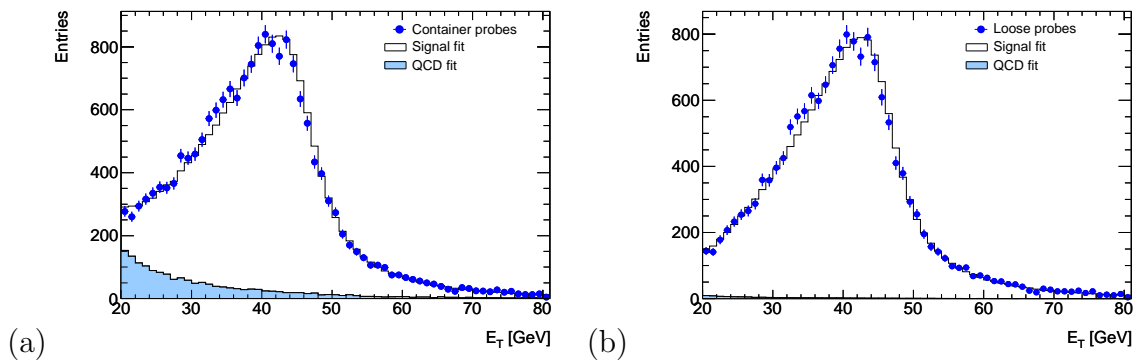


Figure 5.19: Resulting E_T fits at (a) container and (b) loose level. The QCD and signal templates are stacked and normalized to the data that is fitted.

- The method shows unstable results in the lower E_T region (20-30 GeV), possibly due to the trigger used for the background template (EF_e20_loose), which may bias the shape at lower E_T .
- Monte Carlo is used as the signal template and may not perfectly model the data distribution.
- The method suffers from instability due to low statistics, e.g. no background is found at medium and tight level and must be extrapolated from the loose fit. This can induce a bias since the background shape as a function of E_T might not be compatible at loose and medium/tight level.

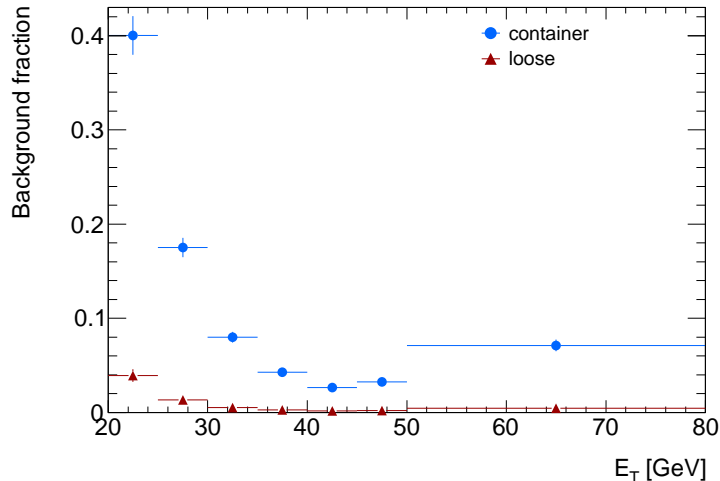


Figure 5.20: Fractional QCD background in the desired efficiency binning as a result of the E_T fit at container and loose level.

Efficiency SFs [%]	Nominal selection	Energy scaling/smearing	re-binning the histogram	$75 < M_{ee} < 105$ GeV
Loose SF	98.6 ± 0.8	-0.1	+1.1	+1.1
Medium SF	97.9 ± 0.7	-0.1	+1.2	+0.4
Tight SF	102.1 ± 0.7	-0.3	+1.2	+0.1

Table 5.14: Estimated overall loose, medium and tight efficiency through fitting the E_T spectrum to assess the amount of background to subtract. The method is varied by applying energy scaling and smearing, re-binning the template histograms before the fit as well as altering the invariant mass region of the tag and the probe pair.

This method provides a cross check for the M_{ee} fit method, which is used to derive the official e/γ E_T dependent efficiency scale factors [81].

5.4.3 Official e/γ ID efficiency scale factors

The E_T dependent identification efficiency scale factors, provided by the e/γ group, uses the method of fitting the invariant mass for the Z tag-and-probe [57, 81]. The computed scale factors are estimated with different variations of the standard RooFit method described above, also including a template method for fitting the invariant mass distribution. As for the η dependent scale factors, the e/γ efficiencies are measured with respect to track quality rather than container in order to combine the

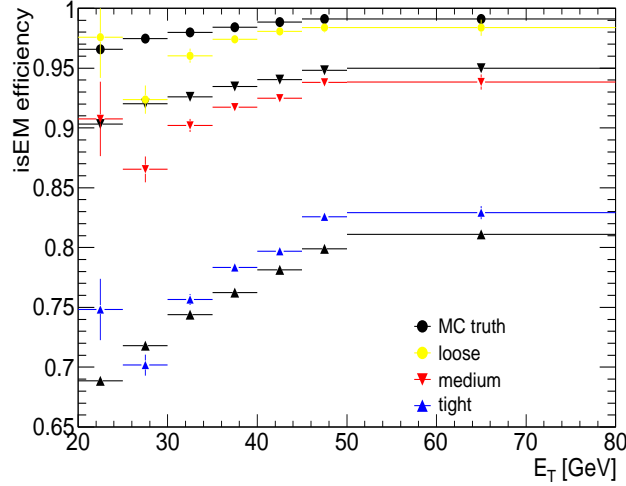


Figure 5.21: Loose, medium and tight identification efficiencies from MC truth (black) and data (color), fitting the E_T spectrum as QCD background estimation method.

results with W tag-and-probe. Variations are made on the signal region, fit range and tag requirements to obtain a distribution of scale factors where the mean yields the central value and the spread the systematic uncertainty. The estimated systematic uncertainty increases towards lower E_T , as expected, since these bins have less signal events and a larger background contamination. In addition, a systematic uncertainty from a MC closure test, showing a bias of the estimated number of signal events from the fits, is added linearly.

The resulting Z and W tag-and-probe efficiency scale factors are shown in Figure 5.22 for medium and tight identification. As for the η dependent scale factors, Z tag-and-probe yields higher values than the W tag-and-probe results. Another difference is that W tag-and-probe displays a stronger E_T dependence with decreasing scale factors for lower E_T . The 15-20 GeV E_T range is also included in the W tag-and-probe results due to the more abundant statistics.

The final combined W and Z tag-and-probe results for medium and tight identification scale factors are shown as a function of E_T in Figure 5.23. The statistical and total uncertainties are indicated.

5.5 Electron trigger efficiency

Measuring the electron trigger efficiency with respect to the offline selection with Z tag-and-probe is less complicated than measuring the identification efficiency, due to the much smaller background at the denominator level of the measurement. As

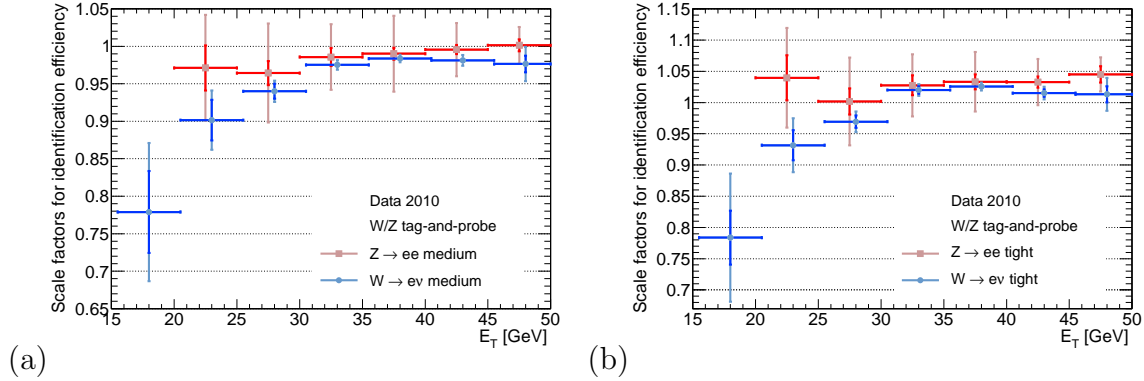


Figure 5.22: Resulting W and Z tag-and-probe efficiency data/MC scale factors for (a) medium and (b) tight identification as a function of electron E_T . The plots display the statistical (clear colors) and total uncertainties (faint colors) for the individual measurements [81].

was described in the methodology section 5.2.1, the tag is matched to the same trigger as the event is required to pass in order to keep the probe unbiased. For 2010 data, the standard electron triggers used are L1_EM14 for data period A-E3 and EF_e15_medium for period E4-I. The probe is then used for measuring the efficiency of an electron firing a specific trigger for an offline electron passing all other selection cuts. The probe is thus matched to the trigger of interest.

The trigger efficiency is calculated according to

$$\epsilon_{trig} = \frac{N_e(\text{passing trigger})}{N_e(\text{tight or medium})}. \quad (5.8)$$

The denominator of the trigger efficiency measurement is defined by the number of electron probes passing medium or tight identification (equivalent to the numerator for identification efficiency measurements). At this level, as was concluded in the previous sections of this chapter, the background is less than the percent level. The numerator of the trigger efficiency is the number of probes matched to the trigger. The background at the trigger efficiency numerator level is compatible with the denominator level. Background subtraction is therefore not applied for the trigger efficiency calculation.

This methodology is used for the W/Z cross section measurements, calculating the trigger efficiency for L1_EM14 and EF_e15_medium with respect to medium for Z analyses and tight for W analyses. The results are shown in Figure 5.24 as a function of η and E_T . The trigger efficiencies obtained with Z tag-and-probe in data are overlaid with the MC trigger efficiencies. Since no background subtraction is applied, bayesian statistical errors can be assigned.

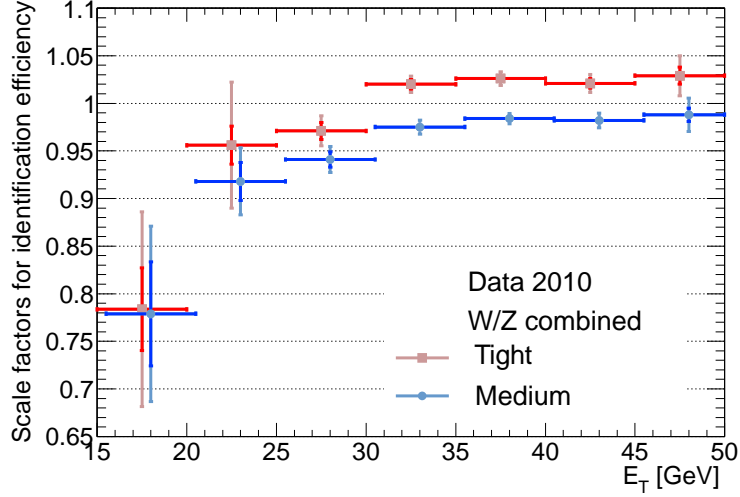


Figure 5.23: Final data/MC E_T dependent efficiency scale factors for medium and tight identification. The results are obtained from combining scale factors from W and Z tag-and-probe. The plot displays the statistical (clear colors) and total uncertainties (faint colors) for the individual measurements [81].

Table 5.15 summarizes the overall values for the data-driven trigger efficiencies and data/MC scale factors. The L1_EM14 trigger has, as expected, a high efficiency for an electron with transverse energy above 20 GeV. A slight turn-on curve is seen in Figure 5.24b, but no large η/E_T dependence. The EF_e15_medium has slightly lower efficiency overall, although still close to 100%. Here, the turn-on curve towards lower E_T is even smaller than for L1_EM14, since EF_e15_medium is seeded by L1_EM10 and the energy threshold is thus lower. Both triggers have been found to have slightly lower efficiency in data than in Monte Carlo.

Trigger efficiency with respect to	[%]	L1_EM14	EF_e15_medium
medium ID	data eff	99.64 ± 0.05	98.71 ± 0.09
	data/MC SF	99.76 ± 0.05	99.34 ± 0.09
tight ID	data eff	99.64 ± 0.05	98.93 ± 0.08
	data/MC SF	99.76 ± 0.05	99.50 ± 0.08

Table 5.15: Overall trigger efficiencies and data/MC scale factors for the L1_EM14 and EF_e15_medium trigger with respect to offline medium and tight electron identification.

The official trigger efficiency data/MC scale factor for physics analyses, provided

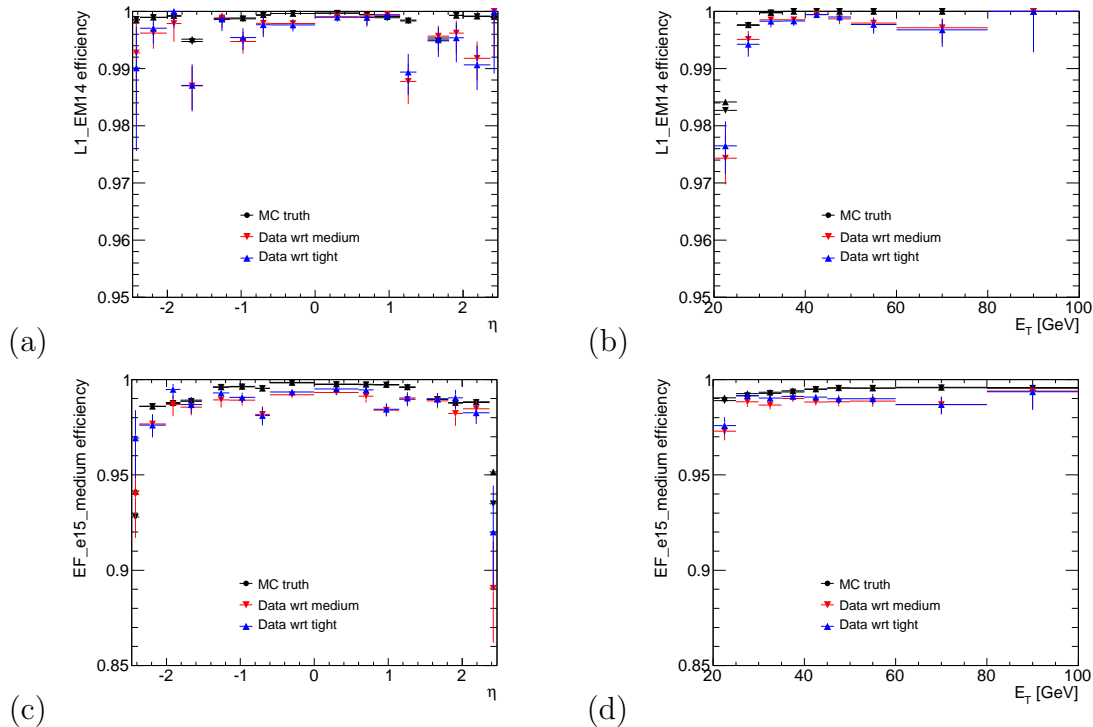


Figure 5.24: Trigger efficiency for L1_EM14 ((a) and (b)) and EF_e15_medium ((c) and (d)) measured with Z tag-and-probe, with respect to medium and tight offline electrons. The colors display the data results while the black shows the true efficiencies from Monte Carlo.

by the e/γ group, is an overall value of $99.5 \pm 0.4(\text{stat+syst})\%$ for EF_e15_medium [57, 81]. This is applied to the R16 W and Z analyses in order to correct for the trigger efficiency, since L1_EM14 only corresponds to about 2% of the data and has a scale factor close to unity.

A separate note on e/γ triggers performances has been produced (see [87]) that includes the trigger efficiency measured with Z tag-and-probe. The document serves as a supporting note for [88] as well as [57].

5.6 Conclusion

The electron reconstruction, identification and trigger efficiencies have been successfully measured with the Z tag-and-probe method on 2010 data. The results have been measured as a function of η and E_T of the electron. The data-driven efficiencies have been compared to true electron efficiencies from Monte Carlo in order to produce data/MC scale factors, which are applied in different physics analyses to correct the

simulated data.

The official e/γ scale factors for medium and tight identification efficiencies are a combination of Z and W tag-and-probe results and are measured with respect to initial track quality cuts, in order to avoid non-collision background in the W tag-and-probe measurement. The efficiency scale factor of the track quality cut itself is measured as part of the reconstruction efficiency, calculated with Z tag-and-probe.

The overall data/MC scale factors for the reconstruction and trigger efficiencies of the electron have both been found to be close to unity, while the medium efficiency has been estimated to be lower in the data than in the MC due to broader shower shapes. The tight identification efficiency scale factor on the other hand has been found to be significantly higher than unity as well as displaying large fluctuations in η . Studies have shown that this is largely due to the cut on the ratio of high threshold hits in the TRT.

Chapter 6

$W \rightarrow e\nu$ and $Z \rightarrow ee$ Inclusive Cross Section Measurements with ATLAS 2010 Data

The first year of data-taking has been a period of intense physics analysis in order to produce the initial results with collision data as quickly as possible as the instantaneous luminosity of the LHC rapidly increased. To better understand the performance of the ATLAS detector and software, the 2010 data has predominantly been used to study the well known physics within the Standard Model. The production cross sections of the W and Z bosons are important measurements that are feasible with the first data. In fact, $W \rightarrow e\nu$ and $W \rightarrow \mu\nu$ were among the initial high transverse energy signatures that were observed in ATLAS and the $Z \rightarrow ee$ and $Z \rightarrow \mu\mu$ signatures followed. In addition, the W and Z bosons provide with the first sample of isolated high energy electrons, which can be used to study the electron performance, such as efficiencies, as was discussed in the previous chapter. The electron reconstruction, identification and trigger efficiencies, measured with W and Z tag-and-probe, are some of the most important ingredients for the $W \rightarrow e\nu$ and $Z \rightarrow ee$ cross section measurements. The efficiency errors are also some of the dominant sources of systematic uncertainties for the cross sections, as is presented in this chapter.

Here, the electron channel analysis is presented in detail. However, the equivalent studies have been performed in the muon channel and the final electron and muon combined results are included in this chapter, with references to the notes and papers where the analyses are documented.

The cross section results are calculated in the fiducial phase space, corresponding to the geometrical and kinematic acceptance of the detector and are then corrected to the full phase space using generator predictions. The advantage of the fiducial

Data (\mathcal{L}^{-1})	Analysis	Documentation
7 nb ⁻¹	First observation of 17 $W \rightarrow e\nu$ and one $Z \rightarrow ee$ candidate(s)	Conference note for PLHC 2010: [89] and supporting notes: [90, 91]
17 nb ⁻¹	First cross section of $W \rightarrow e\nu$ and observation of $Z \rightarrow ee$ events	Conference note for ICHEP 2010: [92] and supporting notes: [93, 94]
225 nb ⁻¹	First $Z \rightarrow ee$ cross section measurement	Conference note for ICHEP 2010: [95]
315 nb ⁻¹	$W \rightarrow e\nu$ and $Z \rightarrow ee$ cross section and W charge asymmetry	Published paper: [96] and supporting notes: [97, 98, 99]
38 pb ⁻¹	$W \rightarrow e\nu$ and $Z \rightarrow ee$ cross section measurements	Conference note for Moriond 2011: [100] and supporting note: [101]
38 pb ⁻¹	$W \rightarrow e\nu$ and $Z \rightarrow ee$ total and differential cross sections	Published paper: [102] with supporting note: [103]

Table 6.1: The inclusive W and Z observation and cross section analyses completed with different integrated luminosity corresponding to parts, or all, of the 2010 7 TeV data.

cross section measurement is the minimal dependence of the correction procedure on the theoretical models used in the Monte Carlo simulation needed to derive the acceptance corrections.

This chapter commences with describing the $W \rightarrow e\nu/Z \rightarrow ee$ event selection and the cross section analysis procedure in section 6.1. The author has been closely involved in all of the W/Z inclusive analyses completed with different amounts of data throughout the 2010 data taking. However, due to space limitations of this thesis, the first W/Z observation and cross section results are only briefly summarized in section 6.2. Section 6.3 discusses in detail the final W^\pm , W^+ , W^- and Z^0 , inclusive and differential ($d\sigma(W)/d\eta^e$ and $d\sigma(Z)/dy^Z$) cross section measurements using the full 2010 dataset. Throughout the chapter, the “ Z ” notation implicitly implies “ Z/γ^* ”, since the Drell-Yan component is included in the measurement. The Drell-Yan contribution is however small in the invariant mass window of 66 to 116 GeV, where the measurement is carried out.

Table 6.1 lists the inclusive W/Z analyses completed during 2010 and in which manner the results have been documented. The listed notes and papers also include equivalent results in the muon channel to those presented here in the electron channel.

Inclusive W and Z cross section measurement results have also been published by the CMS collaboration in [104].

6.1 W/Z cross section analysis methodology

6.1.1 Data and Monte Carlo samples

Since this chapter aims to summarize the different results produced during the course of 2010 data-taking, different datasets are also included. The first cross section results were obtained with less than 1 pb^{-1} of data that were collected during period A-D (see Table A.1 in Appendix A). A conference note and a paper were later completed presenting results including the full 2010 data (period A-I). More detailed information is provided in the sections below.

Simulated Monte Carlo samples are used for acceptance calculations as well as to model the signal and background properties. The samples are generated using PYTHIA and POWHEG, with MRST LO* [105] as parton distribution functions, as well as MC@NLO¹. The simulation of the particles' response in the ATLAS detector is achieved with GEANT4. Table 6.2 lists the simulated samples used for this analysis together with their theoretical cross sections. These values are calculated at NNLO using FEWZ, with the exception of the QCD sample where the LO PYTHIA value is used. PYTHIA is used for modeling the signal process for all results except for the final published 2010 data results, where MC@NLO is used as the baseline MC.

The data and Monte Carlo samples, used for obtaining the results including only part of the 2010 data, are consistently produced using Athena release 15. The samples used for the analyses including the full 2010 data are re-processed with release 16.

Pile-up simulation and re-weighting

The amount of pile-up in collision events increases rapidly with the instantaneous luminosity delivered by the LHC as was described in section 5.2.1. The first W and Z observation results are compared with simulated data without any pile-up (only one primary vertex per event). The results in the W/Z cross section paper including the first 315 nb^{-1} of recorded data, use *in-time pile-up* MC, which increases the number of vertices in the event. The reconstructed vertex multiplicity in data and MC are compared and the MC is re-weighted to match the dataset.

For the W/Z cross section analysis using the full 2010 data, most data analyzed contains a significant number of bunches in the beam and thus *bunch-train pile-up* MC is used. The weights, which correct the primary vertex multiplicity in MC to

¹For further details on MC generators see section 2.3

Physics process	Generator	$\sigma \cdot \text{BR}$ [nb]	
$W \rightarrow \ell\nu$ ($\ell = e, \mu$)	PYTHIA/MC@NLO	10.46 ± 0.52	NNLO
$Z/\gamma^* \rightarrow \ell\ell$ ($M_{\ell\ell} > 60$ GeV)	PYTHIA/MC@NLO	0.989 ± 0.05	NNLO
$W \rightarrow \tau\nu$	PYTHIA	10.46 ± 0.52	NNLO
$Z/\gamma^* \rightarrow \tau\tau$ ($M_{\tau\tau} > 60$ GeV)	PYTHIA	0.989 ± 0.05	NNLO
$t\bar{t}$	MC@NLO	0.16 ± 0.01	NLO+NNLL
WW	HERWIG	0.045 ± 0.003	NLO
WZ	HERWIG	0.0185 ± 0.0009	NLO
ZZ	HERWIG	0.0060 ± 0.0003	NLO
Dijet ($\hat{p}_T > 15$ GeV)	PYTHIA	1.2×10^6	LO

Table 6.2: Monte Carlo samples used for modeling the signal and background processes in the $W \rightarrow e\nu$ and $Z \rightarrow ee$ analysis. For each sample the production cross section, to which the samples are normalized, is given. For the electroweak and $t\bar{t}$ production, contributions from higher order QCD corrections are included, while the inclusive QCD dijet cross section is given at leading order. These samples are generated with requirements on the transverse momentum of the partons involved in the hard-scattering process, \hat{p}_T .

match the data, are calculated for $W \rightarrow e\nu$ events (before the E_T^{miss} and M_T cut) and are shown in Table 6.3.

The weights have also been calculated with the $Z \rightarrow ee$ selection to verify that the results are compatible. Comparing the event weights shown here with the ones obtained with the Z tag-and-probe selection in Table 5.4 yields no significant differences in the distribution.

6.1.2 W/Z event selection

The $W \rightarrow e\nu$ and $Z \rightarrow ee$ event selections show many similarities to the tag-and-probe selection described in section 5.2.1. Note that some of the selection requirements of the W/Z analyses have evolved during the 2010 data-taking period.

As for the Z tag-and-probe, the events must pass a “good run list” (**GRL**), contain a **primary vertex** with at least three tracks and pass a **trigger** requirement (L1_EM14 for data period A-E3 and EF_e15_medium for period E4-I). One (W) or two (Z) **electrons** must pass $E_T > 20$ GeV, $|\eta| < 2.47$ and be outside the calorimeter transition region ($1.37 < |\eta| < 1.52$) and the dead **OTx** regions. The transverse energy of the electron is obtained from the electron cluster energy and electron track pseudorapidity using $E_T = E/\cosh \eta$.

This level defines the “container” level in the selection of the W/Z electron analysis. Hereafter, the selection cuts for the W and Z differ.

N_{vtx}	Event weight
1	1.9601 ± 0.0041
2	1.2264 ± 0.0020
3	0.8527 ± 0.0016
4	0.6454 ± 0.0016
5	0.5283 ± 0.0020
6	0.4514 ± 0.0029
7	0.4205 ± 0.0051
8	0.4104 ± 0.0097
9	0.4195 ± 0.0207
≥ 10	0.5487 ± 0.0490

Table 6.3: Number of reconstructed primary vertices and correspondent pile-up weights for the W/Z electron analysis including the full 2010 dataset.

W selection

In addition, a **jet cleaning** cut is applied to the W selection to measure E_T^{miss} with sufficient accuracy. This cut rejects events where unphysical jets arising from detector effects, affect the measured E_T^{miss} . Such effects are typically due to noise bursts in the hadronic end-cap calorimeter or the EM calorimeter, and out-of-time energy depositions. The cleaning cut assures the reliability of jet reconstruction for jets with transverse momentum exceeding 20 GeV. The effect of this cut is small; only about 0.05% of the $W \rightarrow e\nu$ events are discarded. Further information on jet cleaning can be found in [106].

A **missing transverse energy** cut of 25 GeV can then safely be applied to the W candidate events. The E_T^{miss} algorithm used is “MET_LocHadTopo” [107]; an EM calorimeter cell-based algorithm which measures the energy deposited in topological clusters² corrected for different responses to hadrons, dead material losses and energy leakage in the clusters. For the final differential W analysis the recommendations from the Jet/EtMiss group were updated [108] and the “MET_RefFinal” algorithm was used to calculate the E_T^{miss} . This algorithm makes use of the full event reconstruction, with a calibration based on reconstructed physics objects (refined calibration).

The standard electron requirement for the $W \rightarrow e\nu$ analysis is **tight identification**. Due to the issues described in section 5.3.3, this selection is refined for the final differential W analysis where medium identification together with a requirement of a b-layer hit as well as an isolation cut is used.

To suppress background from $Z \rightarrow ee$ events, a **second electron veto** is applied if there is more than one medium electron in the event, passing all the other electron

²Topological clusters were discussed in section 4.4.5

cuts described above.

A final cut on the **transverse mass** of the W is applied; $M_T > 40$ GeV, where

$$M_T = \sqrt{2E_T^e p_T^\nu (1 - \cos(\phi^e - \phi^\nu))}, \quad (6.1)$$

where the energy of the electron is obtained from the cluster and the direction is acquired from the track.

Z selection

In addition to the container selection, at least two of the electrons must pass **medium identification** requirements. If there are more than two medium electrons in the event, which occurs in less than one per mille of the Z events, the two highest E_T electrons are chosen.

The two electrons are required to have **opposite charge** as well as an **invariant mass** within 66-116 GeV.

6.1.3 Cross section calculation

Once the final W and Z candidates have been selected, the total cross section for each of the bosons can be extrapolated through the cross section formula:

$$\sigma_{tot} = \sigma_{W/Z} \times BR(W/Z \rightarrow e\nu/ee) = \frac{N - B}{A_{W/Z} \cdot C_{W/Z} \cdot L_{int}}, \quad (6.2)$$

where

- N is the number of W or Z candidates measured in data,
- B is the number of estimated QCD and electroweak background events,
- L_{int} is the integrated luminosity corresponding to the dataset and trigger selections,
- $A_{W/Z}$ and $C_{W/Z}$ are factorized acceptances, defined below. In the analysis with the full 2010 data, $C_{W/Z}$ is corrected for any discrepancy in electron energy scale or efficiency between data and Monte Carlo.

Fiducial cross section and generator acceptance $A_{W/Z}$

The more precise fiducial cross section is obtained through applying equation 6.2 without correcting for the acceptance ($A_{W/Z} = 1$). The cross section is hence estimated within the fiducial phase space, which mirror the kinematic selection at reconstruction level, discussed in section 6.1.2:

$$\begin{aligned}
 W \rightarrow e\nu : \quad & p_T^e > 20 \text{ GeV}, |\eta^e| < 2.47 \text{ excluding } 1.37 < |\eta^e| < 1.52, \\
 & p_T^\nu > 25 \text{ GeV}, M_T > 40 \text{ GeV} \\
 Z \rightarrow ee : \quad & p_T^e > 20 \text{ GeV}, |\eta^e| < 2.47 \text{ excluding } 1.37 < |\eta^e| < 1.52, \\
 & 66 < M_{ee} < 116 \text{ GeV}
 \end{aligned}$$

The fiducial cross section can then be extrapolated to the total phase space through the acceptance terms ($A_{W/Z}$) estimated at generator level:

$$A_{W/Z} = \frac{N_{\text{MC,gen,cut}}}{N_{\text{MC,gen,all}}}, \quad (6.3)$$

where $N_{\text{MC,gen,cut}}$ is estimated at generated level after the fiducial cuts have been applied and $N_{\text{MC,gen,all}}$ is the total number of generated MC events. The invariant mass requirement of the Z is applied also for the denominator level of A_Z , such that the total cross section measurement is performed within this mass region. The motivation for this is that virtual photon exchange leads to an exponential increase in the cross section at lower values.

While the total cross section is calculated at Born level, i.e. correcting for all the QED Final State Radiation (FSR) effects, the fiducial cross section can be estimated with slightly different levels of QED FSR correction corresponding to different truth level definitions of $N_{\text{MC,gen,cut}}$:

- Using leptons *before QED FSR*, alias *Born level*, to perform a full QED correction. This is what is required for the combination of electron and muon channels.
- Using leptons *after QED FSR*, alias *bare leptons*, to perform no QED correction.
- Using a hybrid, alias *dressed leptons*, where 4-vectors of the *bare lepton* and all QED FSR photons within a $\Delta R < 0.1$ are re-summed to perform a partial QED FSR correction.

Defining the correction factor $C_{W/Z}$

The remaining acceptance terms, including reconstruction correction factors such as electron efficiencies, are included in:

$$C_{W/Z} = \frac{N_{\text{MC,rec}}}{N_{\text{MC,gen,cut}}}, \quad (6.4)$$

where $N_{\text{MC,rec}}$ is the sum of weights of events after simulation, reconstruction and selection and $N_{\text{MC,gen,cut}}$ equals the numerator level of the fiducial acceptance, $A_{W/Z}$. The correction factors $C_{W/Z}$ thus include the reconstruction, identification and trigger efficiency of the electron(s) for boson decays falling within the geometrical acceptance. $C_{W/Z}$ also incorporate selection requirements of minor impact, such as the primary vertex cut.

In addition, the charge separated W^\pm cross sections are measured and the C_W factor then suitably incorporates a correction for event migration between the W^+ and W^- samples:

$$C_{W^+} = \frac{N_{\text{MC,rec}^+}}{N_{\text{MC,gen}^+,\text{cut}}} \quad \text{and} \quad C_{W^-} = \frac{N_{\text{MC,rec}^-}}{N_{\text{MC,gen}^-,\text{cut}}}, \quad (6.5)$$

where $N_{\text{MC,rec}^\pm}$ and $N_{\text{MC,gen}^\pm,\text{cut}}$ are number of events reconstructed or generated as W^\pm , respectively, without any further charge selection. For example, $N_{\text{MC,rec}^+}$ includes a small component of charge mis-identified events generated as W^- , while for $N_{\text{MC,gen}^+,\text{cut}}$ no requirement on the reconstructed charge is made.

For the earlier measurements, most of the $C_{W/Z}$ components are estimated from Monte Carlo due to lack of statistics in data. For the full 2010 data cross section measurements, the simulated data is corrected for data-MC discrepancies evaluated with data-driven methods (for further details see section 6.3).

The inclusive cross section ratio measurement

As was described in chapter 2.2.3, the cross section ratio $\mathcal{R}_{W/Z}$ (as well as \mathcal{R}_{W^+/W^-}), is an interesting measurement due to full or partial cancellations of uncertainties, such as the complete cancellation of the luminosity uncertainty. The ratio measurement of the W and Z boson cross sections is given by

$$\mathcal{R}_{W/Z} = \frac{\sigma_W}{\sigma_Z} = \frac{\frac{N_{sig}^W}{A_W \cdot C_W \cdot \int L dt}}{\frac{N_{sig}^Z}{A_Z \cdot C_Z \cdot \int L dt}} = \frac{N_{sig}^Z}{N_{sig}^W} \cdot \frac{A_W}{A_Z} \cdot \frac{C_W}{C_Z}. \quad (6.6)$$

The relative uncertainty on \mathcal{R} is thus calculated from

$$\left(\frac{\Delta \mathcal{R}}{\mathcal{R}} \right)^2 = \left(\frac{\Delta N_{sig}^Z}{N_{sig}^Z} \right)^2 + \left(\frac{\Delta N_{sig}^W}{N_{sig}^W} \right)^2 + \left(\frac{\Delta A_{W/Z}}{A_{W/Z}} \right)^2 + \left(\frac{\Delta C_{W/Z}}{C_{W/Z}} \right)^2. \quad (6.7)$$

The first two terms in the above equation are purely statistical and uncorrelated. The last two terms require a specific and separate treatment since different correlations have to be taken into account in the ratio.

Differential W and Z cross section binning	
$ \eta^e $	0.0, 0.21, 0.42, 0.63, 0.84, 1.05, 1.37, 1.52, 1.74, 1.95, 2.18, 2.47
$ y^Z $	0.0, 0.4, 0.8, 1.2, 1.6, 2.0, 2.4, 2.8, 3.6

Table 6.4: Definition of $|\eta^\ell|$ and $|y^Z|$ binning for the W and Z differential cross section measurements respectively, completed with 2010 data.

Differential cross sections

The final cross section results obtained with the full 2010 data includes differential cross section results at the fiducial level. The W cross section is measured as a function of lepton pseudorapidity; $d\sigma_W/d|\eta^\ell|$, and the Z cross section is estimated as a function of boson rapidity; $d\sigma_Z/d|y^Z|$. The granularity for the differential measurement is determined considering the available statistics as well as the detector properties in case of $d\sigma_W/d|\eta^\ell|$. The chosen binning for the differential $W \rightarrow e\nu$ and $Z \rightarrow ee$ cross section is shown in Table 6.4.

6.2 First inclusive W and Z results with $< 1 \text{ pb}^{-1}$

Due to space limitations, the first cross section results are briefly summarized here to give room for further details concerning the more interesting and refined measurements completed with the full 2010 dataset, presented in section 6.3.

6.2.1 W/Z observation and cross section with the very first data

As was shown in Table 6.1, several observation and cross section results were rapidly produced as the data became available in spring and summer 2010. Since the statistics did not permit a precision measurement, the focus lay on producing robust results in an efficient manner and establishing the methodology for the larger statistics sample. The initial challenges of performing an analysis on real data for the first time in ATLAS included the understanding of the trigger, the definition of the GRL and the event selection criteria.

The first ATLAS W/Z result concluded the observation of 17 $W \rightarrow e\nu$ candidates and one $Z \rightarrow ee$ candidate obtained with 7 nb^{-1} (data periods A and B) [89, 90].

First cross section results

The first W cross section measurement was completed shortly after using a data sample of 17 nb^{-1} (data periods A-C) resulting in 46 $W \rightarrow e\nu$ events after full event selection [92, 93, 94]. The selection follows the description in section 6.1.2, applying tight electron identification, with the exception of using a lower energy trigger (L1_EM5), which was not pre-scaled at that stage. The QCD background is estimated to be approximately one event, using a semi data-driven template method with calorimeter isolation as the discriminating variable. The electroweak background as well as the electron efficiencies are estimated from MC. The resulting cross section measurement was:

$$\sigma_W \cdot BR(W \rightarrow e\nu) = 10.3 \pm 1.3(\text{stat}) \pm 0.8(\text{syst}) \pm 1.1(\text{lumi}) \text{ nb} \quad (6.8)$$

The uncertainty of the luminosity, determined from *van der Meer* scans, was at that stage 11%.

The first Z cross section results were produced using a data sample of 225 nb^{-1} collected the following week [95]. A total of 46 $Z \rightarrow ee$ candidates are observed after the full selection has been applied. The measured Z cross section is:

$$\sigma_Z \cdot BR(Z \rightarrow ee) = 0.72 \pm 0.11(\text{stat}) \pm 0.10(\text{syst}) \pm 0.08(\text{lumi}) \text{ nb}. \quad (6.9)$$

The resulting value is lower than the theoretical prediction (see equation 2.13). The measurement and the corresponding systematic studies are however very limited by the poor statistics.

The first W/Z cross section results were presented by the author at the joint MIT-Berkeley workshop in August 2010 [109].

6.2.2 W and Z cross section measurement with 315 nb^{-1}

By the end of summer 2010, ATLAS had collected an integrated luminosity of 315 nb^{-1} (data periods A-D). This allowed a more precise W/Z cross section measurement [96, 97, 98, 99].

All data and Monte Carlo samples were produced using Athena release 15. The simulated Monte Carlo samples used for acceptance calculations as well as to model the signal and background properties were generated using PYTHIA and POWHEG with MRST LO* as parton distribution functions.

The $W \rightarrow e\nu$ and $Z \rightarrow ee$ events were collected with trigger L1_EM10, which was estimated from data to be close to 100% efficient.

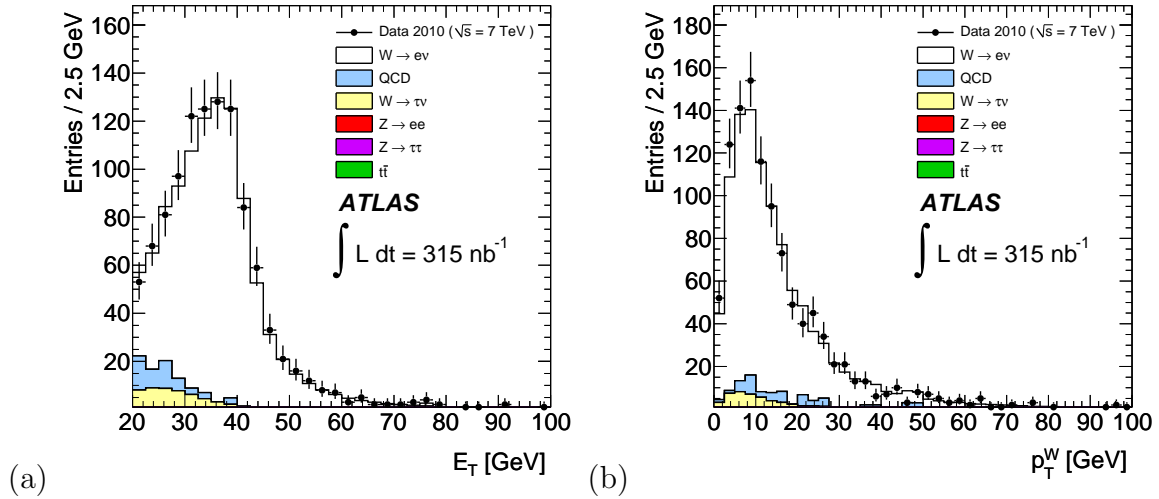


Figure 6.1: The (a) electron E_T and (b) W p_T for the $W \rightarrow e\nu$ candidates in 315 nb^{-1} of data. The data distribution is compared to Monte Carlo simulation, which is broken down into signal and various background components [96].

$W \rightarrow e\nu$ analysis

The $W \rightarrow e\nu$ selection applied to the first 315 nb^{-1} of data results in 1069 $W \rightarrow e\nu$ candidates (637 W^+ and 432 W^-). The transverse energy distribution of the electrons from the $W \rightarrow e\nu$ sample as well as the estimated p_T of the W boson are shown in Figure 6.1.

The QCD background is estimated by fitting the E_T^{miss} distribution with the template method after relaxing the E_T^{miss} cut. The background is then extrapolated for E_T^{miss} values above 25 GeV, which results in an estimate of 28 mis-identified QCD events. The electroweak background is acquired from MC predictions.

Due to the insufficient statistics to perform proper data-driven measurements on the electron efficiencies, the C_W factor is estimated from Monte Carlo. A large uncertainty therefore originates from the amount of material in the detector and its effect on the electron reconstruction and identification efficiencies. The systematic uncertainty related to the material is assessed by estimating the C_W factor for several different MC samples simulated with extra upstream material, as was presented by the author in [110]. Another dominating uncertainty arises from excluding the dead OTx regions in the calorimeter, which rejects about 5% of the $W \rightarrow e\nu$ candidates. The central value and uncertainties for C_W are presented in Table 6.5, broken down into different components.

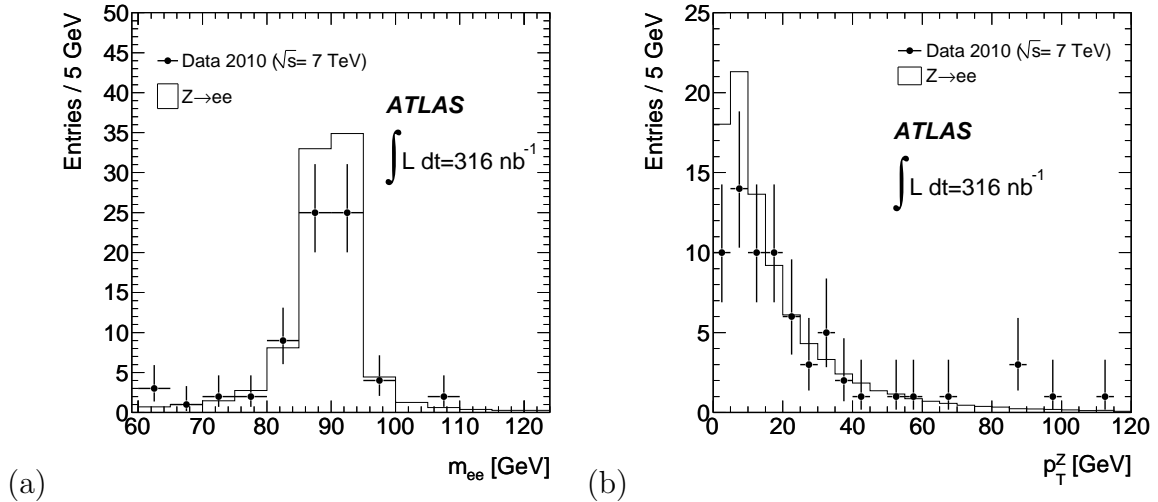


Figure 6.2: The (a) invariant mass and (b) $Z p_T$ for the $Z \rightarrow ee$ candidates in 316 nb^{-1} of data. The data distributions are compared to Monte Carlo expectations [96].

$Z \rightarrow ee$ analysis

A total of 70 $Z \rightarrow ee$ candidates are observed in the invariant mass window of 66-116 GeV, after the full $Z \rightarrow ee$ selection has been applied to the 300 nb^{-1} data. Figure 6.2 shows the invariant mass of the $Z \rightarrow ee$ candidates as well as the p_T of the Z after constraining the invariant mass. The simulated predictions are normalized to the integrated luminosity. A deficit is measured in the data compared to the MC, which is not covered by the large statistical uncertainty. This deficit is further discussed below.

To estimate the small background among the $Z \rightarrow ee$ candidates, the medium identification requirement is relaxed to loose. The invariant mass is then fitted with a Breit-Wigner distribution convoluted with a Gaussian function as signal distribution and a polynomial function as background shape, to obtain the number of loose background events. A loose to medium jet rejection factor is applied, which results in approximately one QCD event. The electroweak background is negligible at this level, but nonetheless included in the cross section calculation, estimated from MC.

The C_Z factor and its uncertainty is acquired in a similar manner to the C_W , as described above. The main differences arise from the fact that there are two electrons in each event as well as no E_T^{miss} requirement or considerable uncertainty from charge mis-identification. The resulting value of C_Z together with the systematic uncertainties are presented in Table 6.5.

	$W \rightarrow e\nu$		$Z \rightarrow ee$	
	Central value	Rel. uncertainty	Central value	Rel. uncertainty
ϵ_{event}	1.000	< 0.2%	1.000	< 0.2%
ϵ_{ID}	0.749	5.2%	0.943	4.2%
ϵ_{trig}	0.998	< 0.2%	0.998	< 0.2%
α_{reco}	0.882	3.9%	0.732	3.2%
C_W, C_Z	0.659	7.0%	0.651	9.4%

Table 6.5: Efficiencies per lepton as well as their relative uncertainties entering the correction factors C_W and C_Z for the electron channel. α_{reco} includes the electron reconstruction efficiency as well as the E_T^{miss} resolution in case of C_W . The trigger efficiency is measured with data, while the other efficiencies and their uncertainties are determined from Monte Carlo simulation [81].

Cross section results

Table 6.5 summarizes the $C_{W/Z}$ factors and uncertainties broken down into the crucial components. The total uncertainties are 7.0% for C_W and 9.4% for C_Z . Equation 6.2 is then used to calculate the fiducial cross section, accounting for the uncertainties from the $C_{W/Z}$ factors, background estimation, etc.

The uncertainty on the C_W/C_Z ratio is estimated to be able to calculate the uncertainty of the cross section ratio according to equation 6.7. Accounting for the proper correlation between the different components in the correction factors results in an uncertainty of 6.0% on the ratio. Some uncertainties cancel partially in the ratio, for example for the identification efficiency where two medium electrons from the Z over one tight electron from the W results in an uncertainty equivalent to one remaining tight electron.

The total cross section is obtained by correcting the fiducial results to the full phase space by applying the theoretical acceptances $A_{W/Z}$, as was discussed in section 6.1.3. The acceptances are calculated using PYTHIA with the modified LO PDF set MRST LO* and results in 0.462 for A_W (0.466 for A_{W^+} and 0.457 for A_{W^-}) and 0.446 for A_Z . The systematic uncertainties on the acceptances are dominated by the limited knowledge of the proton PDFs and the modeling of the W and Z boson production at the LHC. These uncertainties are thus estimated by comparing different PDF sets as well as different MC generators, such as MC@NLO. The resulting systematic uncertainties on the acceptance are 3% for A_W , 4% for the A_Z and 3% for A_{W^+}/A_Z , 2.5% for A_{W^-}/A_Z and 1.5% for the A_W/A_Z ratio. The acceptance uncertainty is added in quadrature to the systematic uncertainty of the fiducial cross section results in order to obtain the total uncertainty of the cross section measurement in full phase space. More carefully evaluated acceptance values with reduced uncertainties, which

CHAPTER 6. $W \rightarrow e\nu$ AND $Z \rightarrow ee$ INCLUSIVE CROSS SECTION MEASUREMENTS WITH ATLAS 2010 DATA

	$\sigma_{W^\pm}^{fid} \cdot \text{BR}(W \rightarrow e\nu)$ [nb]	$\sigma_{W^\pm}^{tot} \cdot \text{BR}(W \rightarrow e\nu)$ [nb]
W^\pm	$4.85 \pm 0.16(\text{stat}) \pm 0.34(\text{syst}) \pm 0.53(\text{lumi})$	$10.51 \pm 0.34(\text{stat}) \pm 0.81(\text{syst}) \pm 1.16(\text{lumi})$
W^+	$2.92 \pm 0.12(\text{stat}) \pm 0.21(\text{syst}) \pm 0.32(\text{lumi})$	$6.27 \pm 0.26(\text{stat}) \pm 0.48(\text{syst}) \pm 0.69(\text{lumi})$
W^-	$1.93 \pm 0.10(\text{stat}) \pm 0.14(\text{syst}) \pm 0.21(\text{lumi})$	$4.23 \pm 0.22(\text{stat}) \pm 0.33(\text{syst}) \pm 0.47(\text{lumi})$
	$\sigma_Z^{fid} \cdot \text{BR}(Z \rightarrow ee)$ [nb], $66 < m_{ee} < 116$ GeV	$\sigma_Z^{tot} \cdot \text{BR}(Z \rightarrow ee)$ [nb], $66 < m_{ee} < 116$ GeV
Z	$0.33 \pm 0.04(\text{stat}) \pm 0.03(\text{syst}) \pm 0.04(\text{lumi})$	$0.75 \pm 0.09(\text{stat}) \pm 0.08(\text{syst}) \pm 0.08(\text{lumi})$

Table 6.6: Measured cross sections values with the first 300 nb⁻¹ of data, in the electron channel for W^+ , W^- , W^\pm and Z production, in the fiducial and total phase space [96].

are applied to the final differential cross section results, are discussed in section 6.3.7.

The fiducial and total cross section values for W , W^+ , W^- and Z obtained with the first 315 nb⁻¹ of 7 TeV data, are summarized in Table 6.6.

Comparing the extracted total cross section values with the theoretical predictions indicated in equations 2.12, 2.13 and 2.14, shows that while the results agree for the W , the measured Z cross section is significantly lower than the predicted Standard Model value. This deficit of Z bosons was also seen in the control distributions shown in Figure 6.2. It has thereafter been understood, with a larger available data sample, that the deficit is due to a combination of several factors. As was discussed in chapter 5, the medium efficiency has been estimated to be lower in data than in Monte Carlo. For Athena release 15, this difference is even larger, yielding a medium scale factor below 98% (see Table 7.1). This has a significant effect on the Z results since both electrons are required to pass medium identification and no scale factors are applied. In addition, the luminosity has subsequently been found to be 3.6% lower than the initial measured value applied to this analysis [41]. The remaining deficit is mainly due to the large statistical uncertainty. These issues have been resolved for the later measurements using the full 2010 data, which are presented in section 6.3.

The total cross sections obtained in the muon channel are slightly lower than the theoretical predictions for both the $W \rightarrow \mu\nu$ and $Z \rightarrow \mu\mu$ measurement, due to the overestimated luminosity value. For further details on the W/Z muon channel analysis with 315 nb⁻¹ of data, consult [96].

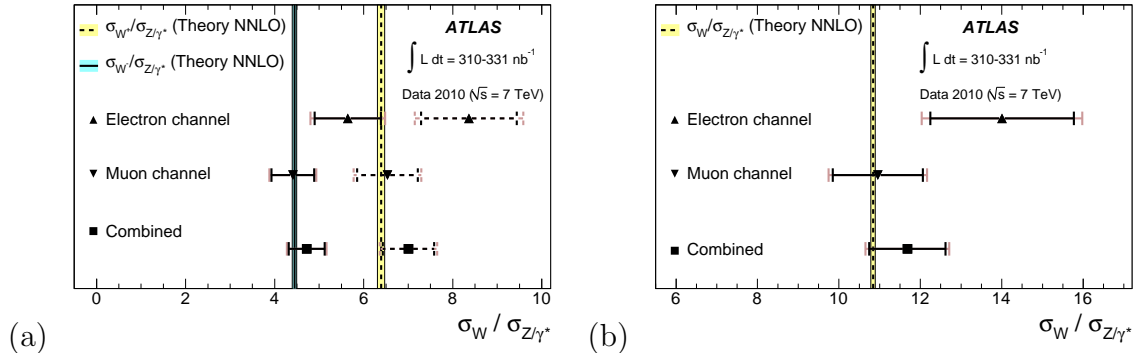


Figure 6.3: The cross section ratios for electron and muon channel as well as the combination for (a) σ_{W^+}/σ_Z and σ_{W^-}/σ_Z and (b) σ_W/σ_Z , obtained with 300 nb^{-1} . The estimated cross section ratios are compared with NNLO theoretical predictions [96].

To decrease the statistical and systematic uncertainties of the cross section measurements the results obtained in the electron and muon channels are combined and the W^\pm and Z cross section ratios are estimated. Figure 6.3 shows the estimated cross section ratios, σ_{W^+}/σ_Z , σ_{W^-}/σ_Z and σ_W/σ_Z , in the electron and muon channels separately as well as combined. The results are compared to NNLO theoretical predictions. The muon results are found to be compatible with theory while the electron results show an overall higher ratio, due to the underestimation of the $Z \rightarrow ee$ cross section as was discussed above.

6.3 W and Z cross section measurement with ATLAS 2010 data (36 pb^{-1})

The W and Z samples in the full 2010 dataset are obtained with the general “WZ-jets_allchannels” GRL. This corresponds to an integrated luminosity estimated to be 36.2 pb^{-1} with a 3.4% relative uncertainty [41]. The data and MC samples are consistently re-processed with Athena release 16.

Preliminary W and Z inclusive cross section results, including the full 2010 dataset, were first completed in a similar manner as the 315 nb^{-1} results described in section 6.2.2 [100]. Improvements due to the larger data sample are made, such as applying data/MC efficiency scale factors obtained with data-driven methods as was described in chapter 5. In addition, the electron energy scale and resolution measured with $Z \rightarrow ee$ events are incorporated into the analysis (see section 6.3.5). The preliminary results are presented in section 6.3.8.

The cross section analysis was further improved in order to measure differential cross sections ($d\sigma(W^\pm)/d\eta^e$ and $d\sigma(Z)/dy^Z$) with a higher precision [102]. The event selection and methodology was modified before finalizing the results, which are presented in section 6.3.9. The adjustments made on the analysis are the following:

- Due to the large η dependence of the tight identification scale factors, discussed in section 5.3.3, and a large charge dependence seen for the tight efficiencies by the W tag-and-probe [81], the tight selection is replaced by medium + b-layer + calorimeter isolation.
- In order to decrease the E_T^{miss} systematic uncertainty and follow the latest recommendation from the Jet/EtMiss group, the E_T^{miss} algorithm is altered from MET_LocHadTopo to MET_RefFinal.
- The W^+ and W^- control distributions have been found to better agree with MC@NLO than PYTHIA. In addition, the QCD estimate more correctly describes the data if the signal template is obtained from MC@NLO. The MC generator used to model the signal processes is hence altered from PYTHIA to MC@NLO. Due to the poor modeling of the boson p_T with NLO generators, the signal samples are normalized to match the W and Z p_T distributions in PYTHIA at generator level.

6.3.1 Reconstruction efficiency

The scale factor correcting the MC to match the electron reconstruction efficiency in data is measured with the Z tag-and-probe method as is discussed in chapter 5. Also the track quality cut (at least one pixel hit and seven silicon hits) is included in this step. For the first preliminary cross section results, the overall reconstruction efficiency scale factor applied is $1.000 \pm 0.015(\text{stat}+\text{syst})$ [82].

For the improved final results, presented in [103], a more precise overall scale factor with reduced systematic uncertainty was applied:

$$SF_{\text{reco} + \text{TQ}} = 1.0126 \pm 0.0019(\text{stat}) \pm 0.0079(\text{syst}). \quad (6.10)$$

The uncertainty of the reconstruction efficiency is added in quadrature to the total uncertainty of the identification efficiency scale factors.

6.3.2 Identification efficiency

The identification efficiency is measured with $W \rightarrow e\nu$ and $Z \rightarrow ee$ tag-and-probe on data in order to derive data/MC scale factors, as was presented in chapter 5. The

final medium and tight efficiency scale factors from the combined W and Z results were shown in Figure 5.11 above.

The data/MC scale factor for medium has been found to be slightly lower than unity with little η dependence and approximately 1% total uncertainty per bin. It is therefore of fundamental importance to propagate this to the Z selection in simulated data, in order to not estimate an incorrect number of Z candidates in MC. The tight identification SF is on the other hand greater than unity overall. It also suffers from a large η dependence, and larger uncertainties of about 1-3% total per bin.

Since the final cross section results used MC@NLO as signal MC rather than PYTHIA, with which the data/MC scale factors have been deduced, the MC true efficiencies were re-computed with MC@NLO. An overall difference below per mille level was concluded and no difference was seen in the η distribution of the efficiencies. The official data/MC scale factors can therefore be directly applied to the MC@NLO distributions.

Medium + b-layer hit + isolation efficiency

For the final differential cross section analysis, tight identification is replaced by medium + b-layer hit + isolation requirements. After the efficiency of different isolation variables had been studied (some of which are included in Appendix B), the “caloIso98” [111] was chosen. *caloIso98* applies a cut on the distribution of the calorimeter isolation within a η - ϕ cone of 0.3 normalized to the electron E_T ($E_T^{\text{cone}(0.3)}/E_T$), which was optimized on release 15 MC to yield a 98% efficiency throughout the electron E_T and η phase space. For the remainder of this chapter “isolation” implies *caloIso98* if not otherwise specified.

The combination of medium + b-layer + isolation was found to increase the efficiency by nearly 10% in comparison with the tight selection, with only a small loss in background rejection. The overall efficiency of the b-layer and isolation requirement with respect to a medium electron, measured with $Z \rightarrow ee$ tag-and-probe is shown in Table 6.7. The background contribution at medium level for Z tag-and-probe is sufficiently low to obtain the efficiencies without applying background subtraction.

The $W \rightarrow e\nu$ differential cross section measurement as a function of η^e , is carried out in a finer binning than the medium efficiency scale factor measurement described above and separately for positive and negative electrons. Since the W tag-and-probe method can directly measure the efficiencies from the positively and negatively reconstructed electrons originating from the W (directly accounting for the fraction of charge mis-identified electrons) this method alone is used to derive the charge dependent medium and b-layer efficiencies. W tag-and-probe also has higher statistics than the Z tag-and-probe method, which facilitates obtaining the efficiency in the

		Efficiency [%]	Data/MC scale factor
b-layer hit	Data	96.94 ± 0.14	1.0066 ± 0.0015
wrt medium ID	MC truth	96.29 ± 0.01	
Isolation requirement	Data	96.83 ± 0.14	0.9902 ± 0.0015
wrt medium + b-layer	MC truth	97.80 ± 0.01	

Table 6.7: Overall b-layer hit and *caloIso98* isolation identification efficiency with respect to electrons passing medium and medium + b-layer respectively, obtained with $Z \rightarrow ee$ tag-and-probe. Data-driven and MC true efficiencies together with their data/MC scale factors are included. No background subtraction has been applied and the errors are statistical only.

finer binning. The medium + b-layer efficiencies are presented in Figure 6.4 for positive and negative electrons as a function of η . The results for data and MC as well as their corresponding ratio (scale factor) are shown.

Table B.13 in Appendix B explicitly documents the medium identification + b-layer hit efficiency and data/MC scale factor, extracted in data with W tag-and-probe for each η bin. The table includes statistical and systematic errors separately for the scale factors, which are propagated to the final differential cross section results. An advantage with this new selection is thus the decreased uncertainties and fluctuations in η for the data/MC scale factors, as well as the smaller charge dependence, in comparison with the tight selection.

Since the W tag-and-probe method uses calorimeter isolation as the discriminating variable for the background subtraction, the efficiency of the the $W \rightarrow e\nu$ isolation cut itself cannot be obtained with this method. Instead, Z tag-and-probe is used to derive the isolation efficiency with respect to electrons passing medium + b-layer cuts. Due to the small background (per mille level) remaining after medium identification has been applied, no background subtraction is applied. This reduces the statistical and systematic uncertainty significantly, which is a great advantage for obtaining the scale factors in the fine differential η binning. Figure 6.5 shows the resulting data and MC isolation efficiencies as well as their scale factor, measured with $Z \rightarrow ee$ tag-and-probe. The isolation scale factor only displays small fluctuations as a function of η .

The scale factor of the isolation cut is deduced without separating the negative and positive probes and the opposite sign cut in the Z tag-and-probe methodology removes the charge mis-identified electrons, that are otherwise included in the $W \rightarrow e\nu$ analysis. The fraction of charge mis-identified events at medium identification level is however very small (see section 6.3.3). To assure that there is no large charge dependence of the isolation efficiency, the ratio of positive and negative efficiency is investigated after the opposite charge requirement between the tag and the probe

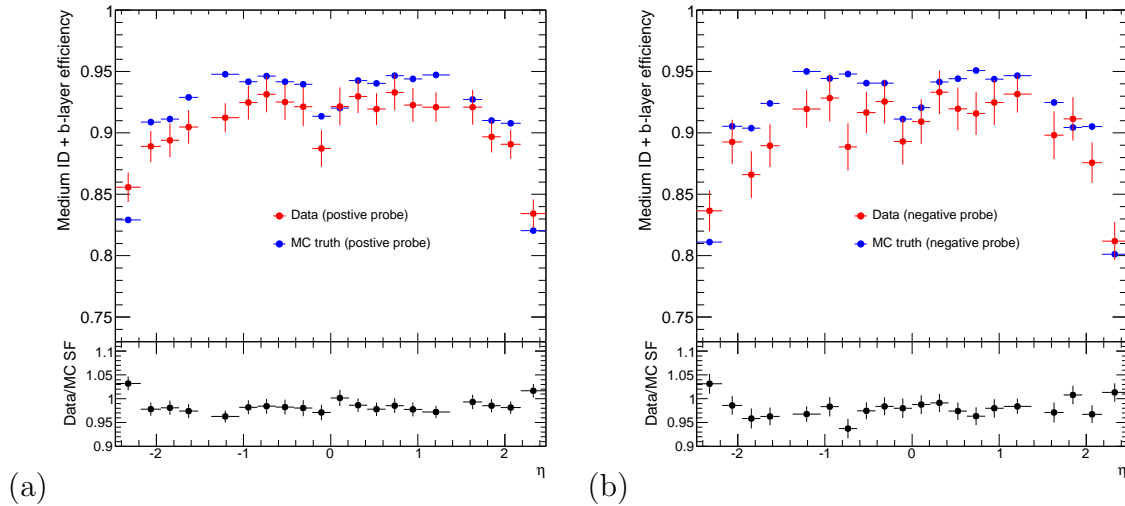


Figure 6.4: Medium + b-layer efficiency of (a) positive and (b) negative electrons as a function of η for data and MC. The data efficiencies are measured with $W \rightarrow e\nu$ tag-and-probe and the MC values reflect true efficiencies. The binning in η is equivalent to that of the $W \rightarrow e\nu$ differential cross section measurement. Errors are statistical only.

has been removed. The results are shown in Figure 6.6 displaying no visible charge dependence as a function of η .

The nominal method of assessing the systematic uncertainty of the efficiency scale factor by varying the background subtraction method, described in [81], is not appropriate for the isolation efficiency measurement since no background subtraction is applied. Instead, the systematic uncertainty is evaluated by investigating the stability of the result after varying the amount of background, applying the standard η binned background subtraction as well as relaxing the opposite sign requirement. In addition, the scale factors are re-evaluated after scaling and smearing the electron energy as described below. The methodology is also modified by choosing one tag and probe pair in the event by selecting the pair with the invariant mass closest to the Z mass, rather than selecting all possible tags and probes. The impact of these variations on the method is small and adding the effect on the scale factor in quadrature yields a systematic uncertainty which is below the statistical error. Figure 6.7 presents the relative uncertainty of the isolation efficiency scale factor, from the different variation of the Z tag-and-probe method as well as the total systematic and statistical errors. The fluctuations seen in the systematic uncertainty as a function of η are primarily due to the relatively large statistical error.

Table B.12 in Appendix B explicitly states the isolation efficiency with statistical uncertainty estimated with Z tag-and-probe in data, as well as the data/MC scale

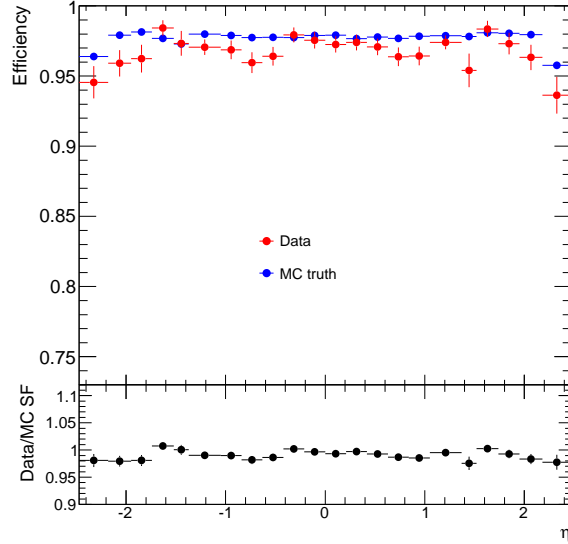


Figure 6.5: Calorimeter isolation efficiency with respect to medium identification + b-layer hit requirement as a function of η for data and MC. The data efficiencies are measured with $Z \rightarrow ee$ tag-and-probe and the MC values reflect true efficiencies. The binning in η is equivalent to that of the W differential cross section measurement. Errors are statistical only.

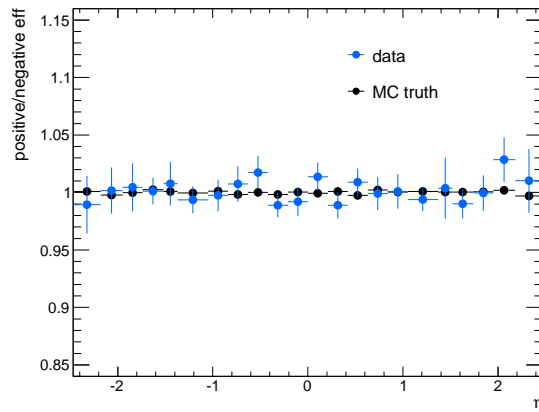


Figure 6.6: Isolation efficiency ratio of positive and negative electrons after relaxing the opposite sign requirement in the $Z \rightarrow ee$ tag-and-probe methodology. The MC values reflect true efficiencies and errors are statistical only.

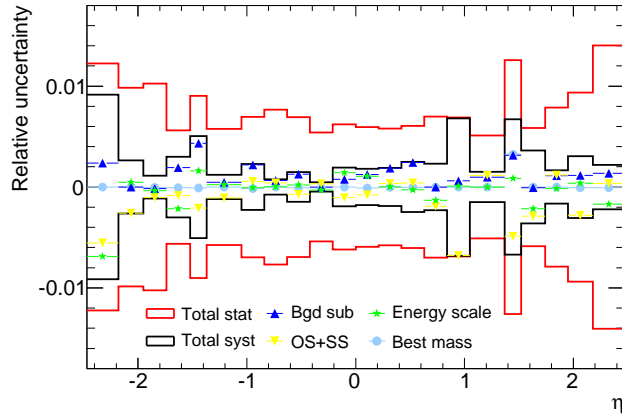


Figure 6.7: Statistical (red) and systematic uncertainty of the data/MC scale factor for isolation efficiency with respect to medium ID + b-layer as a function of η . The total systematic uncertainty is shown (black) together with the individual components; applying background subtraction, relaxing the OS requirement, applying energy scaling/smearing and choosing the tag and probe pairs with the best mass rather than all tags and probes in the event.

factor with resulting statistical and systematic error, for each η bin.

Efficiency scale factors in the cross section evaluation

The data/MC efficiency scale factors are applied to the $W \rightarrow e\nu$ and $Z \rightarrow ee$ cross section analysis to correct the MC. This is performed at the level of identifying the electron(s) originating from the W or the Z .

The statistical and systematic uncertainties of the scale factors are accounted for when computing the total systematic uncertainties of the measurements, i.e. the correction factors C_W and C_Z . Specifically the systematic uncertainty of the SF is treated as fully correlated between η (and charge) bins, while the statistical component is uncorrelated and may average out partially when combining the different bins into an inclusive cross section measurement. The propagation of the statistical uncorrelated component is performed by generating 1000 random samples with Gaussian distributions according to the given uncertainty. The uncertainty applied to the C_W and C_Z factors is then determined as the RMS of these 1000 measurements. The systematic uncertainties of the inclusive and differential C_W and C_Z factors are further discussed in sections 6.3.8 and 6.3.9.

Charge misID rate [%]	Data	MC
Container	$2.17 \pm 0.25 \pm 0.29$	2.74
Track quality	$1.12 \pm 0.20 \pm 0.18$	1.27
Medium	$1.04 \pm 0.11 \pm 0.14$	1.19
Medium + b-layer + caloIso98	$0.63 \pm 0.08 \pm 0.11$	0.81
Tight	$0.37 \pm 0.07 \pm 0.11$	0.5

Table 6.8: Charge mis-identification probability for different levels of electron identification with statistical and systematic error for data. The corresponding values derived in MC are included for comparison [81, 103].

6.3.3 Charge mis-identification probability

The separation of W^+ and W^- cross sections as well as the opposite charge cut applied for the Z measurement rely on a correct description in MC of the probability of measuring the accurate charge of a signal electron. For electrons, the charge mis-identification has been found to be a significant effect of up to several percent with a strong η dependence [81]. The misID occurs when the electrons shower and one of the secondary tracks is matched to the cluster.

The charge mis-identification is measured from data using a Z tag-and-probe selection with same sign electrons. The rates are shown for data and MC in Table 6.8 for the different levels of electron identification. Studying the η dependence of the charge mis-identification concludes that the effect is about a factor ten larger in the end-caps than in the barrel.

There is a further effect of the charge misID on the measured scale factors from the W tag-and-probe analysis as discussed in section 6.3.2. For the analysis of W^+ and W^- cross sections it is important that the efficiencies of an electron and a positron are known, since mis-alignments or other features in the detector may introduce a bias. For the final differential analysis the charge separated identification efficiency scale factors from W tag-and-probe are applied for the W cross section analysis, solving this problem. As was shown for instance in Figure 6.4, the scale factors for e^+ and e^- are measured to be compatible within statistical uncertainties. However, this does not imply that the efficiencies themselves are identical. Typically the identification efficiency of an electron is lower than of a positron, since the electron sample contains a higher fraction of charge mis-identified events due to the higher W^+ cross section. The simulation, however, seems to predict this effect and the final medium + b-layer scale factors for e^+ and e^- are compatible. The effect of the small difference between the charge misID in data and MC is included as a systematic uncertainty.

Periods	Trigger
A,B,C,D,E1 – E3	L1_EM14
E4 – E7,F,G,H,I	EF_e15_medium

Table 6.9: Electron triggers used for the different data periods for the W/Z inclusive cross section results analyzing the full 2010 data.

6.3.4 Trigger efficiency

The electron triggers used in this analysis are listed in Table 6.9 and are equivalent to the triggers used for the tag-and-probe analysis presented in the previous chapter. The efficiencies of these triggers are estimated with respect to offline medium or tight electron identification using a tag-and-probe method applied to the $Z \rightarrow ee$ events, as was discussed in section 5.5.

The analysis requires EF_e15_medium to be passed in the simulated data, due to the small fraction of the data (2%) triggered by the highly efficient L1_EM14 trigger. Due to the flatness in η and E_T for medium and tight electrons, after the $E_T > 20$ GeV cut has been applied, considering an overall scale factor is sufficient. The trigger SF applied to the simulated data is thus $99.5 \pm 0.4\%$ per electron [57].

Considering the event selection of the W and the Z analysis (see section 6.1.2), the trigger efficiencies for the W and Z are calculated in the following manner:

$$\begin{aligned}\epsilon_{trig}^W &= \epsilon_{trig}^{medium/tight} \\ \epsilon_{trig}^Z &= 1 - (1 - \epsilon_{trig}^{medium})^2\end{aligned}$$

The overall trigger efficiency and scale factor for W and Z can be found in Table 6.10 with the combined statistical and systematic uncertainty. Considering that the trigger efficiency for Z is unity after combining the two medium electrons, it is not necessary to apply the SF to the simulated data. In case of the W MC, the SF is applied at the level of identifying the electron from the W boson. The respective uncertainties are added in quadrature with the identification and reconstruction efficiency.

6.3.5 Electron energy scale and resolution

Energy scale corrections to be applied to data are determined in 50 η bins for central electrons using $J/\psi \rightarrow ee$ and $Z \rightarrow ee$ events as well as E/p studies with isolated electrons from W [112, 57]. In addition, corrections in 8 η bins in the forward region are derived using $Z \rightarrow ee$ events. In case of the Z analysis, the scale corrections are

	$W \rightarrow e\nu$	$Z \rightarrow ee$
Trigger ϵ	$0.987 \pm 0.001(\text{stat})$	$1.000 \pm 0.000(\text{stat})$
data/MC SF	$0.995 \pm 0.004(\text{stat+syst})$	$1.000 \pm 0.000(\text{stat+syst})$

Table 6.10: L1_EM14 and EF_e15_medium trigger efficiencies and data/MC scale factors determined with the tag-and-probe method on $Z \rightarrow ee$ events.

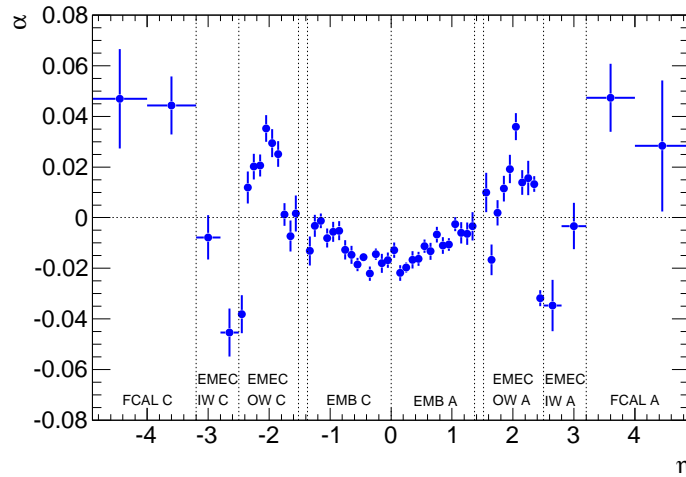


Figure 6.8: Electron energy scale correction factors vs η , obtained with $Z \rightarrow ee$ events, to be applied to electrons in data [57].

estimated by constraining the M_{ee} distribution to follow the Z line shape in MC.

The energy is then scaled in data depending on the η of the electron, by applying the formula $E_{corr} = E_{meas}/(1 + \alpha)$, where α is the correction factor. α varies from approximately 1% in the barrel to 5 – 6% in the FCAL, which is presented in Figure 6.8.

The systematic uncertainty of the energy scaling is provided as a function of electron E_T in 6 η bins. The most dominant sources of uncertainty originate from the limited knowledge of material in front of the calorimeter as well as the presampler energy scale. Overall, the uncertainty is of the level of about 0.5% for the energy range most relevant for W and Z measurements.

The simulated data have been found not to reproduce the $Z \rightarrow ee$ mass resolution in data after the appropriate energy scale correction has been applied. The MC resolution must therefore be smeared to better fit the data. Studies on J/ψ events have shown that the energy resolution for lower energy electrons, where the sampling term dominates, is in good agreement with MC. Only the constant term is thus

adjusted.

The smearing function applied on MC, depends on the energy and pseudorapidity of the electron. The constant term is scaled up/down according to its relative uncertainty in order to gauge the systematic errors due to the energy resolution on the resulting $C_{W/Z}$ factors.

The E_T^{miss} needs to be refined both for the case of correcting the energy in data and smearing the MC resolution. Due to the complexity of the E_T^{miss} calculations, only the vectorial change of the identified electron from the W due to the calibration or smearing is propagated to the E_T^{miss} vector. Comparisons have been made with a more rigorous study, involving correcting the energy of all the topological clusters in the event and re-summing them to obtain the calibrated E_T^{miss} vector. The more advanced study shows an excellent agreement with the approximate method used in this analysis.

6.3.6 Background estimation

QCD background

The QCD background is estimated with a similar method to what was performed for the 315 nb^{-1} cross section results (see section 6.2.2); the E_T^{miss} distribution is fitted with the template method to obtain the QCD background contribution to the observed $W \rightarrow e\nu$ candidates [101, 103]. A signal template, including the electroweak and $t\bar{t}$ background processes, is obtained with simulated data. The QCD template is acquired from electron candidates passing loose and track quality cuts but failing the remainder of the medium and tight requirements. To further reject signal events in the control sample, the isolated electrons are excluded by requiring $E_T^{\text{cone}(0.3)}/E_T > 0.2$. A large statistics QCD dijet MC sample (containing 50 million events) is used to cross check the E_T^{miss} distribution obtained from the data template.

Several parameters are varied in order to estimate the systematic uncertainty on the estimated $W \rightarrow e\nu$ QCD background:

- The nominal **fit range** of the E_T^{miss} is altered from 0-100 GeV to 0-50 GeV and 10-100 GeV.
- The impact on the E_T^{miss} is accounted for by varying the **energy scale** within its uncertainty (see section 6.3.5).
- The **QCD template selection** is adjusted by altering which medium and tight cuts that are required to be failed or passed. In addition, the isolation cut is modified.

- The **signal template** is adjusted by changing from PYTHIA to MC@NLO for the preliminary results and from MC@NLO to POWHEG+PYTHIA for the final differential analysis.

The resulting number of background events for W is shown in Table 6.11.

The QCD background present among the observed $Z \rightarrow ee$ candidates is very small and hence difficult to estimate. A fit is thus performed on the invariant mass distribution for events with the medium-medium selection relaxed to a combination of medium, loose and loose with the additional requirement of 4 hits in the silicon detectors. For the scenario of relaxing the medium requirement for both electrons, the EF_e15_medium trigger is replaced by EF_e20_loose. The fit is performed with a Crystal Ball distribution convoluted with a Breit-Wigner function for the signal shape and Landau, linear and exponential distributions are considered for the background shape. In addition, different ranges of the invariant mass are considered for the fit. The resulting background is scaled by loose-medium background rejection factors. The resulting number of background events for Z is shown in Table 6.12.

Other backgrounds

The electroweak and $t\bar{t}$ backgrounds for $W \rightarrow e\nu$ and $Z \rightarrow ee$ are taken from simulated data, with the samples presented in Table 6.2. A systematic uncertainty on the inclusive cross sections of 5%, 6% and 7% for W/Z , $t\bar{t}$ and diboson backgrounds are concluded. The total uncertainty on the electroweak backgrounds are negligible for the final result.

The inclusive number of QCD and other background events with the corresponding uncertainties are summarized in Table 6.11 for $W \rightarrow e\nu$ and Table 6.12 for $Z \rightarrow ee$. For the differential analysis with the improved $W \rightarrow e\nu$ selection, the QCD background is found to be larger but with smaller relative uncertainty. To obtain differential cross sections the background estimation procedure is performed in each $|\eta^e|$ (W) and $|y^Z|$ (Z) bin. The results are shown in Table C.4 for W^+ , Table C.5 for W^- and Table C.6 for Z , in Appendix C.

6.3.7 Signal acceptances

The $A_{W/Z}$ factors correct the fiducial cross section to full phase space as was described in section 6.1.3, and are quoted as a separate uncertainty for the 2010 data total cross section results. For the preliminary measurements, the $A_{W/Z}$ values and uncertainties derived for the 315 nb^{-1} measurement (see section 6.2.2), are applied.

For the final differential results, the default generator used for the acceptance calculations is MC@NLO, while POWHEG (with PYTHIA and HERWIG as parton shower generators) is used to estimate the theoretical uncertainty [103]. The CTEQ6.6

process	Preliminary analysis		Differential analysis	
	$W \rightarrow e^+\nu$	$W \rightarrow e^-\nu$	$W \rightarrow e^+\nu$	$W \rightarrow e^-\nu$
Candidates	72207	49103	77885	52856
EW+ $t\bar{t}$	$2313 \pm 20 \pm 125$	$1837 \pm 17 \pm 97$	$2445 \pm 19 \pm 126$	$1940 \pm 16 \pm 101$
QCD	$1857 \pm 34 \pm 343$	$2088 \pm 26 \pm 244$	$2681 \pm 47 \pm 325$	$2555 \pm 42 \pm 211$
Total Background	$4170 \pm 39 \pm 343$	$3925 \pm 31 \pm 263$	$5126 \pm 51 \pm 349$	$4495 \pm 45 \pm 234$

Table 6.11: Estimated background events in the $W \rightarrow e\nu$ channels with statistical and systematic uncertainties for cross section results obtained with the preliminary analysis as well as the final differential analysis. The number of observed W candidates are also included [101, 103].

process	$Z \rightarrow ee$
Candidates	9725
EW+ $t\bar{t}$	$45.7 \pm 1.0 \pm 2.7$
QCD	$160.7 \pm 0 \pm 64.3$
Total Background	$206.4 \pm 1.0 \pm 64.4$

Table 6.12: Estimated number of background events in the $Z \rightarrow ee$ channel for the invariant mass window of 66-116 GeV in 36.2 pb^{-1} . The first error is statistical and the second systematic. The number of observed Z candidates are also included [101, 103].

	$A_{W/Z}$	ΔA [%] (error sets)	ΔA [%] (PDF diff)	ΔA [%] (POWHEG)	ΔA [%] (PDF re-weight)	Total [%] uncertainty
W	0.4672	0.9	0.5	1.0	0.5	1.5
W^+	0.4781	0.9	0.7	1.2	0.5	1.7
W^-	0.4516	1.4	1.1	0.8	0.5	2.0
Z	0.4473	1.4	0.6	0.7	1.0	2.0

Table 6.13: Theoretical acceptance values and uncertainties for the final differential total cross section results. The uncertainties are broken down into the different sources [103].

PDF error sets (44 PDF error eigenvector sets) are used to obtain the uncertainties within one PDF. A comparison between different PDFs (ABKM095, HERAPDF10, MSTW2008, CT10, CT10W and NNPDF2.1) is carried out to assess the uncertainties due to the choice of PDF. In addition, the uncertainty due to PDF re-weighting is assessed by re-weighting MC@NLO with CTEQ6.6 and HERAPDF 1.0. The resulting acceptance values and uncertainties can be seen in Table 6.13, together with a breakdown of the uncertainties.

The acceptance uncertainties are reduced with respect to the previous cross section analysis. Accounting for the correlations between the different channels, estimated with the CTEQ6.6 NLO PDF set, the uncertainties on the acceptance ratios are 1.9% for A_{W^+}/A_{W^-} , 1.2% for A_{W^+}/A_Z , 1.1% for A_{W^-}/A_Z and finally 0.8% for A_W/A_Z .

6.3.8 Preliminary results with the 2010 dataset

In this section, the preliminary W and Z inclusive cross section values and uncertainties obtained with 2010 data are summarized. These results were presented by the author, with emphasis on electron performance, in [113].

$W \rightarrow e\nu$ and $Z \rightarrow ee$ candidates

A total of 72207 $W \rightarrow e^+\nu$, 49103 $W \rightarrow e^-\nu$ and 9725 $Z \rightarrow ee$ candidates are observed in the full 2010 data with the preliminary selection. Figure 6.9 shows the charge separated electron E_T distribution comparing data and MC. Despite correcting the data and MC for the discrepancies described in the sections above, the agreement is poor for the lower E_T region. This feature is improved by using MC@NLO rather than PYTHIA to describe the signal and for estimating the background (see section 6.3.9).

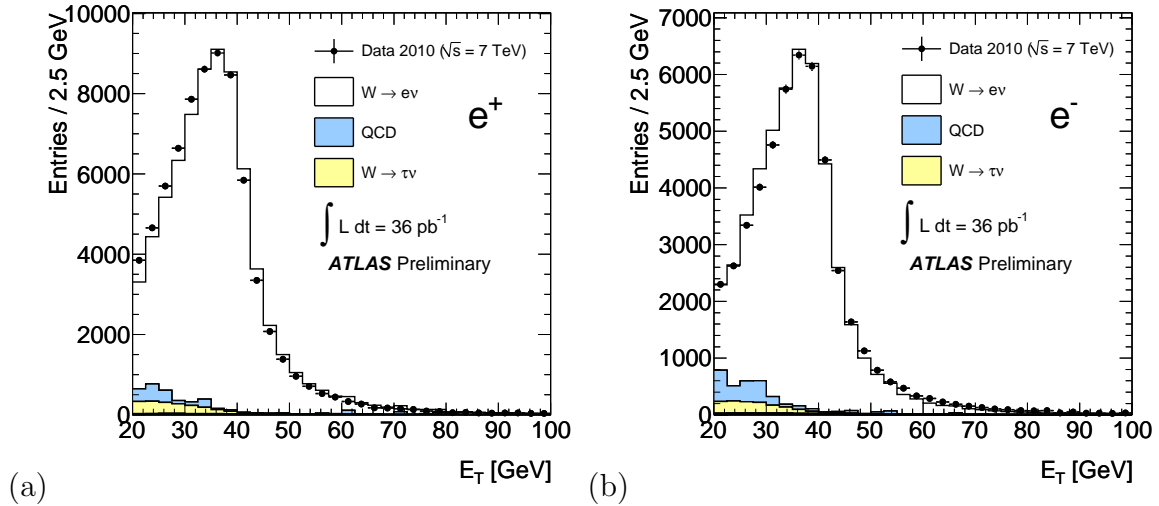


Figure 6.9: The electron E_T from (a) W^+ and (b) W^- , comparing the 2010 data and PYTHIA MC. The energy scaling and smearing has been applied. The MC has been corrected with the electron efficiency scale factors and is normalized to data [100].

$C_{W/Z}$ factors and uncertainties

The $C_{W/Z}$ factors derived with PYTHIA, correcting the electron efficiencies, re-weighting the primary vertex distribution to correct for pile-up and smearing the electron energy, are estimated to be 0.641 for W (0.637 for W^+ and 0.647 for W^-) and 0.606 for Z .

The $C_{W/Z}$ systematic uncertainties described in the previous sections are summarized in Table 6.14. The dominating uncertainties are due to the E_T^{miss} for C_W and the electron reconstruction efficiency for C_Z . In addition, the uncertainties due to the electron identification efficiencies and their charge dependence contribute with a significant fraction.

Cross section results

Table 6.15 reports the number of candidates, estimated background events and the $C_{W/Z}$ and $A_{W/Z}$ correction factors used for the different measurements. Employing equation 6.2 results in the cross sections values presented in Table 6.16 with fiducial and total values. The uncertainties due to data statistics, luminosity, further experimental systematic uncertainties and the acceptance extrapolation in case of the total cross sections are quoted separately. The measurements are dominated by the systematic and luminosity uncertainties.

[%]	$\Delta C_W/C_W$	$\Delta C_{W^+}/C_{W^+}$	$\Delta C_{W^-}/C_{W^-}$	$\Delta C_Z/C_Z$
Trigger	0.5	0.5	0.5	< 0.1
Electron Reconstruction	1.5	1.5	1.5	3.0
Electron ID SF corr	1.11	1.13	1.07	1.55
Electron ID SF uncorr	0.25	0.25	0.25	0.47
Electron Energy scale	0.46	0.50	0.40	0.18
Electron Energy resolution	0.02	0.02	0.02	0.02
OTX	0.4	0.4	0.4	0.8
charge dependent ID	0.1	1.1	1.1	< 0.1
E_T^{miss} scale and resolution	2.0	2.0	2.0	-
pile-up	0.1	0.1	0.1	0.1
Theory (PDF re-weight)	0.3	0.3	0.3	0.5
Total uncertainty	2.8	3.0	3.0	3.5

Table 6.14: Summary of relative systematic uncertainties [%] on C_W and C_Z in the electron channel for the cross section results obtained for the preliminary selection [101].

	N	B	$C_{W/Z}$	$A_{W/Z}$
W^\pm	121310	8095 ± 532	0.641 ± 0.018	0.462 ± 0.014
W^+	72207	4170 ± 345	0.637 ± 0.019	0.466 ± 0.014
W^-	49103	3925 ± 264	0.647 ± 0.019	0.457 ± 0.014
Z	9725	217 ± 31	0.606 ± 0.021	0.445 ± 0.018

Table 6.15: Number of observed $W \rightarrow e\nu$ and $Z \rightarrow ee$ candidates and expected background events as well as efficiency and acceptance correction factors. The $C_{W/Z}$ factors are corrected for MC-data discrepancies. The given uncertainties are statistical and systematic, where the statistical uncertainties of the $C_{W/Z}$ and $A_{W/Z}$ factors are negligible. The integrated luminosity with uncertainty of the 2010 data is $\mathcal{L}^{-1} = 36.2 \pm 1.2 \text{ pb}^{-1}$ [101].

	$\sigma_W^{fid} \cdot \text{BR}(W \rightarrow e\nu)$ [nb]
W	$4.877 \pm 0.015(\text{stat}) \pm 0.138(\text{syst}) \pm 0.166(\text{lumi})$
W^+	$2.950 \pm 0.011(\text{stat}) \pm 0.090(\text{syst}) \pm 0.100(\text{lumi})$
W^-	$1.927 \pm 0.009(\text{stat}) \pm 0.059(\text{syst}) \pm 0.063(\text{lumi})$
	$\sigma_W^{tot} \cdot \text{BR}(W \rightarrow e\nu)$ [nb]
W	$10.551 \pm 0.032(\text{stat}) \pm 0.300(\text{syst}) \pm 0.359(\text{lumi}) \pm 0.316(\text{acc})$
W^+	$6.333 \pm 0.025(\text{stat}) \pm 0.193(\text{syst}) \pm 0.215(\text{lumi}) \pm 0.190(\text{acc})$
W^-	$4.217 \pm 0.021(\text{stat}) \pm 0.129(\text{syst}) \pm 0.138(\text{lumi}) \pm 0.127(\text{acc})$
	$\sigma_{Z/\gamma^*}^{fid} \cdot \text{BR}(Z/\gamma^* \rightarrow ee)$ [nb], $66 < M_{ee} < 116$ GeV
Z/γ^*	$0.433 \pm 0.004(\text{stat}) \pm 0.016(\text{syst}) \pm 0.015(\text{lumi})$
	$\sigma_{Z/\gamma^*}^{tot} \cdot \text{BR}(Z/\gamma^* \rightarrow ee)$ [nb], $66 < M_{ee} < 116$ GeV
Z/γ^*	$0.972 \pm 0.010(\text{stat}) \pm 0.034(\text{syst}) \pm 0.033(\text{lumi}) \pm 0.038(\text{acc})$

Table 6.16: Fiducial and total cross sections times branching ratios, for W , W^+ , W^- and Z production in the electron decay channel. The uncertainties denote the statistical (stat), experimental systematic (syst), acceptance (acc) and luminosity induced errors (lumi) [100].

Comparing the total inclusive cross sections results with NNLO theoretical predictions (see equations 2.12, 2.13 and 2.14) shows a good agreement within uncertainties. At this stage it would hence be favorable to improve the measurement towards reducing the systematic uncertainties in order to gain a larger sensitivity for instance for constraining the PDFs. This is performed for the differential measurement discussed in section 6.3.9.

Combined electron and muon cross sections and ratios

The total cross section results obtained in the muon channel are consistent with the electron channel within uncertainties [100]. The electron and muon cross sections are combined assuming the two decay mode cross sections to be independent, except for the common factors in the acceptance calculation, the E_T^{miss} uncertainty and the luminosity uncertainty. The combined cross sections are obtained by weighting the individual measurements according to their uncorrelated uncertainty.

The measured combined cross sections are compared with NNLO QCD predictions in Figure 6.10 which shows the W^+ cross section versus the corresponding W^- value as well as W^\pm versus Z . The NNLO PDFs included in the figure are MSTW08, ABKM09 [114], HERA-PDF 1.0 [115] and JR09 [116] with uncertainties due to the PDF errors only. Within the total accuracy of the measurement of about 5%, all NNLO predictions are consistent with the data.

Compared to the published ATLAS 315 nb⁻¹ results [96], the statistical uncertainty of the 2010 data preliminary cross section measurement has improved by a factor of ten and the systematic uncertainty by a factor of three.

Further cancellations in the uncertainties can be obtained by estimating the inclusive W/Z cross section ratio, while properly accounting for the uncertainties of the individual factors in the cross section calculations, as was discussed in section 6.1.3. The cross section ratio, σ_W/σ_Z , for the preliminary results is:

$$\mathcal{R}_{W/Z}^{\ell} = 10.906 \pm 0.079(\text{stat}) \pm 0.215(\text{syst}) \pm 0.164(\text{acc}).$$

6.3.9 Improved analysis for differential measurements

$W \rightarrow e\nu$ and $Z \rightarrow ee$ candidates

For the final differential results, the analysis is modified to use medium + b-layer + isolation as the W electron identification and MET_RefFinal as the E_T^{miss} algorithm, as was discussed in section 6.3. The number of observed $W \rightarrow e\nu$ candidates in 2010 data with the new selection is 77885 for W^+ and 52856 for W^- . This is an increase of

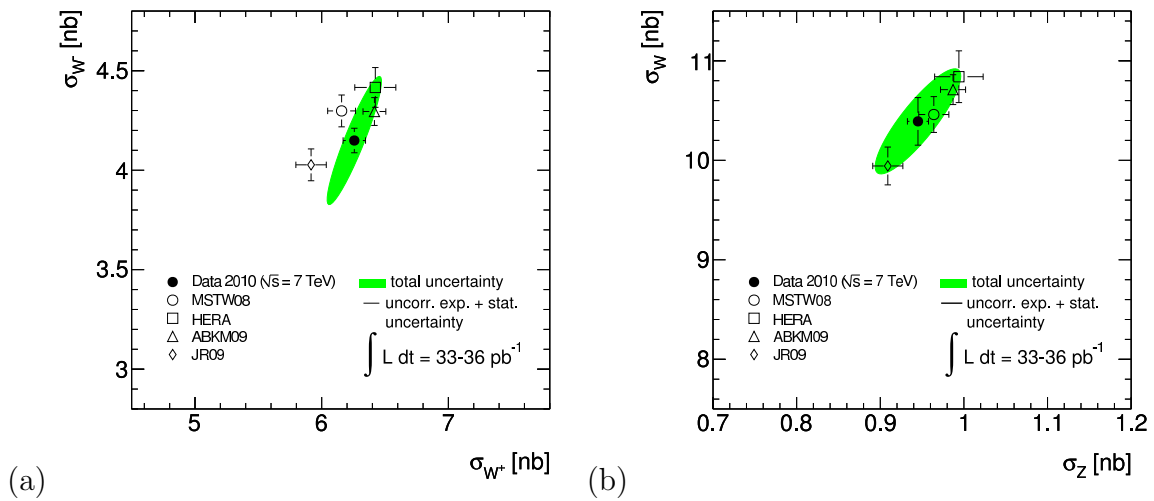


Figure 6.10: Measured and predicted preliminary cross sections with the 2010 data for (a) σ_{W^-} versus σ_{W^+} and (b) σ_{W^\pm} versus σ_Z , after combining the electron and muon channels. The systematic uncertainties due to the luminosity and the acceptance extrapolation are treated as correlated between W and Z channels. In the W^+ and W^- comparison, also the E_T^{miss} uncertainty is treated as fully correlated. The projections of the ellipse to the axes correspond to one standard deviation uncertainty of the cross sections. The errors of the theoretical predictions are solely due to the PDF uncertainties [100].

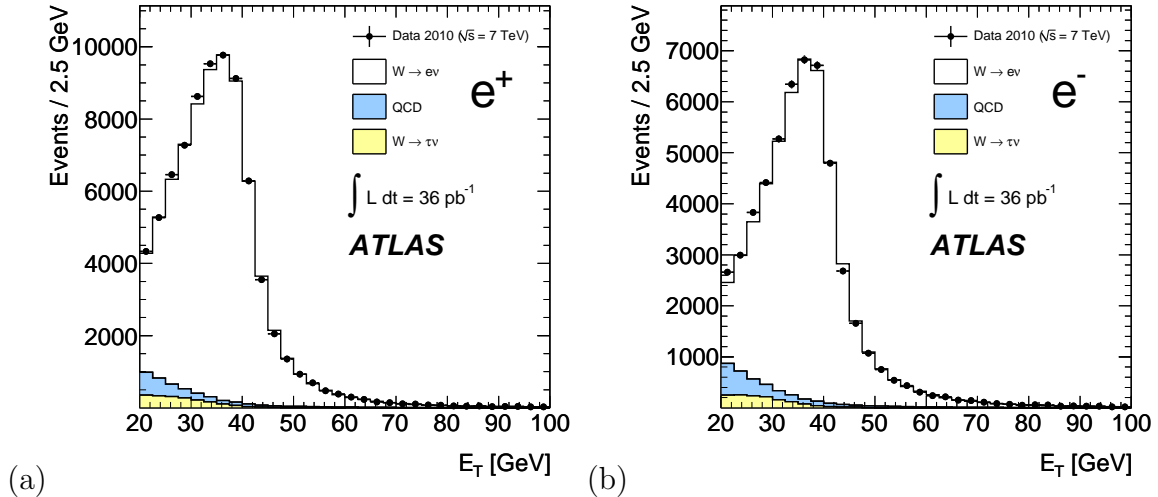


Figure 6.11: The electron E_T from (a) W^+ and (b) W^- , comparing the 2010 data and MC@NLO, applying the medium + b-layer + isolation selection. The QCD shape and normalization is taken from data. The MC@NLO predictions have been corrected for data-MC discrepancies and re-weighted to match the boson p_T distribution in PYTHIA. The MC distributions are normalized to luminosity [102].

about 8% compared to the preliminary results reported in section 6.3.8. The fraction of estimated background is however higher with the improved selection, increasing from 6.7% to 7.4% overall (see Table 6.11). The number of W^+ and W^- candidates observed in the different $|\eta^e|$ bins for the differential cross section calculations are presented in Table C.4 and C.5 in Appendix C.

Figure 6.11 shows the electron E_T for $W^+ \rightarrow e^+\nu$ and $W^- \rightarrow e^-\bar{\nu}$ compared to MC@NLO predictions, which have been corrected for the data-MC discrepancies discussed in the sections above and re-weighted to match the boson p_T distribution in PYTHIA. The QCD background is obtained from the equivalent control sample in data as was used for the background extraction described in section 6.3.6. The agreement between data and MC has improved in comparison to what was seen in Figure 6.9 with tight selection and PYTHIA MC. Figure 6.12 shows the transverse mass distributions for the W^+ and W^- candidates.

The invariant mass spectrum and boson rapidity of the $Z \rightarrow ee$ candidates are displayed in Figure 6.13, comparing data and MC@NLO expectations, which have been corrected for the data-MC discrepancies discussed in the sections above and re-weighted to match the boson p_T distribution in PYTHIA.

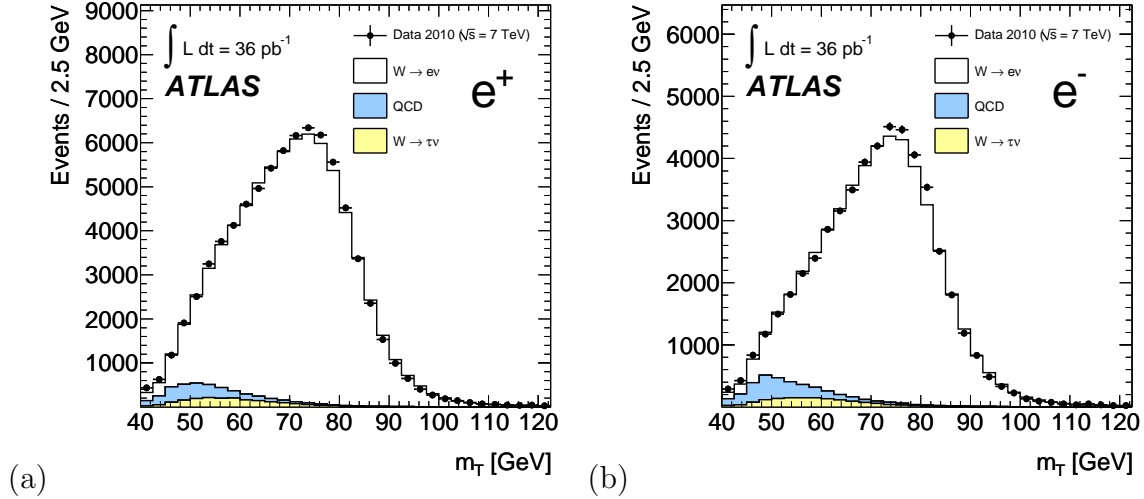


Figure 6.12: The transverse mass for (a) W^+ and (b) W^- , comparing the 2010 data and MC@NLO, applying the medium + b-layer + isolation selection. The QCD shape and normalization is taken from data. The MC@NLO predictions have been corrected for data-MC discrepancies and re-weighted to match the boson p_T distribution in PYTHIA. The MC distributions are normalized to luminosity [102].

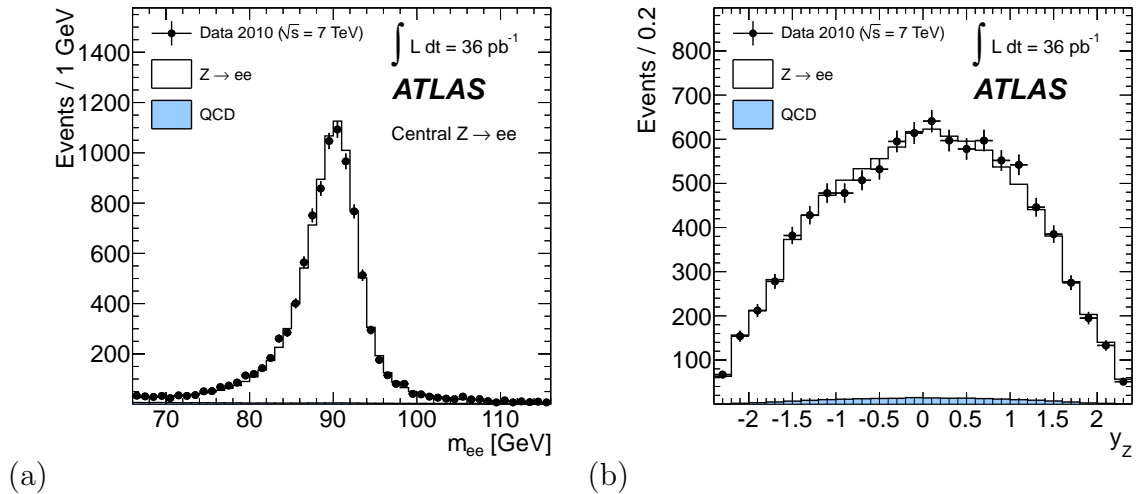


Figure 6.13: The (a) invariant mass and (b) boson rapidity of the $Z \rightarrow ee$ candidates seen in 2010 data compared with MC@NLO predictions, which have been corrected for data-MC discrepancies and re-weighted to match the boson p_T distribution in PYTHIA. The MC distributions are normalized to luminosity [102].

$C_{W/Z}$ factors and uncertainties

The $C_{W/Z}$ factors, derived with MC@NLO, have been corrected to better match the data by applying the electron efficiency scale factors and re-weighting the primary vertex distribution to agree with the amount of pile-up present in the 2010 data. The electron energy has been scaled in data and smeared in the MC. The final inclusive $C_{W/Z}$ correction factors are 0.698 for W (0.693 for W^+ and 0.706 for W^-) and 0.618 for Z [103].

The systematic uncertainties included in the $C_{W/Z}$ factors account for the following corrections.

- The electron reconstruction, identification and trigger efficiency, charge mis-identification and energy scale and resolution (see sections 6.3.1-6.3.5 above for further details).
- The uncertainty due to the exclusion of electrons in the problematic regions in the calorimeter (OTx) has been determined to be 0.4% per electron, implying a 0.8% effect on C_Z [117].
- The $C_W E_T^{\text{miss}}$ uncertainty for the MET_RefFinal algorithm, is estimated by a tool provided by the Jet/EtMiss group [118]. The error accounts for shifts in the jet energy scale and resolution (JES and JER), non-functional calorimeters cells and the uncertainty due to soft jets.
- The uncertainty due to pile-up is estimated by studying the pile-up re-weighting using a second variable, ΣE_T , which is strongly correlated to the amount of pile-up in the event. The difference from using the nominal vertex multiplicity distribution is acquired and a conservative estimate of 0.3% is applied to $C_{W/Z}$ for all η and y bins.
- The uncertainty due to re-weighting the MC@NLO sample to match the boson p_T spectrum in PYTHIA is accounted for by comparing the resulting spectrum with data and PYTHIA. The resulting uncertainty is 0.03% for C_W and less than 0.01% for C_Z , with slight variations between the η and y bins.
- The variation of the primary vertex position in different data periods, due to the variation of the beam spot, is accounted for by re-weighting the MC distribution to data. The 0.1% effect on $C_{W/Z}$ is included as a systematic uncertainty.
- The theoretical uncertainty of $C_{W/Z}$ is assessed by varying the choice of MC generator, PDF set and modeling of the underlying event and parton shower.

[%]	$\Delta C_W/C_W$	$\Delta C_{W^+}/C_{W^+}$	$\Delta C_{W^-}/C_{W^-}$	$\Delta C_Z/C_Z$
Trigger	0.4	0.4	0.4	< 0.1
Electron Reconstruction	0.80	0.80	0.80	1.63
Electron ID SF corr	0.88	0.78	1.02	1.7
Electron ID SF uncorr	0.25	0.33	0.42	0.44
Electron isolation SF corr	0.25	0.25	0.25	-
Electron isolation SF uncorr	0.16	0.17	0.16	-
Electron energy scale	0.49	0.52	0.46	0.18
Electron energy resolution	0.01	0.01	0.01	0.01
OTX	0.4	0.4	0.4	0.8
charge misID	0.0	0.1	0.1	0.6
E_T^{miss} scale and resolution				-
↔ JES	0.43	0.36	0.53	
↔ JER	0.01	0.01	0.01	
↔ AllClusters	0.67	0.59	0.79	
Pile-up	0.3	0.3	0.3	0.3
Boson p_T	0.03	0.03	0.03	0.01
Vertex position	0.09	0.10	0.07	0.08
Theory uncertainty				
↔ PDF	0.2	0.2	0.2	-
↔ Generator	0.35	0.30	0.42	0.29
↔ UE + PS	0.41	0.43	0.39	0.04
Total uncertainty	1.8	1.7	2.0	2.6

Table 6.17: Summary of relative systematic uncertainties [%] on C_W (C_{W^+} and C_{W^-}) and C_Z in the electron channel for the final differential analysis [103].

The resulting error of the inclusive C_W (C_{W^+} and C_{W^-}) and C_Z factors, broken down into the different components, can be seen in Table 6.17. The dominating systematic uncertainties originate from the electron reconstruction and identification efficiency for $C_{W/Z}$ as well as E_T^{miss} for C_W . Table C.1 for C_{W^+} , C.2 for C_{W^-} and C.3 for C_Z , in Appendix C, show the equivalent errors in the differential cross section binning.

Cross section results

Table 6.18 reports the number of $W \rightarrow e\nu$ and $Z \rightarrow ee$ candidates, estimated background events and $C_{W/Z}$ and $A_{W/Z}$ correction factors used for the inclusive cross section calculations. The values and uncertainties can be compared to the preliminary

	N	B	$C_{W/Z}$	$A_{W/Z}$
W^\pm	130741	$9612 \pm 68 \pm 581$	$0.6981 \pm 0.0021 \pm 0.0123$	$0.4672 \pm 0.0002 \pm 0.0071$
W^+	77885	$5126 \pm 51 \pm 349$	$0.6931 \pm 0.0025 \pm 0.0116$	$0.4781 \pm 0.0003 \pm 0.0082$
W^-	52856	$4495 \pm 45 \pm 234$	$0.7056 \pm 0.0032 \pm 0.0135$	$0.4516 \pm 0.0003 \pm 0.0091$
Z	9725	$206 \pm 1 \pm 64$	$0.6175 \pm 0.0003 \pm 0.0162$	$0.4473 \pm 0.0000 \pm 0.0089$

Table 6.18: Number of observed $W \rightarrow e\nu$ and $Z \rightarrow ee$ candidates and expected background events as well as efficiency and acceptance correction factors for the final 2010 data differential analysis. The first given error is due to statistical effects and the second is systematic. The integrated luminosity of the 2010 data with 3.4% uncertainty is $\mathcal{L}^{-1} = 36.2 \pm 1.2 \text{ pb}^{-1}$ [103].

2010 data results shown in Table 6.15. The equivalent ingredients for the differential fiducial cross section calculations are shown in Table C.4 for W^+ , Table C.5 for W^- and Table C.6 for the Z , in Appendix C.

The resulting cross sections are listed in Table 6.19 for the inclusive W and Z . The final inclusive cross section values are overall somewhat lower than what was found for the preliminary results shown in Table 6.16. The systematic uncertainties are reduced by a factor of about 1/3 for all channels due to the improved selection and systematic studies. The total cross section results additionally benefit from the significantly reduced acceptance error (see section 6.3.7).

The differential $W \rightarrow e\nu$ fiducial cross sections as a function of electron pseudorapidity are shown in Figure 6.14 together with theoretical predictions obtained with different NLO MC predictions. The theoretical predictions are normalized to the NNLO cross section, calculated with FEWZ and DYNNLO [119], which are the only programs where the fiducial kinematic requirements can be applied. Figure 6.15 compares the differential $Z \rightarrow ee$ fiducial cross section as a function of boson rapidity with NLO predictions.

Table C.7 and C.8 in Appendix C explicitly states the $W \rightarrow e\nu$ and $Z \rightarrow ee$ differential cross section values and uncertainties for each pseudorapidity and rapidity range.

Combined electron and muon cross sections and ratios

The uncertainty of the W/Z and W^+/W^- cross section ratios are estimated according to equation 6.7, properly accounting for the correlations. In the electron channel, the uncertainties due to the electron reconstruction and identification efficiencies, energy scale and resolution, OTx, pile-up and boson p_T re-weighting, vertex position, theoretical uncertainties, electroweak background and finally luminosity, are considered to be fully correlated. In addition, E_T^{miss} , QCD background and electron isolation efficiency errors are treated as fully correlated for the W^+/W^- ratio. The charge

	$\sigma_W^{fid} \cdot \text{BR}(W \rightarrow e\nu)$ [nb]
W	$4.791 \pm 0.014(\text{stat}) \pm 0.089(\text{syst}) \pm 0.163(\text{lumi})$
W^+	$2.898 \pm 0.011(\text{stat}) \pm 0.052(\text{syst}) \pm 0.099(\text{lumi})$
W^-	$1.893 \pm 0.009(\text{stat}) \pm 0.038(\text{syst}) \pm 0.064(\text{lumi})$
	$\sigma_W^{tot} \cdot \text{BR}(W \rightarrow e\nu)$ [nb]
W	$10.255 \pm 0.031(\text{stat}) \pm 0.190(\text{syst}) \pm 0.349(\text{lumi}) \pm 0.156(\text{acc})$
W^+	$6.063 \pm 0.023(\text{stat}) \pm 0.108(\text{syst}) \pm 0.206(\text{lumi}) \pm 0.104(\text{acc})$
W^-	$4.191 \pm 0.020(\text{stat}) \pm 0.085(\text{syst}) \pm 0.142(\text{lumi}) \pm 0.084(\text{acc})$
	$\sigma_{Z/\gamma^*}^{fid} \cdot \text{BR}(Z/\gamma^* \rightarrow ee)$ [nb], $66 < M_{ee} < 116$ GeV
Z/γ^*	$0.426 \pm 0.004(\text{stat}) \pm 0.012(\text{syst}) \pm 0.014(\text{lumi})$
	$\sigma_{Z/\gamma^*}^{tot} \cdot \text{BR}(Z/\gamma^* \rightarrow ee)$ [nb], $66 < M_{ee} < 116$ GeV
Z/γ^*	$0.952 \pm 0.010(\text{stat}) \pm 0.026(\text{syst}) \pm 0.032(\text{lumi}) \pm 0.019(\text{acc})$

Table 6.19: Fiducial and total cross sections times branching ratios, for W , W^+ , W^- and Z production, in the electron decay channel, obtained with the final differential analysis including the 2010 data. The uncertainties denote the statistical (stat), experimental systematic (syst), acceptance (acc) and luminosity induced errors (lumi) [102].

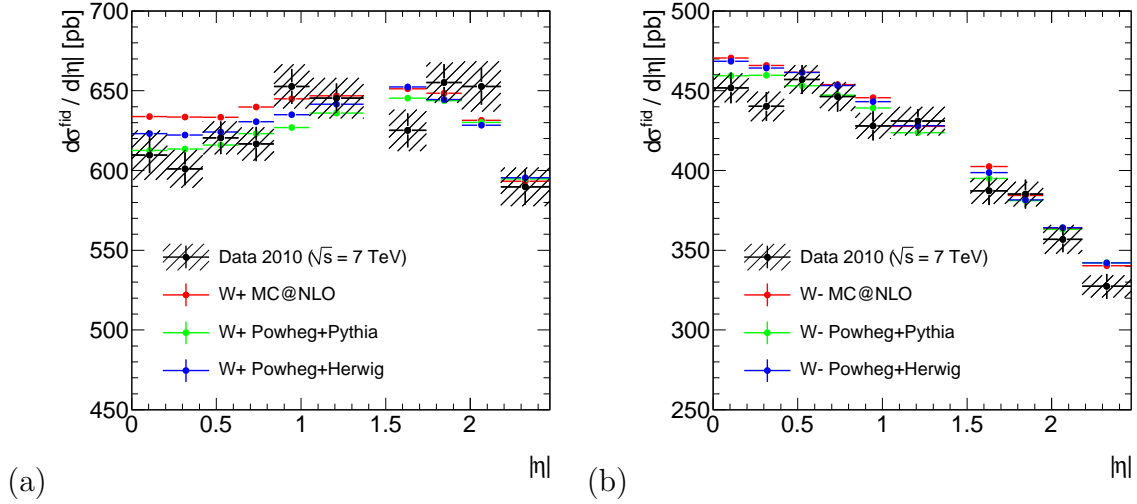


Figure 6.14: Differential $W \rightarrow e\nu$ cross sections for (a) W^+ and (b) W^- in the fiducial volume compared to theoretical predictions normalized to the NNLO total cross sections. The error bars of the measurements show the statistical uncertainties, which are uncorrelated between bins, and the shaded area includes the systematic uncertainties that are correlated between bins [103].

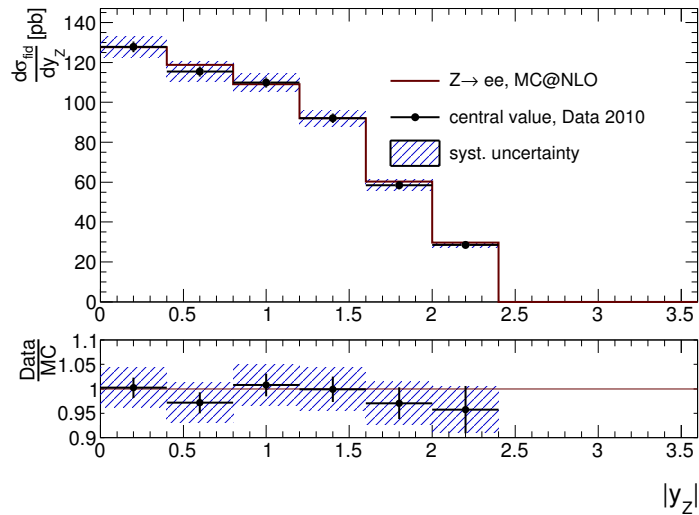


Figure 6.15: Fiducial cross section as a function of absolute Z boson rapidity compared to MC@NLO predictions [103].

mis-identification is considered to be anti-correlated between W^+ and W^- and fully correlated for the W^\pm/Z ratios. The resulting electron channel cross section ratios, in fiducial and full phase space are [103]:

$$\begin{aligned}
 \mathcal{R}_{W^\pm/Z}^{e, fid} &= 10.602 \pm 0.114(\text{stat}) \pm 0.209(\text{sys}) \pm 0.009(\text{acc}) \\
 \mathcal{R}_{W^+/Z}^{e, fid} &= 6.423 \pm 0.071(\text{stat}) \pm 0.127(\text{sys}) \pm 0.005(\text{acc}) \\
 \mathcal{R}_{W^-/Z}^{e, fid} &= 4.180 \pm 0.048(\text{stat}) \pm 0.086(\text{sys}) \pm 0.005(\text{acc}) \\
 \mathcal{R}_{W^+/W^-}^{e, fid} &= 1.537 \pm 0.009(\text{stat}) \pm 0.011(\text{sys}) \pm 0.002(\text{acc}) \\
 \\
 \mathcal{R}_{W^\pm/Z}^{e, tot} &= 10.777 \pm 0.116(\text{stat}) \pm 0.207(\text{syst}) \pm 0.102(\text{acc}) \\
 \mathcal{R}_{W^+/Z}^{e, tot} &= 6.371 \pm 0.070(\text{stat}) \pm 0.123(\text{syst}) \pm 0.089(\text{acc}) \\
 \mathcal{R}_{W^-/Z}^{e, tot} &= 4.404 \pm 0.050(\text{stat}) \pm 0.087(\text{syst}) \pm 0.052(\text{acc}) \\
 \mathcal{R}_{W^+/W^-}^{e, tot} &= 1.447 \pm 0.009(\text{stat}) \pm 0.010(\text{syst}) \pm 0.028(\text{acc})
 \end{aligned}$$

The cross section results obtained in the electron and muon channels are combined in order to further reduce the uncertainties. The differential cross sections must initially be extrapolated to a common fiducial phase space, with $|\eta^\ell| < 2.5$, which is performed with theoretical estimations (for further details on the method see [103]). In addition, the $d\sigma_Z/d|y_Z|$ measurement in the electron channel is combined with a Z analysis using one central ($2.5 < |\eta| < 4.9$) and one forward electron ($|\eta| < 2.47$). This allows for the measurement to be extended to a higher rapidity range. For more information concerning the $Z \rightarrow ee$ central-forward selection consider [102, 103]. The combined fiducial inclusive cross sections are measured to be:

$$\begin{aligned}
 \sigma_W^{fid} \cdot BR(W \rightarrow l\nu) &= 5.127 \pm 0.011(\text{stat}) \pm 0.061(\text{syst}) \pm 0.174(\text{lumi}) \pm 0.005(\text{acc}) [nb], \\
 \sigma_{W^+}^{fid} \cdot BR(W \rightarrow l\nu) &= 3.110 \pm 0.008(\text{stat}) \pm 0.036(\text{syst}) \pm 0.106(\text{lumi}) \pm 0.004(\text{acc}) [nb], \\
 \sigma_{W^-}^{fid} \cdot BR(W \rightarrow l\nu) &= 2.017 \pm 0.007(\text{stat}) \pm 0.028(\text{syst}) \pm 0.069(\text{lumi}) \pm 0.002(\text{acc}) [nb], \\
 \sigma_{Z/\gamma^*}^{fid} \cdot BR(Z/\gamma^* \rightarrow ll) &= 0.479 \pm 0.003(\text{stat}) \pm 0.005(\text{syst}) \pm 0.016(\text{lumi}) \pm 0.001(\text{acc}) [nb].
 \end{aligned}$$

The results for the total cross-sections are:

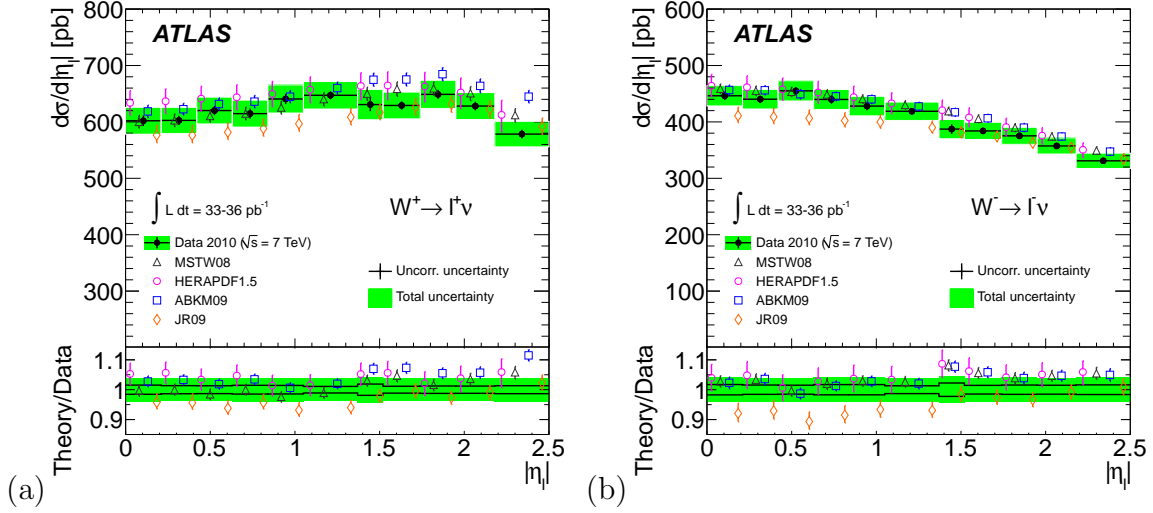


Figure 6.16: Differential (a) $d\sigma_{W^+}/d|\eta_{e^+}|$ and (b) $d\sigma_{W^-}/d|\eta_{e^-}|$ cross section measurements, obtained with combined electron and muon results, compared to NNLO theoretical predictions using various PDF sets [102].

$$\begin{aligned}
 \sigma_{W^+}^{tot} \cdot BR(W \rightarrow l\nu) &= 10.207 \pm 0.021(\text{stat}) \pm 0.121(\text{syst}) \pm 0.347(\text{lumi}) \pm 0.164(\text{acc}) [nb], \\
 \sigma_{W^+}^{tot} \cdot BR(W \rightarrow l\nu) &= 6.048 \pm 0.016(\text{stat}) \pm 0.072(\text{syst}) \pm 0.206(\text{lumi}) \pm 0.096(\text{acc}) [nb], \\
 \sigma_{W^-}^{tot} \cdot BR(W \rightarrow l\nu) &= 4.160 \pm 0.014(\text{stat}) \pm 0.057(\text{syst}) \pm 0.141(\text{lumi}) \pm 0.083(\text{acc}) [nb], \\
 \sigma_{Z/\gamma^*}^{tot} \cdot BR(Z/\gamma^* \rightarrow ll) &= 0.937 \pm 0.006(\text{stat}) \pm 0.009(\text{syst}) \pm 0.032(\text{lumi}) \pm 0.016(\text{acc}) [nb].
 \end{aligned}$$

The differential muon and electron combined results can be seen in Figure 6.16 for W^\pm and Figure 6.17 for Z , together with NNLO theoretical predictions obtained with different PDFs.

The electron and muon combined inclusive fiducial W^\pm/Z and W^+/W^- cross section ratios, extrapolated to the combined phase space, have been estimated to be:

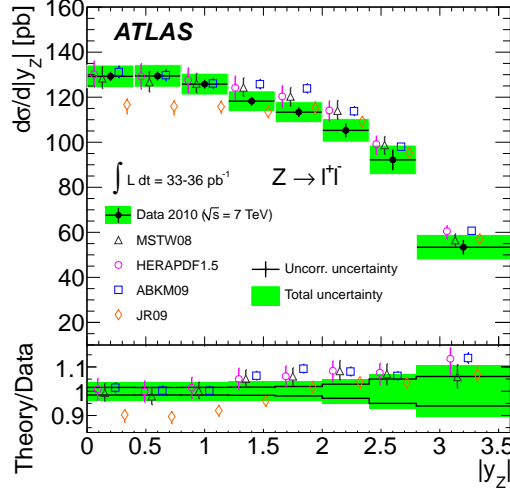


Figure 6.17: Differential $d\sigma_Z/d|y_Z|$ cross section measurement, obtained with combined muon and electron central-central and central-forward channels. The results are compared to NNLO theoretical predictions using various PDF sets [102].

$$\begin{aligned}
 \mathcal{R}_{W^\pm/Z}^{fid} &= 10.703 \pm 0.078(\text{stat}) \pm 0.110(\text{syst}) \pm 0.008(\text{acc}), \\
 \mathcal{R}_{W^+/Z}^{fid} &= 6.493 \pm 0.049(\text{stat}) \pm 0.064(\text{syst}) \pm 0.005(\text{acc}), \\
 \mathcal{R}_{W^-/Z}^{fid} &= 4.210 \pm 0.033(\text{stat}) \pm 0.049(\text{syst}) \pm 0.003(\text{acc}), \\
 \mathcal{R}_{W^+/W^-}^{fid} &= 1.542 \pm 0.007(\text{stat}) \pm 0.012(\text{syst}) \pm 0.001(\text{acc}).
 \end{aligned}$$

The equivalent combined cross section ratios in the full phase space are:

$$\begin{aligned}
 \mathcal{R}_{W^\pm/Z}^{tot} &= 10.893 \pm 0.079(\text{stat}) \pm 0.110(\text{syst}) \pm 0.116(\text{acc}), \\
 \mathcal{R}_{W^+/Z}^{tot} &= 6.454 \pm 0.048(\text{stat}) \pm 0.065(\text{syst}) \pm 0.072(\text{acc}), \\
 \mathcal{R}_{W^-/Z}^{tot} &= 4.439 \pm 0.034(\text{stat}) \pm 0.050(\text{syst}) \pm 0.049(\text{acc}), \\
 \mathcal{R}_{W^+/W^-}^{tot} &= 1.454 \pm 0.006(\text{stat}) \pm 0.012(\text{syst}) \pm 0.022(\text{acc}).
 \end{aligned}$$

The fiducial and total cross sections are additionally illustrated in Figure 6.18 and Figure 6.19 respectively, together with a comparison to theoretical predictions from

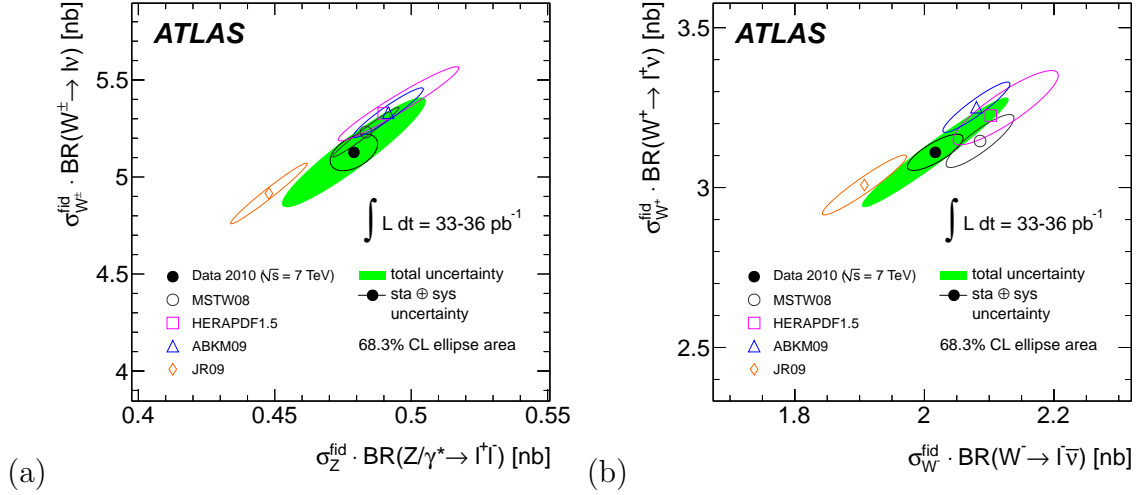


Figure 6.18: Predicted and measured (a) W versus Z and (b) W^+ versus W^- cross sections in the common fiducial volume for the electron and muon channels. The systematic uncertainties due to the luminosity and the acceptance extrapolation are treated as correlated between W and Z channels. In the W^+ and W^- comparison, also the E_T^{miss} uncertainty is treated as fully correlated. The theoretical uncertainties display PDF errors only [102].

MSTW08, ABKM09, HERA1.0NNLO and JR09 NNLO PDFs. The theoretical uncertainties are due to the PDF errors only. The measured results agree in particularly well with the MSTW08 predictions.

The total W^+/Z and W^-/Z cross section ratios are shown in Figure 6.20 compared to the different PDFs. The measured ratio is compatible with all PDF values within the total uncertainty.

6.4 Conclusion

The first year of collision data analysis has been an intense period for the measurement of robust Standard Model results in a limited time frame. The first W and Z cross section measurements at the new kinematic regime of $\sqrt{s} = 7$ TeV were obtained with less than a hundred $W \rightarrow e\nu/Z \rightarrow ee$ candidates observed in ATLAS. These first results were estimated through relying to a large extent on correction efficiencies and acceptances attained using simulated data. As additional data became available and the W/Z sample increased, data-driven measurements, such as electron tag-and-probe efficiency estimations, were incorporated into the cross section analysis. With a

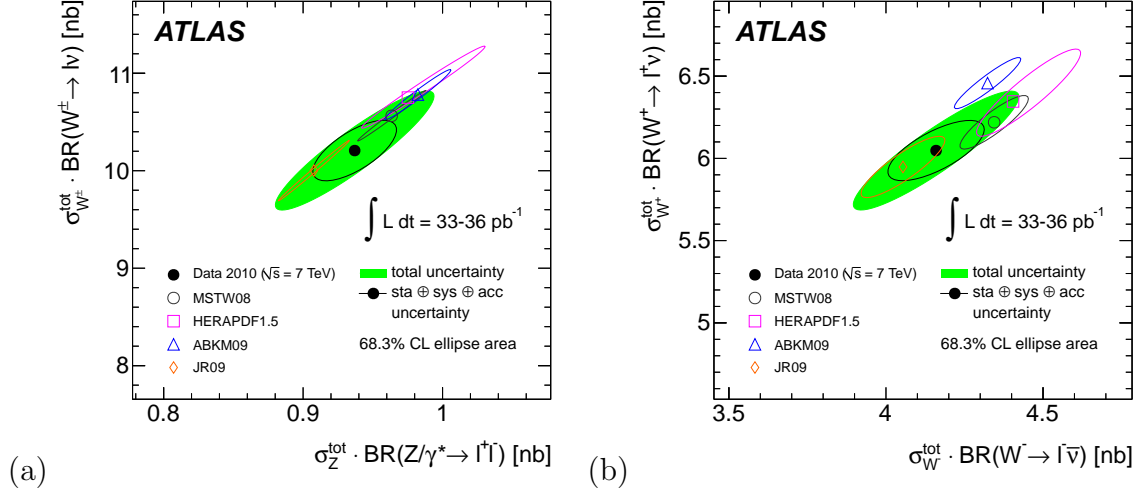


Figure 6.19: Predicted and measured (a) W vs. Z and (b) W^+ vs. W^- cross sections in the total volume for the combined electron and muon results. The systematic uncertainties due to the luminosity and the acceptance extrapolation are treated as correlated between W and Z channels. In the W^+ and W^- comparison, also the E_T^{miss} uncertainty is treated as fully correlated. The theoretical uncertainties display PDF errors only [102].

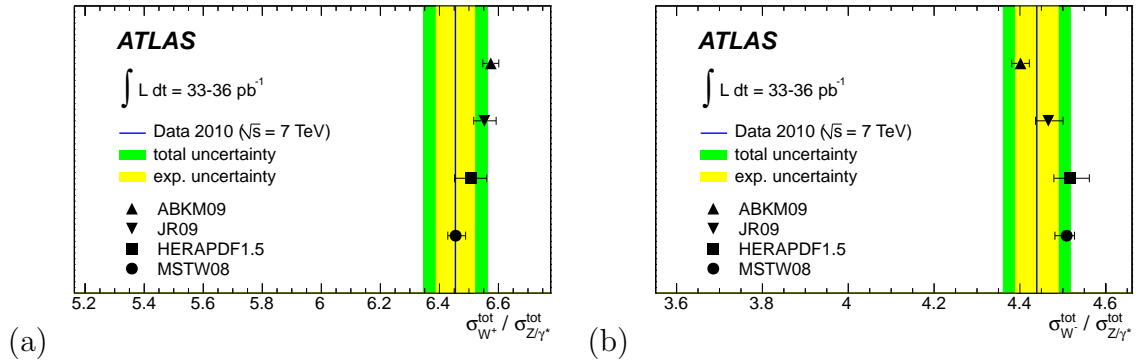


Figure 6.20: Predicted and measured (a) W^+/Z and (b) W^-/Z total cross section ratios for the combined electron and muon channels. The experimental uncertainty (inner yellow band) includes statistical and experimental systematic errors. The total uncertainty (outer green band) includes the small contribution from the acceptance [102].

better understanding of the ATLAS detector and the larger 36 pb^{-1} sample of the full 2010 dataset, precise inclusive and differential W and Z cross section measurements were concluded. The final cross section results, which are no longer statistically limited, agree well with NNLO theoretical predictions.

Future inclusive cross section measurements, incorporating a larger data sample, would benefit from directly including additional data-driven results. The most crucial challenge for improving the inclusive cross section is to measure the integrated luminosity of the larger data sample to high precision. In addition, to reduce the systematic uncertainty and gain PDF sensitivity for the differential results, the electron systematic uncertainties need to be improved. For a precise measurement of the W boson width, Γ_W , the W^\pm/Z cross section ratios would have to be normalized to the pure Z boson contribution, excluding the Drell-Yan component. Also the electroweak corrections would need to be looked at more carefully.

Chapter 7

The \mathcal{R}_{jets} Measurement

Analyses concerning W or Z bosons in association with jets in the final state are interesting processes for several reasons. The wide kinematic range for production of $W/Z + jets$ serves as a testing ground for perturbative QCD predictions, since the gauge boson mass ensures that the interaction scale is sufficiently high for perturbative calculations to be accurate. These studies are particularly important in view of new physics searches since hadronic jets with the leptonic decays of W and Z bosons are crucial backgrounds to both SM and Beyond SM processes, such as top production and searches for Higgs, supersymmetry and extra-dimensions. In addition, signatures with a variety of jet multiplicities in the presence of electrons and E_T^{miss} allow for precision tests of complex reconstruction algorithms and techniques.

The first year of data taking in ATLAS has resulted in several notes and papers presenting intriguing first $W + jets$ and $Z + jets$ results, which are not discussed in this thesis but rather briefly summarized here. Early results showing the ratio $\sigma(W + n)/\sigma(W + n - 1)$ for inclusive jet multiplicities $n = 1 - 4$ with 1.3 pb^{-1} was published in [120] with supporting document [121]. A similar $W + jets$ measurement using the full 2010 data has been published in [122] with supporting note [123] and equivalently for the $Z + jets$ channel in [124] with supporting note [125]. In addition, several conference notes presented $W/Z + jets$ results analyzing parts or all of the 2010 data [126, 127, 128, 129, 130, 131]. A measurement of the cross section of W in association with a b-jet has been published in [132], with supporting document [133].

This chapter presents the \mathcal{R}_{jets} analysis; a measurement of the cross section ratio of $W + jets$ and $Z + jets$. This measurement can be performed in several interesting regions of phase space for example as a function of jet multiplicity and jet H_T (sum of the momenta of the jets in the event) for different jet multiplicities. Due to the limited statistics of the 2010 data and the novelty of the measurement, the first \mathcal{R}_{jets} results presented here measure the ratio in the one jet bin as a function of cumulative jet p_T (jet p_T threshold):

$$\mathcal{R}_{jets}(p_T > x) = \frac{\sigma_{W+1jet}(p_T > x)}{\sigma_{Z+1jet}(p_T > x)}, \quad (7.1)$$

where x ranges from 30 to 190 GeV, in steps of 10 GeV. The exclusive one jet final state is defined such that there is no second jet above 30 GeV. The \mathcal{R}_{jets} analysis has been published in [134] with supporting note [135].

The \mathcal{R}_{jets} measurement has been performed in both the electron and muon channel. The measurement is completed in slightly different phase spaces in both channels due to the characteristics of the particles and the respective detectors such as the EM calorimeter for the electron channel and the muon spectrometer for the muon channel. This chapter focuses on the electron channel, while the results are presented for both analyses. The electron and muon final results are combined, after correcting the individual measurements to a common phase space.

Section 7.1 discusses the theoretical predictions for the \mathcal{R}_{jets} measurement in the fiducial and total phase space, obtained with MCFM as well as other MC generators. This is followed by the \mathcal{R}_{jets} event selection procedure and cross section calculations for the electron channel, focusing on the distinctions from the W/Z inclusive analysis presented in the previous chapter. Section 7.2 discusses how the electron reconstruction, identification and trigger efficiency are dealt with in this particular analysis as well as the efficiency independence of jet kinematic variables. Section 7.3 summarizes the other corrections applied in the \mathcal{R}_{jets} methodology, such as background estimation, correcting from reconstructed to truth jets and jet related uncertainties. Finally, section 7.4 discusses the final result, in both the fiducial and total phase space, and the comparison with the theoretical predictions estimated with Monte Carlo.

7.1 \mathcal{R}_{jets} analysis methodology

7.1.1 Data and MC samples

The results presented here are produced with the data and MC processed with Athena release 15¹. A release 15 “good run list”, applicable to W/Z analyses in both the electron and muon channel² is used and includes an integrated luminosity of 33.3 pb⁻¹. This corresponds to the 2010 ATLAS run periods A-I (see Table A.1, Appendix A). The uncertainty of the luminosity does not affect the precision of the \mathcal{R}_{jets} measurement, since it cancels in the ratio.

¹A decision within ATLAS was taken that the \mathcal{R}_{jets} analysis would not improve significantly by migrating to release 16

²data10_7TeV.periodAllYear_DetStatus-v03-pro05_WZjets_allchannels.xml

NLO perturbative QCD predictions for the $W/Z + jets$ signal processes are calculated using MCFM. Simulated event samples are utilized for the electroweak background estimate, the correction of the signal yields for detector effects and for comparisons of the results and theoretical expectations. ALPGEN is the MC event generator applied for most estimations, but PYTHIA and MC@NLO are also used for different cross checks (further details on MC event generators were given in section 2.3). The parton density functions for the different generators are: CTEQ6L1 [136] for the ALPGEN samples, MRST 2007 LO* [105] for PYTHIA, and MSTW2008 [137] for FEWZ, used for normalizing the samples to NNLO cross sections. The cross section values for the different physics processes samples were shown in Table 6.2.

7.1.2 Theoretical predictions

The measurement is performed at full as well as fiducial phase space, where the electron fiducial volume is defined by:

$$\begin{aligned}
 W \rightarrow e\nu : & \quad p_T^e > 20 \text{ GeV}, |\eta^e| < 2.47 \text{ excluding } 1.37 < |\eta^e| < 1.52, \\
 & \quad p_T^\nu > 25 \text{ GeV}, M_T > 40 \text{ GeV} \\
 Z \rightarrow ee : & \quad p_T^e > 20 \text{ GeV}, |\eta^e| < 2.47 \text{ excluding } 1.37 < |\eta^e| < 1.52, \\
 & \quad 71 < M_{ee} < 111 \text{ GeV} \\
 \text{one jet} : & \quad p_T^j > x \text{ GeV} (x_{min} = 30 \text{ GeV}), |\eta^j| < 2.8, \text{ overlap removal} \\
 & \quad \text{for } \Delta R(e, j) < 0.2, \text{ event veto for } \Delta R(e, j) < 0.6
 \end{aligned}$$

Electrons are defined after a re-summation of the soft and collinear QED radiation (4-vector sum over all the photons in a cone of 0.1 around the direction of the electron), referred to as “dressed” electrons (as was mentioned in section 6.1.3). For the total phase space only the Z invariant mass requirement remains, except for the single jet multiplicity requirements. Only events with exactly one true jet fulfilling the above requirements at generator level are considered both for the case of fiducial and full phase space.

The muon channel has a slightly different phase space at fiducial level due to different characteristics of the muon spectrometer; $|\eta^\mu| < 2.4$ and there is no requirement on muon-jet overlap removal or isolation requirement. The latter constitutes the only difference between the electron and muon full phase space.

The theoretical predictions are calculated at NLO particle level, where jets are reconstructed from hadrons rather than partons. Since MCFM predictions are only available at the parton level, the effects of initial state radiation (ISR), final state radiation (FSR), hadronization and the underlying event must be corrected to arrive

at the particle level. For the predictions at fiducial level in the electron channel, the dressing of the electrons and the electron-jet overlap removal and isolation requirement must be corrected for. These corrections are performed with PYTHIA $V + jets$ ($2 \rightarrow 2$) process MC and are also accounted for in the uncertainty calculations [135].

The MCFM calculations are subject to three main sources of theoretical uncertainty:

- **Scale uncertainties:** the choice of unphysical renormalization and factorization scales
- **PDF uncertainties:** the parameters of the global PDFs
- **Strong coupling uncertainties:** the measured value of the strong coupling at the mass of the Z boson $\alpha_S(M_Z)$

These uncertainties have been found to be quite large, even at NLO, for the $W + jet$ and $Z + jet$ cross sections separately, especially for higher jet p_T . For the ratio, however, the uncertainties partly cancel and the measurement is largely insensitive to the theoretical uncertainty, also at higher jet p_T . This is beneficial for using the \mathcal{R}_{jets} measurement for validating the understanding of detector effects as well as probing for new physics.

The MCFM predictions together with the corresponding theoretical uncertainty are shown in Figure 7.1 as a function of jet p_T threshold, for fiducial and total phase space.

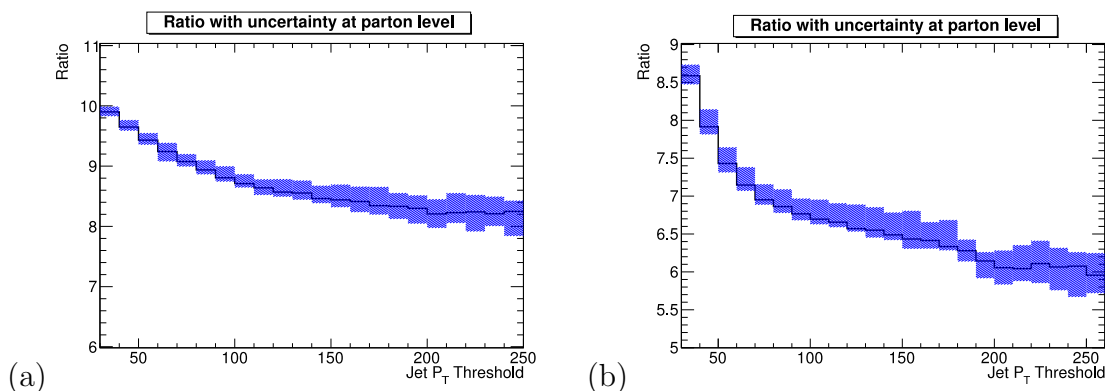


Figure 7.1: The \mathcal{R}_{jets} value with theoretical uncertainties estimated with MCFM for (a) full phase space and (b) fiducial volume in the electron channel [135].

The \mathcal{R}_{jets} value decreases as a function of jet p_T threshold, especially for the fiducial phase space. This is due to the difference of the vector boson masses, resulting in different Q^2 transfers from the vector boson to the jets in the PDFs, which mainly

affects the lower jet energy scale. At fiducial level, the effect is enhanced by measuring the $W \rightarrow e\nu$ and $Z \rightarrow ee$ cross sections in a slightly different phase space (no η and a higher p_T requirement is applied to the neutrino).

As comparison, the ratio is also calculated with some of the standard MC generators (ALPGEN, PYTHIA and MC@NLO), where no corrections from parton to particle level is required. This is shown in Figure 7.2 for both the total and fiducial volume. PYTHIA and MC@NLO agree well, as well as with the MCFM predictions shown in Figure 7.1, while ALPGEN predicts an overall higher ratio. This discrepancy is further discussed in section 7.4.3.

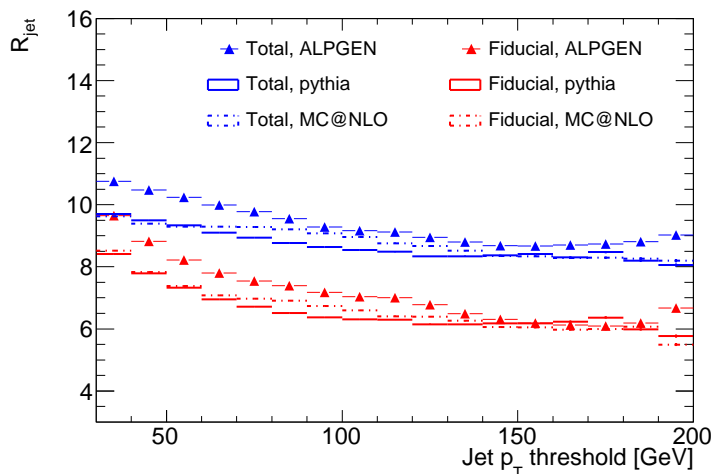


Figure 7.2: The theoretical \mathcal{R}_{jets} value for fiducial and total phase space predicted by ALPGEN, PYTHIA and MC@NLO. The electrons are dressed at the fiducial level.

7.1.3 Jet reconstruction

To be able to reconstruct a jet in the detector a *jet algorithm* is required, which relates the produced partons to the objects detected experimentally (charged particles and energy deposition in the calorimeter cells) [138]. Since a parton hadronizes and is thus not a well defined stable object, the jet definition is also not unique. A jet algorithm typically defines a set of rules, which specify what objects to associate to the jet (*jet finding*), and secondly define how the 4-momenta of the objects have to be recombined to construct the kinematics of the jet (*recombination scheme*). Some of the theoretical and experimental features of an ideal jet reconstruction algorithm are:

- **Order independence:** the algorithm should yield a similar description of the

hard scatter event, regardless of whether applied at parton, hadron or detector level.

- **Infrared and collinear safety:** the algorithm should be insensitive to the emission of extra soft and/or collinear radiation in the event.
- **Detector independence:** the performance should be independent of the signal source. Any effect due to detector segmentation and energy response or resolution should be corrected for by proper calibration.
- **Environment independence:** the algorithm should be stable under increase of activity in the event due to multiple interactions and pile-up.

There are two main classes of jet reconstruction algorithms; cone algorithms and k_t algorithms. The **cone algorithms** define jets as dominant directions of energy flow. *Stable cones* of fixed radius R in the y - ϕ plane are searched for, such that the sum of the particle momenta within the cone points in the same direction as the circle of the cone. The cone algorithms attempt to identify all the stable cones with an iterative method, usually with a seeded approach. The seed can be a set of initial particles or the midpoint of previously found stable cones. However, the iterative method fails to identify exactly all cones, leading to infrared or collinear unsafety in the perturbative computations.

The second class of jet algorithms is the k_t **algorithm**, which uses a sequential recombination of pairs of close particles until a certain distance. The distance between particles i and j is measured as

$$d_{ij}^2 = \min(k_{t,i}^{2p}, k_{t,j}^{2p})(\Delta y_{ij}^2 + \Delta\phi_{i,j}^2). \quad (7.2)$$

The case for which $p = -1$, is known as the **anti- k_t algorithm**. For this algorithm, pairs involving a hard particle will be given smaller distances, implying that soft particles are recombined with hard particles before recombining amongst themselves. This results in regular hard jets and the anti- k_t algorithm is thus seen as IR and collinear safe. Furthermore, the implementation of the algorithm is of high efficiency making it suitable for experimental purposes. Additionally, the regular jet shapes facilitates the experimental jet calibration. This algorithm is therefore chosen for reconstructing jets in the \mathcal{R}_{jets} measurement.

The choice of jet size should be dictated by experimental considerations. Jets at lower p_T are wider, which therefore demands a larger jet size. For higher jet multiplicities, the jets can be quite collimated due to the jets recoiling against the boson. A more narrow jet algorithm is then preferred due to the limitations in phase space. For this analysis considering the wide spectra of jet p_T thresholds, a jet size of $\Delta R = 0.4$ is chosen.

7.1.4 Event selection

The \mathcal{R}_{jets} event selection largely follows that of the W/Z inclusive (see section 6.1.2). Some discrepancies are however introduced to improve the robustness of the ratio measurement as well as additional jet selection requirements:

- One of the electrons from the Z boson is required to fulfill tight identification requirements (the second electron must pass medium ID), in order to obtain further uncertainty cancellations with the tight electron from the W boson³.
- Jet cleaning, which ensures an accurate E_T^{miss} measurement, is applied for both the W and Z selection in order to keep the ratio as consistent as possible. (Note that the jet cleaning only affects a very small fraction of events and does not have any significant impact on the analysis.) The algorithm used for the E_T^{miss} calculation is MET_LocHadTopo, as was described in section 6.1.2.
- The invariant mass range of the Z cross section measurement is narrower than for the inclusive cross section: $71 < M_{ee} < 111$ GeV. This is to further reject the more abundant QCD background in $Z + jets$ events, in comparison with inclusive Z events.
- Jets are reconstructed using the ATLAS AntiKt4H1TopoJets algorithm, which exerts the anti- k_t algorithm described in section 7.1.3. The momentum is calculated from TopoClusters taken at the EM scale and is calibrated using the jet energy scale (JES) correction obtained from the Jet/EtMiss group using a numerical inversion method [139].
- Jets are required to be located within $|\eta^{jet}| < 2.8$ as well as having $p_T^{jet} > 30$ GeV, due to the large uncertainties associated with lower energy jets.
- To remove additional jets originating from pile-up events, a jet vertex fraction (JVF) cut is placed on the jet. The JVF is a discriminating variable for the jet vertex association. It is defined by the fraction of p_T of all tracks from a given vertex and the total jet-matched track p_T from all vertices [140]. A jet with JVF = 1 hence corresponds to a pure hard-scatter jet, while JVF = 0 corresponds to a jet from a pile-up event. A requirement of JVF > 0.75 is applied to the jets, according to the recommendations from the Jet/EtMiss group [141].
- To avoid an overlap from counting electrons as jets, the nearest jet to each selected electron from the W/Z boson is removed within a cone of $\Delta R(e, jet) < 0.2$.

³“robustMedium” and “robusterTight” are used as the standard medium and tight identification in release 15

- A further electron-jet isolation requirement of $\Delta R(e, jet) > 0.6$ is applied (after the jet overlap removal has been performed) to prevent a distortion of the jet energy response (scale and resolution) due to the proximity of an electromagnetic shower. In order to avoid migration between different jet multiplicity bins due to this requirement, events failing this cut are vetoed and hence excluded from the measurement.

Only events with exactly one jet passing the above requirements are considered in the \mathcal{R}_{jets} measurement. The resulting number of events observed in the 2010 data, with the \mathcal{R}_{jets} selection applied, are 12112 $W \rightarrow e\nu + 1$ jet and 948 $Z \rightarrow ee + 1$ jet events for a jet p_T threshold of 30 GeV. A successively higher p_T threshold, starting from 30 GeV is then applied to the jet.

7.1.5 Control distributions

Figure 7.3 shows the leading jet p_T (not cumulative) for $W + 1$ jet and $Z + 1$ jet events passing the event selection described in section 7.1.4 above. The data is overlaid with ALPGEN predictions of signal and background. No corrections for data-MC discrepancies are applied to the MC at this stage.

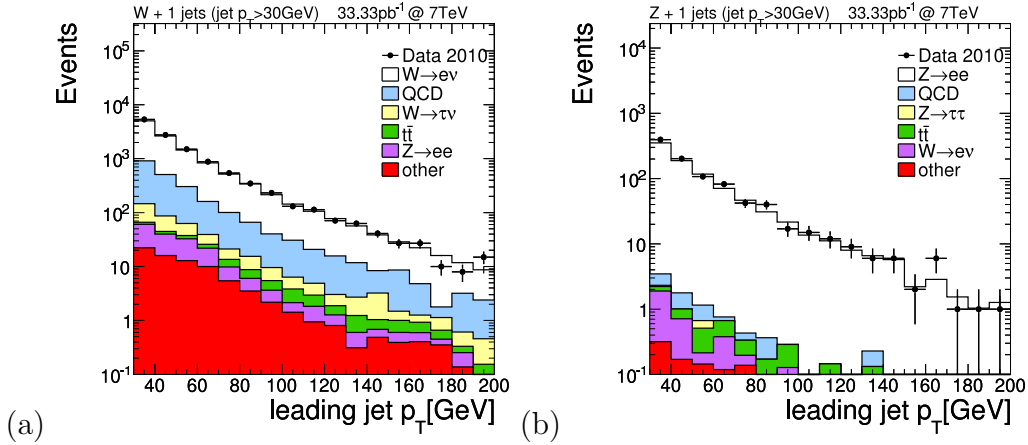


Figure 7.3: The leading jet p_T distribution (not cumulative) for (a) $W + 1$ jet and (b) $Z + 1$ jet events in data and with comparison with MC, where no corrections for data-MC discrepancies have been applied. The MC distributions are normalized to luminosity and the plots are in logarithmic scale [135].

7.1.6 Cross section ratio calculation

In order to derive the \mathcal{R}_{jets} measurement at particle level from the observed $W + \text{jet}$ and $Z + \text{jet}$ events in data, several corrections must be applied. The cross section formula presented in equation 6.2 is employed to obtain $\sigma(W + 1 \text{ jet})$ and $\sigma(Z + 1 \text{ jet})$ individually before the ratio is estimated. The luminosity term, however, can be excluded due to the full cancellation in the ratio.

The background is first estimated and subtracted from the observed events to obtain the number of pure signal events, N_{sig}^V . N_{sig}^V is then corrected back to particle level, N_{part}^V , by taking the detector and reconstruction efficiencies into account. This is performed for each jet p_T threshold within the fiducial phase space of the measurement, which was defined in section 7.1.2.

For the electron channel, the corrections applied accounts for the boson reconstruction correction, C_V , the electron identification efficiency, ϵ_{ID} , the electron trigger efficiency, ϵ_{trig} , and finally the correction of the jet spectrum from reconstruction to truth level, C_{jet} .

$$N_{part}^V = \frac{N_{sig}^V}{C_V \cdot \epsilon_{ID} \cdot \epsilon_{trig} \cdot C_{jet}} \quad (7.3)$$

The ratio N_{part}^W/N_{part}^Z yields the \mathcal{R}_{jets} value in the fiducial volume.

Note that ϵ_{ID} and ϵ_{trig} are separated from the C_V factor, in contrast to the inclusive W/Z cross section methodology discussed in 6.1.3 ($C_V \cdot \epsilon_{ID} \cdot \epsilon_{trig} = C_{W/Z}^{incl}$). This is due to the fact that the electron ID and trigger efficiencies have been found to be independent of the jet kinematics in the event (see section 7.2.4) and can be applied as an overall factor regardless of the jet p_T threshold. The individual corrections and their respective uncertainties are discussed in the following sections.

7.2 Electron efficiencies in the \mathcal{R}_{jets} measurement

This section discusses the electron identification, trigger and reconstruction efficiencies, ϵ , estimated in Athena release 15 for the W and Z selections described in section 7.1.4.

Since \mathcal{R}_{jets} is a correction based measurement, the identification efficiency distributions in the η, E_T space are first derived from signal MC following the \mathcal{R}_{jets} selection, and are then corrected by the global data-driven tag-and-probe results presented below. The resulting efficiency ratio, with a systematic uncertainty obtained from incorporating the uncertainty of the data/MC scale factors, is then applied as a correction to the \mathcal{R}_{jets} measurement.

The trigger efficiency is a simple overall correction factor obtained with $Z \rightarrow ee$ tag-and-probe, while the reconstruction efficiency is a jet dependent correction

acquired from simulated data.

7.2.1 Tag-and-probe results with release 15

The electron efficiencies discussed in this chapter concerns the definitions and selections relevant to Athena release 15, rather than release 16 which was discussed in detail in chapter 5. Tight identification, for instance, does not include the $\Delta\eta$ cluster-track match cut in release 15, and several other variables have been altered and further optimized for release 16.

The efficiency data/MC scale factors used for correcting the MC in the \mathcal{R}_{jets} analysis are based on a release 15 tag-and-probe methodology that is compatible with the one described in chapter 5; $W \rightarrow e\nu$ and $Z \rightarrow ee$ tag-and-probe efficiency scale factors are combined to yield η dependent results for the suitable W/Z energy range of 20-50 GeV. One discrepancy is that the scale factors are produced with respect to container level rather than track quality for the Z tag-and-probe and the track quality scale factors themselves are assumed to be compatible with unity for the combination with W tag-and-probe. The resulting scale factors are shown in Table 7.1.

η	[-2.47 , -2.01]	[-2.01,-1.52]	[-1.37,-0.8]	[-0.8,0]
SF Loose	0.976 ± 0.016	0.990 ± 0.015	0.982 ± 0.015	0.991 ± 0.015
SF Medium	0.945 ± 0.017	0.988 ± 0.016	0.972 ± 0.016	0.974 ± 0.015
SF Tight	0.925 ± 0.034	0.995 ± 0.024	1.006 ± 0.021	0.982 ± 0.018
η	[0,0.8]	[0.8,1.37]	[1.52,2.01]	[2.01,2.47]
SF Loose	0.988 ± 0.015	0.982 ± 0.015	0.996 ± 0.015	0.974 ± 0.016
SF Medium	0.972 ± 0.015	0.967 ± 0.015	0.995 ± 0.029	0.961 ± 0.017
SF Tight	0.987 ± 0.018	1.033 ± 0.025	1.028 ± 0.045	0.936 ± 0.034

Table 7.1: Release 15 identification efficiency data/MC scale factors as a function of η measured for probes within $20 < E_T < 50$ GeV [82].

Comparing the release 15 and release 16 identification scale factors (presented in chapter 5) shows that the SFs are overall lower in release 15; overall around 98% for loose and medium while the tight ID SFs are compatible with unity if integrated over η . It is thus especially important to correct the Z MC for this discrepancy since a $\sim 2\%$ deficit would otherwise be seen in data compared to the MC, which would affect the ratio. The tight SF on the other hand display a large η dependence, which must be accounted for. The uncertainties of the release 15 SFs are larger than for release 16, especially for tight identification. This is mainly due to the short time scale that was available for studying the release 15 efficiencies in great detail before moving on to the improved release 16 re-processed data.

The reconstruction efficiency data/MC scale factor in release 15 is measured to be compatible with unity with an uncertainty of 1.5%, overall. No η dependent results were deduced [82].

7.2.2 Boson reconstruction correction

The boson reconstruction efficiency corrects the \mathcal{R}_{jets} measurement from one/two electron(s) at container level and E_T^{miss} above 25 GeV, to the lepton(s) and neutrino passing the fiducial cuts at generator level defined in section 7.1.2. The correction is estimated for events with one reconstructed jet passing the cuts discussed in section 7.1.4. ALPGEN is used for the central value of the correction, which is estimated as a function of jet p_T threshold. Several uncertainties are considered [135]:

- The differences between predictions made with ALPGEN and PYTHIA results in a 2% uncertainty for the W and Z reconstruction correction separately, reduced to 1% for the ratio.
- The electron energy scale is shifted up/down according to release 15 recommendations by the e/γ group [142]. A resulting 1% uncertainty is obtained for W and Z as well as the ratio. The effect of the electron energy resolution is negligible ($< 0.2\%$).
- The difference in calibration of the LCTopoClusters in data and MC gives rise to an uncertainty of the E_T^{miss} reconstruction. The effect on the E_T^{miss} from the uncertainty of the jet energy scale (JES) and resolution (JER) is evaluated on an event-by-event basis. A dominant uncertainty of up to 4% for lower jet p_T is obtained. Figure 7.4 shows the central value for the \mathcal{R}_{jets} reconstruction correction together with the E_T^{miss} uncertainty.

7.2.3 Electron identification efficiencies in MC

In order to determine the efficiency of the electron identification from MC, all \mathcal{R}_{jets} selection cuts except for the electron ID requirements are first applied. The electron at container level is then loosely truth matched (see section 5.2.4 for more details) before investigating whether it passes the identification requirements for medium or tight electrons from the W or Z . The requirement of only considering events with one exclusive jet is relaxed in order to increase the statistics of the PYTHIA sample (containing 1 million events) used for the efficiency extraction. The efficiency independence of the jet kinematics in the event is discussed in the following section.

Figure 7.5 shows the tight electron identification map in E_T, η space and the projections on E_T and η for tight and medium electrons, for the \mathcal{R}_{jets} selection relaxing

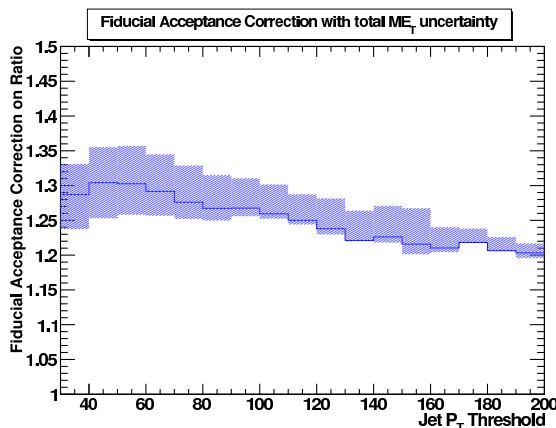


Figure 7.4: The boson reconstruction correction for the \mathcal{R}_{jets} measurement including the systematic uncertainty due to variation of E_T^{miss} [135].

the one exclusive jet requirement. The average efficiency derived from MC for tight electron identification in the W selection is 75.1%. The corresponding value for the medium and tight identification efficiency for the Z selection is 94.5% and 78.5%, respectively.

These MC efficiencies are then corrected to better match the data by applying the data-driven tag-and-probe scale factors available in eight η bins (see Table 7.1).

7.2.4 Electron efficiencies as a function of jet kinematics

To be able to apply the equivalent electron identification efficiency independently of the jet multiplicity and jet kinematics in the event, several studies have been performed to reassure the efficiency independence of these variables, some of which are detailed here. Figure 7.6a shows that the electron ID efficiency, derived with ALPGEN, is not effected by the jet multiplicity in the event. (Direct truth matching is applied for the ALPGEN results, since loose truth matching is not available for the release 15 ALPGEN samples.) Figure 7.6b shows that the electron efficiency drops in the vicinity of a jet, which further justifies the $\Delta R(e, jet) > 0.6$ veto applied in the \mathcal{R}_{jets} selection. The overall effect of this veto on the electron ID efficiency is, however, smaller than 0.01% since there are very few events that constitute an electron and a jet in such proximity after the overlap removal has been performed.

The above results for the MC identification efficiencies are compared with data-driven efficiencies obtained with the Z tag-and-probe method. Here, the PYTHIA sample with loose truth matching is used. Figure 7.7 shows the data-driven efficiency dependence of jet multiplicity as well as the distance between the electron and the nearest jet (in coarser binning than above) after the isolation veto has been

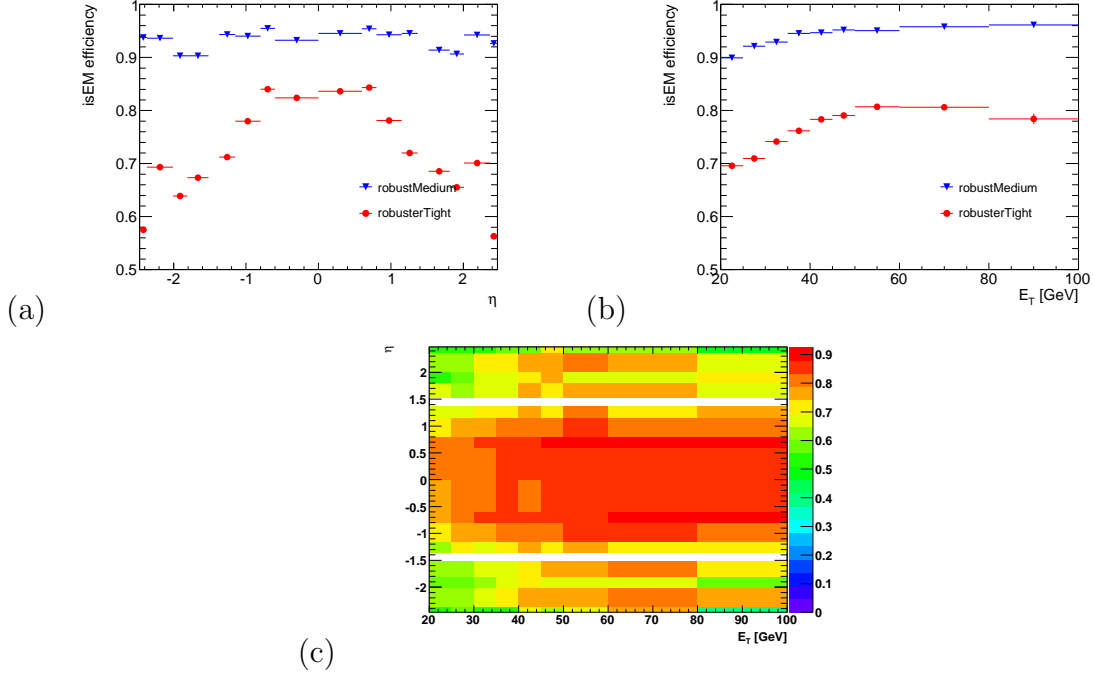


Figure 7.5: Electron ID efficiencies versus (a) η and (b) E_T derived with loosely truth matched electrons (PYTHIA) for tight and medium selection. Figure (c) displays the efficiency map in E_T and η space for tight identification.

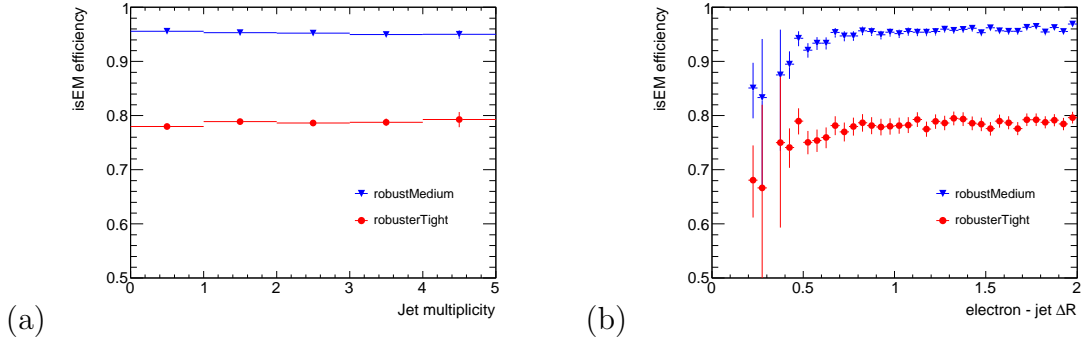


Figure 7.6: Electron efficiencies as function of (a) the dependence on jet multiplicity and (b) the distance between the electron and the nearest jet. The efficiencies are derived with ALPGEN.

applied. Data and MC are overlaid and their respective ratio is shown below the main histogram. The number of $Z \rightarrow ee + jets$ events in the 2010 data is low and the statistical fluctuations in data are hence large. No overall dependence is however seen in data.

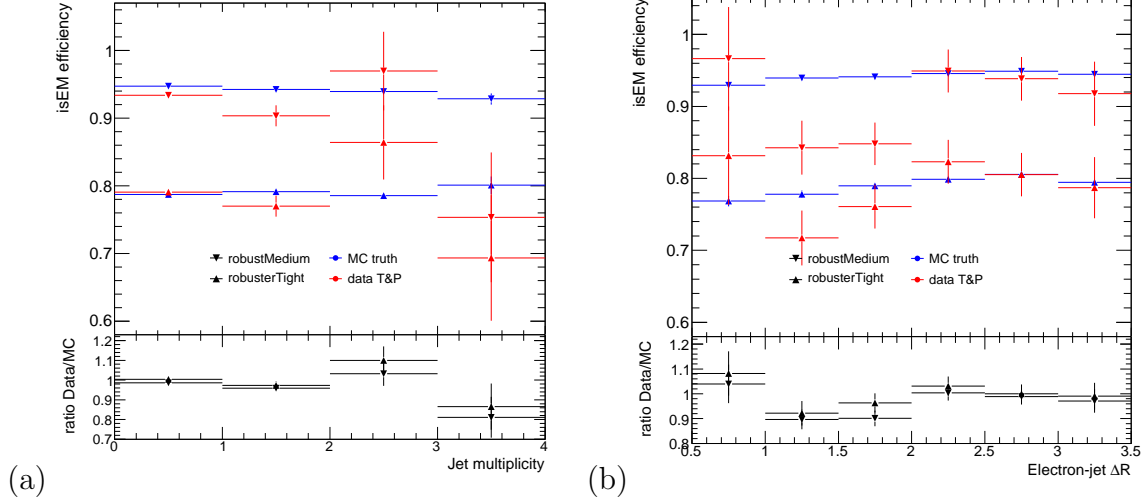


Figure 7.7: Medium and tight efficiency as function of (a) jet multiplicity and (b) electron-jet ΔR for MC and data using the $Z \rightarrow ee$ tag-and-probe method. The data/MC ratio is shown in the lower part of the histograms. No efficiency dependence is seen, within the large statistical errors, on the jet kinematics in the event.

Figure 7.8 displays a further cross check between MC and data-driven efficiencies as function of leading jet p_T for $Z + jets$ events. Due to the limited statistics for the tag-and-probe efficiencies, especially at higher jet p_T , only results below 90 GeV are shown. For this range, no jet p_T dependence is seen within the statistical uncertainty. A requirement of binning the \mathcal{R}_{jets} efficiency correction in jet p_T is therefore not necessary and a more reliable estimate obtained with the full statistics without any jet requirement can be used.

7.2.5 Correcting the \mathcal{R}_{jets} results for the efficiency ratio

After the data/MC scale factors have been applied to the medium and tight MC efficiencies from W and Z , the E_T, η dependence is unfolded to derive the final \mathcal{R}_{jets} correction as a function of jet p_T threshold. To achieve this, the average medium and tight electron efficiencies are estimated using the data and background distribution, after the full \mathcal{R}_{jets} selection have been applied, in E_T, η space:

$$\frac{1}{\epsilon_{med/tight}^V(jet p_T^{thr})} = \frac{\sum_{ij} 1/\epsilon_{med/tight}^{ij} \cdot (N_{data}^{ij} - N_{QCD}^{ij})(1 - f_{ewk}^{ij})}{(N_{data} - N_{QCD})(1 - f_{ewk})} \quad (7.4)$$

where i, j are the electron E_T, η bins, respectively and V the W or Z boson. The number of events in data (N_{data}) and the estimated QCD and electroweak background

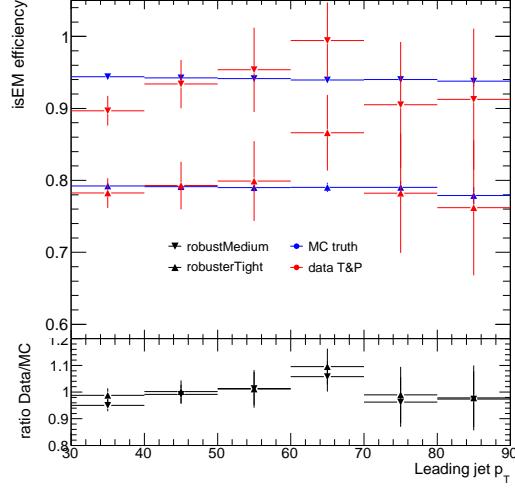


Figure 7.8: Medium and tight efficiency as function of leading jet p_T for MC and data, using the $Z \rightarrow ee$ tag-and-probe method and their ratio (below). There is no efficiency dependence on the jet p_T visible within the statistical errors.

(N_{QCD} and f_{ewk}) depend on the jet p_T threshold in addition to the electron E_T and η .

After the medium and tight efficiencies have been unfolded as a function of jet p_T threshold, the average W and Z efficiencies are calculated as

$$\epsilon^W(jet p_T^{thr}) = \epsilon_{tight}^W$$

and

$$\epsilon^Z(jet p_T^{thr}) = \epsilon_{tight}^Z (2\epsilon_{med}^Z - \epsilon_{tight}^Z).$$

The results are shown in Figure 7.9. The final efficiency correction for the \mathcal{R}_{jets} measurement is thus

$$\epsilon^R(jet p_T^{thr}) = \epsilon^W / \epsilon^Z.$$

7.2.6 Systematic uncertainty on the efficiency ratio

The systematic uncertainty associated with the efficiency ratio ϵ_W / ϵ_Z is assessed by scaling the medium and tight efficiencies up/down by the maximum value of the statistical + systematic uncertainty of the tag-and-probe scale factors in accordance with Table 7.1. This corresponds to the largest effect on the ratio assuming that the medium and tight ID efficiencies are positively correlated. The efficiency ratio is then re-calculated and the difference is taken as a conservative estimate. The

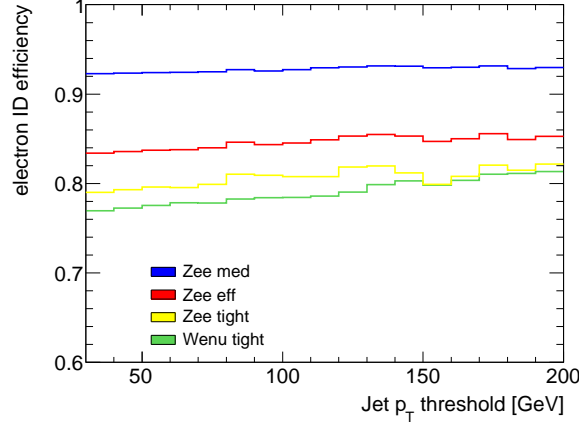


Figure 7.9: Electron average ID efficiencies as function of jet p_T threshold, after unfolding for the distribution of the efficiencies as well as the data candidates and estimated background in E_T, η space.

resulting relative systematic uncertainty on $\epsilon_{ID,W}/\epsilon_{ID,Z}$ amounts to 1.1%. This value is significantly smaller than the individual uncertainties of the scale factors in Table 7.1 as a consequence of the cancellations in the ratio.

7.2.7 Trigger efficiency

Equivalent to what was presented in the chapters 5 and 6, the early data (data period A-E3) used for this analysis have been collected with trigger L1_EM14, while the majority of the data (data period E4-I) have been collected with trigger EF_e15_medium. The efficiencies of these triggers are estimated with respect to offline medium or tight electron identification, according to equation 5.8, using the tag-and-probe method applied to $Z \rightarrow ee$ events as was described in section 5.5. One discrepancy, in order to follow the \mathcal{R}_{jets} selection, is that the denominator of this measurement is a medium or tight probe forming an invariant mass within $[71,111]$ GeV with the tag.

Considering the \mathcal{R}_{jets} selection for the W and the Z (see section 7.1.4), the trigger efficiencies for the W the Z and the correction factor for the ratio are calculated in the following manner:

$$\begin{aligned}
 \epsilon_{trig}^W &= \epsilon_{trig}^{tight} \\
 \epsilon_{trig}^Z &= 1 - (1 - \epsilon_{trig}^{medium})(1 - \epsilon_{trig}^{tight}) \\
 \epsilon_{trig}^R &= \frac{\epsilon_{trig}^{tight}}{1 - (1 - \epsilon_{trig}^{medium})(1 - \epsilon_{trig}^{tight})}
 \end{aligned} \tag{7.5}$$

The resulting trigger efficiencies, obtained with the \mathcal{R}_{jets} selection in release 15 processed data, are listed in Table 7.2. The trigger efficiency dependence on E_T and η are displayed in Figure 7.10 for L1_EM14 and EF_e15_medium individually.

Weighting the trigger efficiencies with their corresponding integrated luminosity yields an overall trigger efficiency for the \mathcal{R}_{jets} measurement of $\epsilon_{trig}^R = 99.3 \pm 0.1(\text{stat})\%$. A conservative statistical + systematic uncertainty of 0.5% is given for the resulting trigger efficiency.

Trigger ϵ [%] with respect to	L1_EM14	EF_e15_medium
medium	$99.7 \pm 0.0(\text{stat})$	$99.0 \pm 0.1(\text{stat})$
tight	$99.7 \pm 0.1(\text{stat})$	$99.3 \pm 0.1(\text{stat})$
$R = W/Z$	$99.7 \pm 0.1(\text{stat})$	$99.3 \pm 0.1(\text{stat})$

Table 7.2: L1_EM14 and EF_e15_medium trigger efficiencies determined from data using the tag-and-probe method for $Z \rightarrow ee$ events. Weighting the two trigger efficiencies with their corresponding integrated luminosity, yields an overall trigger efficiency for the \mathcal{R}_{jets} measurement of $99.3 \pm 0.1(\text{stat})\%$. A conservative statistical + systematic uncertainty of 0.5% is given for the resulting trigger efficiency.

7.3 Additional corrections and uncertainties

7.3.1 Background estimation

QCD background

The QCD background fraction (f_{QCD}) of the $W \rightarrow e\nu + 1$ jet events is estimated with a similar method to that of the W/Z inclusive analysis, described in section 6.3.6. A partially data-driven method employing the template method with E_T^{miss} as the discriminating variable is used [135]. The range of $15 < E_T^{\text{miss}} < 55$ GeV is fitted ensuring that both the signal and background template are reasonably well-populated. A combined signal and electroweak background template is acquired from MC, while the QCD template is obtained by using *anti-electrons*. The QCD anti-electrons are required to pass medium identification but fail two out of five tight criteria; b-layer, E/p , $\Delta\phi_2$, nTRT and TRratio (see Table 5.1 for further explanation). This minimizes the contamination of signal events, while the QCD shape is preserved as unbiased as possible. To improve the purity of the QCD template, the anti-electrons are required to fail a set of track and calorimeter isolation requirements. The results are obtained for jet p_T thresholds from 30 GeV up to 110 GeV (after which the statistics becomes

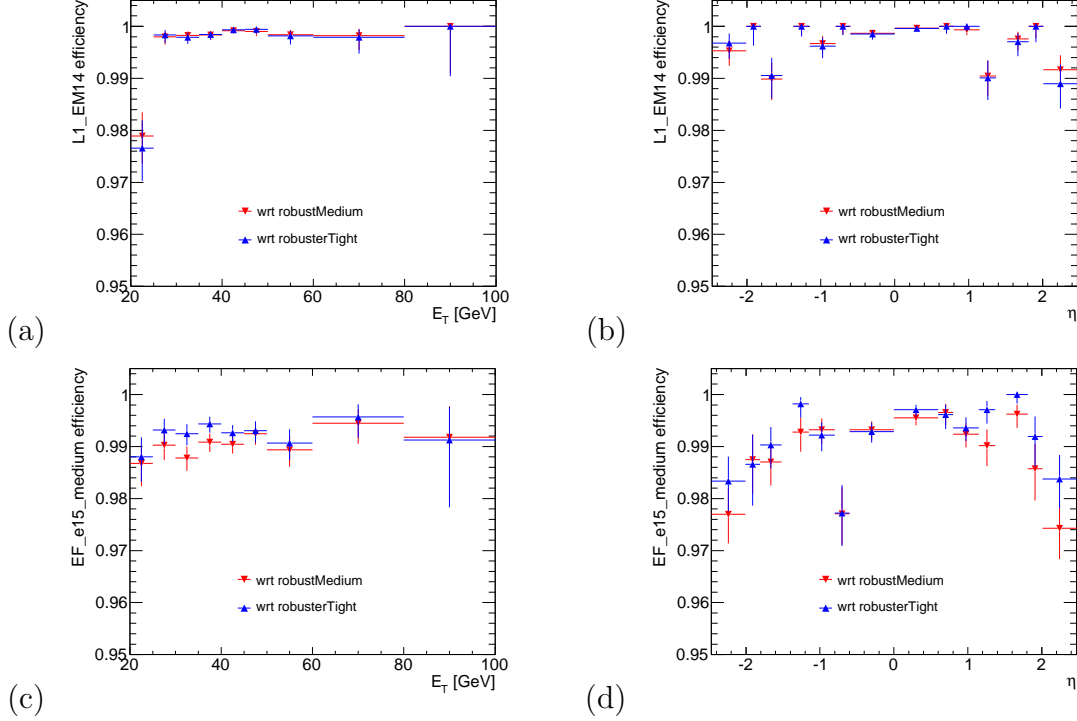


Figure 7.10: L1_EM14 trigger efficiency (top) and EF_e15_medium trigger efficiency (bottom) with respect to a medium and tight offline electron. Figures (a) and (c) show the E_T dependence, while (b) and (d) show the η dependence.

too poor), and are shown in Table 7.3. The table also includes the background estimated for the inclusive selection yielding 4.8%, which is significantly smaller than the 14.9% background estimated for $W + 1$ jet events with a jet p_T threshold of 30 GeV. This is due to the additional hadronic activity in the $W + jets$ events.

The background in the $Z + 1$ jet events, following the medium + tight electron selection, is small and hence difficult to estimate with the low statistics available. In order to obtain a more reliable result, the tight requirement is relaxed to medium, such that the data fitted contains events passing medium-medium selection. The obtained fraction is then scaled by a background rejection factor (see section 5.4.2). The template method is again used, with the invariant mass as the discriminating variable. The QCD template is obtained by selecting anti-electron pairs which fail medium identification. A resulting QCD fraction of $0.4 \pm 0.3\%$ is found for $Z \rightarrow ee + 1$ jet events with a jet p_T threshold of 30 GeV. The statistics is too scarce to obtain a results for higher jet p_T thresholds and this value is used overall. Applying the same technique on the inclusive sample results in a similar QCD background fraction as for the $Z \rightarrow ee + 1$ jet case.

	Inclusive	30 GeV	40 GeV	50 GeV	60 GeV
$f_{QCD}[\%]$	4.8 ± 0.1	14.9 ± 0.5	14.6 ± 0.6	13.7 ± 0.7	12.6 ± 0.9
	70 GeV	80 GeV	90 GeV	100 GeV	110 GeV
$f_{QCD}[\%]$	13.2 ± 1.1	12.6 ± 1.4	12.8 ± 1.7	13.3 ± 2.6	13.4 ± 3.5

Table 7.3: QCD background fraction for $W \rightarrow e\nu + 1$ jet events in various jet p_T thresholds obtained with the template method with E_T^{miss} as the discriminating variable. The inclusive case (no jet requirement) is also included [135].

Additional backgrounds

The remaining sources of background is estimated using simulated data, with ALPGEN constituting the central value. The effect of each of the background processes included can be expressed via a background fraction defined as the fraction of background events N_i originating from a given process i divided by the sum of all background and signal contributions as follows:

$$f_{ewk,V}^i = \frac{N_i}{N_V + \sum_j N_j}. \quad (7.6)$$

The remaining background processes can then be easily subtracted from the signal in data, after the QCD background subtraction has been performed, according to:

$$N_{V,sig} = (1 - f_{ewk,V})N_{V,sig+ewk}, \quad (7.7)$$

where $f_{ewk,V} = \sum_i f_{ewk,V}^i$. This method has the advantage of not depending on the knowledge of the absolute luminosity in data. The resulting background fraction for different processes is shown in Table 7.4. The total non-QCD background adds up to 4.2% for $W + 1$ jet and 0.7 % for $Z + 1$ jet.

Several methods are used to assess different sources of systematic uncertainty. The dominant uncertainty originates from the choice of MC generator, which is estimated by calculating the difference between ALPGEN and PYTHIA. This has an overall effect of 0.7% on the W/Z ratio. The range of resulting systematic uncertainties for the \mathcal{R}_{jets} results as a function of jet p_T threshold are summarized in Figure 7.13.

7.3.2 Pile-up and JVF

Pile-up events can cause migrations in the jet multiplicity distribution and mis-measurement of the jet energy scale. While the latter effect is addressed in the jet energy scale uncertainty (see section 7.3.4), jets from pile-up events are excluded from the analysis by the jet vertex fraction (JVF) cut. A study has been performed comparing the theoretical \mathcal{R}_{jets} predictions obtained with pile-up samples with the

Process	$f_{ewk,W}$ [%]	$f_{ewk,Z}$ [%]
$W \rightarrow e\nu$	-	0.30
$Z \rightarrow ee$	1.09	-
$W \rightarrow \mu\nu$	0.03	0.00
$W \rightarrow \tau\nu$	1.96	0.02
$Z \rightarrow \mu\mu$	0.00	0.00
$Z \rightarrow \tau\tau$	0.20	0.03
$t\bar{t}$	0.34	0.21
single top	0.46	0.03
diboson	0.10	0.09
Total	4.19	0.68

Table 7.4: Background fractions from different physics processes for $W \rightarrow e\nu + \text{jet}$ and $Z \rightarrow ee + \text{jet}$ events with a jet p_T threshold of 30 GeV [135].

JVF cut applied and samples without pile-up and hence no JVf requirement. The results have been found compatible. Note that pile-up events should have a small impact on the ratio since possible extra jets affect the W and Z events to the same extent. Due to low statistics in the high jet p_T region for the MC samples, the derived systematic uncertainty increases considerably for higher jet p_T .

7.3.3 Correction of the jet spectrum

The final remaining correction in order to fully correct back the \mathcal{R}_{jets} measurement to the fiducial level is to unfold for the reconstructed jet distribution. This accommodates the difference of the ratio when calculated in terms of truth particle jets and reconstructed jets. The correction factor is different from unity if migrations occur in the jet p_T distribution between truth and detector level, which in that case needs to be accounted for. Such an effect can occur if different requirements are applied to the $W + \text{jets}$ and $Z + \text{jets}$ events prior to the jet selections, projecting the jets into slightly different phase spaces for the numerator ($W + \text{jets}$) and the denominator ($Z + \text{jets}$) of the measurement. This is the case for the fiducial measurement. For the \mathcal{R}_{jets} measurement at full phase space only the selection on the invariant mass of the Z differs: $71 < M_Z < 111$ GeV. However, the electron-jet overlap removal and isolation criteria can also affect the phase space of the jets and is applied for both electrons of the Z while there is only one electron originating from the W .

One must thus correct for the migrations of the reconstructed jets after the kinematic cuts have been applied. The ratio of reconstructed to true jets is thus calculated as a function of jet p_T threshold, at fiducial and full phase space level. Figure 7.11 shows the results for W and Z separately (a and c) as well as their ratio (b and d).

Note that the correction from reconstructed jets to truth jets is only applied at the fiducial level of the \mathcal{R}_{jets} measurement (Fig. 7.11b) and the correction at full phase space is included here mainly as a curiosity. The overall ratio estimated with PYTHIA, with jet p_T above 30 GeV, is stated explicitly below.

$$R_{reco/truth\ jet}^{fid} = 1.017 \pm 0.000(\text{stat}) \quad (7.8)$$

$$R_{reco/truth\ jet}^{tot} = 0.998 \pm 0.000(\text{stat}) \quad (7.9)$$

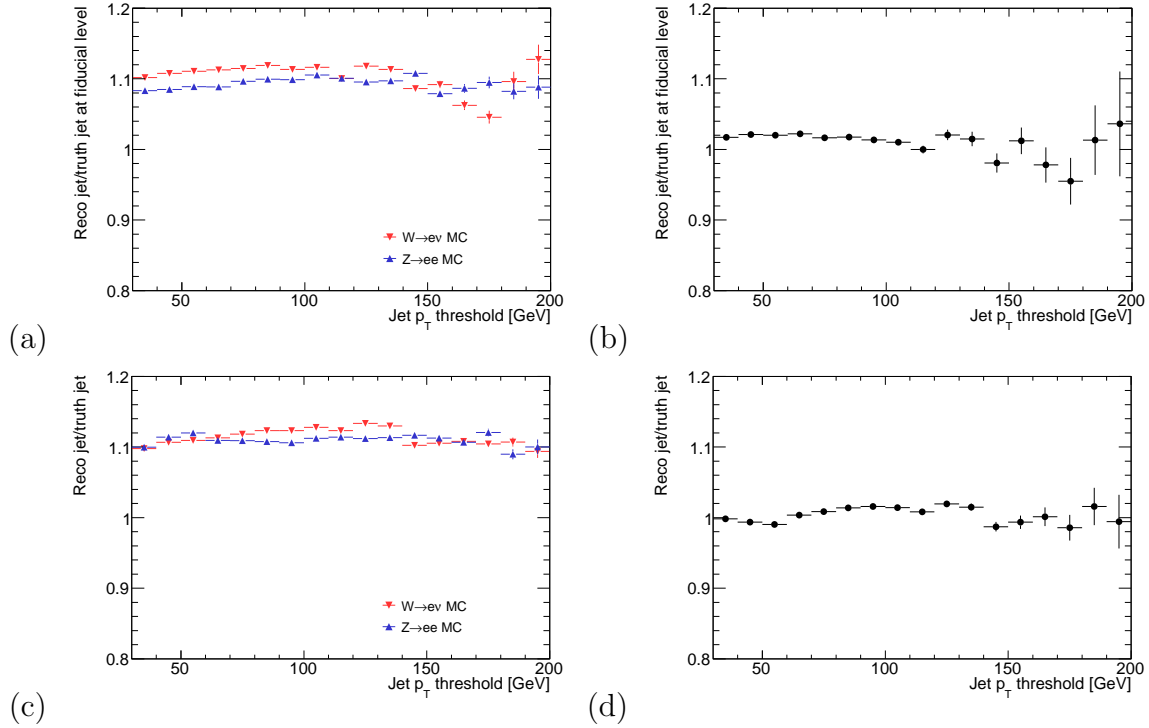


Figure 7.11: The ratio of reconstructed and true jets passing the kinematic cuts for (a) W and Z separately and (b) their respective ratio at fiducial level. Figure (c) and (d) show the equivalent results at full phase space.

As expected, the results show an overall larger correction for the fiducial phase space than for the total phase space, which is close to unity.

The fluctuations increase for the higher kinematic region due to the limited statistics of the MC samples used. The difference between ALPGEN and PYTHIA is taken as the systematic uncertainty, which increases with jet p_T threshold due to the low statistics in that region (see Figure 7.13).

7.3.4 Jet energy scale and resolution

The effect of the jet energy scale and resolution uncertainties on the \mathcal{R}_{jets} ratio are briefly summarized here. Jet energy mis-calibration can cause migration between the jet p_T and jet multiplicity bins and hence distort the \mathcal{R}_{jets} measurement. For further details than what is outlined here, consult [135].

Jet Energy Scale

Calibrations and corrections are applied to the measured jet energy in order to account for the different effects that could distort the jet energy measurement, making a comparison between observations and theoretical predictions possible. The ATLAS official Jet Energy Scale (JES) correction is used, which is based on the electromagnetic scale [143]. The JES uncertainties included here accounts for effects due to dead material in front of the calorimeter, noise thresholds, beam spot variation, underlying event tune, uncertainty on the EM scale, fragmentation model, MC/data discrepancies in the η calibration and finally the effect of in-time pile-up.

In order to obtain the final JES uncertainty of the \mathcal{R}_{jets} measurement, the JES corrections are shifted by $\pm\sigma$, which depend on the η and p_T of the jet. The resulting uncertainty lies between 1.5% and 1.8% for all jet p_T thresholds.

Jet Energy Resolution

The Jet Energy Resolution (JER) has been measured with Athena release 15 and has been found to agree between data and MC within 14% [144]. The JER essentially corresponds to the width of the distribution used to smear the true jet energy. A tool used for smearing the energy of the jets is provided in [145]. To estimate the uncertainty due to this effect the results are compared with and without applying the smearing and results in an uncertainty below 0.6% for all jet p_T thresholds.

7.4 The resulting ratio

7.4.1 \mathcal{R}_{jets} results in the fiducial phase space

The final \mathcal{R}_{jets} results after all corrections have been applied, measured within the fiducial volume, can be seen in Figure 7.12 for the electron channel as well as the muon channel. Note that the electron and muon results are not directly comparable since the measurements are obtained in slightly different phase spaces as was mentioned in section 7.1.2. The black markers represent the data with statistical uncertainty and are placed at the beginning of each bin to illustrate the value of the jet p_T threshold applied for that particular \mathcal{R}_{jets} result. The statistical uncertainty is obtained by

using 10000 pseudo-experiments, based on the assumption of Poisson distributed data. Each pseudo-experiment re-evaluates the \mathcal{R}_{jets} value in each bin after the W and Z selection are fluctuated independently. The quoted statistical uncertainty corresponds to the 68% quantile.

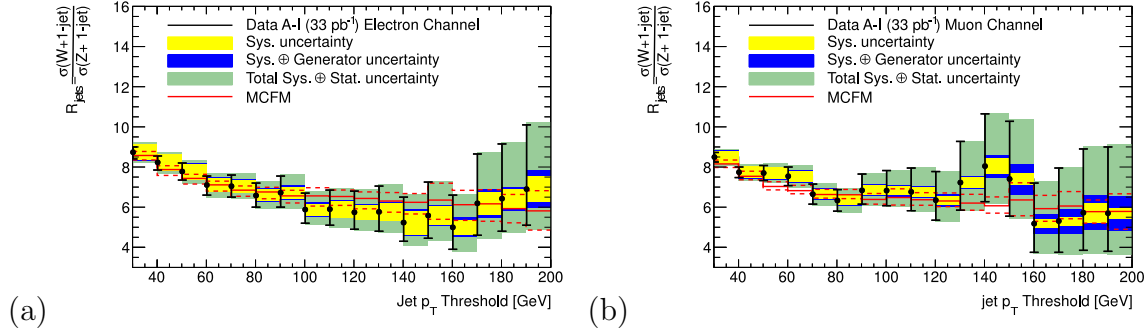


Figure 7.12: \mathcal{R}_{jets} results in the fiducial phase space for (a) the electron channel and (b) the muon channel. The results are compared to MCFM predictions (corrected to particle level). The yellow band shows the total systematic uncertainty, the blue band the addition of the generator uncertainty and the green band adds the statistical uncertainty. The black error bars show the pure statistical uncertainties [135].

The yellow and blue band show the total systematic uncertainty where the blue band represents the uncertainty due to the choice of generator and the yellow band all other systematic errors. Figure 7.13 shows the range of the systematic error broken down into the different components for the electron channel. The systematic uncertainties are grouped into different categories. The boson reconstruction correction uncertainty is displayed together with the jet p_T independent electron identification and trigger efficiency uncertainties. Jet related uncertainties accounting for the JES, JER and jet spectrum unfolding are also displayed together. The dominant systematic uncertainty originates from the boson reconstruction efficiencies at lower jet p_T and choice of generator for higher jet p_T thresholds. Note that the latter displays large uncertainties at high p_T mainly due to lack of statistics in the MC for that region and the ability of acquiring a reliable systematic error is thus limited.

The green band in Figure 7.12 shows the statistical errors added in quadrature to the systematic errors. The red line displays the MCFM predictions together with the uncertainty. The results agree with the MCFM predictions within the respective errors, both in the electron and muon channel. The measurements are dominated by the systematic uncertainty up to a jet p_T threshold of around 50 GeV where the statistical error becomes more and more dominating. The transition occurs at a slightly higher jet p_T for the muon results than for the electron channel, due to the smaller systematic uncertainty at lower jet p_T thresholds.

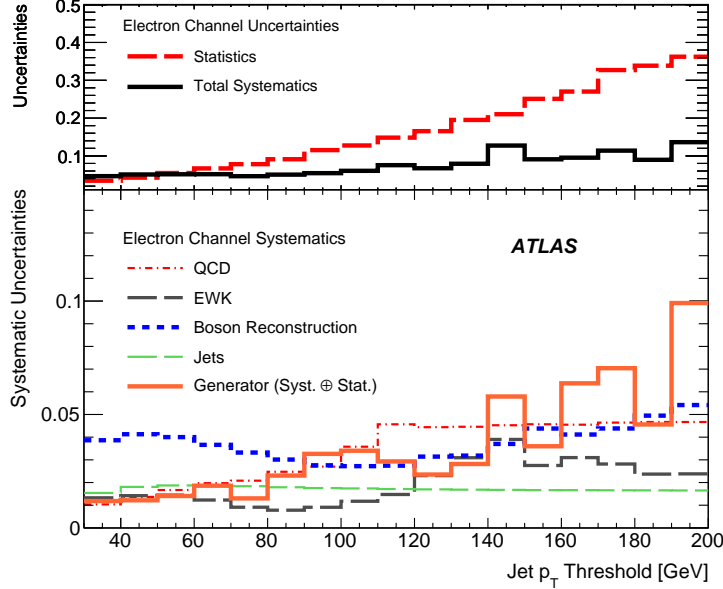


Figure 7.13: The upper histogram shows the total systematic and statistical uncertainty for the \mathcal{R}_{jets} measurement in the electron channel while the lower histogram shows a breakdown of the systematic uncertainties [134].

Figure 7.14 shows the equivalent results to those displayed in Figure 7.12, normalizing the distributions to data. In addition, the theoretical predictions made by PYTHIA and ALPGEN predictions are included in the histogram for comparison. In the electron channel, the data agrees better with MCFM and PYTHIA, than with ALPGEN which estimates a higher \mathcal{R}_{jets} value, as was seen in section 7.1.2.

Combined electron and muon results

In order to reduce the statistical uncertainty, the results obtained in the electron and muon channel are combined. To be able to perform the combination, both channels must be corrected to a common fiducial phase space and particle level definition, which is performed with MC. The corrections applied are the following:

- Both electron and muons results are extended up to $|\eta| < 2.5$ and the electron crack region in $|\eta|$ is interpolated. This is performed with ALPGEN.
- The electron-jet overlap removal and isolation cuts are corrected for in the electron channel, which is performed with PYTHIA.
- The dressed electrons are corrected to bare level using PYTHIA.

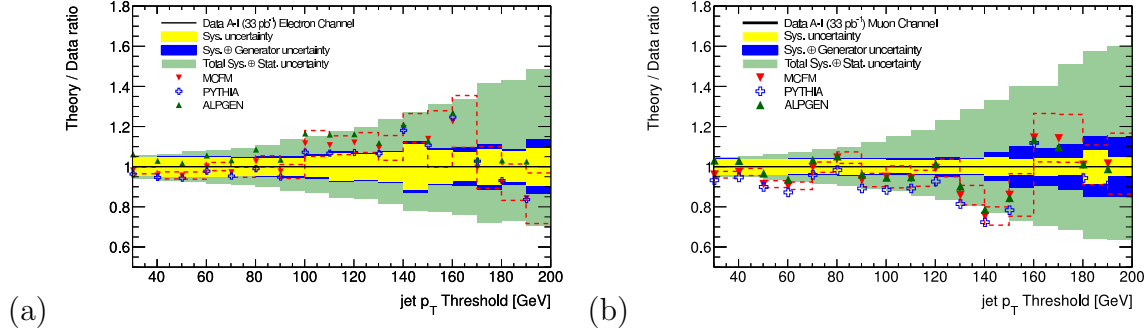


Figure 7.14: Theory/data ratio for the \mathcal{R}_{jets} results in the fiducial phase space for (a) the electron channel and (b) the muon channel. The yellow and blue bands show the total systematic uncertainties and the green band adds the statistical uncertainty. The results are compared to MCFM with errors as well as PYTHIA and ALPGEN without errors [135].

The correlation between the systematic errors in each channel are propagated using the Bayesian Analysis Toolkit (BAT) [146]. The resulting \mathcal{R}_{jets} value as well as the theory/data ratio can be seen in Figure 7.15. The combined results agree well with theoretical predictions and the statistical fluctuations and uncertainties are significantly reduced for higher jet p_T thresholds in comparison with the individual electron and muon results.

7.4.2 Generator level acceptances

In order to correct the fiducial \mathcal{R}_{jets} measurement to full phase space, the generator level acceptance ratio $A_{R_{jets}}$ must be estimated. The acceptances are calculated with respect to exactly one truth jet passing the kinematic cuts ($p_T > 30$ GeV and $|\eta| < 2.8$) as well as the electron-jet overlap removal ($\Delta R < 0.2$) and isolation veto ($\Delta R < 0.6$). The individual acceptances for W and Z are first estimated as a function of jet p_T threshold. $A_{R_{jets}}$ can then be obtained as the ratio of the respective acceptances:

$$A_{W|1jet} = \frac{N_{MC,gen,cuts}}{N_{MC,gen,all|1jet}} \quad (7.10)$$

$$A_{Z|1jet} = \frac{N_{MC,gen,cuts}}{N_{MC,gen,M_{ee}cut|1jet}} \quad (7.11)$$

$$A_{R_{jets}} = \frac{A_{W|1jet}}{A_{Z|1jet}} \quad (7.12)$$

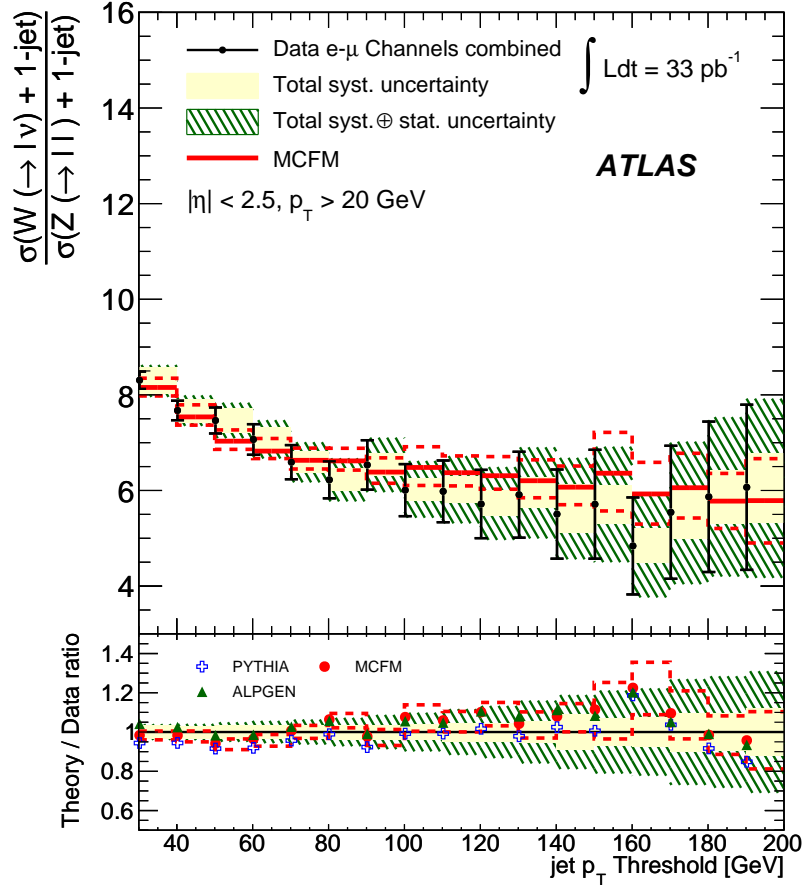


Figure 7.15: The combined \mathcal{R}_{jets} results for the electron and muon channel as well as the theory/data ratio, obtained in a common fiducial phase space ($|\eta| < 2.5$). The yellow band shows the total systematic uncertainties and the green band adds the statistical uncertainty in quadrature. The results are compared to MCFM with errors as well as MCFM, PYTHIA and ALPGEN without errors for the theory/data ratio [134].

In case of $A_{Z|1jet}$, the invariant mass cut is kept at the denominator level.

Dressed electrons are used for the acceptance calculations and the difference between ALPGEN and PYTHIA is taken as the systematic uncertainty. The overall fiducial acceptance ratio for the \mathcal{R}_{jets} measurement has been found to be:

$$A_{Rjets} = 0.897 \pm 0.003(\text{stat}) \pm 0.033(\text{syst}) \quad (7.13)$$

The total systematic uncertainty of 3.3% is a conservative estimate in comparison with the 1.5% that was quoted for the inclusive A_W/A_Z in section 6.2.2.

The resulting acceptance as a function of jet p_T threshold is shown in Figure 7.16, for both the W and Z separately as well as the resulting \mathcal{R}_{jets} acceptance ratio. The fiducial acceptance increases with jet p_T threshold in case of the Z , while the W acceptance show a more flat behavior at lower jet p_T followed by a slight increase.

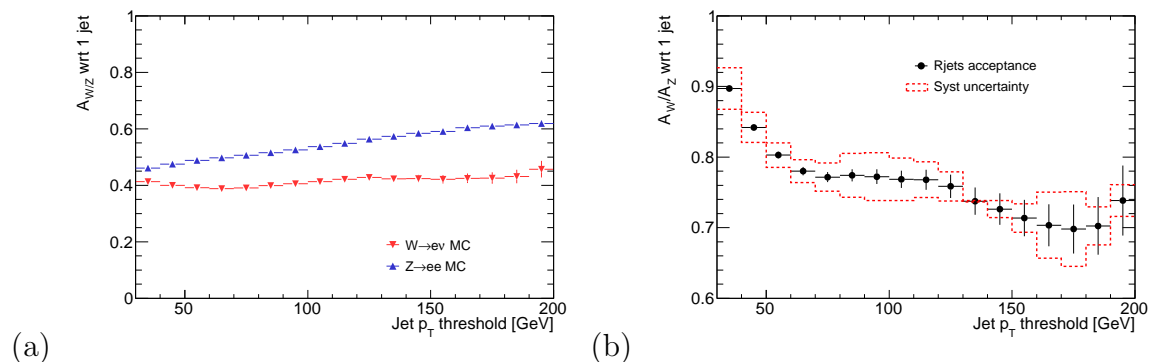


Figure 7.16: The generator level acceptance of the fiducial phase space with respect to exactly one jet passing the jet kinematic cuts. Figure (a) displays the acceptances for W and Z separately and (b) their respective ratio, A_{Rjets} . The ratio hence shows the acceptance used to correct the fiducial \mathcal{R}_{jets} measurement to full phase space. The red line illustrates the difference obtained between ALPGEN and PYTHIA.

Additionally, the dependence of the acceptance as a function of jet multiplicity has been investigated for W , Z and their ratio and is shown in Figure 7.17. The \mathcal{R}_{jets} acceptance ratio decreases with number of jets in the event, mainly due to the increasing of the Z acceptance. The fiducial acceptance of the W does not show any strong trend as a function of jet multiplicity. The value presented in Equation 7.13 thus corresponds to the one jet bin in Figure 7.17b.

7.4.3 \mathcal{R}_{jets} results extrapolated to full phase space

To obtain the \mathcal{R}_{jets} measurement in the total phase space, the estimated acceptance ratio (A_{Rjets}), shown in Figure 7.16b, is applied to the fiducial measurement. The

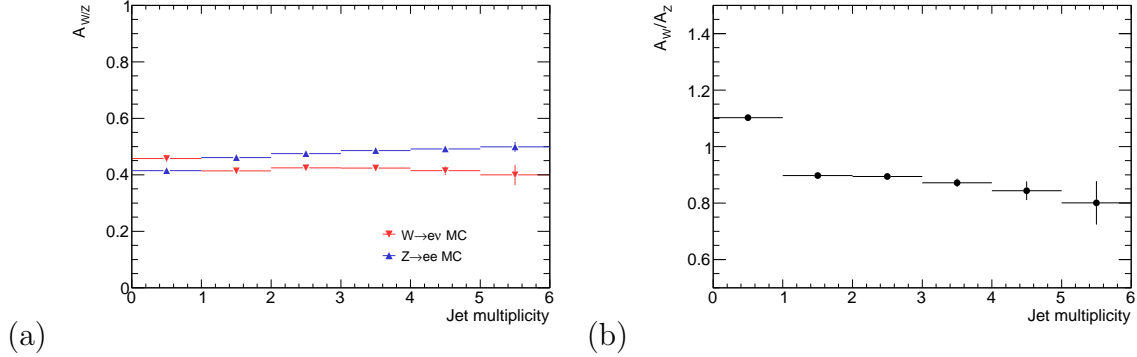


Figure 7.17: The generator level acceptance of the fiducial phase space versus total phase space as a function of jet multiplicity for (a) W and Z separately and (b) their respective ratio.

results can be seen in Figure 7.18 for the electron as well as the muon channel. The results agree also here with theoretical predictions within uncertainties, which are larger than for the fiducial measurement due to the additional error on the acceptance correction.

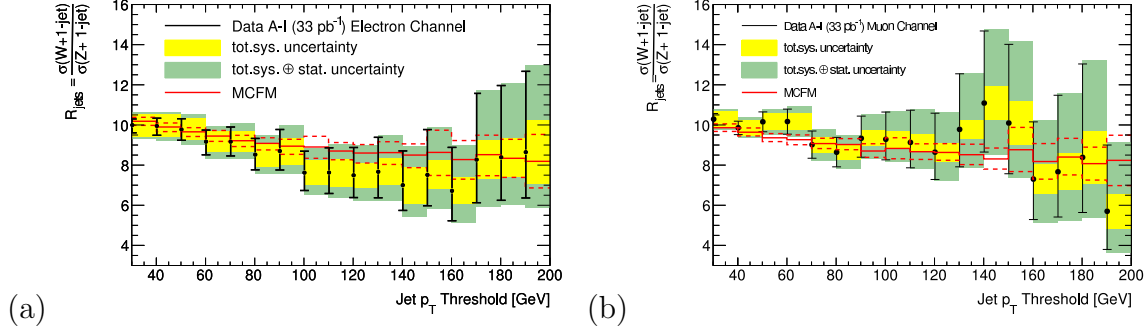


Figure 7.18: \mathcal{R}_{jets} results in the total phase space for (a) the electron channel and (b) the muon channel. The results are compared to MCFM predictions. The yellow band shows the total systematic uncertainty and the green band adds the statistical uncertainty in quadrature. The black error bars show the pure statistical uncertainties [135].

Combined electron and muon results

Also for the full phase space results, the electron and muon channels are combined in order to reduce the statistical uncertainty. Here, only the electron-jet overlap removal and isolation requirement must be corrected for in the electron channel in order to

have a common phase space for the electron and muon results. This correction is performed with PYTHIA.

The results are shown in Figure 7.19 and agree well with MC predictions for all the different generators. At this level, the measurement is dominated by systematic uncertainties up to a higher jet p_T threshold, due to the additional uncertainty from the generator level acceptance correction as well as the decreased statistical uncertainty obtained by combining the results. The statistical uncertainty becomes dominating at a jet p_T threshold of about 60 GeV.

ALPGEN-Pythia comparison

Figure 7.2 above shows that the \mathcal{R}_{jets} prediction for the electron channel, obtained with ALPGEN yields an overall higher results than PYTHIA and MC@NLO. This was again confirmed for the fiducial results in Figure 7.14a, where the theory/data ratio is shown, including ALPGEN and PYTHIA. Here, MCFM is also included which agrees well with the PYTHIA prediction and disagrees with the high ALPGEN value. Figure 7.14b shows the equivalent results for the muon channel where the ALPGEN prediction agrees somewhat better with the other MC generators as well as data. Figure 7.15 shows the combined electron and muon results for the common fiducial phase space and here the discrepancy between ALPGEN and the other results is almost negligible.

The main difference between these predictions is the fiducial region in η as well as whether or not the electron-jet overlap removal and isolation veto is applied. In order to further investigate the dependence of the choice of generator for different η regions, the \mathcal{R}_{jets} measurement with a jet p_T threshold of 30 GeV is shown in Figure 7.20 as a function of η . The figure shows the prediction for full phase space and indeed there is a large discrepancy between PYTHIA and ALPGEN explaining the different levels of agreement seen for different fiducial regions.

The predictions for the \mathcal{R}_{jets} measurement at full phase space for the muon (common) phase space presented in Figure 7.19, only shows a discrepancy of a few percent. The PYTHIA-ALPGEN discrepancy for the electron channel at full phase space, displayed in Figure 7.2, is about twice as large, implying that also the modeling of the distance between electrons and jets has an impact on the generator predictions, since the electron-jet overlap removal and isolation is the only difference between the distributions in the two figures.

7.5 Conclusion

The \mathcal{R}_{jets} analysis is an interesting measurement that can be used as a precise Standard Model probe and is sensitive to new physics with final states of one or two

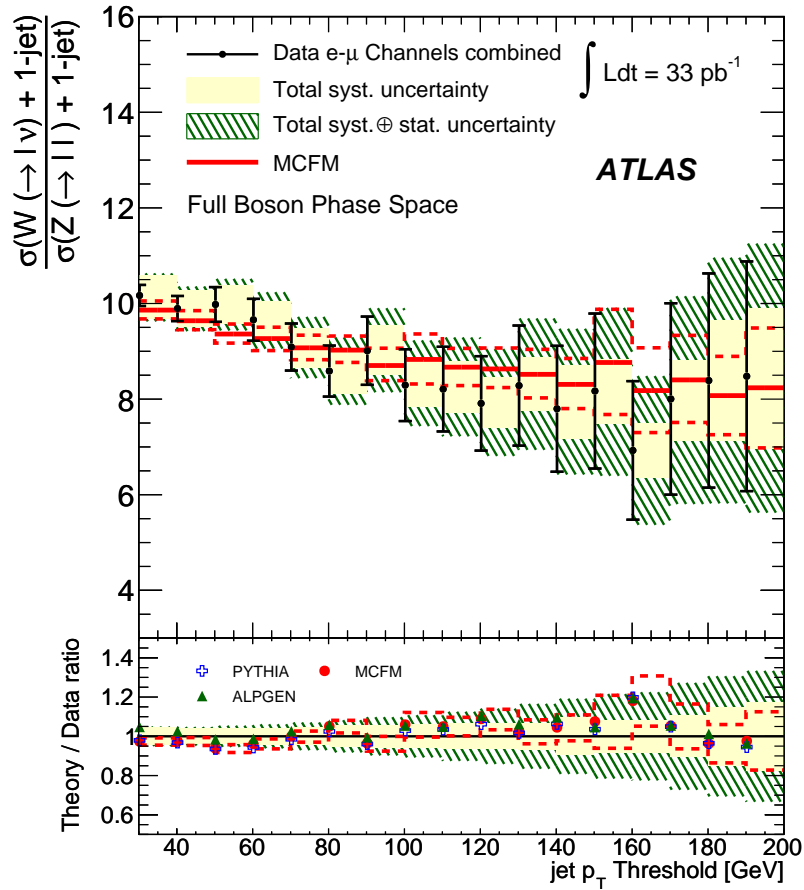


Figure 7.19: The combined \mathcal{R}_{jets} results for the electron and muon channel as well as the theory/data ratio, obtained at the full phase space. The yellow band shows the total systematic uncertainties and the green band adds the statistical uncertainty in quadrature. The results are compared to MCFM with errors as well as MCFM, PYTHIA and ALPGEN without errors for the theory/data ratio [134].

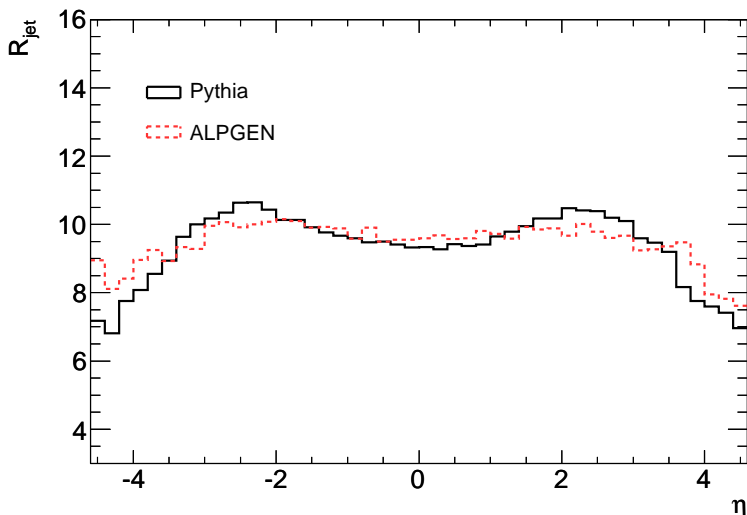


Figure 7.20: \mathcal{R}_{jets} predictions as a function of electron η for a jet p_T threshold of 30 GeV obtained with ALPGEN and PYTHIA at full phase space level.

leptons in the presence of hard jets. The measurement can be performed in several dimensions, such as as a function of jet multiplicity or jet H_T for different jet multiplicities.

Due to the limited statistics of the 2010 data, the \mathcal{R}_{jets} measurement presented in this thesis is completed in the exclusive one-jet bin; $\mathcal{R}_{jets} = \sigma(W + 1jet)/\sigma(Z + 1jet)$, as a function of cumulative jet p_T threshold ranging from 30 to 190 GeV. This is the first time such a measurement has been performed and the results agree with perturbative LO and NLO QCD predictions both for the electron and muon channel as well as combined. The results are shown both for the fiducial volume, which the measurement is performed within, as well as corrected to the full phase space.

The statistical and systematic uncertainty of the \mathcal{R}_{jets} results are compatible in the low kinematic region, while the statistical uncertainty completely dominates the uncertainty of the ratio for the higher jet p_T thresholds, starting from 50-60 GeV.

With larger statistics at hand, the \mathcal{R}_{jets} measurement can be completed also for higher jet multiplicities as well as for higher jet p_T thresholds. It would then be important to reduce the systematic uncertainty to improve the sensitivity of the measurement. This, however, is not a simple task since the analysis includes many crucial components which need to be well understood, such as leptons, jets and E_T^{miss} . One prerequisite to decrease the uncertainties in the higher p_T region is to increase the size of the simulated $W + jets$ and $Z + jets$ samples, which lack the statistics to study the high jet p_T range with sufficient precision.

Chapter 8

Conclusions

The first years of ATLAS operation have resulted in successful data taking and physics analysis results. Prior to first LHC collisions, the detector recorded cosmic ray muon events, which assisted in studying the performance and calibration of the detector. In particular, this thesis presents the commissioning of the Semiconductor Tracker with cosmic ray data, with emphasis on the development of the data quality monitoring framework. In addition, an analysis identifying 834 delta-ray electrons, extracted from the millions of cosmic ray muon tracks recorded by ATLAS in 2008 and 2009, was completed.

Approximately 40 pb^{-1} of 7 TeV p - p collision data were recorded by ATLAS during 2010, which was used to analyze $W \rightarrow e\nu$ and $Z \rightarrow ee$ signatures in this thesis. Some of the most crucial components of W/Z cross section measurements originate from electron performance studies in data. The electron reconstruction, identification and trigger efficiencies have been measured with a data-driven tag-and-probe technique using $Z \rightarrow ee$ events. In the 2010 data, the statistics of about 10k $Z \rightarrow ee$ events permit the efficiencies to be derived in one dimension, as a function of electron η and E_T separately. The results have been found to deviate from the Monte Carlo predictions at the level of a couple of percent. The development of a robust electron efficiency measurement in data is of crucial importance for any physics analysis conducted in the electron channel.

The first W and Z inclusive cross section measurements in ATLAS were completed with less than a hundred $W \rightarrow e\nu/Z \rightarrow ee$ candidates. These first measurements lacked of data-driven studies and thus relied to a large extent on MC predictions. Although the first results were assigned large systematic errors, the dominating uncertainties were due to the limited statistics. As more data became available, data-driven techniques were incorporated into the analysis, such as for the electron efficiencies. The final inclusive cross section results, measured with the full 2010 dataset, have a reduced systematic uncertainty of about a factor four in comparison with the first

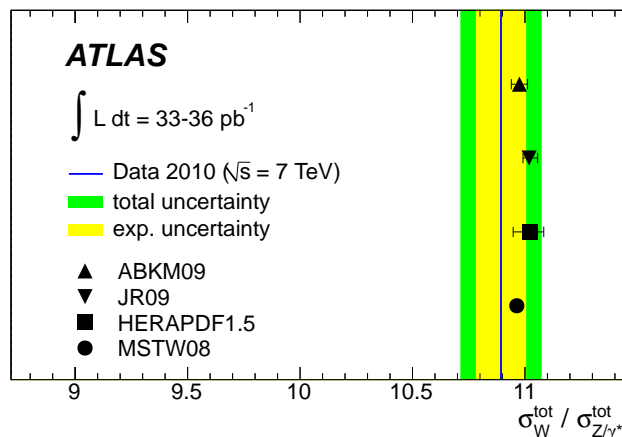


Figure 8.1: Measured and predicted W/Z cross section ratio, estimated with the combined electron and muon 2010 data results. The experimental uncertainty of the measurement includes statistical and systematic errors. The ratio is compared to NNLO theoretical predictions obtained with different PDF sets, where the uncertainty is due to the PDFs only [102].

measurements. The measured final $W \rightarrow e\nu$ and $Z \rightarrow ee$ production cross section values are:

$$\begin{aligned}\sigma(W \rightarrow e\nu) &= 10.255 \pm 0.031(\text{stat}) \pm 0.190(\text{syst}) \pm 0.349(\text{lumi}) \pm 0.156(\text{acc}) \text{ nb} \\ \sigma(Z \rightarrow ee) &= 0.952 \pm 0.010(\text{stat}) \pm 0.026(\text{syst}) \pm 0.032(\text{lumi}) \pm 0.019(\text{acc}) \text{ nb}\end{aligned}$$

The results agree with NNLO theoretical predictions within the uncertainties, and are no longer limited by the statistics, but rather the uncertainty of the luminosity. The dominating systematic uncertainties of the cross section measurements originate from the electron reconstruction and identification efficiencies as well as the missing transverse energy in case of the W . Combining the electron and muon cross section results and computing the W/Z cross section ratio has the advantage of several cancellations of uncertainties, such as partial cancellation of the electron reconstruction and identification efficiency uncertainties and full cancellation of the luminosity uncertainty. Figure 8.1 shows the measured cross section ratio together with NNLO theoretical predictions obtained with different PDFs. The measured ratio is compatible with all PDF values within the total uncertainty.

Differential cross section results, derived as a function of electron pseudorapidity in case of the W and boson rapidity in case of the Z , are also presented in this thesis. Differential measurements display a larger sensitivity to the PDFs and can hence

be used for improving the theoretical modeling of perturbative QCD. The measured differential cross section results are subject to statistical and systematic uncertainties at an equal level. Conducting performance studies in order to reduce the systematic uncertainties together with incorporating larger statistics would therefore improve future measurements.

As an extension of the W/Z inclusive cross section, measurements concerning W/Z bosons in association with jets have been performed. In particular, the W and Z cross section ratio in association with one jet (\mathcal{R}_{jets}) has been measured as a function of minimum jet p_T threshold ranging from 30 to 190 GeV. A great advantage of this analysis is the cancellation of uncertainties in the ratio, especially jet uncertainties such as for example the energy scale corrections. Due to the reduced uncertainty, the measurement has an elevated sensitivity to potential new physics with leptons, E_T^{miss} and hard jets as final state signatures. In addition, the \mathcal{R}_{jets} measurement provides a stringent test of the Standard Model description of the strong interaction in perturbative QCD.

With the 2010 data sample, the \mathcal{R}_{jets} measurement is statistically limited by the $Z + 1$ jet events in the interesting region of higher jet p_T thresholds. The results are found to be in agreement with perturbative LO and NLO QCD predictions within uncertainties, which are statistically dominated for jet p_T thresholds above 60 GeV. It would thus be of great interest to conduct the \mathcal{R}_{jets} measurement with the larger data sample collected by ATLAS in 2011. With more statistics at hand, the measurement could be completed for higher jet p_T thresholds as well as for higher jet multiplicities.

Appendix A

2010 Data Periods

Table A.1 shows the integrated luminosity recorded by ATLAS for the different data periods in 2010. No good run list is applied. The exponential increase in instantaneous luminosity is reflected in the amount of recorded data per period.

data period	subperiod	run number range	integrated luminosity (nb ⁻¹)
A	-	152166-153200	0.4
B	B1-B2	153565-155160	9
C	C1-C2	155228-156682	9.5
D	D1-D6	158045-159224	320
E	E1-E7	160387-161948	1118
F	F1-F2	162347-162882	1980
G	G1-G6	165591-166383	9070
H	H1-H2	166466-166964	9300
I	I1-I2	167575-167844	23000

Table A.1: Table showing the different data periods in 2010 without any good run list applied.

Appendix B

Tag-and-probe efficiency and background tables

Track quality		
η	data efficiency (%)	data/MC SF (%)
-2.47,-2.01	93.09 ± 1.05	99.30 ± 1.13
-2.01,-1.52	95.15 ± 0.95	101.18 ± 1.02
-1.52,-1.37	96.15 ± 1.61	100.13 ± 1.68
-1.37,-0.8	97.67 ± 0.56	99.94 ± 0.58
-0.8,0	98.93 ± 0.36	100.33 ± 0.36
0,0.8	98.48 ± 0.37	99.81 ± 0.37
0.8,1.37	98.18 ± 0.51	100.45 ± 0.53
1.37,1.52	96.46 ± 1.82	100.44 ± 1.90
1.52,2.01	96.25 ± 0.91	102.51 ± 0.98
2.01,2.47	93.67 ± 1.07	100.28 ± 1.15

Table B.1: Data-driven efficiencies from Z tag-and-probe and data/MC scale factors as a function of η for the track quality cut with respect to container. Track quality implies at least 7 silicon hits whereas at least one hit in the Pixel detector. The numbers are obtained for electron within $20 < E_T < 50$ GeV.

Loose identification		
η	data efficiency (%)	data/MC SF (%)
-2.47,-2.01	97.24 ± 1.50	98.83 ± 1.52
-2.01,-1.52	94.02 ± 1.20	95.12 ± 1.21
-1.52,-1.37	96.55 ± 2.29	101.69 ± 2.41
-1.37,-0.8	97.45 ± 0.95	99.08 ± 0.97
-0.8,0	97.61 ± 0.70	99.48 ± 0.71
0,0.8	98.64 ± 0.64	100.51 ± 0.66
0.8,1.37	99.32 ± 0.85	100.86 ± 0.86
1.37,1.52	95.26 ± 2.46	100.52 ± 2.59
1.52,2.01	99.37 ± 1.12	100.50 ± 1.13
2.01,2.47	97.25 ± 1.53	98.72 ± 1.56

Table B.2: Data-driven efficiencies from Z tag-and-probe and data/MC scale factors as a function of η for loose identification cuts with respect to track quality. The numbers are obtained for electron within $20 < E_T < 50$ GeV.

Medium identification		
η	data efficiency (%)	data/MC SF (%)
-2.47,-2.01	95.21 ± 1.56	98.14 ± 1.61
-2.01,-1.52	92.66 ± 1.25	95.54 ± 1.29
-1.52,-1.37	95.44 ± 2.40	101.14 ± 2.54
-1.37,-0.8	95.72 ± 1.00	98.84 ± 1.03
-0.8,0	93.26 ± 0.77	98.27 ± 0.81
0,0.8	95.15 ± 0.71	99.44 ± 0.74
0.8,1.37	96.93 ± 0.91	99.98 ± 0.94
1.37,1.52	95.72 ± 2.48	101.53 ± 2.63
1.52,2.01	97.89 ± 1.17	100.88 ± 1.21
2.01,2.47	95.87 ± 1.57	98.69 ± 1.62

Table B.3: Data-driven efficiencies from Z tag-and-probe and data/MC scale factors as a function of η for medium identification cuts with respect to track quality. The numbers are obtained for electron within $20 < E_T < 50$ GeV.

Tight identification		
η	data efficiency (%)	data/MC SF (%)
-2.47,-2.01	71.95 ± 1.89	97.37 ± 2.57
-2.01,-1.52	74.54 ± 1.52	101.79 ± 2.09
-1.52,-1.37	72.79 ± 2.87	116.90 ± 4.63
-1.37,-0.8	80.26 ± 1.19	105.95 ± 1.58
-0.8,0	82.90 ± 0.88	100.22 ± 1.07
0,0.8	84.47 ± 0.83	100.89 ± 0.99
0.8,1.37	83.61 ± 1.09	109.97 ± 1.43
1.37,1.52	69.57 ± 3.03	111.81 ± 4.88
1.52,2.01	80.19 ± 1.50	109.35 ± 2.05
2.01,2.47	75.41 ± 1.92	102.45 ± 2.62

Table B.4: Data-driven efficiencies from Z tag-and-probe and data/MC scale factors as a function of η for tight identification cuts with respect to track quality. The numbers are obtained for electron within $20 < E_T < 50$ GeV.

Background (%)	Total	20,25 GeV	25,30 GeV	30,35 GeV	35,40 GeV	40,45 GeV	45,50 GeV	50,80 GeV
Container	9.92 ± 0.76	39.4 ± 3.0	19.9 ± 2.5	8.1 ± 2.0	2.8 ± 1.7	1.3 ± 1.7	2.4 ± 2.2	7.5 ± 2.3
Loose	1.40 ± 0.78	6.3 ± 3.7	2.3 ± 2.7	0.4 ± 2.0	0.0 ± 1.7	0.0 ± 1.5	0.3 ± 2.1	3.2 ± 2.4
Medium	0.64 ± 0.81	1.9 ± 3.7	1.3 ± 2.7	0.1 ± 2.0	0.0 ± 1.7	0.0 ± 1.6	0.2 ± 2.2	2.8 ± 2.4
Tight	0.60 ± 0.89	0.0 ± 2.5	0.0 ± 2.5	0.0 ± 2.5	0.0 ± 2.5	0.0 ± 2.5	0.0 ± 2.5	0.0 ± 2.5

Table B.5: Estimated background fractions binned in E_T for container, loose, medium and tight probes through the method of fitting the the invariant mass.

Efficiency (%)	Total	20,25 GeV	25,30 GeV	30,35 GeV	35,40 GeV	40,45 GeV	45,50 GeV	50,80 GeV
Loose Eff	97.27 ± 1.16	95.13 ± 6.23	94.27 ± 4.04	96.25 ± 2.94	96.11 ± 2.35	96.90 ± 2.23	97.19 ± 3.04	95.91 ± 3.36
Loose SF	98.80 ± 1.18	98.50 ± 6.45	96.71 ± 4.15	98.23 ± 3.00	97.67 ± 2.39	98.02 ± 2.25	98.08 ± 3.07	96.77 ± 3.39
Medium Eff	92.00 ± 1.09	89.49 ± 5.66	88.10 ± 3.67	90.14 ± 2.69	90.26 ± 2.18	91.25 ± 2.10	92.62 ± 2.86	91.25 ± 3.15
Medium SF	98.34 ± 1.16	92.66 ± 5.86	90.39 ± 3.77	91.99 ± 2.74	91.73 ± 2.22	92.31 ± 2.12	93.46 ± 2.89	92.07 ± 3.17
Tight Eff	78.69 ± 0.91	75.41 ± 3.92	71.86 ± 2.39	75.65 ± 1.75	77.23 ± 1.43	78.89 ± 1.37	81.85 ± 1.90	83.11 ± 2.11
Tight SF	102.52 ± 1.19	78.08 ± 4.06	73.72 ± 2.45	77.21 ± 1.79	78.48 ± 1.45	79.80 ± 1.39	82.59 ± 1.92	83.86 ± 2.13

Table B.6: Data-driven efficiencies and data/MC scale factors as a function of E_T for loose, medium and tight identification. The background has been subtracted in data through the method of fitting the invariant mass.

Background (%)	Total	20,25 GeV	25,30 GeV	30,35 GeV	35,40 GeV	40,45 GeV	45,50 GeV	50,80 GeV
Container	9.2 ± 0.6	40.0 ± 2.1	17.5 ± 1.0	8.0 ± 0.6	4.3 ± 0.4	2.7 ± 0.3	3.3 ± 0.4	7.1 ± 0.6
Loose	0.6 ± 0.6	3.9 ± 0.7	1.4 ± 0.3	0.5 ± 0.1	0.3 ± 0.1	0.2 ± 0.1	0.2 ± 0.1	0.5 ± 0.2
Medium	0.1 ± 0.1	0.5 ± 0.1	0.2 ± 0.0	0.1 ± 0.0	0.0 ± 0.0	0.0 ± 0.0	0.0 ± 0.0	0.1 ± 0.0
Tight	0.0 ± 0.0	0.1 ± 0.0	0.0 ± 0.0					

Table B.7: Estimated background fractions binned in E_T for container, loose, medium and tight probes through the method of fitting the E_T spectrum directly to assess the background shape.

Efficiency (%)	Total	20,25 GeV	25,30 GeV	30,35 GeV	35,40 GeV	40,45 GeV	45,50 GeV	50,80 GeV
Loose Eff	97.1 ± 0.8	97.6 ± 3.4	92.4 ± 1.2	96.0 ± 0.6	97.4 ± 0.4	98.1 ± 0.3	98.4 ± 0.4	98.4 ± 0.7
Loose SF	98.6 ± 0.8	101.0 ± 3.5	94.8 ± 1.2	98.0 ± 0.6	99.0 ± 0.4	99.2 ± 0.3	99.3 ± 0.4	99.3 ± 0.7
Medium Eff	91.6 ± 0.6	90.8 ± 3.1	86.5 ± 1.1	90.2 ± 0.5	91.7 ± 0.3	92.5 ± 0.2	93.8 ± 0.4	93.8 ± 0.6
Medium SF	97.9 ± 0.7	100.5 ± 3.4	94.0 ± 1.2	97.4 ± 0.6	98.1 ± 0.4	98.4 ± 0.3	98.9 ± 0.4	98.8 ± 0.7
Tight Eff	78.4 ± 0.5	74.8 ± 2.6	70.2 ± 0.9	75.6 ± 0.5	78.3 ± 0.3	79.7 ± 0.2	82.6 ± 0.3	82.9 ± 0.5
Tight SF	102.1 ± 0.7	108.7 ± 3.7	97.8 ± 1.2	101.7 ± 0.6	102.8 ± 0.4	102.0 ± 0.3	103.4 ± 0.4	102.2 ± 0.7

Table B.8: Data-driven efficiencies and data/MC scale factors as a function of E_T for loose, medium and tight identification. The background has been subtracted in data through the method of fitting the E_T spectrum directly to assess the shape.

APPENDIX B. TAG-AND-PROBE EFFICIENCY AND BACKGROUND TABLES

b-layer				
η	No bkg subtraction (%)		With bkg subtraction (%)	
	data efficiency	data/MC SF	data efficiency	data/MC SF
-2.47,-2.18	88.74 ± 1.52	103.22 ± 1.77	88.88 ± 1.54	103.38 ± 1.79
-2.18,-1.95	94.43 ± 1.06	100.58 ± 1.13	94.64 ± 1.07	100.80 ± 1.15
-1.95,-1.74	91.20 ± 1.40	97.00 ± 1.49	91.50 ± 1.42	97.32 ± 1.52
-1.74,-1.52	96.41 ± 0.81	101.37 ± 0.85	96.57 ± 0.82	101.55 ± 0.87
-1.52,-1.37	96.85 ± 0.94	99.87 ± 0.97	96.82 ± 0.94	99.84 ± 0.98
-1.37,-1.05	97.66 ± 0.49	100.34 ± 0.51	97.71 ± 0.50	100.38 ± 0.51
-1.05,-0.84	97.53 ± 0.59	100.01 ± 0.61	97.59 ± 0.60	100.07 ± 0.62
-0.84,-0.63	98.22 ± 0.49	100.64 ± 0.50	98.22 ± 0.49	100.63 ± 0.50
-0.63,-0.42	97.26 ± 0.58	99.62 ± 0.59	97.25 ± 0.58	99.62 ± 0.59
-0.42,-0.21	99.05 ± 0.36	101.46 ± 0.37	99.05 ± 0.36	101.46 ± 0.37
-0.21,0	98.80 ± 0.42	101.31 ± 0.44	98.87 ± 0.43	101.39 ± 0.44
0,0.21	97.69 ± 0.52	100.14 ± 0.54	97.69 ± 0.52	100.14 ± 0.54
0.21,0.42	98.41 ± 0.44	100.79 ± 0.45	98.53 ± 0.45	100.91 ± 0.46
0.42,0.63	98.21 ± 0.46	100.48 ± 0.47	98.26 ± 0.46	100.54 ± 0.48
0.63,0.84	98.10 ± 0.49	100.32 ± 0.50	98.10 ± 0.49	100.32 ± 0.50
0.84,1.05	98.99 ± 0.35	101.26 ± 0.37	99.05 ± 0.36	101.32 ± 0.37
1.05,1.37	98.02 ± 0.43	100.49 ± 0.44	98.06 ± 0.43	100.54 ± 0.44
1.37,1.52	96.83 ± 0.99	99.41 ± 1.02	96.81 ± 0.99	99.39 ± 1.02
1.52,1.74	96.45 ± 0.82	101.00 ± 0.86	96.63 ± 0.84	101.19 ± 0.88
1.74,1.95	94.70 ± 1.03	100.97 ± 1.10	94.80 ± 1.04	101.07 ± 1.1
1.95,2.18	96.04 ± 0.92	101.92 ± 0.98	96.14 ± 0.92	102.03 ± 0.99
2.18,2.47	86.93 ± 1.69	101.73 ± 1.98	87.34 ± 1.72	102.21 ± 2.02

Table B.9: Data-driven efficiencies from Z tag-and-probe and data/MC scale factors as a function of η for the b-layer cut with respect to medium identification. The numbers are obtained for electron within $20 < E_T < 50$ GeV with and without background subtraction applied.

Isolation		
η	data efficiency (%)	data/MC SF (%)
-2.47,-2.18	94.25 \pm 1.12	97.84 \pm 1.16
-2.18,-1.95	95.50 \pm 0.96	97.59 \pm 0.98
-1.95,-1.74	96.58 \pm 0.90	98.45 \pm 0.92
-1.74,-1.52	98.49 \pm 0.53	100.82 \pm 0.55
-1.52,-1.37	97.42 \pm 0.85	100.16 \pm 0.88
-1.37,-1.05	97.02 \pm 0.55	99.06 \pm 0.57
-1.05,-0.84	96.66 \pm 0.69	98.78 \pm 0.70
-0.84,-0.63	96.03 \pm 0.72	98.30 \pm 0.74
-0.63,-0.42	96.38 \pm 0.66	98.62 \pm 0.68
-0.42,-0.21	97.96 \pm 0.52	100.26 \pm 0.54
-0.21,0	97.59 \pm 0.60	99.72 \pm 0.61
0,0.21	97.32 \pm 0.56	99.44 \pm 0.58
0.21,0.42	97.19 \pm 0.58	99.55 \pm 0.59
0.42,0.63	97.14 \pm 0.58	99.38 \pm 0.59
0.63,0.84	96.32 \pm 0.67	98.63 \pm 0.69
0.84,1.05	96.34 \pm 0.67	98.50 \pm 0.68
1.05,1.37	97.45 \pm 0.48	99.60 \pm 0.50
1.37,1.52	94.29 \pm 1.31	96.40 \pm 1.34
1.52,1.74	98.42 \pm 0.55	100.37 \pm 0.57
1.74,1.95	97.46 \pm 0.72	99.46 \pm 0.74
1.95,2.18	96.48 \pm 0.87	98.54 \pm 0.89
2.18,2.47	93.47 \pm 1.24	97.76 \pm 1.30

Table B.10: Data-driven efficiencies from Z tag-and-probe and data/MC scale factors as a function of η for the isolation cut (*caloIso98*) with respect to medium identification. The numbers are obtained for electron within $20 < E_T < 50$ GeV.

Isolation + b-layer		
η	data efficiency (%)	data/MC SF (%)
-2.47,-2.18	83.91 ± 1.76	101.25 ± 2.13
-2.18,-1.95	90.58 ± 1.35	98.52 ± 1.48
-1.95,-1.74	87.78 ± 1.62	95.13 ± 1.76
-1.74,-1.52	94.90 ± 0.96	102.15 ± 1.04
-1.52,-1.37	94.27 ± 1.24	99.92 ± 1.32
-1.37,-1.05	94.79 ± 0.73	99.38 ± 0.76
-1.05,-0.84	94.48 ± 0.87	98.97 ± 0.91
-0.84,-0.63	94.25 ± 0.86	98.81 ± 0.90
-0.63,-0.42	93.77 ± 0.85	98.24 ± 0.90
-0.42,-0.21	97.01 ± 0.63	101.67 ± 0.66
-0.21,0	96.39 ± 0.72	100.96 ± 0.76
0,0.21	95.01 ± 0.76	99.46 ± 0.80
0.21,0.42	95.85 ± 0.70	100.51 ± 0.73
0.42,0.63	95.35 ± 0.73	99.77 ± 0.76
0.63,0.84	94.54 ± 0.81	98.97 ± 0.85
0.84,1.05	95.46 ± 0.74	99.79 ± 0.78
1.05,1.37	95.46 ± 0.64	100.01 ± 0.67
1.37,1.52	92.38 ± 1.49	96.96 ± 1.57
1.52,1.74	94.87 ± 0.98	101.28 ± 1.05
1.74,1.95	92.16 ± 1.24	100.22 ± 1.35
1.95,2.18	92.51 ± 1.24	100.22 ± 1.34
2.18,2.47	81.41 ± 1.95	99.47 ± 2.39

Table B.11: Data-driven efficiencies from Z tag-and-probe and data/MC scale factors as a function of η for the isolation and b-layer cuts with respect to medium identification. The numbers are obtained for electron within $20 < E_T < 50$ GeV.

Isolation with respect to medium + b-layer		
η	data efficiency (%)	data/MC SF (%)
-2.47,-2.18	94.56 \pm 1.15	98.09 \pm 1.20(stat) \pm 0.91(syst)
-2.18,-1.95	95.92 \pm 0.94	97.95 \pm 0.96(stat) \pm 0.26(syst)
-1.95,-1.74	96.25 \pm 0.98	98.08 \pm 1.00(stat) \pm 0.11(syst)
-1.74,-1.52	98.43 \pm 0.55	100.76 \pm 0.57(stat) \pm 0.30(syst)
-1.52,-1.37	97.34 \pm 0.88	100.05 \pm 0.90(stat) \pm 0.51(syst)
-1.37,-1.05	97.06 \pm 0.56	99.05 \pm 0.57(stat) \pm 0.12(syst)
-1.05,-0.84	96.87 \pm 0.67	98.96 \pm 0.69(stat) \pm 0.23(syst)
-0.84,-0.63	95.96 \pm 0.73	98.18 \pm 0.75(stat) \pm 0.08(syst)
-0.63,-0.42	96.41 \pm 0.67	98.61 \pm 0.68(stat) \pm 0.15(syst)
-0.42,-0.21	97.94 \pm 0.53	100.20 \pm 0.54(stat) \pm 0.05(syst)
-0.21,0	97.56 \pm 0.60	99.65 \pm 0.62(stat) \pm 0.19(syst)
0,0.21	97.26 \pm 0.58	99.32 \pm 0.59(stat) \pm 0.18(syst)
0.21,0.42	97.39 \pm 0.56	99.72 \pm 0.58(stat) \pm 0.19(syst)
0.42,0.63	97.08 \pm 0.59	99.29 \pm 0.60(stat) \pm 0.25(syst)
0.63,0.84	96.38 \pm 0.67	98.66 \pm 0.69(stat) \pm 0.23(syst)
0.84,1.05	96.43 \pm 0.66	98.55 \pm 0.68(stat) \pm 0.68(syst)
1.05,1.37	97.40 \pm 0.49	99.52 \pm 0.51(stat) \pm 0.15(syst)
1.37,1.52	95.41 \pm 1.20	97.54 \pm 1.23(stat) \pm 0.67(syst)
1.52,1.74	98.36 \pm 0.57	100.27 \pm 0.59(stat) \pm 0.36(syst)
1.74,1.95	97.32 \pm 0.76	99.26 \pm 0.78(stat) \pm 0.16(syst)
1.95,2.18	96.33 \pm 0.90	98.33 \pm 0.92(stat) \pm 0.31(syst)
2.18,2.47	93.64 \pm 1.31	97.77 \pm 1.37(stat) \pm 0.22(syst)

Table B.12: Data-driven efficiencies from Z tag-and-probe and data/MC scale factors as a function of η for the isolation cut with respect to medium ID + b-layer. The numbers are obtained for electron within $20 < E_T < 50$ GeV.

Medium + b-layer (%)						
η	positive electron			negative electron		
	data efficiency	data/MC SF	data/MC SF	data efficiency	data/MC SF	data/MC SF
-2.47,-2.18	85.58 \pm 1.20	103.21 \pm 1.45(stat) \pm 0.81(syst)	83.65 \pm 1.67	103.13 \pm 2.06(stat) \pm 0.73(syst)		
-2.18,-1.95	88.90 \pm 1.26	97.81 \pm 1.39(stat) \pm 0.55(syst)	89.27 \pm 1.80	98.60 \pm 1.99 (stat) \pm 1.45(syst)		
-1.95,-1.74	89.40 \pm 1.36	98.10 \pm 1.50(stat) \pm 0.90(syst)	86.61 \pm 1.90	95.83 \pm 2.10 (stat) \pm 1.08(syst)		
-1.74,-1.52	90.49 \pm 1.36	97.41 \pm 1.47(stat) \pm 0.66(syst)	88.97 \pm 1.73	96.28 \pm 1.87 (stat) \pm 0.78(syst)		
-1.52,-1.37	-	-	-	-		
-1.37,-1.05	91.24 \pm 1.19	96.27 \pm 1.26(stat) \pm 0.64(syst)	91.95 \pm 1.53	96.78 \pm 1.61(stat) \pm 1.28(syst)		
-1.05,-0.84	92.48 \pm 1.39	98.19 \pm 1.48(stat) \pm 1.53(syst)	92.85 \pm 1.92	98.32 \pm 2.04(stat) \pm 1.02(syst)		
-0.84,-0.63	93.14 \pm 1.45	98.43 \pm 1.54(stat) \pm 0.50(syst)	88.87 \pm 1.92	93.74 \pm 2.03(stat) \pm 0.66(syst)		
-0.63,-0.42	92.52 \pm 1.47	98.25 \pm 1.56(stat) \pm 0.57(syst)	91.66 \pm 1.68	97.46 \pm 1.79(stat) \pm 0.61(syst)		
-0.42,-0.21	92.13 \pm 1.59	98.04 \pm 1.70(stat) \pm 0.68(syst)	92.56 \pm 1.77	98.41 \pm 1.88(stat) \pm 0.98(syst)		
-0.21,0	88.73 \pm 1.48	97.13 \pm 1.62(stat) \pm 0.58(syst)	89.31 \pm 1.89	98.00 \pm 2.08(stat) \pm 0.35(syst)		
0,0.21	92.16 \pm 1.55	100.15 \pm 1.69(stat) \pm 0.99(syst)	90.93 \pm 1.82	98.77 \pm 1.98(stat) \pm 1.25(syst)		
0.21,0.42	92.97 \pm 1.35	98.63 \pm 1.44(stat) \pm 0.58(syst)	93.31 \pm 1.78	99.11 \pm 1.89(stat) \pm 0.76(syst)		
0.42,0.63	91.94 \pm 1.29	97.78 \pm 1.38(stat) \pm 0.68(syst)	91.96 \pm 1.74	97.39 \pm 1.85(stat) \pm 0.61(syst)		
0.63,0.84	93.30 \pm 1.47	98.55 \pm 1.56(stat) \pm 0.47(syst)	91.59 \pm 1.76	96.32 \pm 1.85(stat) \pm 1.07(syst)		
0.84,1.05	92.28 \pm 1.38	97.75 \pm 1.47(stat) \pm 0.52(syst)	92.48 \pm 1.83	97.98 \pm 1.94(stat) \pm 0.78(syst)		
1.05,1.37	92.10 \pm 1.20	97.22 \pm 1.27(stat) \pm 0.75(syst)	93.16 \pm 1.50	98.40 \pm 1.59(stat) \pm 1.17(syst)		
1.37,1.52	-	-	-	-		
1.52,1.74	92.09 \pm 1.41	99.31 \pm 1.52(stat) \pm 0.81(syst)	89.82 \pm 1.94	97.12 \pm 2.10(stat) \pm 1.35(syst)		
1.74,1.95	89.68 \pm 1.26	98.54 \pm 1.39(stat) \pm 0.81(syst)	91.15 \pm 1.76	100.79 \pm 1.95(stat) \pm 1.07(syst)		
1.95,2.18	89.08 \pm 1.18	98.13 \pm 1.30(stat) \pm 1.59(syst)	87.58 \pm 1.65	96.74 \pm 1.83(stat) \pm 1.32(syst)		
2.18,2.47	83.43 \pm 1.16	101.68 \pm 1.42(stat) \pm 1.02(syst)	81.19 \pm 1.55	101.32 \pm 1.94(stat) \pm 1.78(syst)		

Table B.13: Medium + b-layer hit efficiencies (with statistical uncertainties only) and data/MC scale factors from W tag-and-probe as a function of η . The numbers are obtained for electron within $20 < E_T < 50$ GeV.

Appendix C

W/Z differential cross section tables

$ \eta_{\min} $	0.00	0.21	0.42	0.63	0.84	1.05	1.37	1.52	1.74	1.95	2.18
$ \eta_{\max} $	0.21	0.42	0.63	0.84	1.05	1.37	1.52	1.74	1.95	2.18	2.47
Trigger	0.40	0.40	0.40	0.40	0.40	0.40	–	0.40	0.40	0.40	0.40
Electron Reconstruction	0.80	0.80	0.80	0.80	0.80	0.80	–	0.80	0.80	0.80	0.80
Electron ID SF corr	0.81	0.64	0.64	0.49	1.02	0.72	–	0.74	0.87	1.08	0.89
Electron ID SF uncorr	1.44	1.34	1.31	1.42	1.44	1.16	–	1.52	1.48	1.34	1.36
Electron isolation SF corr	0.18	0.12	0.20	0.16	0.47	0.14	–	0.33	0.14	0.29	0.59
Electron isolation SF uncorr	0.42	0.38	0.45	0.51	0.49	0.39	–	0.40	0.64	0.66	0.90
Electron energy scale	0.43	0.38	0.41	0.45	0.49	0.58	–	0.67	0.65	0.56	0.53
Electron energy resolution	0.01	0.00	0.00	0.01	0.02	0.00	–	0.00	0.01	0.05	0.02
charge misID	< 0.01	0.01	0.01	0.03	0.01	0.06	–	0.10	0.12	0.25	0.37
OTX	0.40	0.40	0.40	0.40	0.40	0.40	–	0.40	0.40	0.40	0.40
$E_{\text{T}}^{\text{miss}}$ scale and resolution											
↔ JES	0.43	0.41	0.41	0.44	0.37	0.32	–	0.37	0.33	0.29	0.26
↔ JER	0.08	0.02	0.01	0.04	0.02	0.02	–	0.04	0.01	0.00	0.05
↔ AllClusters	0.74	0.70	0.72	0.63	0.57	0.66	–	0.06	0.66	0.63	0.69
Pile-up	0.3	0.3	0.3	0.3	0.3	0.3	–	0.3	0.3	0.3	0.3
Boson p_{T}	0.03	0.03	0.03	0.03	0.03	0.02	–	0.01	0.02	0.01	0.03
Vertex position	0.14	0.07	0.16	0.14	0.20	0.08	–	0.24	0.45	0.08	0.02
Theory uncertainty											
↔ PDF	0.20	0.20	0.20	0.20	0.20	0.20	–	0.20	0.20	0.20	0.20
↔ Generator	1.10	0.49	0.22	0.18	0.31	0.22	–	0.09	0.35	0.39	0.45
↔ UE + PS	1.02	0.49	0.16	0.19	0.69	0.49	–	0.73	0.07	0.74	0.39

Table C.1: Relative systematic uncertainties on C_{W^+} for the differential $W^+ \rightarrow e^+\bar{\nu}$ cross section measurement. All uncertainties are given in percent [103].

APPENDIX C. W/Z DIFFERENTIAL CROSS SECTION TABLES

$ \eta_{\min} $	0.00	0.21	0.42	0.63	0.84	1.05	1.37	1.52	1.74	1.95	2.18
$ \eta_{\max} $	0.21	0.42	0.63	0.84	1.05	1.37	1.52	1.74	1.95	2.18	2.47
Trigger	0.40	0.40	0.40	0.40	0.40	0.40	–	0.40	0.40	0.40	0.40
Electron Reconstruction	0.80	0.80	0.80	0.80	0.80	0.80	–	0.80	0.80	0.80	0.80
Electron ID SF corr	0.86	0.87	0.62	0.92	0.91	1.25	–	1.09	1.09	1.42	1.21
Electron ID SF uncorr	1.44	1.34	1.31	1.42	1.44	1.16	–	1.52	1.48	1.34	1.36
Electron isolation SF corr	0.19	0.12	0.20	0.16	0.47	0.14	–	0.33	0.14	0.29	0.59
Electron isolation SF uncorr	0.42	0.38	0.45	0.51	0.49	0.39	–	0.40	0.64	0.66	0.90
Electron energy scale	0.35	0.34	0.36	0.42	0.43	0.51	–	0.60	0.53	0.54	0.55
Electron energy resolution	0.00	0.01	0.03	0.02	0.01	0.01	–	0.01	0.01	0.00	0.04
charge misID	< 0.01	0.02	0.01	0.04	0.02	0.09	–	0.15	0.21	0.41	0.61
OTX	0.40	0.40	0.40	0.40	0.40	0.40	–	0.40	0.40	0.40	0.40
E_T^{miss} scale and resolution											
↔ JES	0.52	0.52	0.54	0.50	0.52	0.50	–	0.52	0.58	0.53	0.55
↔ JER	0.02	0.07	0.06	0.08	0.03	0.03	–	0.04	0.02	0.06	0.02
↔ AllClusters	0.87	0.86	0.87	0.90	0.88	0.86	–	0.12	0.85	0.83	0.81
Pile-up	0.3	0.3	0.3	0.3	0.3	0.3	–	0.3	0.3	0.3	0.3
Boson p_T	0.03	0.03	0.02	0.03	0.03	0.03	–	0.04	0.03	0.02	0.03
Vertex position	0.04	0.06	0.18	0.25	0.01	0.05	–	0.02	0.22	0.07	0.08
Theory uncertainty											
↔ PDF	0.20	0.20	0.20	0.20	0.20	0.20	–	0.20	0.20	0.20	0.20
↔ Generator	0.51	0.50	0.73	0.24	0.45	0.28	–	0.05	0.23	0.93	0.31
↔ UE + PS	0.79	0.64	0.86	0.71	0.14	0.17	–	0.23	0.31	0.61	0.14

Table C.2: Relative systematic uncertainties on C_{W^-} for the differential $W^- \rightarrow e^- \nu$ cross section measurement. All uncertainties are given in percent [103].

$ y $ [%]	Trig. Eff.	Rec. Eff.	IDeff stat.	IDeff syst.	E-scale	E-res	pile-up	OTX	Z_{vert}	Z_{pt}	MC1	MC2	PDF	charge misID
0.0,0.4	0.0	1.6	0.6	1.4	0.2	0.0	0.3	0.8	-0.1	0.0	0.1	0.1	0.2	-0.2
0.4,0.8	0.0	1.6	0.5	1.5	0.2	0.0	0.3	0.8	0.1	0.0	0.3	-0.1	0.2	-0.3
0.8,1.2	0.0	1.6	0.5	1.6	0.2	-0.0	0.3	0.8	-0.2	0.0	0.4	-0.2	0.2	-0.5
1.2,1.6	0.0	1.6	0.6	1.9	0.2	-0.0	0.3	0.8	-0.0	0.0	0.2	0.1	0.2	-0.9
1.6,2.0	0.0	1.6	0.8	2.2	0.1	-0.0	0.3	0.8	-0.3	0.0	0.5	-0.0	0.2	-1.2
2.0,2.4	0.0	1.6	1.1	2.9	0.1	-0.0	0.3	0.8	0.1	0.0	1.4	-0.6	0.2	-1.9

Table C.3: Systematic uncertainties for C_Z for the differential $|y^Z|$ cross section measurement for the $Z \rightarrow ee$ channel. MC1 implies a comparison of MC@NLO+HERWIG with POWHEG+HERWIG and MC2 a comparison of POWHEG+HERWIG with POWHEG+PYTHIA. All uncertainties are given in percent [103].

APPENDIX C. W/Z DIFFERENTIAL CROSS SECTION TABLES

$ \eta $	N_{data}	N_{EW}	N_{QCD}	C_W
0.00, 0.21	6672	$229.3 \pm 6.3 \pm 12.0$	$118.5 \pm 12.5 \pm 19.4$	$0.6849 \pm 0.0089 \pm 0.0153$
0.21, 0.42	7036	$236.3 \pm 6.4 \pm 12.3$	$124.2 \pm 12.7 \pm 20.2$	$0.7313 \pm 0.0083 \pm 0.0123$
0.42, 0.63	7786	$253.0 \pm 6.5 \pm 13.2$	$137.6 \pm 13.7 \pm 20.1$	$0.7838 \pm 0.0089 \pm 0.0124$
0.63, 0.84	7712	$253.8 \pm 6.6 \pm 13.2$	$197.0 \pm 14.3 \pm 29.2$	$0.7761 \pm 0.0096 \pm 0.0116$
0.84, 1.05	8054	$246.5 \pm 6.5 \pm 12.8$	$229.1 \pm 14.3 \pm 28.2$	$0.7656 \pm 0.0089 \pm 0.0147$
1.05, 1.37	12044	$377.7 \pm 8.2 \pm 19.5$	$601.3 \pm 21.1 \pm 58.0$	$0.7407 \pm 0.0073 \pm 0.0124$
1.37, 1.52				
1.52, 1.74	7747	$241.0 \pm 6.6 \pm 12.3$	$512.7 \pm 18.3 \pm 48.9$	$0.7041 \pm 0.0078 \pm 0.0121$
1.74, 1.95	6720	$199.2 \pm 6.0 \pm 10.2$	$248.0 \pm 13.0 \pm 30.5$	$0.6325 \pm 0.0075 \pm 0.0113$
1.95, 2.18	7274	$207.3 \pm 6.2 \pm 10.6$	$210.4 \pm 12.5 \pm 26.9$	$0.6313 \pm 0.0077 \pm 0.0125$
2.18, 2.47	6840	$208.8 \pm 6.4 \pm 10.6$	$305.0 \pm 13.7 \pm 43.1$	$0.5117 \pm 0.0068 \pm 0.0097$

Table C.4: Inputs for the fiducial differential cross section calculation in the $W^+ \rightarrow e^+\nu$ channel with 2010 data. The first error is due to statistical effects (uncorrelated between bins), while the second is systematic (correlated between bins) [103].

$ \eta $	N_{data}	N_{EW}	N_{QCD}	C_W
0.00, 0.21	4991	$193.5 \pm 5.6 \pm 10.2$	$132.1 \pm 11.4 \pm 14.1$	$0.6806 \pm 0.0102 \pm 0.0135$
0.21, 0.42	5249	$210.8 \pm 5.9 \pm 11.1$	$137.9 \pm 11.7 \pm 12.4$	$0.7345 \pm 0.0102 \pm 0.0141$
0.42, 0.63	5794	$221.2 \pm 5.9 \pm 11.6$	$146.7 \pm 12.7 \pm 15.1$	$0.7828 \pm 0.0108 \pm 0.0157$
0.63, 0.84	5488	$215.5 \pm 5.9 \pm 11.3$	$204.5 \pm 12.6 \pm 13.1$	$0.7490 \pm 0.0112 \pm 0.0147$
0.84, 1.05	5466	$196.2 \pm 5.6 \pm 10.3$	$224.6 \pm 12.9 \pm 16.6$	$0.7757 \pm 0.0118 \pm 0.0147$
1.05, 1.37	8360	$301.5 \pm 7.1 \pm 15.7$	$525.3 \pm 18.5 \pm 42.8$	$0.7549 \pm 0.0092 \pm 0.0152$
1.37, 1.52				
1.52, 1.74	5003	$188.0 \pm 5.7 \pm 9.7$	$456.6 \pm 16.0 \pm 36.9$	$0.7065 \pm 0.0111 \pm 0.0125$
1.74, 1.95	4137	$141.3 \pm 5.0 \pm 7.3$	$213.6 \pm 11.9 \pm 19.1$	$0.6472 \pm 0.0103 \pm 0.0128$
1.95, 2.18	4237	$146.2 \pm 5.2 \pm 7.5$	$211.5 \pm 11.7 \pm 16.7$	$0.6532 \pm 0.0097 \pm 0.0158$
2.18, 2.47	4131	$132.9 \pm 4.9 \pm 6.8$	$290.6 \pm 12.4 \pm 23.9$	$0.5404 \pm 0.0087 \pm 0.0117$

Table C.5: Inputs for the fiducial differential cross section calculation in the $W^- \rightarrow e^-\bar{\nu}$ channel with 2010 data. The first error is due to statistical effects (uncorrelated between bins), while the second is systematic (correlated between bins) [103].

APPENDIX C. W/Z DIFFERENTIAL CROSS SECTION TABLES

$ y $	N_{Data}	N_{EW}	N_{QCD}	C_Z
0.00,0.40	2447	$11.8 \pm 0.6 \pm 0.7$	$36.2 \pm 9.1 \pm 14.5$	$0.650 \pm 0.001 \pm 0.016$
0.40,0.80	2214	$12.1 \pm 0.6 \pm 0.7$	$36.3 \pm 9.1 \pm 14.5$	$0.649 \pm 0.001 \pm 0.016$
0.80,1.20	2050	$8.9 \pm 0.5 \pm 0.5$	$35.3 \pm 8.8 \pm 14.1$	$0.631 \pm 0.001 \pm 0.017$
1.20,1.60	1641	$6.6 \pm 0.5 \pm 0.4$	$29.1 \pm 7.3 \pm 11.7$	$0.602 \pm 0.001 \pm 0.017$
1.60,2.00	960	$4.4 \pm 0.4 \pm 0.3$	$17.3 \pm 4.3 \pm 6.9$	$0.556 \pm 0.002 \pm 0.018$
2.00,2.40	405	$2.1 \pm 0.4 \pm 0.1$	$6.4 \pm 1.6 \pm 2.6$	$0.482 \pm 0.003 \pm 0.021$

Table C.6: Inputs for the fiducial differential cross section calculation in the $Z \rightarrow ee$ channel with 2010 data. The first error is due to statistical effects (uncorrelated between bins), while the second is systematic (correlated between bins) [103].

η	$\sigma_{W^+}^{fid}$	$\sigma_{W^-}^{fid}$
0.00,0.21	$607.0 \pm 11.2 \pm 13.7$	$450.6 \pm 9.7 \pm 9.1$
0.21,0.42	$600.1 \pm 10.3 \pm 10.3$	$438.6 \pm 9.0 \pm 8.6$
0.42,0.63	$620.3 \pm 10.3 \pm 10.0$	$455.7 \pm 9.0 \pm 9.3$
0.63,0.84	$615.1 \pm 10.7 \pm 9.6$	$444.8 \pm 9.4 \pm 8.9$
0.84,1.05	$650.7 \pm 10.9 \pm 12.8$	$427.6 \pm 9.1 \pm 8.3$
1.05,1.37	$644.5 \pm 9.1 \pm 11.4$	$430.5 \pm 7.5 \pm 9.1$
1.37,1.52		
1.52,1.74	$623.3 \pm 10.6 \pm 11.6$	$387.1 \pm 8.9 \pm 7.6$
1.74,1.95	$652.0 \pm 11.6 \pm 12.1$	$384.2 \pm 9.1 \pm 7.9$
1.95,2.18	$651.9 \pm 11.4 \pm 13.2$	$356.4 \pm 8.1 \pm 8.8$
2.18,2.47	$588.5 \pm 11.0 \pm 11.8$	$326.6 \pm 7.8 \pm 7.4$

Table C.7: Differential $W \rightarrow e\nu$ cross sections in the fiducial volume [103].

$ y $	σ_Z^{fid}
0.00,0.40	$127.5 \pm 2.7 \pm 3.2$
0.40,0.80	$115.2 \pm 2.5 \pm 3.0$
0.80,1.20	$109.7 \pm 2.5 \pm 3.0$
1.20,1.60	$92.0 \pm 2.4 \pm 2.7$
1.60,2.00	$58.3 \pm 1.9 \pm 2.0$
2.00,2.40	$28.4 \pm 1.4 \pm 1.2$

Table C.8: Differential $Z \rightarrow ee$ cross section in the fiducial volume [103].

Bibliography

- [1] M. E. Peskin and D. V. Schroeder, *An Introduction to Quantum Field Theory; 1995 ed.* Westview, Boulder, CO, 1995.
- [2] W. N. Cottingham and D. A. Greenwood, *An Introduction to the Standard Model of Particle Physics; 2nd ed.* Cambridge Univ. Press, Cambridge, 2007.
- [3] Y. Fukuda et al., *Measurements of the Solar Neutrino Flux from Super-Kamiokande's First 300 Days*, Phys. Rev. Lett. **81** (1998) no. 6, 4.
- [4] UA1 Collaboration, G. T. J. Arnison et al., *Experimental observation of isolated large transverse energy electrons with associated missing energy at $\sqrt{s} = 540$ GeV*, Phys. Lett. B **122** (1983) no. CERN-EP-83-13, .
- [5] UA2 Collaboration, M. Banner et al., *Observation of single isolated electrons of high transverse momentum in events with missing transverse energy at the CERN $\bar{p}p$ collider. oai:cds.cern.ch:142759*, Phys. Lett. B **122** (1983) no. CERN-EP-83-25, 476–485. 15 p.
- [6] UA1 Collaboration, G. T. J. Arnison et al., *Observation of muonic Z^0 decay at the $\bar{p}p$ collider. oai:cds.cern.ch:154095*, Phys. Lett. B **147** (1984) no. CERN-EP-84-100, 241–248. 18 p.
- [7] UA2 Collaboration, P. Bagnaia et al., *Evidence for $Z^0 \rightarrow e^+e^-$ at the CERN $\bar{p}p$ collider. oai:cds.cern.ch:146503*, Phys. Lett. B **129** (1983) no. CERN-EP-83-112, 130–140. 21 p.
- [8] J. Alcaraz et al., *A combination of preliminary electroweak measurements and constraints on the Standard Model*, arXiv:hep-ex/0612034.
- [9] P. Z. Quintas, *Measurement of W and Z production cross-sections in $\bar{p}p$ collisions at $\sqrt{s} = 1.8$ TeV*, hep-ex/9412016.
- [10] A. Abulencia et al., *Observation of WZ Production*, Tech. Rep. hep-ex/0702027. FERMILAB-PUB-2007-042-E, FERMILAB, Batavia, IL, Feb, 2007.

-
- [11] K. Nakamura and others (Particle Data Group), *Review of Particle Physics, 2010. Review of Particle Properties, 2010*, J. Phys. **G 37** (2010) no. 075021, .
- [12] R. Hamberg, W. L. van Neerven, and T. Matsuura, *A complete calculation of the order α_s^2 correction to the Drell-Yan K-factor*, Nucl. Phys. B **359** (1990) no. DESY-90-129, 343–405. 70 p.
- [13] R. K. Ellis, W. J. Stirling, and B. R. Webber, *QCD and Collider Physics*. Cambridge monographs on particle physics, nuclear physics, and cosmology. Cambridge Univ. Press, Cambridge, 2003. Photography by S. Vascotto.
- [14] G. Watt, *Parton distributions: HERA-Tevatron-LHC*. *oai:cds.cern.ch:1235257*, Tech. Rep. arXiv:1001.3954. CERN-PH-TH-2010-013, CERN, Jan, 2010.
- [15] W. J. Stirling, *Progress in Parton Distribution Functions*, private communication, 2010.
- [16] C. Anastasiou, L. Dixon, K. Melnikov, and F. J. Petriello, *High-precision QCD at hadron colliders: electroweak gauge boson rapidity distributions at NNLO*, Phys. Rev. D **69** (2003) no. hep-ph/0312266. SLAC-PUB-10288. UH-511-1042. 9, 94008–1–27. 47 p.
- [17] A. D. Martin, W. J. Stirling, R. S. Thorne, and G. Watt, *Parton distributions for the LHC*, Tech. Rep. arXiv:0901.0002. IPPP-08-95. DCPT-08-190.CAVENDISH-HEP-08-16, CERN, Jan, 2009.
- [18] M. Dittmar, F. Pauss, and D. Zrcher, *Towards a Precise Parton Luminosity Determination at the CERN LHC*, Phys. Rev. D **56** (1997) no. hep-ex/9705004. ETHZ-IPP-P-97-01. 11, 7284–7290.
- [19] I. W. Stewart, F. J. Tackmann, and W. J. Waalewijn, *Factorization at the LHC: From parton distribution functions to initial state jets*, Phys. Rev. D **10.1103/PhysRevD.81.094035** (2010) .
- [20] C. F. Berger, Z. Bern, L. J. Dixon, F. F. Cordero, D. Forde, T. Gleisberg, H. Ita, D. A. Kosower, and D. Maitre, *Precise Predictions for $W + 4$ Jet Production at the Large Hadron Collider*. *oai:cds.cern.ch:1291446*, Tech. Rep. arXiv:1009.2338, CERN-PH-TH-2010-184, CERN, Sep, 2010. Comments: 5 pages, 3 figures, 2 tables.
- [21] J. M. Campbell and R. K. Ellis, *MCFM for the Tevatron and the LHC*, arXiv/1007.3492.

BIBLIOGRAPHY

- [22] T. C. Collaboration, *First Measurements of Inclusive W and Z Cross Sections from Run II of the Tevatron Collider*, Tech. Rep. hep-ex/0406078, Fermilab, 2004.
- [23] The ATLAS Collaboration, G. Aad et al., *Expected Performance of the ATLAS Experiment - Detector, Trigger and Physics*, arXiv:0901.0512 [hep-ex].
- [24] J. F. Arguin, M. Barisonzi, H. Beauchemin, E. Berglund, et al., *Prospects for W/Z+jets early data measurements with the ATLAS detector at the LHC: An analysis walkthrough*, Tech. Rep. ATL-COM-PHYS-2010-150, CERN, Geneva, Mar, 2010.
- [25] T. Sjostrand, S. Mrenna, and P. Z. Skands, *PYTHIA 6.4 Physics and Manual*, J. High Energy Phys. **05** (2006) no. hep-ph/0603175. FERMILAB-Pub-2006-052-CD-T. LU-TP-2006-13, 570.
- [26] E. Barberio and Z. Was, *PHOTOS: a universal Monte Carlo for QED radiative corrections; version 2.0*. oai:cds.cern.ch:254343, Comput. Phys. Commun. **79** (1993) no. CERN-TH-7033-93, 23.
- [27] S. Gieseke et al., *Herwig++ 2.5 Release Note*, Tech. Rep. arXiv:1102.1672. DCPT-11-18. DESY 11-018. IPPP-11-09. KA-TP-04-2011. MCNET-11-04, Feb, 2011.
- [28] M. L. Mangano, M. Moretti, F. Piccinini, R. Pittau, and A. Polosa, *ALPGEN, a generator for hard multiparton processes in hadronic collisions*, J. High Energy Phys. **07** (2002) no. hep-ph/0206293. CERN-TH-2002-129, 001. 35 p.
- [29] T. A. Collaboration, *First tuning of HERWIG/JIMMY to ATLAS data*, Tech. Rep. ATL-PHYS-PUB-2010-014, CERN, Geneva, Oct, 2010.
- [30] S. Frixione, F. Stoeckli, P. Torrielli, B. R. Webber, and C. D. White, *The MC@NLO 4.0 Event Generator*. oai:cds.cern.ch:1297827, Tech. Rep. arXiv:1010.0819. CAVENDISH-HEP-10-12. CERN-TH-2010-216-[SIC!]. CERN-PH-TH-2010-216. IPPP-10-62. DCPT-10-124, Oct, 2010. Comments: 36 pages, no figures.
- [31] P. Nason, *Recent developments in POWHEG*, . Comments: 7 pages, 2 figures.
- [32] O. S. Brning et al., *LHC Design Report, volume 1*. CERN, Geneva, 2004.
- [33] R. W. Assmann, M. Lamont, and S. Myers, *A Brief History of the LEP Collider*, Nucl. Phys. B, Proc. Suppl. **109** (2002) no. CERN-SL-2002-009-OP, 17–31. 15 p.

- [34] S. Holmes, R. S. Moore, and V. Shiltsev, *Overview of the Tevatron Collider Complex: Goals, Operations and Performance*, Tech. Rep. arXiv:1106.0909, Jun, 2011.
- [35] M. Benedikt, P. Collier, V. Mertens, J. Poole, and K. Schindl, *LHC Design Report v.3: the LHC Injector Chain*. CERN, Geneva, 2004. Tech. Rep. CERN-2004-003-V-3.
- [36] C. Lefvre, *The CERN accelerator complex. Complexe des accrateurs du CERN*, Dec, 2008.
- [37] O. S. Brning, P. Collier, P. Lebrun, S. Myers, R. Ostojic, J. Poole, and P. Proudlock, *LHC Design Report v.1: the LHC main ring*. CERN, Geneva, 2004.
- [38] M. Lamont and M. Meddahi, *LHC operation: experience from 2010 and plans for 2011*, February, 2010. Invited talk at ATLAS week.
- [39] CERN/AT/PhL, *INTERIM SUMMARY REPORT ON THE ANALYSIS OF THE 19 SEPTEMBER 2008 INCIDENT AT THE LHC*, Document edms 973073, October, 2008.
- [40] The ATLAS Collaboration, G. Aad et al., *Luminosity Determination in pp Collisions at $\sqrt{s} = 7$ TeV using the ATLAS Detector at the LHC*. *oai:cds.cern.ch:1323586*, . submitted to Journal EPJC.
- [41] The ATLAS Collaboration, G. Aad et al., *Updated Luminosity Determination in pp Collisions at $\sqrt{s}=7$ TeV using the ATLAS Detector*, Tech. Rep. ATLAS-CONF-2011-011, CERN, Geneva, Mar, 2011.
- [42] The ATLAS Collaboration, G. Aad et al., *ATLAS public results*, <https://twiki.cern.ch/twiki/bin/view/AtlasPublic/WebHome>.
- [43] R. Adolphi et al., *The CMS experiment at the CERN LHC. The Compact Muon Solenoid experiment*, tech. rep., CERN, 2008. Also published by CERN Geneva in 2010.
- [44] The ALICE Collaboration, K. Aamodt et al., *The ALICE experiment at the CERN LHC. A Large Ion Collider Experiment*, tech. rep., CERN, 2008. Also published by CERN Geneva in 2010.
- [45] The LHCb Collaboration, A. A. Alves et al., *The LHCb Detector at the LHC*, tech. rep., CERN, 2008. Also published by CERN Geneva in 2010.

- [46] The TOTEM Collaboration, G. Anelli et al., *The TOTEM Experiment at the CERN Large Hadron Collider*, tech. rep., CERN, 2008.
- [47] The LHCf Collaboration, O. Adriani et al., *The LHCf detector at the CERN Large Hadron Collider*, J. Instrum. **3** (2008) S08006.
- [48] J. Pinfold et al., *Technical Design Report of the MoEDAL Experiment*, Tech. Rep. CERN-LHCC-2009-006. MoEDAL-TDR-001, CERN, Geneva, Jun, 2009.
- [49] The ATLAS Collaboration, G. Aad et al., *ATLAS: Detector and physics performance technical design report. Volume 1*, . CERN-LHCC-99-14.
- [50] The ATLAS Collaboration, G. Aad et al., *ATLAS: Detector and physics performance technical design report. Volume 2*, . CERN-LHCC-99-15.
- [51] The ATLAS Collaboration, G. Aad et al., *The ATLAS Experiment at the CERN Large Hadron Collider*, J. Instrum. **3** (2008) S08003. 437 p. Also published by CERN Geneva in 2010.
- [52] *The ATLAS homepage*, <http://www.cern.ch/atlas/>.
- [53] J. Pequeno, *Event Cross Section in a computer generated image of the ATLAS detector.*, <http://cdsweb.cern.ch/record/1096081>, Mar, 2008.
- [54] S. M. Sze, *Semiconductor devices: physics and technology; 2nd ed.* Wiley, New York, NY, 2002.
- [55] K. Reeves, *Commissioning and Operation of the ATLAS Pixel Detector*, Presented at IEEE Nuclear Science Symposium, Knoxville, TE, Nov, 2010.
- [56] J. Degenhardt, *Performance of the ATLAS Transition Radiation Tracker with Cosmic Rays and First High Energy Collisions at the LHC*, Tech. Rep. ATL-INDET-PROC-2010-040, CERN, Geneva, Nov, 2010.
- [57] The ATLAS Collaboration, G. Aad et al., *Electron performance measurements with the ATLAS detector using the 2010 LHC proton-proton collision data*, Eur. Phys. J. C (2011) no. ATLAS-PERF-2010-04-002; CERN-PH-EP-2011-117, .
- [58] S. Arfaoui and R. Calkins, *2010 ATLAS Detector Performance II*, Poster presented at LHCC, Apr, 2011.
- [59] The ATLAS Collaboration, G. Aad et al., *Jet energy measurement with the ATLAS detector in proton-proton collisions at $\sqrt{s} = 7$ TeV in 2010*, Europ Phys. Journal (2011) no. ATLAS-PERF-2011-03, 102 p.

-
- [60] M. Bindi, *Performance of the ATLAS muon spectrometer*, Presented at Kruger 2010, South Africa, Jan, 2011.
- [61] The ATLAS Collaboration, G. Aad et al., *Muon Momentum Resolution in First Pass Reconstruction of pp Collision Data Recorded by ATLAS in 2010*, Tech. Rep. ATLAS-CONF-2011-046, CERN, Geneva, Mar, 2011.
- [62] A. Sbrizzi, *LUCID: A Cherenkov Tube Based Detector for Monitoring the ATLAS Experiment Luminosity*, Talk at IEEE Nuclear Science Symposium, Honolulu, HI, Oct, 2007.
- [63] S. Jakobsen, *Calibration, testing, commissioning and first data of ALFA at LHC*, New Developments in Photodetection, Lyon, France, Jul, 2011.
- [64] The ATLAS Collaboration, G. Aad et al., *ATLAS computing: Technical Design Report*. Technical Design Report ATLAS. CERN, Geneva, 2005.
- [65] R. Brenner, W. Dabrowski, J. Kaplon, U. Ktz, W. Langhans, C. Posch, S. Roe, and P. Weilhammer, *Overview and initial specification for DMILL analogue readout protocol in the ATLAS semiconductor Tracker*, Tech. Rep. ATL-INDET-97-158. ATL-I-PN-158, CERN, Geneva, Feb, 1997.
- [66] *SCT hardware description*,
<https://twiki.cern.ch/twiki/bin/view/Atlas/SctCommissioningDocumentation>.
- [67] E. Berglund, *ATLAS Silicon Microstrip Operation*, October, 2009. Presented at IEEE Nuclear Science Symposium, Orlando, FL.
- [68] *Approved SCT Cosmic Data plots*,
<https://twiki.cern.ch/twiki/bin/view/AtlasPublic/ApprovedPlotsSCT>.
- [69] *Public SCT Plots for Collision Data*,
<https://twiki.cern.ch/twiki/bin/view/AtlasPublic/SCTPublicResults>.
- [70] E. Coniavitis, A. Okamoto, and R. Tanaka, *Lorentz Angle and Cluster Width Studies for the ATLAS SCT*, Tech. Rep. ATL-INDET-INT-2010-008, CERN, Geneva, Mar, 2010.
- [71] The ATLAS Collaboration, G. Aad et al., *Studies of the performance of the ATLAS detector using cosmic-ray muons*. *oai:cds.cern.ch:1311111*, Eur. Phys. J. C **71** (2011) 1–36. arXiv:1011.6665. CERN-PH-EP-2010-070.
- [72] E. Berglund, D. Froidevaux, J. E. Garcia Navarro, and T. Koffas, *Low momentum electrons in ATLAS cosmic ray data*, Tech. Rep. ATL-PHYS-INT-2010-033, CERN, Geneva, Apr, 2010.

- [73] M. R. Sutton, *Commissioning the ATLAS Inner Detector Trigger*, Tech. Rep. ATL-DAQ-PROC-2009-015. ATL-COM-DAQ-2009-036, CERN, Geneva, May, 2009. 15/05/2009.
- [74] S. Fratina, M. Hance, M. Newcomer, D. Olivito, R. Van Berg, P. Wagner, H. Williams, B. Auerbach, D. Dobos, and P. Lichard, *The TRT Fast-OR Trigger*, Tech. Rep. ATL-COM-INDET-2009-042, CERN, Geneva, Aug, 2009.
- [75] *Analysis of Inner Detector Cosmic-Ray Data 2008*, Available from the ATLAS twiki page:
<https://twiki.cern.ch/twiki/bin/view/Atlas/InDetCosmic08Analyses>.
- [76] *ATLAS public results - Approved Transition Radiation Tracker Plots*, Available from the ATLAS twiki page:
<https://twiki.cern.ch/twiki/bin/view/Atlas/ApprovedPlotsTRT>.
- [77] A. Bocci, *Commissioning of the TRT with cosmic rays*, Tech. Rep. ATL-COM-INDET-2009-066, CERN, Geneva, Sep, 2009.
- [78] W. Lampl, S. Laplace, D. Lelas, P. Loch, H. Ma, S. Menke, S. Rajagopalan, D. Rousseau, S. Snyder, and G. Unal, *Calorimeter Clustering Algorithms: Description and Performance*, Tech. Rep. ATL-LARG-PUB-2008-002. ATL-COM-LARG-2008-003, CERN, Geneva, Apr, 2008.
- [79] *Cluster Moments*, Available from the ATLAS twiki page:
<https://twiki.cern.ch/twiki/bin/view/Atlas/ClusterMoments>.
- [80] R. Barlow and C. Beeston, *Fitting using finite Monte Carlo samples*, Computer Physics Communications **77** (1993) no. 2, 219 – 228.
- [81] The ATLAS Collaboration, G. Aad et al., *Electron efficiency measurements using ATLAS 2010 data at $\sqrt{s} = 7$ TeV: Supporting note for the 2010 egamma paper*, Tech. Rep. ATL-COM-PHYS-2011-322, CERN, Geneva, Mar, 2011.
- [82] Egamma group, *Official electron efficiencies and scale factor recommendation*, <https://twiki.cern.ch/twiki/bin/view/AtlasProtected/EfficiencyMeasurements>.
- [83] The ATLAS Collaboration, G. Aad et al., *Electron and photon reconstruction and identification in ATLAS: expected performance at high energy and results at 900 GeV*, Tech. Rep. ATLAS-CONF-2010-005, CERN, Geneva, Jun, 2010.
- [84] E. Berglund, *Photon Reconstruction and Identification with the ATLAS Detector*, PoS **EPS-HEP** (2009) 430.

-
- [85] The ATLAS Collaboration, G. Aad et al., *ATLAS public event displays*, <https://twiki.cern.ch/twiki/bin/view/AtlasPublic/EventDisplayPublicResults>.
- [86] C. Blocker, *Uncertainties on Efficiencies*, CDF/MEMO/STATISTICS/PUBLIC/7168, August, 2004. CDF memo.
- [87] X. Anduaga, R. Apolle, H. S. Bansil, K. Benslama, E. F. Berglund, et al., *Performance of the Electron and Photon Trigger in p - p Collisions at $\sqrt{s} = 7$ TeV with the ATLAS Detector at the LHC*, Tech. Rep. ATL-COM-DAQ-2011-038, CERN, Geneva, May, 2011. Supporting internal note.
- [88] The ATLAS Collaboration, G. Aad et al., *Performance of the ATLAS Trigger System in 2010*, Eur. Phys. J. C (2011) no. CERN-PH-EP-2011-078, .
- [89] The ATLAS Collaboration, G. Aad et al., *Observation of $W \rightarrow l\nu$ and $Z \rightarrow ll$ production in proton-proton collisions at roots=7 TeV with the ATLAS detector*, Tech. Rep. ATLAS-CONF-2010-044, CERN, Geneva, Jul, 2010.
- [90] A. Ahmad, J. Alison, A. Arnaez, I. Besana, T. Berry, H. Bawa, K. Benslama, E. Berglund, et al., *$W \rightarrow e\nu$ and $Z \rightarrow ee$ Observations supporting note.*, Tech. Rep. ATL-PHYS-INT-2010-108, CERN, Geneva, Sep, 2010.
- [91] M. Bellomo et al., *Observation of $W \rightarrow \mu\nu$ and $Z \rightarrow \mu\nu$ in proton-proton collisions at $\sqrt{s} = 7$ TeV with the ATLAS Detector*, Tech. Rep. ATL-PHYS-INT-2010-087, CERN, Geneva, Sep, 2010.
- [92] The ATLAS Collaboration, G. Aad et al., *Measurement of the $W \rightarrow l\nu$ production cross-section and observation of $Z \rightarrow ll$ production in proton-proton collisions at $\sqrt{s} = 7$ TeV with the ATLAS detector*, Tech. Rep. ATLAS-CONF-2010-051, CERN, Geneva, Jul, 2010.
- [93] A. Ahmed, J. Alison, M. Bellomo, A. Belloni, E. Berglund, et al., *Supporting Document: Measurement of the W cross section and asymmetry in the electron and muon decay channels at $\sqrt{s} = 7$ TeV*, Tech. Rep. ATL-PHYS-INT-2010-116, CERN, Geneva, Sep, 2010.
- [94] M. Aharrouche, A. Ahmad, J. Alison, A. Arnaez, I. Besana, T. Berry, H. Bawa, K. Benslama, E. Berglund, et al., *$W \rightarrow e\nu$ and $Z \rightarrow ee$ observation supporting note*, Tech. Rep. ATL-PHYS-INT-2010-109, CERN, Geneva, Sep, 2010.

- [95] The ATLAS Collaboration, G. Aad et al., *Measurement of the $Z \rightarrow ll$ production cross section in proton-proton collisions at $\sqrt{s} = 7$ TeV with the ATLAS detector*, Tech. Rep. ATLAS-CONF-2010-076, CERN, Geneva, Jul, 2010.
- [96] The ATLAS Collaboration, G. Aad et al., *Measurement of the $W \rightarrow l\nu$ and $Z/\gamma^* \rightarrow ll$ production cross sections in proton-proton collisions at $\sqrt{s} = 7$ TeV with the ATLAS detector*. *oai:cds.cern.ch:1299479*, Journal of High Energy Physics **12** (2010) no. arXiv:1010.2130. CERN-PH-EP-2010-037, 1–65.
- [97] M. Aharrouche, A. Ahmad, J. Alison, O. Arnaez, I. Besana, T. Berry, H. S. Bawa, K. Benslama, E. Berglund, et al., *$W \rightarrow e\nu$ and $Z \rightarrow ee$ cross-section measurements in proton-proton collisions at $\sqrt{s} = 7$ TeV with the ATLAS Detector*, Tech. Rep. ATL-PHYS-INT-2010-130, CERN, Geneva, Dec, 2010.
- [98] M. Aharrouche, A. Ahmad, J. Alison, O. Arnaez, J. Barreiro Guimaraes da Costa, H. S. Bawa, M. Bellomo, A. Belloni, K. Benslama, E. F. Berglund, et al., *Supporting Document: Total inclusive W and Z boson cross-section measurements, cross-section ratios and combinations in the electron and muon decay channels at 7 TeV based on 300 nb^{-1}* , Tech. Rep. ATL-PHYS-INT-2010-125, CERN, Geneva, Nov, 2010.
- [99] A. Belloni, M. Aharrouche, A. Ahmad, J. Alison, O. Arnaez, J. Barreiro Guimaraes da Costa, H. S. Bawa, M. Bellomo, A. Belloni, K. Benslama, E. F. Berglund, et al., *Measurement of $W \rightarrow l\nu$ charge asymmetry in proton-proton collisions at $\sqrt{s} = 7$ TeV with the ATLAS detector*, Tech. Rep. ATL-COM-PHYS-2010-696, CERN, Geneva, Aug, 2010.
- [100] The ATLAS Collaboration, G. Aad et al., *A measurement of the total W^\pm and Z/γ^* cross sections in the e and μ decay channels and of their ratios in pp collisions at $\sqrt{s} = 7$ TeV with the ATLAS detector*, Tech. Rep. ATLAS-CONF-2011-041, CERN, Geneva, Mar, 2011.
- [101] M. Aharrouche, G. Artoni, J. Barreiro Guimaraes da Costa, M. Bellomo, A. Belloni, E. Berglund, et al., *W and Z cross-sections measurements in proton-proton collisions at $\sqrt{s} = 7$ TeV with the ATLAS Detector*, Tech. Rep. ATL-COM-PHYS-2011-178, CERN, Geneva, Feb, 2011.
- [102] The ATLAS Collaboration, G. Aad et al., *A measurement of the inclusive W^\pm and Z/γ^* cross sections in the e and μ decay channels in pp collisions at $\sqrt{s} = 7$ TeV with the ATLAS detector*, Physical Review D (2011) no. CERN-PH-EP-2011-143, 1–44.

-
- [103] M. Aharrouche, G. Artoni, M. Bellomo, A. Belloni, E. F. Berglund, et al., *Total and differential $W \rightarrow \ell\nu$ and $Z \rightarrow \ell\ell$ cross-sections measurements in proton-proton collisions at $\sqrt{s} = 7\text{TeV}$ with the ATLAS Detector*, Tech. Rep. ATL-COM-PHYS-2011-751, CERN, Geneva, Jun, 2011.
- [104] The CMS Collaboration, A. M. et al., *Measurements of Inclusive W and Z Cross Sections in pp Collisions at $\sqrt{s} = 7\text{ TeV}$* . *oai:cds.cern.ch:1313495*, Journal of High Energy Physics **1** (2011) no. arXiv:1012.2466; CERN-PH-EP-2010-050, .
- [105] A. Sherstnev and R. Thorne, *Parton distributions for LO generators*, Eur. Phys. J. **C55** (2008) 553.
- [106] Jet/EtMiss group, *How to clean jets*, <https://twiki.cern.ch/twiki/bin/view/AtlasProtected/HowToCleanJets>.
- [107] T. Barillari et al., *Local Hadronic Calibration*, Tech. Rep. ATL-LARG-PUB-2009-001-2. ATL-COM-LARG-2008-006. ATL-LARG-PUB-2009-001, CERN, Geneva, Jun, 2008.
- [108] The ATLAS Collaboration, G. Aad et al., *Reconstruction and Calibration of Missing Transverse Energy and Performance in Z and W events in ATLAS Proton-Proton Collisions at 7 TeV* , Tech. Rep. ATLAS-CONF-2011-080, CERN, Geneva, Jun, 2011.
- [109] E. Berglund, *W and Z cross sections in pp collisions at 7 TeV with the ATLAS detector*, Presented at the Berkeley-MIT workshop, MIT, Sep, 2010.
- [110] E. Berglund, *Summary of impact of material distortions on efficiencies (identification, reconstruction, trigger, charge misidentification)*, <https://indico.cern.ch/getFile.py/access?contribId=13&sessionId=10&resId=0&materialId=slides&confId=99950>, November, 2010. Invited talk at the e/γ Workshop in Marseille.
- [111] egamma group, *EgammaIsolationMVA TopTool*, Can be found on the ATLAS twiki: <https://twiki.cern.ch/twiki/bin/view/AtlasProtected/EgammaIsolationMVA TopTool>.
- [112] M. Agustoni et al., *Electromagnetic energy scale in-situ calibration and performance: Supporting document for the egamma performance paper*, Mar, 2011.

- [113] E. Berglund, *Electrons reconstruction and identification with ATLAS and the measurement of W/Z cross sections*, tech. rep., March, 2011. Presented poster at LHCC.
- [114] S. Alekhin, J. Blumlein, and S. Moch, *Update of the NNLO PDFs in the 3-, 4-, and 5-flavour scheme*, Tech. Rep. arXiv:1007.3657. DESY 10-103, Jul, 2010.
- [115] T. H1, *Combined Measurement and QCD Analysis of the Inclusive ep Scattering Cross Sections at HERA*, J. High Energy Phys. **1001** (2009) no. arXiv:0911.0884. DESY09-158, 109. Comments: 61 pages, 21 figures.
- [116] P. Jimenez-Delgado and E. Reya, *Dynamical parton distributions and weak-gauge and Higgs boson production at hadron colliders at NNLO of QCD*, Tech. Rep. arXiv:1006.5890, Jul, 2010.
- [117] Q. Buat, F. Polci, and R. Ishmukhametov, *Systematic uncertainties for dead OTx cut*, <http://indico.cern.ch/getFile.py/access?contribId=6&resId=0&materialId=slides&confId=116188>, 2011.
- [118] Jet/EtMiss group, *MissingETUtility*, <https://twiki.cern.ch/twiki/bin/view/AtlasProtected/MissingETUtility>.
- [119] S. Catani, L. Cieri, G. Ferrera, D. de Florian, and M. Grazzini, *Vector boson production at hadron colliders: a fully exclusive QCD calculation at NNLO*, Tech. Rep. arXiv:0903.2120, Mar, 2009. DYNNLO v1.1.
- [120] The ATLAS Collaboration, G. Aad et al., *Measurement of the production cross section for W -bosons in association with jets in pp collisions at $\sqrt{s} = 7$ TeV with the ATLAS detector*, Phys.Lett.B **698** (2011) no. arXiv:1012.5382. CERN-PH-EP-2010-081, 12.
- [121] A. Ahmad, P. Beauchemin, E. Berglund, et al., *Measurement of the cross-section for jets produced in association with a W -boson in pp collisions at $\sqrt{s} = 7$ TeV*, Tech. Rep. ATL-PHYS-INT-2011-020, CERN, Geneva, Mar, 2011.
- [122] The ATLAS Collaboration, G. Aad et al., *Study of the W -boson production with jets in pp collisions at $\sqrt{s} = 7$ TeV with the ATLAS detector*, Phys. Rev. D (2011) no. ATLAS-STDM-2011-08, 5.
- [123] G. Arabidze, E. Berglund, et al., *Measurement of the cross section for jets produced in association with a W -boson in pp collisions at $\sqrt{s} = 7$ TeV*, Tech. Rep. ATL-COM-PHYS-2011-769, CERN, Geneva, Jun, 2011.

-
- [124] The ATLAS Collaboration, G. Aad et al., *Measurement of the production cross section for Z/γ^* in association with jets in pp collisions at $\sqrt{s} = 7$ TeV with the ATLAS Detector*, Phys. Rev. D (2011) no. ATLAS-STDM-2011-27, . This is a draft of a PRD.
- [125] G. Artoni, E. Berglund, et al., *Measurement of the cross section for jets produced in association with Z bosons*, Tech. Rep. ATL-COM-PHYS-2011-647, CERN, Geneva, Jun, 2011.
- [126] The ATLAS Collaboration, G. Aad et al., *Measurement of the production cross section for Z/γ in association with jets in pp collisions at $\sqrt{s} = 7$ TeV with the ATLAS Detector*, Tech. Rep. ATLAS-CONF-2011-001, CERN, Geneva, Feb, 2011.
- [127] H. Beauchemin, E. Berglund, et al., *Measurement of the cross-section for jets produced in association with a Z -boson in pp collisions at $\sqrt{s} = 7$ TeV*, Tech. Rep. ATL-PHYS-INT-2011-006, CERN, Geneva, Feb, 2011.
- [128] The ATLAS Collaboration, G. Aad et al., *Measurement of the production cross section for W -bosons in association with jets in pp collisions using 33 pb^{-1} at $\sqrt{s} = 7$ TeV with the ATLAS detector*, Tech. Rep. ATLAS-CONF-2011-060, CERN, Geneva, Apr, 2011.
- [129] G. Arabidze, E. Berglund, et al., *Measurement of the cross-section for jets produced in association with a W -boson in pp collisions at $\sqrt{s} = 7$ TeV*, Tech. Rep. ATL-COM-PHYS-2011-280, CERN, Geneva, Mar, 2011.
- [130] The ATLAS Collaboration, G. Aad et al., *Measurement of the production cross section for Z/γ in association with jets in pp collisions at $\sqrt{s} = 7$ TeV with the ATLAS Detector*, Tech. Rep. ATLAS-CONF-2011-042, CERN, Geneva, Mar, 2011.
- [131] H. Beauchemin, E. Berglund, et al., *Measurement of the cross section for jets produced in association with Z bosons*, Tech. Rep. ATL-COM-PHYS-2011-141, CERN, Geneva, Feb, 2011.
- [132] The ATLAS Collaboration, G. Aad et al., *Measurement of the b -jet cross section in events with a W boson in pp collisions at $\sqrt{s} = 7$ TeV with the ATLAS detector*, Phys. Lett. B (2011) no. ATL-COM-PHYS-2011-742, .
- [133] G. Aad, E. Berglund, et al., *Measurement of the b -jet cross section in events with a W boson*, Tech. Rep. ATL-COM-PHYS-2011-411, CERN, Geneva, Apr, 2011.

- [134] The ATLAS Collaboration, G. Aad et al., *A measurement of the ratio of the W and Z cross sections with one associated jet in pp collisions at $\sqrt{s} = 7$ TeV with the ATLAS detector*, Phys. Lett. B (2011) no. CERN-PH-EP-2011-126; arXiv:1108.4908v1, .
- [135] R. Apolle, S. Ask, M. Barisonzi, H. Beauchemin, E. Berglund, W. Brandt, B. Brau, J. Buchanan, D. Casadei, S. Chouridou, C. Doglioni, J. E. Garcia-Navarro, Hansl-Kozanecka, T. Kuhl, Z. Liang, A. Meade, J. Nielsen, M. Sandhoff, T. Sandoval, and C. Xug, *A measurement of the ratio of the $W + 1$ jet to $Z + 1$ jet cross sections with ATLAS*, Tech. Rep. ATL-COM-PHYS-2011-457, CERN, Geneva, May, 2011.
- [136] J. Pumplin et al., *New generation of parton distributions with uncertainties from global QCD analysis*, JHEP **07** (2002) 012.
- [137] A. D. Martin, W. J. Stirling, R. S. Thorne, and G. Watt, *Parton distributions for the LHC*, Eur. Phys. J. **C63** (2009) 189.
- [138] G. Soyez, *The SISCone and anti- k_t jet algorithms*, arXiv:0807.0021 (2008) 4. Presented at the 16th workshop on Deep Inelastic Scattering, 7-11 April 2008, UCL, London, UK.
- [139] D. Lopez Mateos, E. W. Hughes, and A. Schwartzman, *A Simple p_T - and η -Dependent Monte Carlo-Based Jet Calibration*, Tech. Rep. ATL-PHYS-INT-2009-077, CERN, Geneva, Aug, 2009.
- [140] D. W. Miller, A. Schwartzman, and D. Su, *Pile-up jet energy scale corrections using the jet-vertex fraction method*, Tech. Rep. ATL-PHYS-INT-2009-090, CERN, Geneva, Sep, 2009.
- [141] Jet/EtMiss group, *Recommendation for jet quality and selection in events with pile-up*, Can be found on the atlas twiki:
<https://twiki.cern.ch/twiki/bin/view/AtlasProtected/JetQualityAndSelectionForPileup>.
- [142] egamma group, *Energy scale resolution recommendations*,
<https://twiki.cern.ch/twiki/bin/view/AtlasProtected/EnergyScaleResolutionRecommendations>.
- [143] Jet/EtMiss group, *Jet Energy Scale Uncertainty provider*, Can be found on the atlas twiki:
<https://twiki.cern.ch/twiki/bin/view/AtlasProtected/JESUncertaintyProvider>.

- [144] The ATLAS Collaboration, G. Aad et al., *Jet energy resolution and selection efficiency relative to track jets from in-situ techniques with the ATLAS Detector Using Proton-Proton Collisions at a Center of Mass Energy $\sqrt{s} = 7$ TeV*, Tech. Rep. ATLAS-CONF-2010-054, CERN, Geneva, Jul, 2010.
- [145] Jet/EtMiss group, *JERProvider for Winter Conferences 2011*, Can be found on the atlas twiki:
<https://twiki.cern.ch/twiki/bin/view/Main/JetEnergyResolutionProvider>.
- [146] A. C. Caldwell, D. Kollar, and K. Kroninger, *BAT: The Bayesian analysis toolkit*, J. Phys.: Conf. Ser. **219** (2010) 032013. 10 p.